Assessment and Repair of Prestressed Bridge Girders Subjected to Over-height Truck Impacts

September 2025 Final Report	Project number TR202011/TPF-5(462) MoDOT Research Report number cmr 25-013

PREPARED BY:

Haitham AbdelMalek, Francis Ashun, Mohamed Elshazli, Mohanad Abdulazeez, Ahmed Gheni, Ahmed Ibrahim, and Mohamed ElGawady

Missouri University of Science and Technology and University of Idaho

PREPARED FOR:

Missouri Department of Transportation

Construction and Materials Division, Research Section

Technical Report Documentation Page

1. Report No. cmr 25-013	2. Government Accession No.	3. Recipient's Catalog No.
4. Title and Subtitle Assessment and Repair of Prestressed Bridge Girders Subjected to Over-height Truck Impacts		5. Report Date April 2025 Published: September 2025 6. Performing Organization Code
7. Author(s) Haitham AbdelMalek Francis Ashun Mohamed Elshazli Mohanad Abdulazeez Ahmed Gheni Ahmed Ibrahim Mohamed ElGawady		8. Performing Organization Report No.
9. Performing Organization Name and Address Missouri University of Science and Technology 1401 N. Pine St. Rolla, MO 65401 University of Idaho 875 Perimeter Dr. Moscow, ID 83844		10. Work Unit No. (TRAIS) 11. Contract or Grant No. MoDOT project #TR202011/TPF-5(462)
12. Sponsoring Agency Name and Address Missouri Department of Transportation (SPR-B) 1617 Missouri Blvd. Jefferson City, MO 65109		13. Type of Report and Period Covered Final Report (January 2021-April 2025) 14. Sponsoring Agency Code
15. Supplementary Notes Conducted in cooperation with the U.S. Department of Transportation, Federal Highway Administration. MoDOT research reports are available in the Innovation Library at https://www.modot.org/research-publications.		
16. Abstract This research investigates the impact of over-height vehicle collisions on prestressed concrete bridge girders and explores effective repair strategies to restore their structural integrity. The study addresses a critical concern in bridge resilience, as vehicle impacts can cause varying degrees of damage and severe prestressing strands which compromise girder flexural strength and overall safety. A comprehensive approach was employed, integrating numerical modeling and experimental testing to assess damage mechanisms and evaluate the effectiveness of different repair techniques. Key findings include the determination of equivalent static force for semi-tractor trailers and rigid objects. Shear failure was identified as the dominant failure mode of prestressed concrete girders under impact loading. Additionally, accidental lateral eccentricity was found to reduce flexural resistance, necessitating a 15% reduction factor in AASHTO LRFD guidelines. A practical technique for measuring residual prestress forces was developed and validated with an experimental test and found to be conservative by 9.4%. Repair methods using mechanical strand splicing successfully restored up to 95% of the original strength for strand losses ranging from 17% to 33% using innovative confinement techniques. Moreover, externally bonded carbon fiber-reinforced polymer (CFRP) repairs fully restored flexural strength for up to 33% strand loss, with an additional strength reserve of 15%–23%.		
17. Key Words Over-height vehicle collisions; Prestressed concrete; Bridge girders; Repair strategies; Flexural strength; Equivalent static force; Accidental lateral eccentricity; Residual prestress forces; Strand splicing; CFRP	18. Distribution Statement No restrictions. This document is available through the National Technical Information Service, Springfield, VA 22161.	

19. Security Classification (of this report)	20. Security Classification (of this page)	21. No. of Pages	22. Price
Unclassified	Unclassified	271	

Assessment And Repair of Prestressed Bridge Girders Subjected to Over-height Truck Impacts

By

Haitham AbdelMalek, MSc

Francis Ashun

Mohamed Elshazli, PhD

Mohanad Abdulazeez, PhD

Ahmed Gheni, PhD

Ahmed Ibrahim, PhD

Mohamed ElGawady, PhD

Civil, Architectural, and Environmental Engineering Department

Missouri University of Science and Technology

and

University of Idaho

Prepared for

Missouri Department of Transportation (MoDOT)

Copyright permissions

Disclaimer

Acknowledgments

The authors would like to extend their sincere gratitude to all the individuals and organizations that contributed to the success of this research project. Special thanks go to the Pooled Fund Study (PFS) TPF-5(462), with contributors from the Departments of Transportation in Missouri, Alaska, Idaho, Mississippi, Ohio, and Texas, along with the Federal Highway Administration. Their financial support, vision, and commitment to advancing innovative concepts have been instrumental in pushing the boundaries of current practices. The numerical analyses in this project were conducted using the Foundry cluster at Missouri University of Science and Technology and thereby supported in part by the National Science Foundation (NSF) under Grant No. OAC-1919789.

We also wish to extend our sincere gratitude to Missouri S&T for their substantial contributions to this research and their administrative staff. The unwavering support and expertise provided by the dedicated staff from the department of Civil, Architectural, and Environmental Engineering, as well as the Center for Infrastructure Engineering Studies, were instrumental in the success of this project. Their efforts in facilitating research activities, providing technical guidance, and ensuring smooth collaboration were invaluable.

A special note of appreciation goes to Jason Cox for his exceptional technical support throughout the experimental work. His deep knowledge and expertise in bridge repair techniques were pivotal to the successful execution of the repair strategies for the damaged girders. His hands-on assistance and insightful input played a crucial role in refining and implementing the repair methods.

We would also like to express our heartfelt gratitude to John Whitchurch for his extensive contributions. His assistance with testing procedures, instrumentation setup, and the

development of the data acquisition system was critical to the accuracy and reliability of the experimental results.

Finally, we express our heartfelt thanks to PhD student Tousif Mahmoud and many undergraduate students who tirelessly assisted at various stages of the experimental work. Their collective efforts played a key role in bringing this project to completion.

Table of Contents

List of Tables

List of Figures

List of Equations

List of Abbreviations and Acronyms

AASHTO Officials	…….	American Association of State Highway and Transportation
ACI	…….	American Concrete Institute
ASTM	…….	American Society for Testing and Materials
CFRP	…….	Carbon Fiber-Reinforced Polymer
DOT	…….	Department of Transportation
FEM	…….	Finite Element Method
FHWA	…….	Federal Highway Administration
FRCM	…….	Fabric-Reinforced Cementitious Matrix
Inc.	…….	Incorporated
LRFD	…….	Load and Resistance Factor Design
MoDOT	…….	Missouri Department of Transportation
NCHRP	…….	National Cooperative Highway Research Program
NDT	…….	Non-Destructive Testing
NHTSA	…….	National Highway Traffic Safety Administration
NYSDOT	…….	New York State Department of Transportation
PC	…….	Prestressed Concrete
PCI	…….	Precast/Prestressed Concrete Institute
RC	…….	Reinforced Concrete
US	…….	United States of America

Executive Summary

This report presents the findings and recommendations of a comprehensive study on the effects of over-height vehicle collisions on prestressed concrete bridge girders, focusing on damage assessment and effective repair techniques to restore structural integrity. Conducted in collaboration with the Transportation Pooled Fund (TPF-5(462)), this research addresses ongoing challenges in maintaining and repairing bridges impacted by vehicle collisions. Over-height vehicle collisions pose a persistent risk to highway infrastructure, causing varying levels of damage to critical structural elements. Such impacts can significantly reduce girder flexural and shear strength, compromising bridge safety and serviceability. This study simulates impact-induced damage, assesses its severity, and develops effective repair strategies. A combined approach involving experimental testing, numerical modeling, and practical techniques was used to evaluate damage mechanisms and repair effectiveness.

The research objectives encompassed developing a robust framework for damage classification, assessing the residual strength of impacted girders, and evaluating the effectiveness of repair techniques such as mechanical strand splicing and externally bonded carbon fiber-reinforced polymer (CFRP). The experimental program involved conducting twenty-three full-scale tests using fourteen MoDOT Type II prestressed concrete bridge girders, each measuring 46 feet in length. To replicate real-world conditions, the laterally impacted girders sustained strand damage of up to 33% loss. Four-point flexural load testing was performed on both damaged and repaired girders to systematically evaluate their residual flexural capacity and the efficiency of various repair strategies.

Through this study, an equivalent static force (ESF) was established for semi-tractor trailers and rigid objects to aid in impact force estimation. Shear failure emerged as the predominant failure mode under impact loading, highlighting the vulnerability of prestressed girders to such forces. Additionally, accidental lateral eccentricity was found to significantly reduce flexural resistance, warranting the incorporation of a 15% reduction factor in AASHTO LRFD guidelines. Furthermore, an innovative technique for measuring residual prestress forces was developed and validated, achieving an accuracy of 9.6%.

The effectiveness of different repair techniques was evaluated, showing that mechanical strand splicing successfully restored up to 95% of original strength at 17%–33% strand loss but was less effective beyond 25%. Externally bonded CFRP fully restored flexural strength for up to 33% strand loss, with an additional strength reserve of 15%–23%. These findings provide crucial insights for bridge engineers and transportation agencies, offering improved methods for evaluating and repairing impact-damaged girders to ensure long-term safety and serviceability.

These findings contribute valuable insights into the assessment and retrofitting of impact-damaged girders, ensuring their structural performance, safety, and resilience.

Chapter 1. Introduction

1.1 Background

Collisions involving moving objects and bridges present significant challenges in bridge engineering (Shanafelt and Horn 1980; 1985; Harries et al. 2012), with extensive economic, operational, and safety implications. Between 2013 and 2018, the National Highway Traffic Safety Administration (NHTSA) reported an average of 15,000 motor vehicle collisions with bridges annually in the U.S., with the New York State Department of Transportation noting 200 hits per year (Agrawal 2011; Cook, Barr, and Halling 2015). These incidents often result in structural damage, leading to expensive repairs, prolonged closures, and occasionally catastrophic failures. Such collisions rank as the third leading cause of bridge collapses in the U.S.

Over-height truck impacts with prestressed bridge girders are particularly common, with repair costs for damaged girders reaching up to 69% of replacement costs (Dunne and Eric, Thorkildsen 2020; Radlinska et al. 2012). Beyond financial losses, these collisions disrupt transportation networks, threaten public safety, and highlight vulnerabilities in the aging bridge inventory. For instance, the 2013 collapse of the I-5 Bridge over the Skagit River in Washington State, caused by a truck collision, led to significant closures and one injury (Cao et al. 2021). These issues are exacerbated by the condition of U.S. bridges, 25% of which are classified as structurally deficient or functionally obsolete (Azizinamini 2020). Damage to such aging structures increases their susceptibility to failure, complicating bridge management and maintenance.

1.2 Problem statement and research significance

Over-height truck collisions with bridge girders present an escalating threat to the safety of bridge structures in the United States. These impacts, often concentrated at the mid-span of girders, result in severe flexural deficiencies that can lead to catastrophic failures, including potential bridge collapse. Despite the serious consequences, there are no comprehensive guidelines for assessing and restoring damaged girders. Furthermore, research on effective repair strategies for prestressed girders remains limited. This critical gap motivates the current research, which seeks to deepen the understanding of girder behavior under lateral impacts and identify optimal repair methods.

Prestressed concrete girders subjected to impact loads exhibit complex structural and dynamic behaviors influenced by factors such as prestressing forces, material properties, impact speed, mass, and contact area. These challenges necessitate a multidisciplinary approach that integrates experimental, analytical, and numerical methods to develop a robust understanding of girder responses.

Singular approaches to addressing these challenges are insufficient:

- Experimental testing provides valuable data but is constrained by high costs, extended timelines, and scalability limitations.
- Numerical simulations enable diverse scenario modeling but depend on assumptions and require empirical validation.
- Analytical models offer theoretical insights but often oversimplify complex interactions, limiting practical applicability.

To overcome these limitations, an integrated research strategy is essential. Controlled experiments provide critical data on failure mechanisms and deformation patterns. Numerical simulations model high-energy impacts and assess complex damage scenarios. Analytical models offer foundational insights and support the interpretation of experimental and simulation results. Together, these methods create a comprehensive framework for evaluating damage and developing effective retrofitting strategies.

Existing repair methods, such as internal strand splicing and fiber-reinforced polymer (FRP) wrapping, remain insufficiently validated under full-scale testing conditions. This lack of validation leaves bridge owners and engineers without clear guidance on whether to repair, replace, or leave girders untreated. This study evaluates these advanced repair techniques to determine their effectiveness in restoring the flexural resistance of damaged girders. By integrating these findings into practical standards and guidelines, the research aims to improve bridge resilience and ensure the safety of critical infrastructure.

This research addresses an urgent infrastructure issue with potentially life-threatening consequences. Bridging the knowledge gap in damage assessment and repair strategies will provide actionable insights for state Departments of Transportation and bridge engineers, ultimately contributing to the safety, resilience, and longevity of bridge infrastructure.

1.3 Research tasks

The main objective of this research is to evaluate the damage caused to bridge girders by over-height truck impacts and to suggest repair methods. Specifically, the project seeks to:

- Assess the remaining load-bearing capacity of the damaged bridge girders to help stakeholders, such as Department of Transportation (DOT) engineers, and prioritize which girders require repair.
- Develop analytical and numerical models that enable bridge engineers to assess the residual strength of damaged girders.
- Identify the most effective repair method to restore the original strength of the damaged girders.

1.4 Methodology

To replicate impact damage, an impact simulator was developed at the structural laboratory of the civil engineering department at Missouri university of science and technology (Figure 1-1). The simulator includes a 13-foot-high elevated track and a 7,000 lb. steel impact bogie (Figure 1-1). The 60-foot-long track, fabricated in-house, generates speeds up to 22 ft/sec for the bogie.

Fourteen 46-feet MoDOT type II prestressed concrete girders were fabricated at Coreslab Structures Inc. and transported to the lab after 28 days of curing. Twelve girders were constructed with twelve 0.5-inch 270 ksi low-relaxation prestressing strands (Figure 1-2a), while two were reinforced with 16 strands (Figure 1-2b). One girder had increased midspan shear reinforcement, with the remaining 13 having identical shear reinforcement (Figure 1-2c).

The testing involved total of twenty-two sub-tests, covering a range of conditions as follows and shown in Table 1-1. Nine lateral impact tests on eight girders with varying boundary conditions: free top flange, restrained top flange, and free top flange with intermediate diaphragm. Two flexural four-point static loading on two girders to determine their as-built flexural capacity. Three residual capacity tests on three girders with 25%, 50% and 63% prestressing loss. One test of a three-point out-of-plane loading on one girder to study the out-of-plane flexural resistance. Four-point static loading on seven repaired girders to determine their flexural capacity. The girders were repaired using strand splicing, externally bonded CFRP, and a hybrid approach.

Figures 1-3 and 1-4 provide an overview of the research plan and the experimental program, respectively. Figure 1-3 summarizes the research plan, highlighting the tests conducted and the repair strategies implemented. The detailed experimental program, including methodologies and setups, is outlined in Figure 1-4.

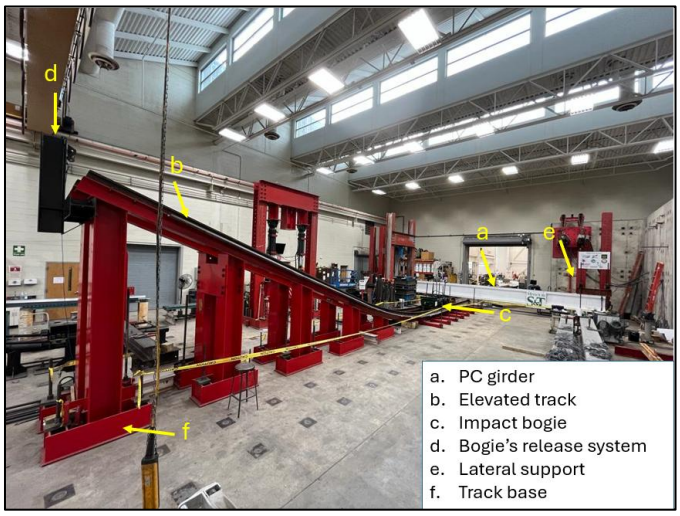

Figure 1-1. Impact simulator test setup

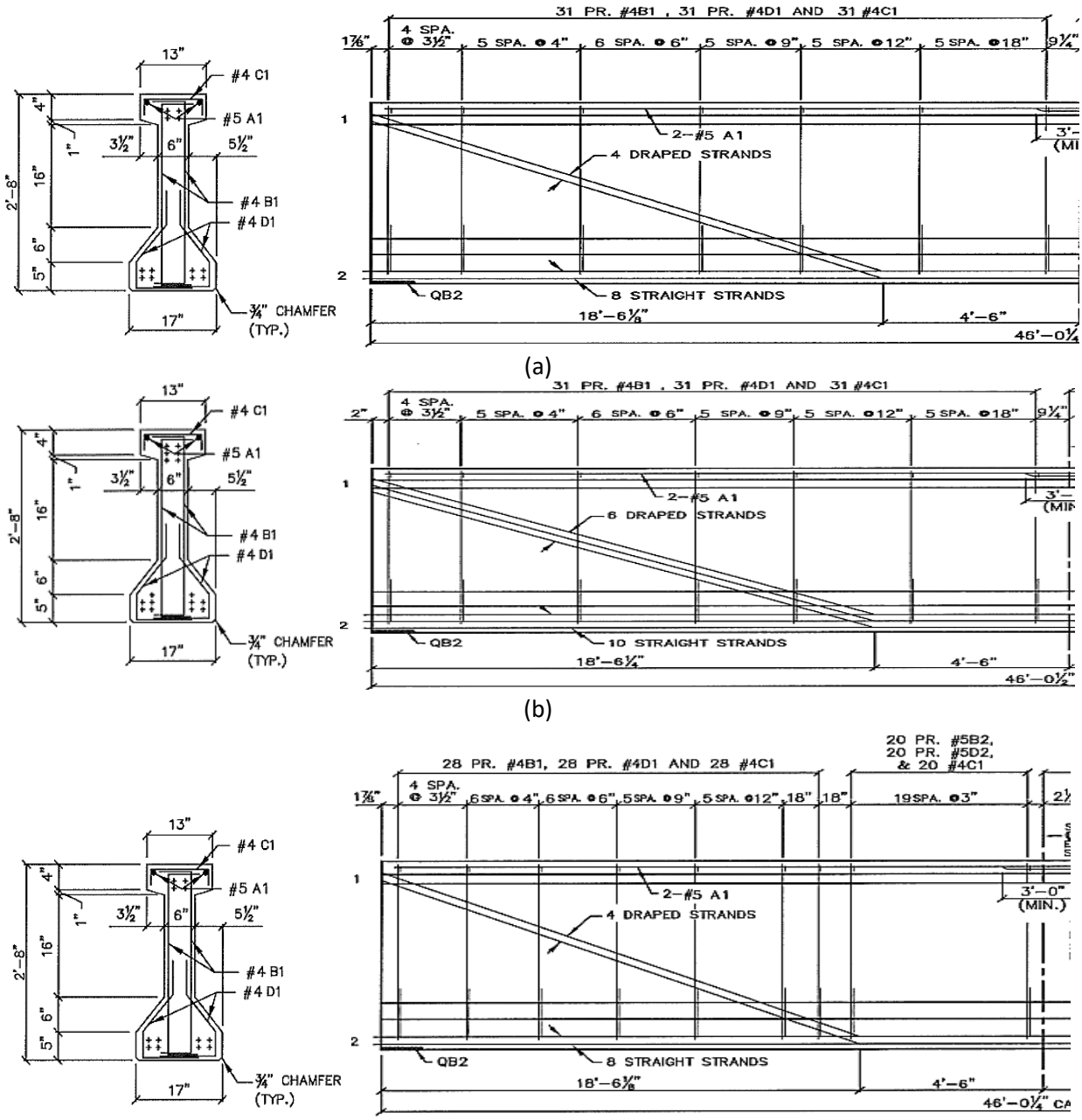

Figure 1-2. Test specimens reinforcement details (a) 12 strands, (b) 16 strands, and(c) 12 strands – additional stirrups

1.5 Report contents

This chapter serves as an introductory chapter, offering a broad overview of the study. It includes a concise background of the topic, a clear description of the research problem, and the objectives driving the investigation. Additionally, this chapter outlines the methodology employed to systematically explore the subject matter, establishing a foundation for the detailed discussions that follow.

Chapter 2 presents an extensive literature review, structured to cover four major themes. The first section provides an overview of the problem, examining the impact of over-height vehicles on bridge prestressed concrete (PC) girders and highlighting the significance of this issue. The second section focuses on the role of numerical modeling in simulating these impacts, showcasing its importance in understanding and predicting damage mechanisms. The third section offers an in-depth synthesis of damage assessment techniques, evaluating traditional methods alongside emerging technologies. Finally, the fourth chapter concludes with an exploration of repair techniques, presenting a critical analysis of their effectiveness and applicability in various scenarios.

Chapter 3 presents the development and validation of a three-dimensional nonlinear finite element (FE) model. This chapter provides a detailed discussion of the modeling process. Using the validated FE model, two parametric studies are described, focusing on two critical themes. The first explores the failure modes and impact loading experienced by PC girders subjected to over-height vehicle collisions. The second examines the effects of biaxial bending, resulting from the accidental eccentricity of asymmetric prestressing strands, on the flexural strength of the girders.

Chapter 4 offers a comprehensive overview of the experimental impact program. The chapter begins with a detailed description of the impact simulator used in the study, followed by an analysis of the various damage categories observed, ranging from minor to severe, under different impact scenarios.

Chapter 5 discusses the test setup and results of flexural strength testing, focusing on the residual flexural capacity of damaged girders. The practical non-destructive field method to determine the prestress losses is presented alongside its validation through destructive testing.

Chapter 6 shifts focus to the repair methodologies. Primary repair techniques, including mechanical splicing and externally bonded carbon fiber-reinforced polymer (CFRP), are described in detail. The chapter provides practical insights into repair installation procedures and offers recommendations for implementation. The effectiveness of these repair methods is evaluated through destructive flexural testing, with results thoroughly analyzed and discussed.

Chapter 7 concludes the report with a summary of findings and actionable design recommendations. These conclusions and guidelines are presented to aid in the development

of more robust and resilient solutions for addressing the damage caused by over-height vehicle impacts on PC girders.

Appendix A presents the numerical parametric studies

Appendix B provides detailed information on the design and fabrication of the impact simulator.

Appendix C presents more information regarding the impact testing results.

Appendix D outlines the material testing procedures.

Appendix E includes additional details on the experimental lateral static loading.

Appendix F covers the calculation of effective prestress, residual flexural strength, and load rating. Additionally, a load rating assessment is included, serving as a foundation for developing repair techniques.

Appendix G presents a numerical parametric study on impact using rigid objects.

Appendix H details the experimental testing of prestressing strands under high strain rates.

Appendix I: provides experimental testing of prestressing strands under high strain rates.

Table 1-1. Overview of the experimental program

Girder	NDR - Impact	DR - Impact	NDR-ID - Impact	None	C - Repair	S - Repair	H - Repair	In-plane (Flexural testing)	Out-of-plane (Flexural testing)
Girder G01	✓			✓				-	
Girder G02	✓			✓				✓	
Girder G03		✓		✓				✓	
Girder G04		✓[a]		✓				✓	
Girder G05		✓✓[a,b]				✓		✓	
Girder G06	✓			✓				✓[d]	
Girder G07			✓[c]		✓			✓	
Girder G08			✓		✓			✓	
Girder G09				✓					✓
Girder G10						✓		✓	
Girder G11						✓		✓	
Girder G12						✓		✓	
Girder G13							✓	✓	
Girder G14				✓				✓[d]	

No deck restrainer: NDR; Deck restrainer: DR; No deck restrainer with intermediate steel diaphragm: NDR-ID

C: Externally bonded CFRP; S: Mechanical splicing; H: Hybrid of externally bonded CFRP and mechanical splicing

[a] Fork-headed impactor; [b] Double impact; [c] Increased shear stirrups; [d] Sixteen prestressing strands girder

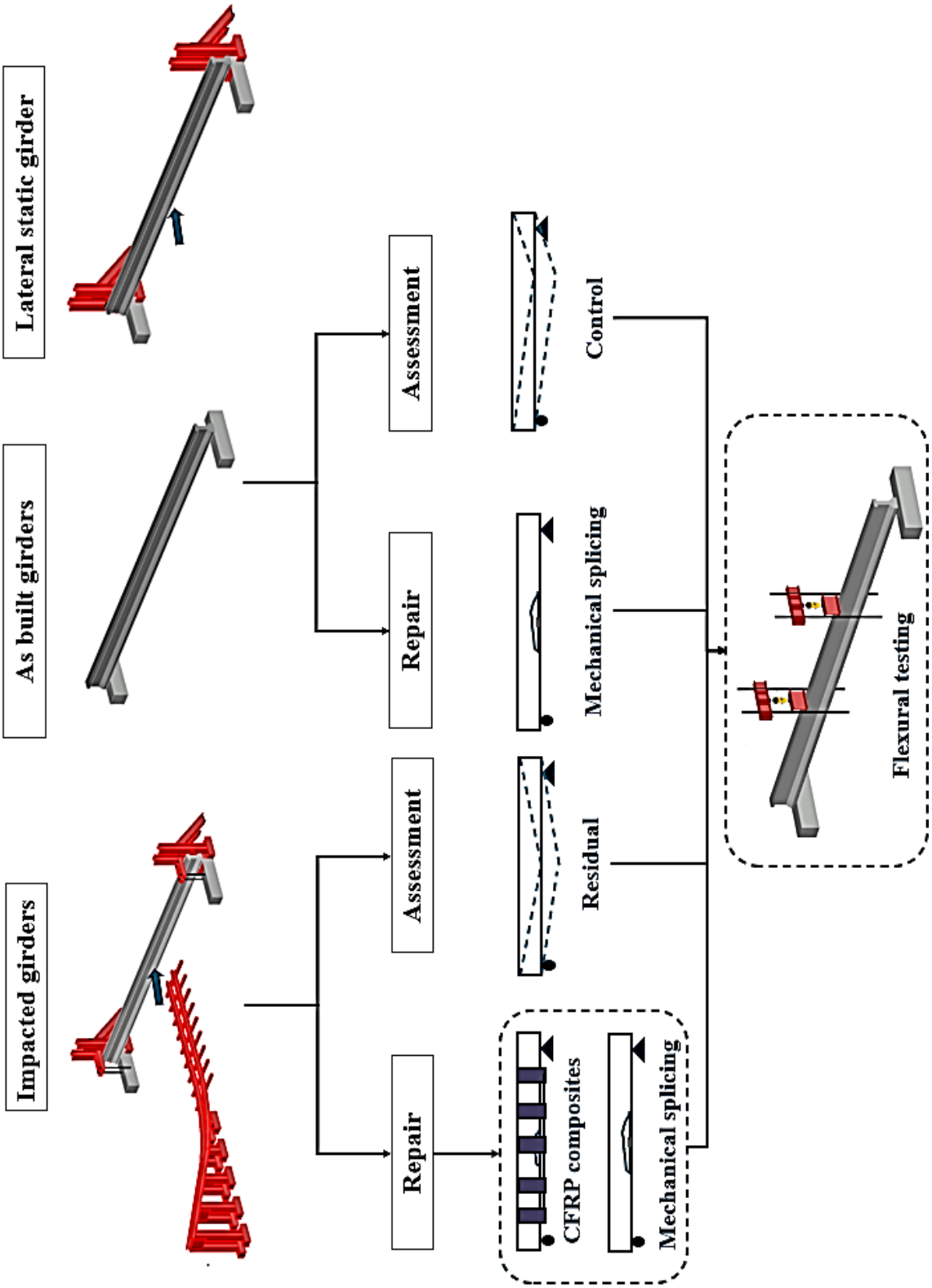

Figure 1-3. Graphical abstract for the research plan

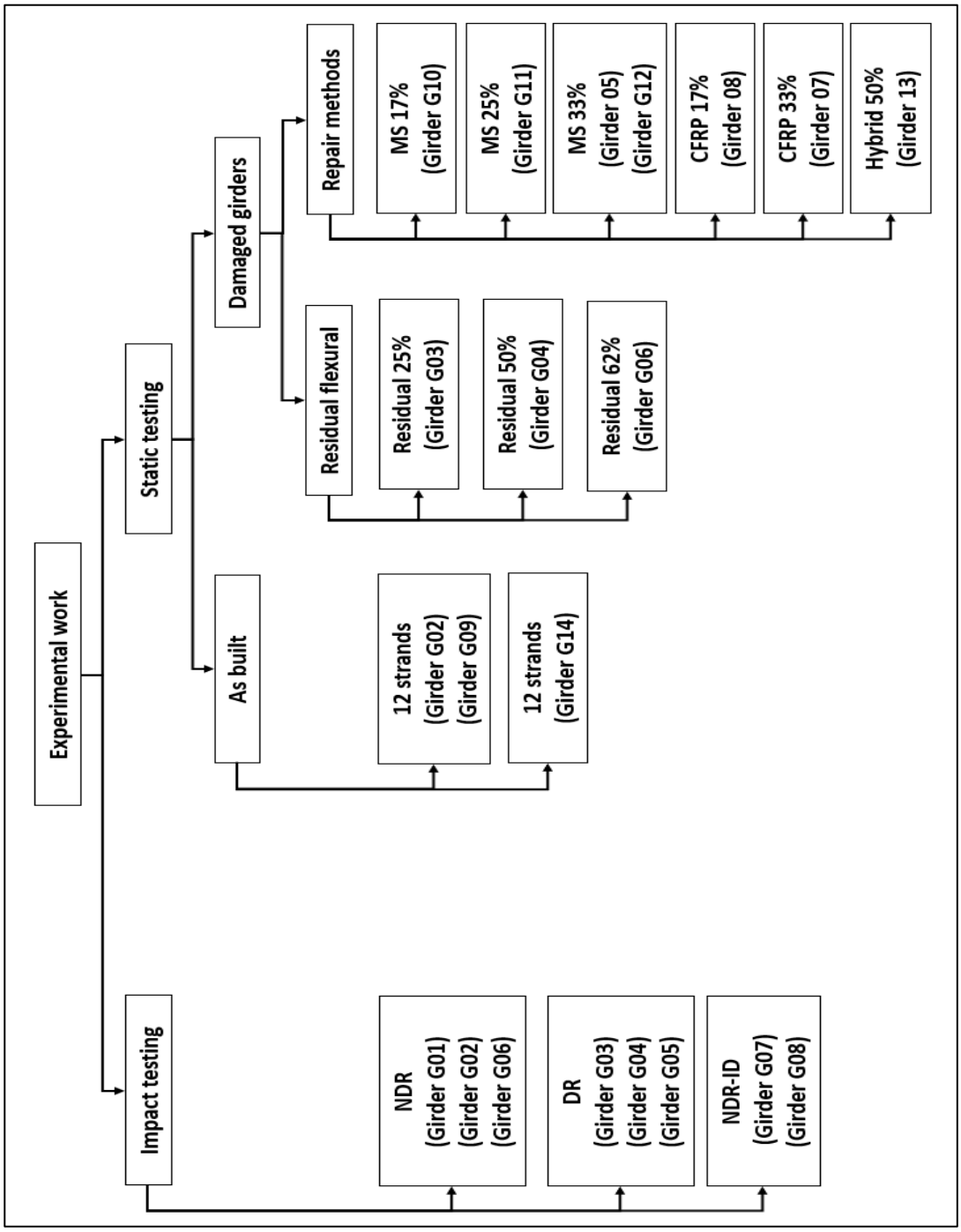

Figure 1-4. Flowchart of the experimental work

No deck restrainer: NDR; Deck restrainer: DR; No deck restrainer with intermediate steel diaphragm: NDR-ID

MS: Mechanical splicing; CFRP: Externally bonded CFRP; Hybrid: Combination of mechanical splicing and externally bonded CFRP

Chapter 2. Literature Review

This chapter presents a comprehensive review of existing literature on the behavior of bridge girders subjected to over-height vehicle collisions. It focuses on both impact experimental and numerical investigations, damage mechanisms, and impact effects. The review also explores key studies on damage assessment and the various methods proposed to restore the structural integrity of damaged girders, such as external post-tensioning, carbon fiber-reinforced polymer (CFRP) wrapping, and strand splicing.

2.1 Impact testing and simulation

2.1.1 Prestressed concrete bridge girders

Despite the severity of over-height vehicle collisions, experimental research on the impact behavior of prestressed concrete girders remains limited. Jing et al. (2016) conducted the only experimental study involving vehicle impacts with prestressed concrete girders. Their experiment tested a full-scale AASHTO Type I prestressed girder under lateral impact using a 9,000-lb. cart traveling at 22.5 ft/sec (Jing, Ma, and Clarke 2016). The girder, 56 feet long with a 36.5-foot span, was simply supported on concrete footings with lateral supports at the web ends. However, no restraints were applied to prevent upward movement or to restrain the top flange. While the study provided valuable data on concrete strain and vertical displacement, impact forces were not measured. The beam failed due to punching shear, underscoring the significant influence of rigid impactors on girder response and the need for further research.

Finite element (FE) modeling of prestressed bridge girders under impact loads is also underdeveloped. Jing et al. (2016) developed an FE model using LS-DYNA software for the experimentally tested beam. The model was calibrated based on the measured concrete strain and vertical displacement data. However, the validated model was not leveraged for comprehensive analyses.

More recently, Oppong, Saini, and Shafei (2021b) validated FE models for reinforced concrete (RC) beams using data from three previous experimental studies (Fujikake, Li, and Soeun 2009; Yoo, Banthia, and Yoon 2017; Wei et al. 2021). These models utilized the Karagozian and Case Concrete (KCC) material model in LS-DYNA to simulate concrete behavior (Wu and Crawford 2015). However, the research did not extend to the impact performance of prestressed girders. Instead, it focused on assessing the performance improvements of bridge girders subjected to over-height collisions through the application of ultra-high-performance concrete (UHPC) in both as-built and repair scenarios. One key parameter investigated was the effect of impact surface area on the performance of impacted girders. The simulations included three impact objects: a concrete conduit pipe, a cylindrical steel tank, and a semi-trailer truck. The findings indicated that concrete pipes and steel tanks generated significantly higher impact forces and girder deflections compared to semi-trailer trucks, a result attributed to the greater rigidity and smaller contact areas of the pipes and tanks. Oppong, Saini, and Shafei (2021a) extended their

research to analyze impact forces in greater detail. This follow-up study provided detailed impact time histories for various objects. Unlike the earlier study, which utilized the KCC model, this research adopted the Continuous Surface Cap Model (CSCM) (Schwer and Murray 2002) for concrete material simulation. However, the validity of switching to the CSCM model was not explained, leaving questions about the consistency and applicability of the chosen material model.

2.1.2 Non-prestressed concrete girders

Most experimental studies on impact behavior have focused on non-prestressed reinforced concrete (RC) beams. These beams predominantly featured rectangular cross-sections (N. Kishi, Mikami, et al. 2002; N. Kishi et al. 2006; Fujikake, Li, and Soeun 2009; Adhikary, Li, and Fujikake 2015; Saatci and Vecchio 2009; Zhan, Wang, and Ning 2015; Pham and Hao 2017; Pham, Hao, and Hao 2018; Li, Chen, and Hao 2019; W. Zhao, Qian, and Jia 2019; Fu et al. 2020), with some studies involving T-shaped sections (Xu et al. 2012). While the majority of tests utilized drop-weight impactors, one study employed a pendulum impactor (Xu et al. 2012). Tested beams spanned between 4.6 and 19.7 feet, with impact masses ranging from 68 to 772 lb. and impact speeds varying from 3.3 to 49.8 ft/sec. These conditions produced peak impact forces between 14.6 kips and 507 kips.

Shear failure was the predominant failure mode in RC beams under impact loads, similar to the failure mode observed in prestressed concrete (PC) girders (Jing, Ma, and Clarke 2016). This failure is often manifested as a shear plug, characterized by cone-shaped concrete displacement originating at the impact point due to excessive shear forces. Additionally, the impactor's material properties and geometric shape significantly influenced localized failures, such as spalling of concrete.

Research on non-prestressed RC beams under impact loads using FE models was carried out to investigate different parameters that affect the impact load demand and the beam response. The peak impact force was found to be directly influenced by the beam characteristics, impactor stiffness, and contact area. Furthermore, there was a consensus on a direct increase of the peak impact force with increasing the impact speed. That force increase was accredited to the increase of kinetic energy of the impact. The effect of the beam span was found to be insignificant to the peak impact force, while it had a great influence on the beam vibrations and thus on the beam deflection and damage (N. Kishi, Konno, et al. 2002; Adhikary, Li, and Fujikake 2015; D. B. Zhao, Yi, and Kunnath 2018; Pham and Hao 2018; D. B. Zhao, Yi, and Kunnath 2018; Norimitsu Kishi 2019; Li, Chen, and Hao 2019; Hao et al. 2021).

2.2 Static testing and simulation of prestressed bridge girders

While there has been only one experimental test of prestressed girders under impact loads, extensive research has examined the failure modes of prestressed concrete (PC) girders under static loading, focusing on flexural behavior (Olsen 1992; Deng et al. 2001; Ludovico 2005; Higgs, Barr, and Halling 2015; Nanni 2018) and shear behavior(Shahawy and Batchelor 1996;

Griffin 2014; Chehab et al. 2018). The tested girders spanned between 25 ft and 65 ft, with flexural and shear failure emerging as the primary failure modes, consistent with the respective experimental emphasis. PC girders designed to fail in flexure, with adequate shear reinforcement, can fail under static loading in shear due to relatively low shear span-to-depth ratios (a/d) ranging from 2 to 3.4 (Shahawy et al. 1996; Chehab et al. 2018).

2.3 Damage classification and residual flexural strength of girders

Lateral impact loads from over-height vehicles can cause significant structural damage, often leading to flexural deficiencies in the middle portions of exterior girders. Several reports have provided frameworks for categorizing damage to girders following vehicle impacts (Shanafelt and Horn, 1980, Shanafelt and Horn, 1985, Harries et al., 2012, Feldman et al., 1996, WisDOT Report 2019 (Tabatabai and Nabizadeh, 2019), and Nebraska DOT 2020). The classification based on the report by the National Cooperative Highway Research Program NCHRP 20-07/Task 307 has been widely recognized as the most comprehensive system for categorizing the extent of damage due to its simplicity and practicality (Harries et al., 2012). This classification system distinguishes between various levels of structural impairment, ranging from superficial surface cracks to severe flexural deficiencies and complete girder failure (Table 2-1).

Research consistently identifies visual inspection as the most employed method for assessing damage to bridge girders following lateral vehicle impacts. This technique is particularly effective for detecting surface-level damage, such as cracks and spalling on concrete surfaces. Visual inspection allows engineers to quickly determine the need for more detailed assessments or immediate repairs based on visible structural distress. However, it is important to note that visual methods may overlook subsurface damage or internal structural compromise, which could lead to misjudgments in the assessment of structural integrity.

Reports have highlighted that only 10-15% of departments of transportation across the United States apply non-destructive testing (NDT) techniques for assessing girder damage (Tabatabai and Nabizadeh 2019). NDT techniques, such as ground-penetrating radar, ultrasonic testing, and infrared thermography, offer the potential to detect hidden damage, including voids, fractures, and compromised prestressing strands, thus providing a more comprehensive evaluation of structural health (Helal, Sofi, and Mendis 2015; Jia et al. 2023).

As shown in Table 2-1, prestress loss is a major parameter in damage classification. While there has been no specific research on determining the residual stresses in prestress strands post-vehicle impact, the literature has several methods to estimate the prestress losses, and they are divided into destructive and non-destructive approaches.

2.4 Non-destructive testing of prestress losses

Non-destructive methods assess prestress losses without causing harm to the structure, making them more practical for operational assessments. Vibration-based techniques analyze natural

frequencies and dynamic responses to estimate prestress levels (Agredo Chávez et al. 2022; Jia et al. 2023; Helal, Sofi, and Mendis 2015).

These approaches are non-invasive and widely applicable but require skilled interpretation, and their accuracy depends heavily on selecting appropriate modal characteristics. Another promising non-destructive approach involves inducing small deflections in exposed strands and correlating these deflections with prestress force levels (Civjan et al. 1998). This method uses a prototype device to apply lateral forces and measure the resulting axial load, achieving an accuracy within 10% of actual prestress levels. Despite being limited to cases with exposed strands, this method represents an important step toward more reliable field evaluations.

2.5 Destructive testing for prestress losses

Destructive methods, such as static load testing (Garber et al. 2015; Labia and Douglas 1997; Azizinamini et al. 1996) and tendon severing (Czaderski and Fh, 2006~~)~~, offer high accuracy but at significant cost and damage. Static load testing involves applying vertical loads to induce cracking, enabling the evaluation of flexural strength and compressive stress in the bottom flange relative to prestress levels. Although precise, this method is costly and permanently damages the structure, making it suitable primarily for research or extreme cases. Tendon severing, a semi-destructive approach, involves cutting a single strand and measuring strain before and after severing (Czaderski and Fh, 2006). While less damaging than the static load testing destructive tests, it demands precise strain and displacement measurements, which can be technically challenging.

Table 2-1. Damage classification for prestressed concrete girders (Harries et al. 2012)

Damage level	Description of damage	Strand loss	Camber
Minor	Concrete with shallow spalls, nicks and cracks, scrapes, and some efflorescence, rust, or water stains. Damage does not affect member capacity. Repairs are for aesthetic and preventative purposes only (NCHRP 280).	No exposed strands	No effect of girder camber
Moderate	Larger cracks and sufficient spalling or loss of concrete to expose strands. Damage does not affect member capacity. Repairs are intended to prevent further deterioration (NCHRP 280).	Exposed strands, no severed strands	No effect of girder camber
Severe I	Damage affects member capacity but may not be critical – being sufficiently minor or not located at a critical section along the span. Repairs to prevent further deterioration are warranted although structural repair is typically not required.	Less than 5% strand loss	Partial loss of camber
Severe II	Damage requires a structural repair that can be affected using a non-prestressed/post-tensioned method. This may be considered as repair to affect the STRENGTH (or ultimate) limit state.	Strand loss greater than 5% and less than 20%	Complete loss of camber
Severe III	Decompression of the tensile soffit has resulted. Damage requires structural repair involving replacement of prestressing force through new prestress or post-tensioning. This may be considered as repair to affect the SERVICE limit state in addition to the STRENGTH limit state.	Strand loss exceeding 20%. In longer and heavily loaded sections, decompression may not occur until close to 30% strand loss.	Vertical deflection less than 0.5%
Severe IV	The damage is too extensive. Repair is not practical, and the element must be replaced.	Strand loss greater than 35%	Vertical deflection greater than 0.5%

2.6 Mechanical strand splicing in repair

Few studies have investigated strand splicing technique for repairing prestressed concrete girders damaged by vehicle collisions (Shanafelt and Horn, 1985; Olsen, 1992; Labia and Douglas, 1997; Zobel and Jirsa, 1998; Gangi, 2015; Jones et al., 2017; Nanni, 2018). While the NCHRP 280 report conducted pioneering work on strand splicing, the repaired girder using mechanical splicing was only loaded up to 96% of the service loads, without evaluation at the ultimate strength state. Zobel and Jirsa (1998) investigated the performance of three different types of strand splicing under service loads. The study recommended limiting strand splicing to cases involving up to 15% loss of strands.

The NCHRP 20-07/Task 307 recommended designing spliced strands by multiplying the spliced strand strength by a factor of 0.85. However, data available in the literature does not support this design approach. Figure 2-1 illustrates the relationship between the restored flexural strength ratio and the percentage of spliced strands collected from the literature review (Olsen 1992; Labia and Douglas 1997; Gangi 2015; Jones et al. 2017; Nanni 2018). As shown in Figure 2-1, the literature is limited to only four girders involving 8-15% strand loss. Additionally, those studies exhibited significant scatter in the results, frequently falling below the NCHRP 20-07/Task 307 estimate.

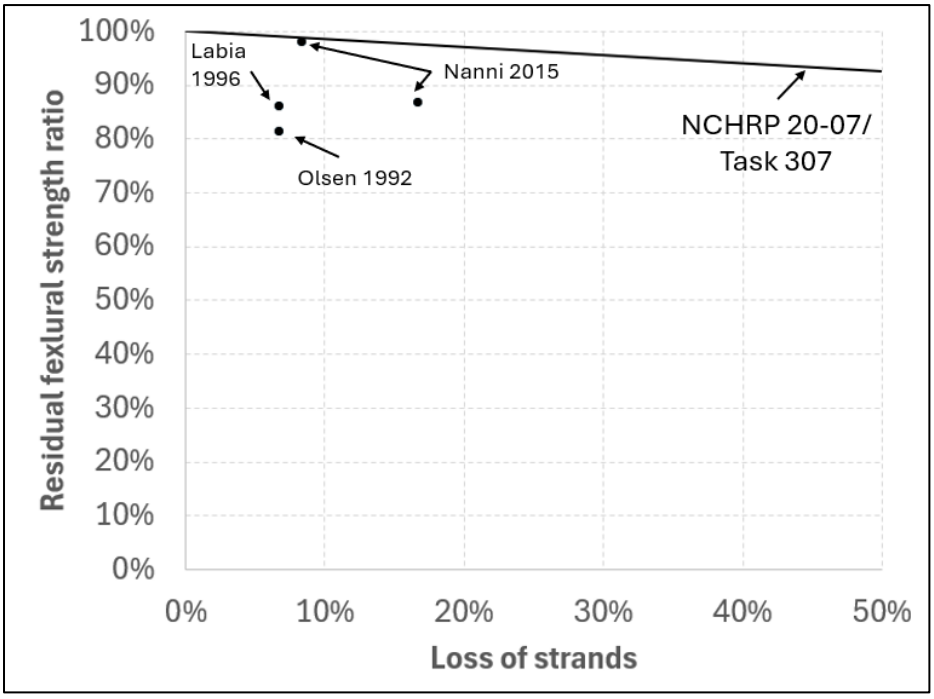

Figure 2-1. Literature data for strand splice repaired girders

2.7 Fiber-reinforced polymer (FRP) composites in repair

Fiber-reinforced polymer (FRP) materials, particularly carbon fiber-reinforced polymer (CFRP), provide several advantages over traditional repair methods such as mechanical splicing, external post-tensioning, and metal jacketing. These advantages include a high strength-to-weight ratio, corrosion resistance, and ease of application (Harries et al., 2012). As a result, CFRP repairs have quickly become attractive alternatives to older methods like concrete jacketing and externally bonded steel plates (Ludovico 2005). Studies have demonstrated that CFRP repairs of prestressed concrete (PC) girders can restore 100% of the original girder capacity (Nanni 2018; Wipt 2004; Ludovico 2005; ElSafty, Graeff, and Fallaha 2014).

However, challenges such as premature debonding and brittle failure have been identified, emphasizing the need for improved confinement strategies (Jones et al., 2017; Nanni, 2018). Figure 2-2 illustrates the relationship between the restored flexural strength ratio and the loss of strands as reported in the literature. The graph highlights that experimental testing on full-scale prestressed concrete girders is limited. For full-scale girders with 8-17% strand loss, the restored flexural strength ranged from 93% to 115% of the strength of the reference specimen. In cases with 33% strand loss, the restored flexural strength ranged from 86% to 102%. Debonding of longitudinal plies is the most common failure mode reported by previous studies. This type of failure is often initiated by the debonding of the anchorage system.

Half-scale prestressed girder testing with various CFRP U-wrapping configurations (ElSafty, Graeff, and Fallaha, 2014) has also been conducted. At 20% strand loss, significant variation in restored flexural strength was observed, ranging from 103% to 138%. The study recommended that for optimal flexural strength, the spacing between U-wraps should range from half to the full depth of the girder.

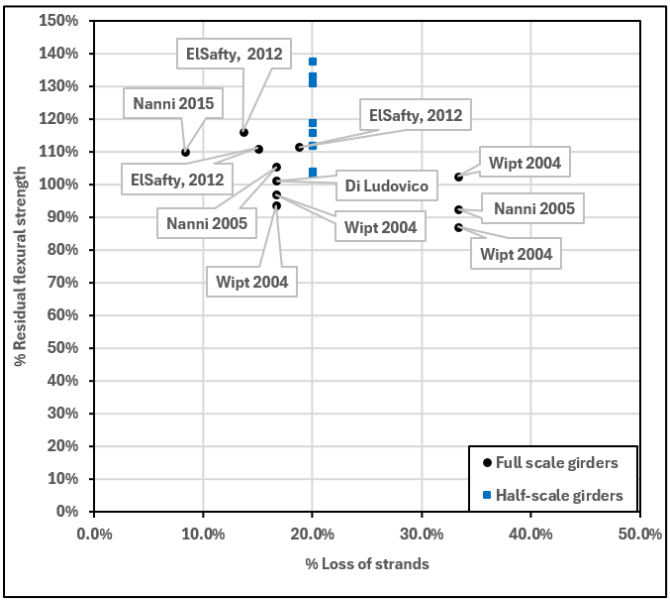

Figure 2-2. Literature data for CFRP repaired girders

Chapter 3. Developing a 3D Non-linear Finite Element Model

3.1 Introduction

The primary objective of this stage was to develop a highly accurate 3D non-linear finite element (FE) model capable of capturing the complex behavior of prestressed concrete under various failure modes and loading conditions. To achieve this, several past studies were utilized for validation, comparing the developed FE model against experimental results from these studies. This validation process ensures that the model reliably reflects the real-world performance of prestressed concrete girders under different scenarios.

3.2 Finite element modeling and validation

LS-DYNA, a state-of-the-art general-purpose multiphysics software, was utilized in this study. The FE model was validated using thirteen physical test models, comprised of four prestressed girders subjected to static loading and nine reinforced concrete girders subjected to impact loading. The static tests included a 63.5 feet long AASHTO Type III girder with a composite deck slab (Olsen 1992), a 45.9 feet long Missouri Department of Transportation (MoDOT) Type II girder (Ludovico 2005), and two 36 feet long AASHTO Type II girders (Chehab et al. 2018), all of which were tested to failure in flexure and shear. For dynamic impact validation, nine reinforced concrete beams, each 5.6 feet in length, were selected from experimental tests (Fujikake, Li, and Soeun 2009).

The static models under static load testing were primarily implemented to validate modeling techniques, including the strand prestressing process, material models, boundary conditions, loading techniques, etc. The validation of impact load models focused on verifying the accuracy of dynamic characteristics, the contact algorithm, and contact scale factors. The FE model's performance was evaluated by comparing its results against experimental data, with a particular focus on key engineering demand parameters such as force-deflection curves and impact response time histories.

3.3 Modeling parameters

3.3.1 Concrete modelling

Concrete elements were modeled using under-integrated eight-node constant stress solid elements, which are susceptible to non-physical zero-energy deformation modes, known as hourglass modes. To address this, a stiffness-based Flanagan-Belytschko hourglass control algorithm was employed, introducing internal forces to enhance system stiffness. An hourglass coefficient (QH) of 0.03 was applied to all models. The hourglass energy, representing the work done by these artificial forces, was closely monitored to ensure it remained below 10% of the internal energy. If this threshold was exceeded, adjustments to the model were made to preserve the physical accuracy and stability of the simulations, as recommended by LS-DYNA.

These guidelines ensure the hourglass control mechanism effectively mitigates non-physical deformations without significantly altering the model's physical behavior.

The Karagozian & Case Concrete Model-Release III (KCC model) was integrated into LS-DYNA. The KCC model is widely recognized for its reliability in predicting the dynamic response of concrete structures, with numerous studies affirming its accuracy (Wu and Crawford 2015). This model incorporates three failure surfaces to account for strain hardening, damage, and strain softening effects. Parameters were auto-generated by specifying the compressive strength, concrete density, and Poisson's ratio. The compression and tension damage evolution parameters, b1 and b2 respectively, were calculated using empirical equations developed by Wu and Crawford (2015) as shown in Table 3-1. Adjustments to these parameters were necessary for mesh regularization and accurate representation of local failure zones. The parameter ω was taken at a value of 0.5 for all models as recommended by previous studies (Wu and Crawford 2015; Wu, Crawford, and Magallanes, n.d.) Under high loading rates, material performance was modified using dynamic increase factors (DIF) to account for strain rate effects per Equations 3.1 and 3.2 (Wu and Crawford 2015).

$$\text{Compression DIF} = r_{fc} = \begin{cases} \left(\frac{\acute{\varepsilon}}{\acute{\varepsilon}_s}\right) & \acute{\varepsilon} \leq 10^6\, /s \\ \gamma \left(\frac{\acute{\varepsilon}}{\acute{\varepsilon}_s}\right)^{1/3} & \acute{\varepsilon} > 10^6\, /s \end{cases}$$

Equation 3-1

$$\text{Where, } \gamma = 10^{6.156\alpha - 2}\ , \alpha = \frac{1}{5 + 0.9\, f_c^{'}}$$

Equation 3-2

$$\text{Tension DIF} = r_{ft} = \begin{cases} \left(\frac{\acute{\varepsilon}}{\acute{\varepsilon}_s}\right)^{\delta} & \acute{\varepsilon} \leq 1.0/s \\ \beta \left(\frac{\acute{\varepsilon}}{\acute{\varepsilon}_s}\right)^{1/3} & \acute{\varepsilon} > 1.0/s \end{cases}$$

Equation 3-3

$$\text{Where, } \beta = 10^{6\delta - 2}\ , \delta = \frac{1}{1 + 0.8\, f_c^{'}}$$

Equation 3-4

Where $\acute{\varepsilon}$ is the strain rate; $\acute{\varepsilon}_s$ is a reference strain in compression and tension with a value of 3×10^{-5} /s and 10^{-6}/s, respectively; f'_c is the concrete compressive strength in MPa. Poisson's ratio was taken as 0.2 for all models (Wight and MacGregor 2012). Concrete material properties are summarized in Table 3-1.

Table 3-1. Concrete material parameters for each static model

Specimen	f'_c (Ksi)	E_c(Ksi)	b1	b2
S1616-S1322-S2222 (Fujikake et al. 2009)	6.10	4448.19	0.925	1.35
Girder 1-Test 1 (Chehab et al. 2018)	7.65	4985.05	1.059	1.90
Girder 1-Test 3 (Chehab et al. 2018)	7.65	4985.05	1.059	1.90
Girder 1-Ultimate Load Test (Olsen 1992)	8.39	5220.61	1.127	2.80
Control Girder-S1 (Ludovico et al. 2005)	8.01	5101.89	1.125	2.11

3.3.2 Modeling of prestressing strands and mild steel

Hughes-Liu beam elements with 2x2 Gauss quadrature points were employed to model the prestressing strands and mild steel (i.e., rebars and stirrups). The plastic kinematic material model (MAT003) was utilized, requiring the definition of elastic modulus, yield strength, tangent modulus, and failure strain. For mild steel, the strain rate effect was incorporated into the PLASTIC_KINEMATIC_steel model using Cowper-Symonds strain rate parameters C = 50 and P = 6 s^{-1} (Chen et al., 2019).

The material properties of the prestressing strands, specifically typical 1860 MPa low-relaxation 12.6 mm, seven-wire strands, were defined according to the Precast/Prestressed Concrete Institute (PCI) design manual (Wilden, 2010). Due to the lack of available data, strain rate effects were not assigned to the prestressing strands. A perfect bond between the prestressing strands, mild steel rebars, and the concrete matrix was achieved using the built-in algorithm CONSTRAINED_BEAM_IN_SOLID.

3.3.3 Contact, boundary, and load conditions modeling

The AUTOMATIC_SURFACE_TO_SURFACE contact with soft segment-based algorithm (SOFT=2) was implemented to model interactions between dissimilar materials such as concrete and impactor's plates, loading plate, supporting plate at the boundary conditions, etc. Contact stiffness factors for the slave and master surfaces (SFS/SFM) were set to 0.01/0.1 for all impact models (Pham et al. 2018). Proper boundary and loading conditions were modeled, corresponding to each experimental test separately (Table 3-2).

3.3.4 Applying prestressing force

Prestressing was simulated through the following two-step process:

- The prestressing strands were fixed at both ends and subjected to a thermal load curve (THERMAL_LOAD_CURVE) with a negative temperature, calculated to induce the required prestressing stresses. This temperature reduction simulated the effective prestress level determined according to the level of effective prestress that was reported in the corresponding experimental test (Olsen 1992; Ludovico 2005; Chehab et

al. 2018). A thermal expansion coefficient of 0.000012 inch/inch/°F was assigned to the strands using the MAT_ADD_THERMAL_EXPANSION keyword.

- The induced stresses in the strands were transferred to a new, unaltered beam model using dynamic relaxation. This pseudo-transient phase ensured the accurate transfer of strand stresses to the concrete elements, simulating the effective prestress condition, including losses. Following this, static loads were applied to the beams.

3.3.5 Self-weight and deck girder interface

Gravity was incorporated into only the impact models using the LOAD_BODY_Z card with a step function, accounting for the self-weight of the girders and deck. To ensure composite action, the solid element nodes at the interface between the deck slab and the top flange of the girder were merged. This integration accounted for the interaction between the deck slab and the girder in the simulations.

Table 3-2. Model boundary and contact parameters

Model	Contact type	Boundary condition	Loading condition
G1-Test1(Chehab et al., 2018)	Automatic_Surface_to_Surface	Pin - Roller	Force control
G1-Test3 (Chehab et al., 2018)	Automatic_Surface_to_Surface	Pin - Roller	Force control
G1 (Olsen, 1992)	Automatic_Surface_to_Surface	Pin - Roller	Force control
Control girder S1-(Ludovico et al. 2005)	Automatic_Surface_to_Surface	Pin - Roller	Force control
S1616-S1322-S2222 (Fujikake et al. 2009)	Automatic_Surface_to_Surface	Pin-Roller (Bottom) Fixed-Fixed (Top)	Initial velocity

3.3.6 Validation of the FE model

3.3.6.1 Static load models

The FE results closely matched the experimental data, confirming the successful application of prestressing and the reliability of material models for further analyses (Figure 3-1). The numerical and experimental applied force and mid-span deflection were plotted for models subjected to static loads (Figure 3-2). The models effectively replicated the initial stiffness and stiffness degradation of the beams, except for Girder G01-Test 3. In this case, the model aligned with experimental results up to 50% of the beam's ultimate capacity, after which the FE model underestimated the strength, exhibiting a steeper decline. For ultimate strength predictions, the models performed well across all specimens, with absolute errors ranging from 6% to 18%,

averaging 10% (Table 3-3). Errors were normalized by dividing the difference between experimental and numerical strengths by the numerical strength.

While the FE models did not simulate detailed crack patterns, they accurately identified stress concentration zones corresponding to observed cracking types. Stress concentrations (Figure 3-1) aligned with experimental crack locations, providing reliable indicators of potential cracking behavior:

- Girder G01-Test 1: Shear failure with diagonal plastic strain concentrations matching experimental diagonal cracks (Figure 3-1a).
- Girder G01-Test 3: Similar diagonal stress concentrations in the web, consistent with shear cracks (Figure 3-1b).
- Ultimate Load Test and Control Test: Vertical plastic strain concentrations at the girder soffit correlated with flexural cracks (Figures 3-1c and 3-1d).

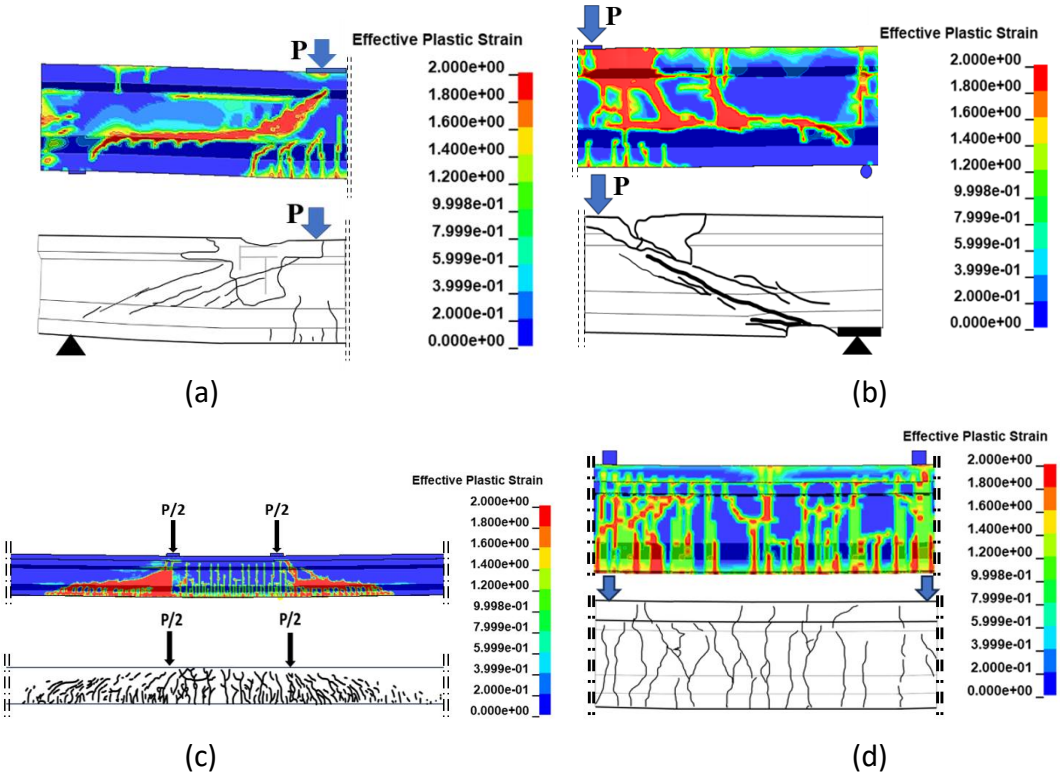

Figure 3-1. Static testing and finite element validation: Experimental cracking patterns reproduced from (a) Girder G01 – Test 1 (Chehab et al., 2018), (b) Girder G01 – Test 3 (Chehab et al., 2018), (c) Girder G01 – Ultimate Load Test (Olsen, 1992), and (d) Control Girder – S1 (Ludovico, 2005)

Table 3-3. Comparison of experimental and finite element analysis results for structural models

Model	Test - Mode of failure	FE - Mode of failure	F -Test (kips)	D -Test (Inch)	F – FE (kips)	D – FE (Inch)	%F - Error	%D - Error
Girder G01-Test1[1]	Shear	Shear	177.6	1.0	192.9	1.2	-8.6%	-17.0%
Girder G01-Test3[1]	Shear	Shear	216.9	0.6	177.2	0.8	18.0%	15.0%
Girder G01-Ultimate Load Test [2]	Flexural	Flexural	290.0	22.1	315.0	23.6	-8.6%	-41.0%
Test-Control[3]	Flexural	Flexural	133.7	7.5	141.9	6.7	-6.0%	10.0%
						Absolute mean error	10%	21%

Peak force: F; D: Maximum mid-span displacement; [1](Chehab et al. 2018);[2](Olsen 1992);[3](Ludovico 2005)

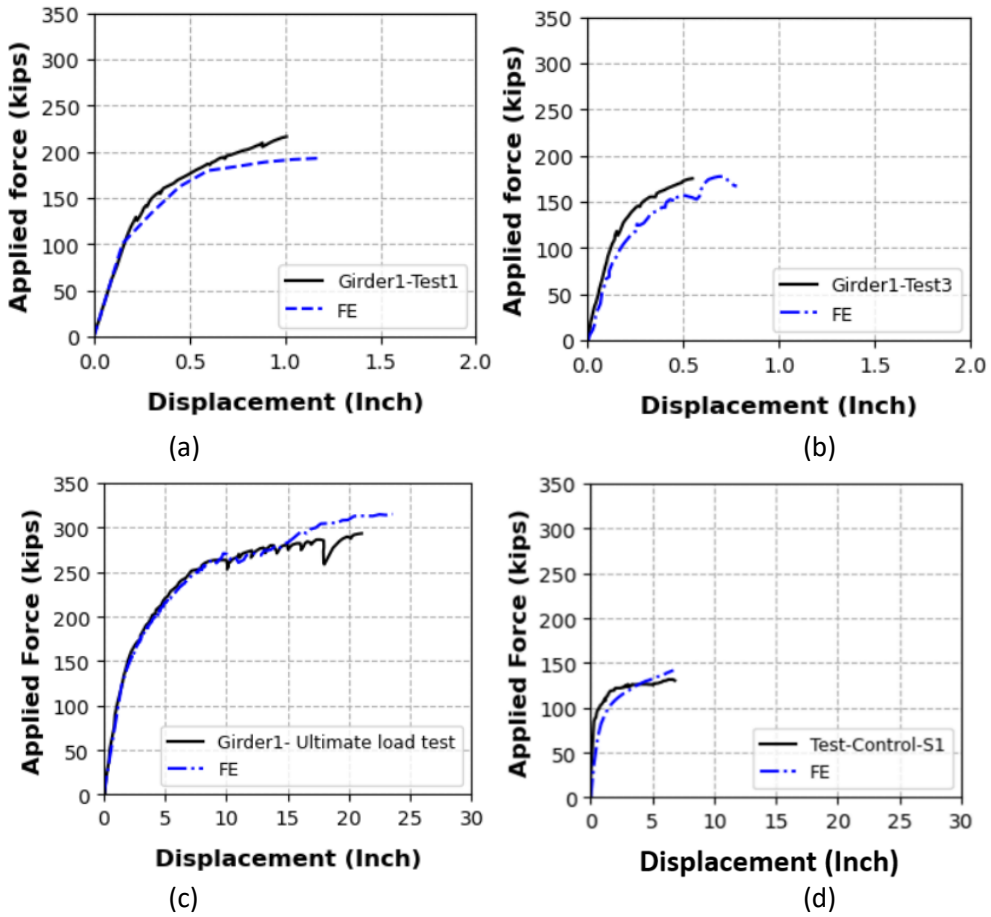

Figure 3-2. Static testing FE validation (the experimental curves were reproduced after (a, b) Chehab et al. 2018, (c) Olsen 1992, and (d) Ludovico 2005

3.3.6.2 Impact load models

Dynamic impact simulations were conducted on a Linux cluster with four nodes**,** 16 CPUs per node**,** and 200 GB of memory**.** Each simulation had a termination time of 1.5 seconds and required approximately 80 hours to complete using a Message Passing Parallel (MPP) double-precision solver. This computational setup provided accurate and efficient modeling of dynamic impact phenomena.

Finite Element (FE) simulations of impact force and mid-span displacement time histories were compared against experimental results (Figures 3-3,3-4,3-5), showing strong overall agreement. Error analyses evaluated discrepancies between test and FE results, with a Gaussian distribution applied to assess the error patterns across nine models. The mean and standard deviation of errors were used to compute the probability density function (Equation 3-5). The mean errors for key parameters were: 11% for peak impact force, 27% for peak mid-span displacement, and 8% for impulse (Table 3-4). The errors followed a Gaussian normal distribution (Figure 3-6), indicating randomness and lack of bias. Among the metrics, impulse exhibited the narrowest distribution spread and lowest standard deviation, making it a particularly reliable parameter for comparing FE simulations with experimental data, as it integrates the dynamic characteristics of both the beam and the impactor.

$$f(x) = \frac{1}{\sigma\sqrt{2\pi}}\, e^{-\frac{(x-\mu)^2}{2\sigma^2}}$$

Equation 3-5

Where x is the parameter value, μ mean and σ is the standard deviation.

3.4 Numerical parametric studies

To better understand the effects of over-height truck collisions with prestressed concrete (PC) girders, two comprehensive numerical parametric analyses were conducted using a FE model. Refer to Appendix A and G for the details of the numerical parametric studies.

- Failure modes and damage assessment**:** The impact analyses in Appendix A and G focused on identifying failure modes, quantifying damage, and estimating the forces generated by vehicle impacts with PC girders. These studies provided critical insights into the mechanics of these collisions and their effects on girder integrity.
- Evaluation of AASHTO LRFD design provisions: The static analysis in Appendix A evaluated the reliability of AASHTO LRFD flexural design provisions in estimating the residual strength of PC girders that sustained asymmetric damage. It examined scenarios involving biaxial bending and partial loss of strands or cross-section integrity, assessing the accuracy of current standards in predicting the performance of damaged girders.

Table 3-4. Comparison of experimental and finite element analysis results for beam forces, displacements, and impulse (Test results were reproduced after (Fujikake et al. 2009))

S1616-0.15m	26.9	0.25	0.22	35.1	0.24	0.22	23%	5%	4%
S1616-0.3m	37.1	0.44	0.28	42.3	0.54	0.26	12%	19%	9%
S1616-0.6m	55.7	0.80	0.37	54.0	0.89	0.34	3%	011	10%
S1322-0.3m	40.1	0.30	0.30	36.4	0.43	0.27	10%	0.29	9%
S1322-0.6m	59.3	0.45	0.40	58.0	0.57	0.35	2%	0.26	12%
S1322-1.2m	67.3	0.90	0.53	77.8	0.90	0.48	13%	0.00	10%
S2222-0.3m	44.4	0.29	0.30	37.7	0.36	0.29	17%	0.20	4%
S2222-0.6m	58.5	0.44	0.41	54.6	0.50	0.36	7%	0.15	13%
S2222-1.2m	68.3	0.84	0.50	78.9	0.98	0.49	13%	0.15	3%
						Absolute mean error	11%	22%	8%

F: Peak impact force; D: Mid-span displacement; I: Impulse

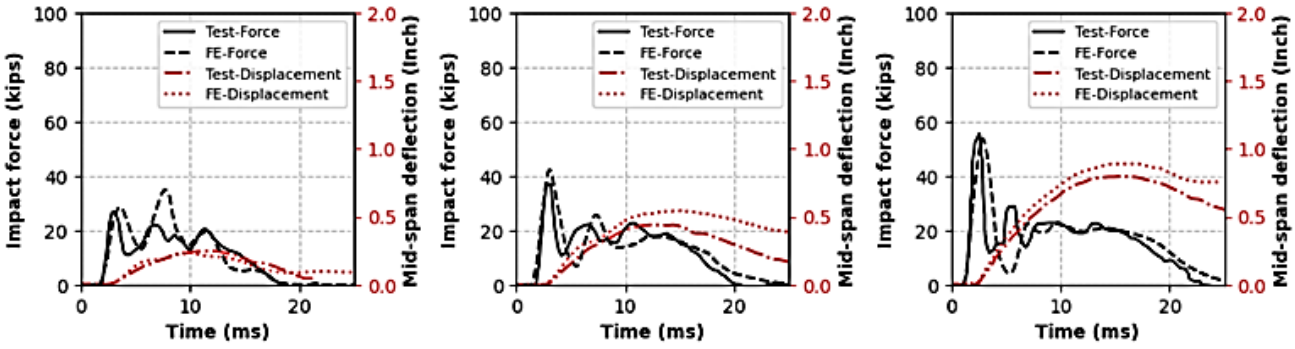

Figure 3-3. Experimental and FE impact time histories for beam series S1616 (a) H= 0.15m, (b) H= 0.3m, and (c) H=0.6m, the test results were reproduced after (Fujikake et al. 2009)

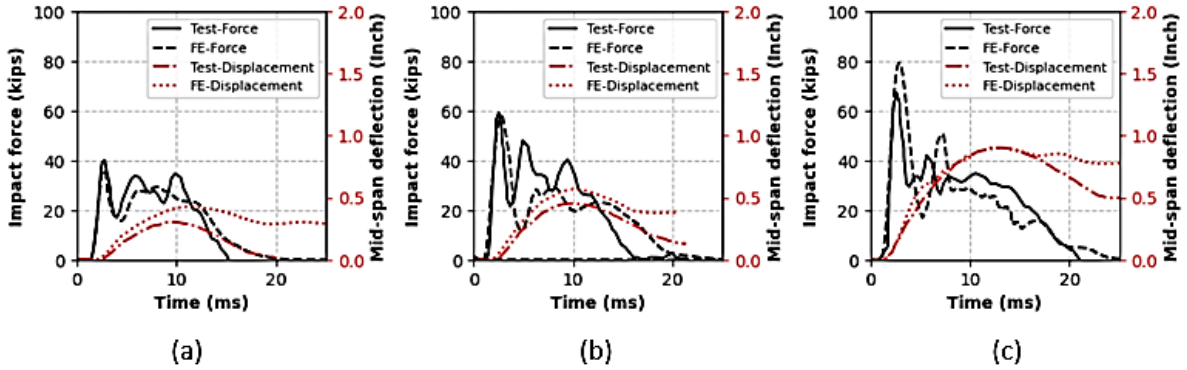

Figure 3-4. Experimental and FE impact time histories for beam series S1322 (a) H= 0.3m, (b) H= 0.6m, and (c) H=1.2m, the test results were reproduced after (Fujikake et al. 2009)

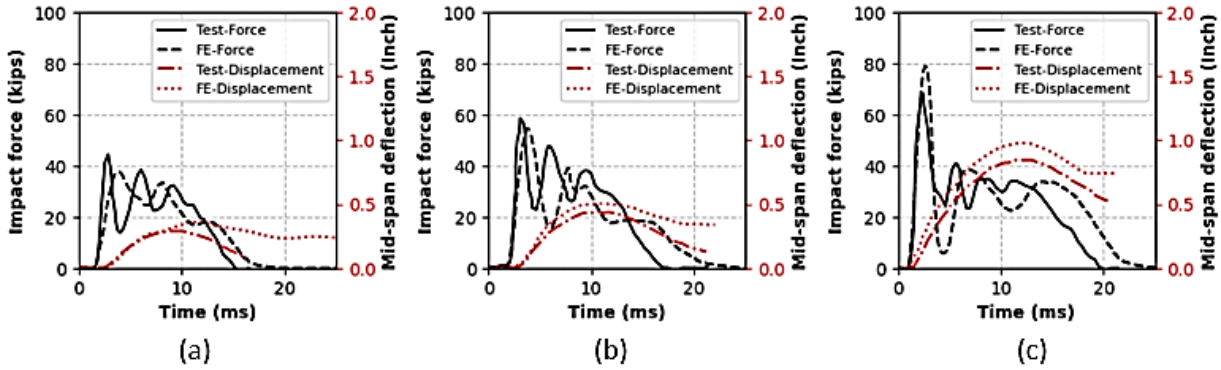

Figure 3-5. Experimental and FE impact time histories for beam series S2222 (a) H= 0.3m, (b) H= 0.6m, (c) H=1.2m, the test results were reproduced after (Fujikake et al. 2009)

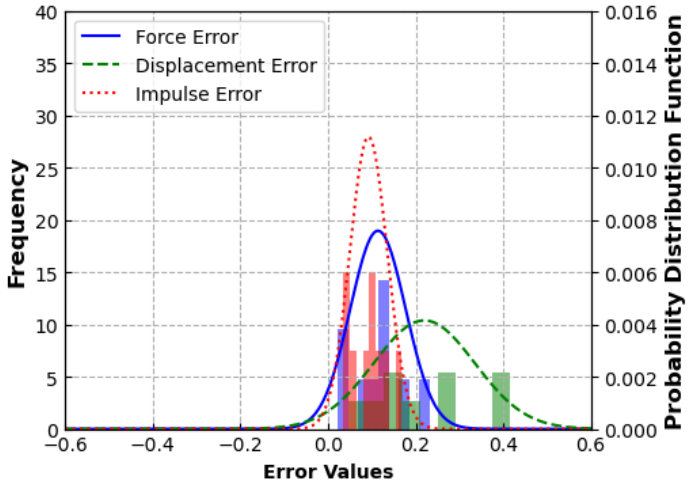

Figure 3-6. Gaussian distribution of errors in finite element impact model results

Chapter 4. Experimental Testing Program

4.1 Overview of the experimental program

The experimental testing program comprises two primary components designed to evaluate the impact damage and subsequent flexural performance of the 14 prestressed concrete girders. The first component is a lateral impact simulator, which was utilized to subject eight prestressed girders to controlled lateral impact forces. The impact simulator simulates real-world vehicular collisions under different boundary and loading conditions. Different levels of damage from minor to moderate to severe resulted from the testing. The second component is a four-point flexural test setup, which is used to determine the residual flexural capacity of both the damaged and repaired girders. This setup was crucial in assessing how the impact damage affects the load-carrying capacity of the girders and how effective various repair strategies are at restoring the structural integrity of the girders.

4.1.1 Residual flexural capacity assessment

This section focuses on evaluating the flexural performance of five girders, which will be further discussed in Chapter 5. Two of the girders served as control specimens, one with 12 prestressing strands and another with 16 strands, representing undamaged conditions. The inclusion of control specimens provides a baseline for comparing the flexural capacity of the damaged girders. This in turn allows for a clearer understanding of the extent to which the impact affects the girders' structural performance in comparison to the theoretical calculation based on the AASHTO LRFD. The remaining three girders represent varying levels of strand loss, between 25% to 50% for the girders that had 12 strands and 62% for the girders that had 16 strands, simulating different severities of impact-induced damage.

4.1.2 Repair of the damaged girders

After evaluating the control and damaged girders, it is time to evaluate the flexural performance of eight repaired girders. Four of these girders were repaired using mechanical splicing (Grabb-It) for damage levels corresponding to 17%, 25%, and 33% loss of prestressing strands. Another two girders were repaired using externally bonded CFRP composites with damage levels corresponding to 17% and 33% loss of prestressing strands.

4.1.3 Description of the test specimens

A total of fourteen prestressed concrete girders (46 feet long, MoDOT type II) were used in the study. Eleven girders had twelve prestressing strands ½ inch low-relaxation 270 ksi. These girders were designed in accordance with AASHTO LRFD 9th edition (AASHTO 2015). Adequate shear reinforcement was provided and detailed to satisfy the code provisions and ensure a typical flexural failure. Two girders had sixteen prestressing strands. One girder had additional shear reinforcement at the mid-span region to mitigate the torsion. Refer to section 1.4 for more information.

4.1.4 Overview of the lateral impact simulator test setup

The lateral impact load was applied to the girder using an impact bogie, which was released from an elevated track under gravity acceleration. The impact point was located in the middle of the bottom flange and the mid-span region of the girder.

4.1.4.1 Elevated track structure

The elevated track was constructed to generate speed for the impact bogie (Figure 4-1). It spanned 60 ft in length and reached a height of 11 ft. The track was comprised of three sections: a 22 ft inclined segment, a 20 ft horizontal segment, and an 18 ft curved transition. Made of A992-grade steel, the track's substructure was composed of hollow steel sections anchored to the laboratory's strong floor, while its superstructure consisted of HP steel beams and rail sections anchored at regular intervals. Refer to Appendix B For more information about the design and fabrication of the impact simulator.

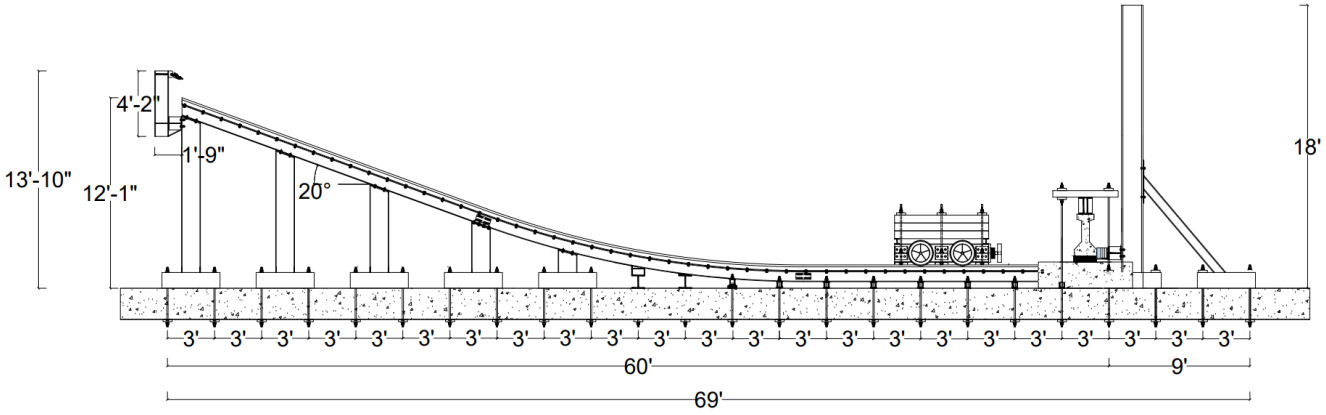

Figure 4-1. Elevation of the impact testing setup

4.1.4.2 Impact bogie

The impact bogie, weighing 2800 lb., was designed to withstand the AASHTO LRFD equivalent static force of 600 kips. Its steel frame measured 7 feet x 3 feet and housed three concrete slabs for additional weight with each weighing 1400 lb. A steel bumper at the front accommodated load cells for impact force measurement. The total weight of the impact bogie was 7000 lb. (Figure 4-2).

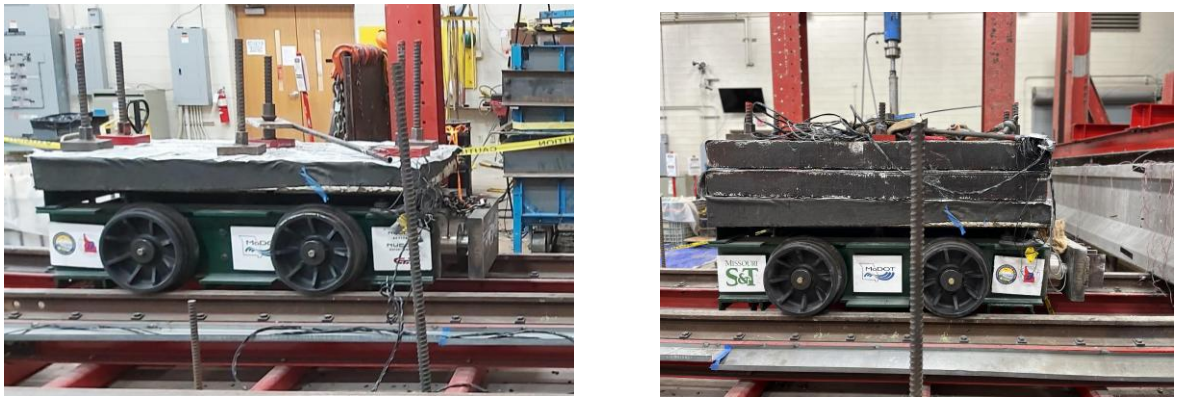

(a) (b)

Figure 4-2. Bogie with different weights (a) 4200 lb., (b) 7000 lb.

4.1.4.3 Support systems

The support systems used in the impact testing included gravity supports, lateral supports, uplift supports, top flange restrainers, and intermediate steel diaphragms. Figure 4-3 shows photographs from the test setup for the 46-ft-long prestressed girder, which is supported vertically on reinforced concrete footings with a steel roller at one end and a fixed steel plate at the other, simulating simply supported pin-roller conditions, providing gravity support. Lateral movement was restrained by two vertical steel columns, braced vertically with W-sections. These vertical supports allowed the beam to deflect laterally, as a simply supported beam. To restrict vertical translation upon impact loading, uplift supports consisting of built-up steel channels and hollow steel sections (HSS) were anchored to the strong floor using post-tensioned dywidag rebars at both ends of the girder over a length of four feet.

Figure 4-4 shows the impact testing setup that was used on girders G03, G04, and G05. Additional supports were implemented alongside the typical setup to ensure stability and accuracy in simulating bridge deck conditions. These included a 36-ft-long lateral steel beam (HP 10x42), which restrained the lateral translation of the top flange. This beam was supported vertically by cantilever beams connected to vertical columns behind the girder. A top steel beam (HP 10x42), also 36-ft-long, restricted vertical movement of the top flange and girder while preventing rotation with steel cantilevers bolted at the top and connected to vertical supports.

Figure 4-5 shows the impact testing setup that was used on Girders G07 and G08, with additional supports added in order to investigate the effect of steel intermediate diaphragms on absorbing and mitigating impact energy. Two built-up intermediate steel diaphragms were installed at the girder web, positioned at mid-span with 9-foot spacing, providing enhanced stability by supporting vertical and lateral reactions. Vertical reaction frames were also used to support these diaphragms, effectively managing both vertical and lateral forces during the impact tests.

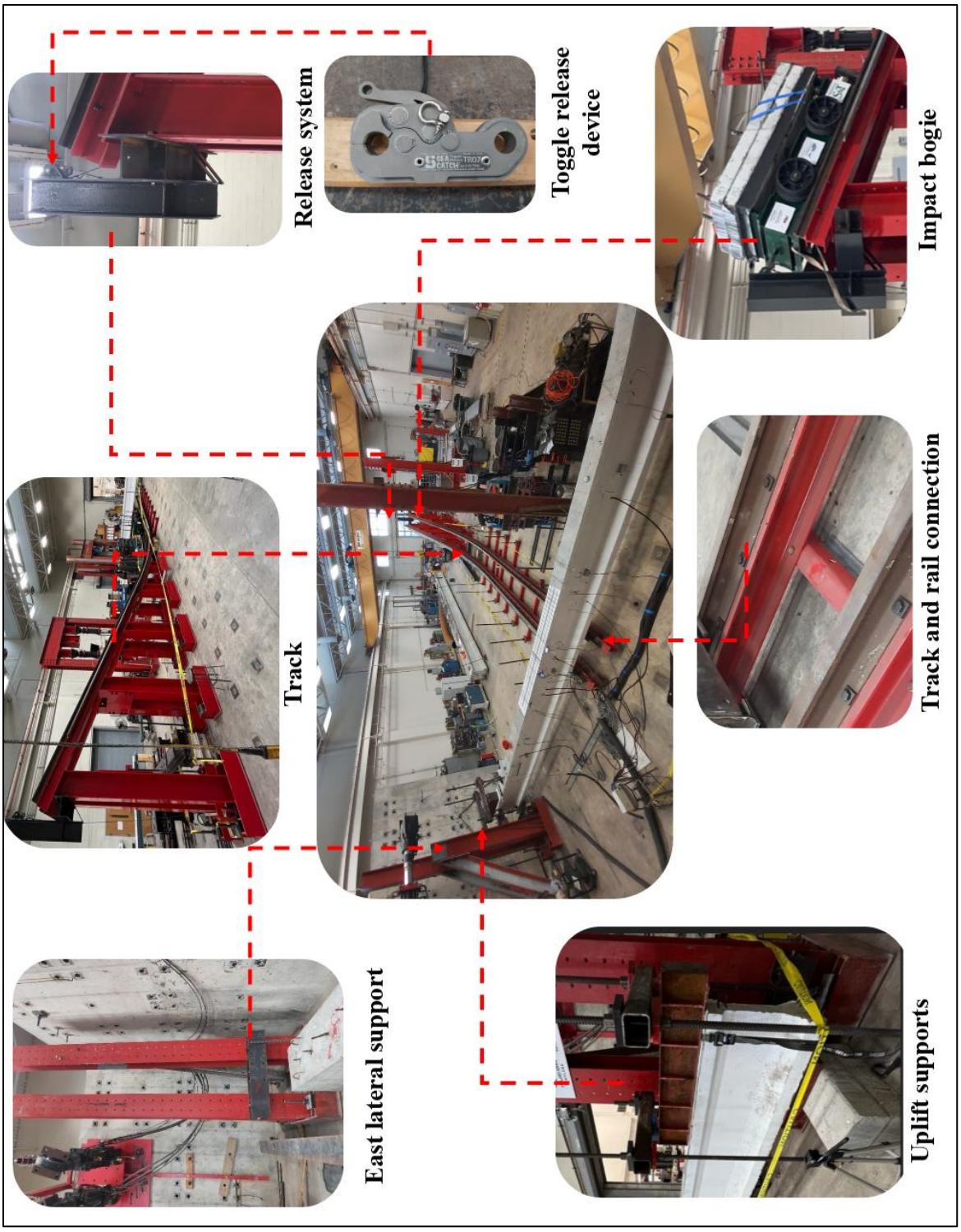

Figure 4-3. No restrainer of the top flange impact testing configuration (Girders G01-G02-G06)

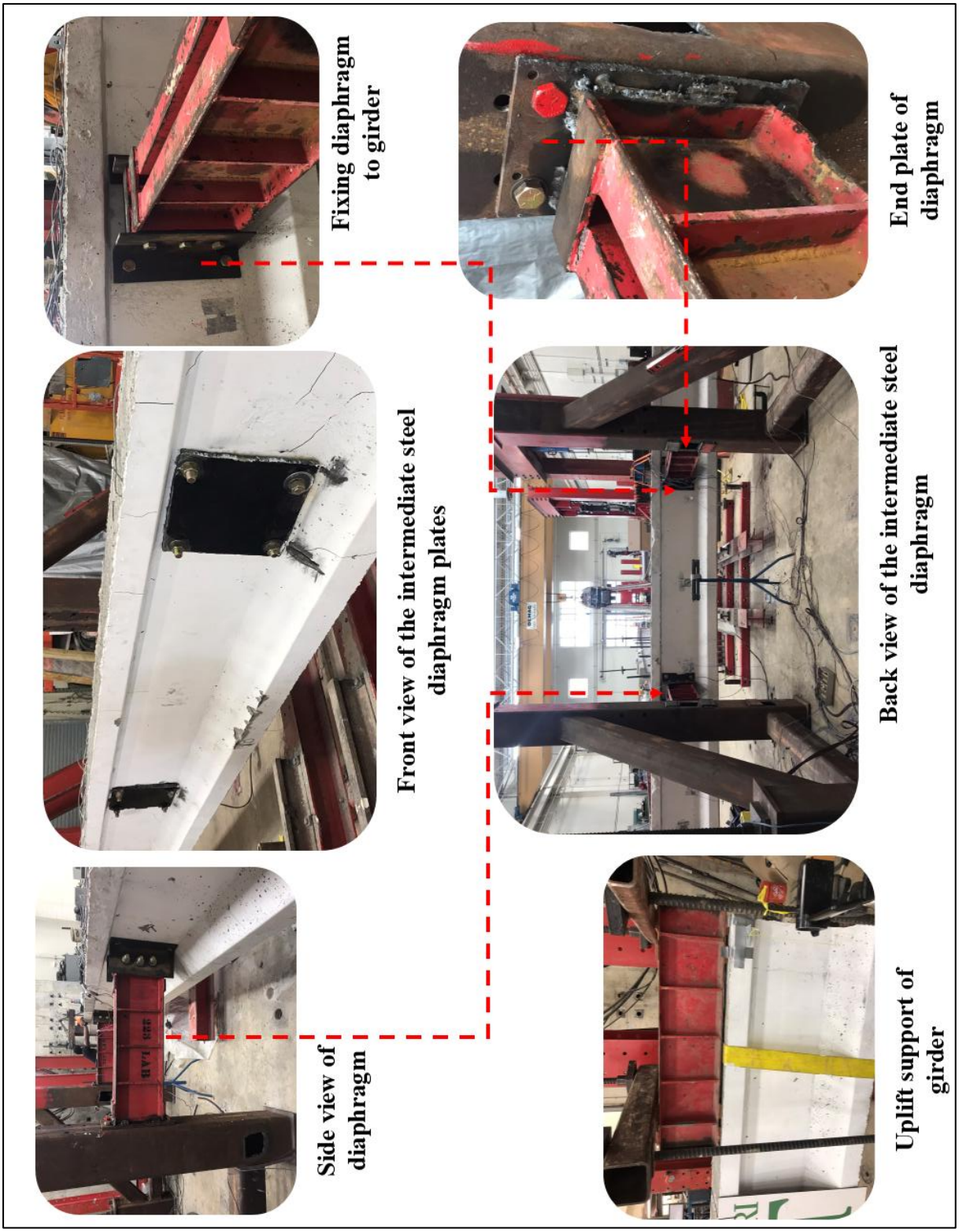

Figure 4-4. Restrainer of the top flange impact testing configuration (Girders G03-G04-G05)

Figure 4-5. No restrainer of the top flange with intermediate steel diagram impact testing configuration (Girders G07-G08)

4.1.5 Instrumentation and data collection

The test instrumentation for this study was extensive. Three load cells were mounted on the impactor head to record the impact forces. Three load cells were mounted on the lateral support columns to record reaction forces (all load cells had a capacity of 225 kips). Over 30 strain gages were installed at the fabrication stage of the PC girders before the concrete casting (Figure 4-6) occurred. The strain gages monitored strain on strands and stirrups, both within and outside the impact region. Two potentiometers were used to capture the vertical displacement of the top flange to monitor the rotation of the girder ends. Three strain potentiometers were mounted at the web of the girder at one-third, two-thirds, and mid-span to monitor the lateral displacement of the girder during the impact. Finally, a high-speed camera with a maximum range of one million frames per second (fps) was used to capture the lateral deflection of the girder and crack propagation at a rate of 7500 fps.

All the measurements were captured using a high-resolution data acquisition system at 50 kHz. No physical filters were installed, and raw voltage data was obtained to ensure accuracy. Figure 4-6 shows a typical layout of the instrumentation used and measurements taken during the impact testing.

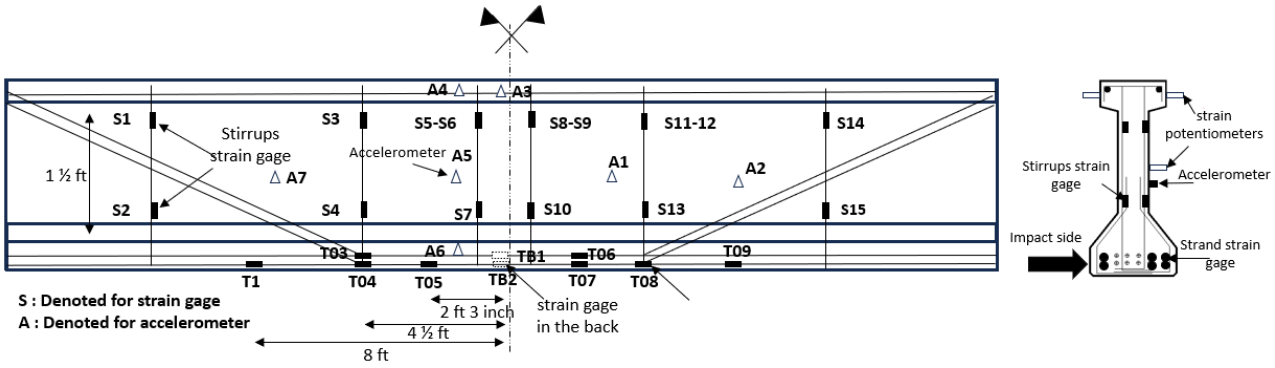

Figure 4-6. Typical layout of the impact testing instrumentation

4.2 Damage-inducing methods of the PC girders

4.2.1 Lateral Impact Load

A total of eight girders were subjected to lateral impact loads with varying impact parameters. The primary objective was to induce damage in the prestressed concrete (PC) girders to replicate the types of damage observed in real-life overheight vehicle collisions. This damage, described in subsequent sections, includes cracking, concrete spalling, and strand damage. It is categorized into minor, moderate, and severe levels as outlined previously in Table 2-1. Two different impact head shapes were utilized as shown in Figure 4-7. Three distinct impact configurations were employed for this purpose, as shown in Figure 4-8.

Figure 4-8a shows the first configuration, which included no restrainer for the top flange and no intermediate diaphragms. Three Girders (G01, G02, and G06) were restrained laterally and

vertically at both end supports. Girders G01 and G06 were tested with the same impact intensity, maintaining consistent impact speed and mass, while Girder G02 was impacted with a lower mass, as summarized in Table 4-1. The primary difference between Girders G01 and G06 was their flexural stiffness; Girder G06 featured 16 strands, compared to Girder G01 which has 12 strands. Girder G02, which had the same strand configuration as Girder G01, was included for comparison under reduced impact mass.

Figure 4-8b shows the second configuration, which introduced a deck restrainer for the top flange while excluding intermediate diaphragms. Three Girders (G03, G04, and G05) were tested under this configuration. The top flange was supported laterally to prevent both lateral displacement and rotation, as previously described. All three girders were subjected to the same impact intensity. However, the impactor head differed; Girder G03 was impacted using a flat impactor head (Figure 4-8b), while Girders G04 and G05 were tested with fork-head-shaped impactors (Figure 4-8a). Additionally, Girder G05 underwent a second impact to evaluate repeated loading effects.

Figure 4-8c shows the third configuration, which excluded a restrainer for the top flange but included two intermediate steel diaphragms positioned in the mid-span region, spaced nine feet apart. The diaphragms, designed to withstand a static force of 600 kips, were constructed using double C-sections (C 12x25) and L-shaped angles (L 7x4x3/8). They were placed at one-third of the span length and attached to the girder web. Steel plates, ¾ inch thick, were affixed to the opposite side of the girder web and connected to the diaphragms using high-strength A325 bolts passing through the web. The depth of the double C-section represented 37.5% of the girder's depth, ensuring sufficient stiffness.

Table 4-1 provides a summary of these configurations, and the parameters investigated, highlighting the differences in lateral support conditions, impact intensities, and girder reinforcement details across the experimental program.

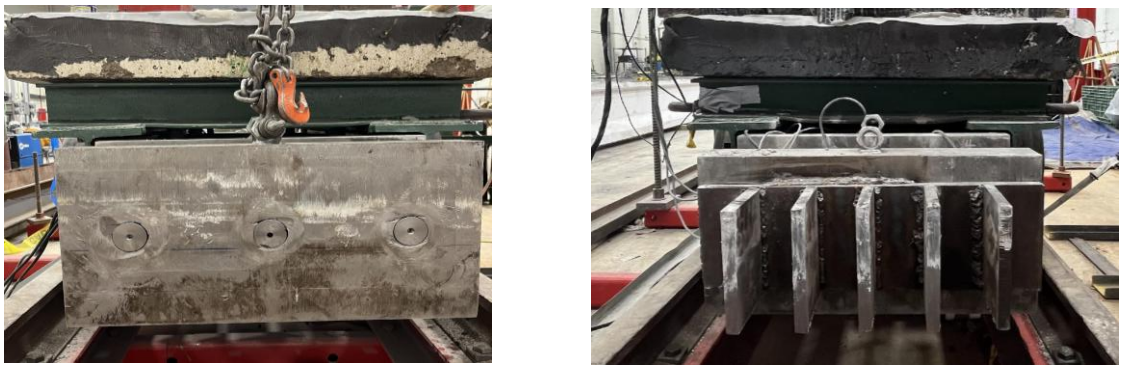

(a) (b)

Figure 4-7. Impactor shape (a) Flat, (b) Fork-head

Impact side

Back side

(a)

Impact side

Back side

(b)

Impact side

Back side

(c)

Figure 4-8. Impact testing configurations

Table 4-1. Impact test matrix summary

Girder G01	12	Code-based	Not restrained	No	Flat	7000	21.5	Impact Mass
Girder G02	12	Code-based	Not restrained	No	Flat	4200	22.5	Reducing Impact Mass
Girder G03	12	Code-based	Restrained	No	Flat	7000	21.5	Restrain the top flange
Girder G04	12	Code-based	Restrained	No	Fork-head	7000	21.5	Impact contact area
Girder G05	12	Code-based	Restrained	No	Fork-head	7000	6.58	Two impacts
Girder G06	16	Code-based	Restrained	No	Flat	7000	6.58	Increasing Flexural strength
Girder G07	12	Designed for torsion	Not Restrained	Yes	Flat	7000	6.58	Effect of intermediate diaphragm/Increased stirrups
Girder G08	12	Code-based	Not Restrained	Yes	Flat	7000	6.58	Effect of intermediate diaphragm

BC: Boundary condition; ID: Intermediate diaphragm; IH: Impactor head; IM: Impact mass: IS: Impact speed

4.2.2 Lateral static load

Girder 09 was tested laterally under a static load at mid-span, using the same boundary conditions as G1. The primary objective of this lateral test was to compare the static failure load to the dynamic impact load. Additionally, a comparison of the mode of failure from impact to static was required. Girders G01 and G09, tested under impact and static loading respectively, shared identical boundary conditions and were both loaded at the bottom flange (Figure 4-9).

Girder G01 exhibited significant shear and torsional cracking, culminating in a shear plug failure—a failure mode characterized by the rapid formation of a localized shear plane through the girder. This type of failure is typically associated with sudden, brittle failure under dynamic impact loading, highlighting the girder's vulnerability to lateral forces. In contrast, Girder G09, subjected to static loading, developed a flexural plastic hinge at the mid-span loading point. This flexural failure is indicative of a more ductile response, where the girder's capacity was governed by bending rather than shear, allowing it to undergo noticeable deformation before failure (Figure 4-9).

Additional details regarding the testing procedures and observations are provided in Appendix E. A simplified analytical evaluation was performed using the flexural strength provisions outlined in the AASHTO LRFD 9th Edition. The experimentally observed failure load for Girder G09 was 22.1 kips, corresponding to a bending moment of 442 kip-ft (Figure 4-10). In

comparison, the calculated failure load based on AASHTO provisions was 20.2 kips, corresponding to a bending moment of 404 kips-ft, demonstrating the analytical model's accuracy in predicting the static load capacity.

Figure 4-9. Girder G09 testing

Figure 4-10a illustrates the force-deflection curve for the flexural failure of the girder under static lateral loading, clearly showing the formation of the plastic hinge. Figure 4-10b provides a comparison between the static failure load and the impact failure load, revealing that the ratio of ultimate static strength to dynamic impact load is approximately 4%. This notably low ratio underscores the critical importance of understanding and accurately quantifying the effects of impact loading on structural behavior, as the dynamic response is vastly different from static loading scenarios. A detailed summary of the force-deflection curves and analytical calculations can be found in Appendix B.

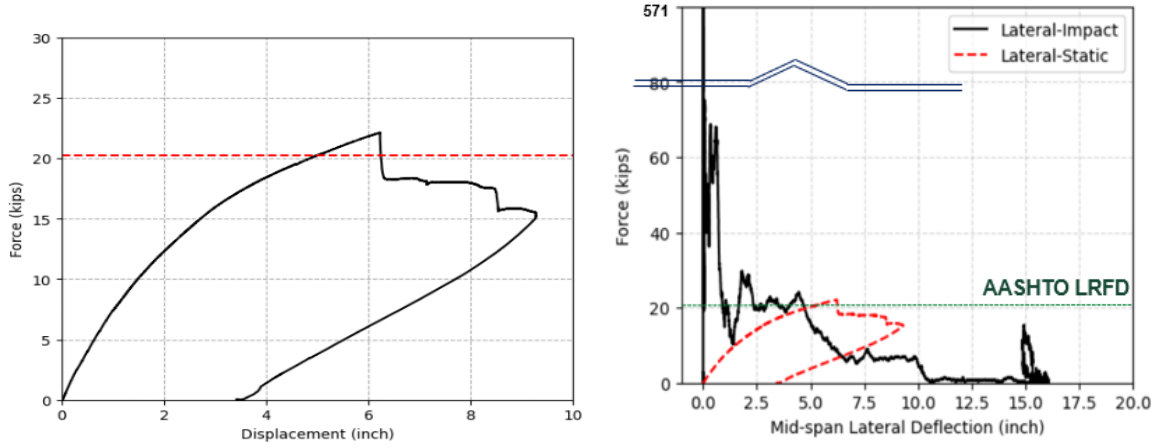

(a) (b)

Figure 4-10. Force deflection curves (a) Lateral static load of Girder G09, (b) Impact force-deflection curve of Girder G01 against lateral static deflection of Girder G09

4.3 Classification of damage levels

The damage classification framework provided by NCHRP 20-07/Task 307 was adopted into this study to systematically categorize the levels of damage and to establish realistic target damage scenarios for the impact and repair test matrix.

The following sections provide a detailed comparison between the damage patterns observed in each impact test and the actual damage documented in real-world bridge collisions. The comparisons highlight the similarities in structural impairments, including localized concrete spalling, strand ruptures, and the resultant biaxial bending effects.

4.3.1 Minor damage (No intermediate steel diaphragms)

Figure 4-11 shows minor damage to both Girders G02 and G04. The same damage level occurred despite the different loading and boundary conditions that were discussed previously. In both girders, concrete spalling was observed over a localized area along the length of the impactor head, spanning approximately 2.5 feet. In Girder G04, the impact caused the exposure of a single prestressing strand, emphasizing the severity of localized damage. Additionally, both girders displayed shear and torsional cracking extending from the impact zone to the supports. Comparisons between test and real-life damage sustained due to vehicles impacting bridge girders were made (Figure 4-11). These comparisons show the similarities between the two damage cases and the influence of boundary conditions and loading conditions on the damage mechanisms of PC girders.

Figure 4-12 shows the dynamic response of the two girders, with Girder G02 having more lateral displacement than Girder G04 due to the deck restrainer of Girder G04. Despite this, Girder G04 sustained a higher impact mass.

(a) (b)

(c) (d)

Figure 4-11. (a) Tamm over I-64 bridge impact (The photograph is courtesy of MoDOT), (b) Girder G02, (c) Bridge 4.3 W. Caldwell, (c) Girder G04 (The photograph is courtesy of Idaho DOT)

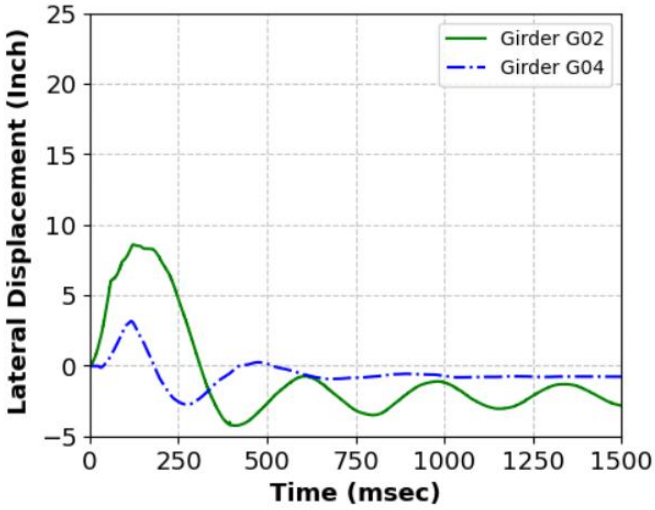

Figure 4-12. The dynamic response of Girders G02 and G04

4.3.2 Minor damage (intermediate steel diaphragms)

In Figure 4-13, Girders G07 and G08 were both subjected to impacts with the highest kinetic energy and with no restraint applied to their top flanges. These girders shared identical boundary conditions and were supported with two intermediate steel diaphragms at mid-span, spaced nine feet apart. However, the shear design of the two girders varied significantly to meet different performance criteria.

Girder G08 was designed primarily to satisfy minimum shear requirements as per AASHTO LRFD Bridge Design Specifications. In contrast, Girder G07 was designed to sustain a lateral load of an equivalent static load of 600 kips applied to the bottom flange, inducing torsion and necessitating additional shear reinforcement. With the absence of any guidelines or standards that provide an estimate of the lateral impact force to bridge girders, 600 kips corresponded to the equivalent static load of the bridge pier collision force provided by the AASHTO LRFD.

Based on this value, the shear reinforcement in Girder G07 was found to be six times higher than the minimum shear reinforcement required at the mid-span, following AASHTO LRFD shear provisions, to address the combined shear under gravity loads and torsional demands based on the lateral load.

Despite being subjected to high-energy impacts, neither girder exhibited permanent deflection after the test, demonstrating their structural resilience. Both girders experienced only slight concrete spalling with no exposed prestressing strands. The presence of intermediate diaphragms played a critical role in mitigating damage by absorbing a significant portion of the impact energy, thereby reducing the severity of lateral deflection in both specimens. The lateral deflection of Girders G07 and G08 was almost identical to that of Girders G03, G04, and G05, which had no intermediate diaphragms but the restraint of the top flange (Figure 4-14).

However, the additional shear reinforcement in Girder G08 had a pronounced effect on its damage response. It eliminated torsional and shear cracks, leaving only flexural cracks as the primary form of damage. This contrasted with Girder G07, which displayed typical shear and torsional cracking patterns due to its lower shear reinforcement (Figure 4-10). The comparison highlights the effectiveness of additional shear reinforcement and intermediate diaphragms in enhancing the structural performance of girders under high-energy impacts, especially in mitigating torsional effects and concentrating damage to less critical regions. For details about provisions for sections subjected to combined shear and torsion in accordance with AASHTO LRFD section 5.8.3.6.

(a) (b) (c)

Figure 4-13. (a) Tamm over I-64 bridge impact (The photograph is courtesy of MoDOT), (b) Girder G07, (c) Girder G08

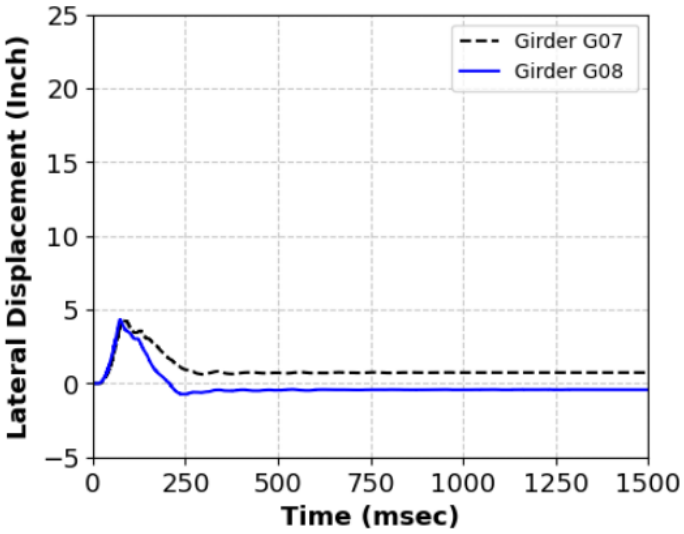

Figure 4-14. The dynamic response of Girders G07 and G08

4.3.3 Moderate damage

In Figure 4-15, Girder G05 shares the same boundary conditions and impact loading as Girders G03 and G04, with one key distinction: unlike the other girders, Girder G05 was impacted twice. This simulates a real-world scenario in which an over-height object first collides with an exterior bridge girder before subsequently striking interior girders. The double impact on Girder G05 represents the cumulative damage an exterior girder may sustain when subjected to multiple collisions, providing insight into its structural response under repeated loading.

Despite the high-energy impacts, Girder G05 exhibited no significant permanent deflection, highlighting the robustness of the experimental setup and the effectiveness of the restrained top flange in replicating realistic bridge deck conditions (Figure 4-16). The results demonstrated the capability of the experimental configuration to handle high-impact scenarios without compromising the structural stability of the girder.

Cumulative damage after the two impacts was carefully documented and several critical observations were made. Significant shear and torsional cracks were distributed across the entire span of the girder, accompanied by extensive concrete spalling on the bottom flange both inside and outside the impact zone. Two prestressing strands were exposed in the impact zone, with noticeable necking in the two prestressing strand wires due to direct contact with the impactor head. This level of strand damage indicates the intensity of the impacts and their effects on the girder's structural integrity. The observed damage patterns in Girder G05 closely resembled those documented in a real-life bridge collision on I-44 in Missouri.

(a) (b)

Figure 4-15. (a) I-270 over I-44 bridge impact (Courtesy of MoDOT), (b) Girder G05

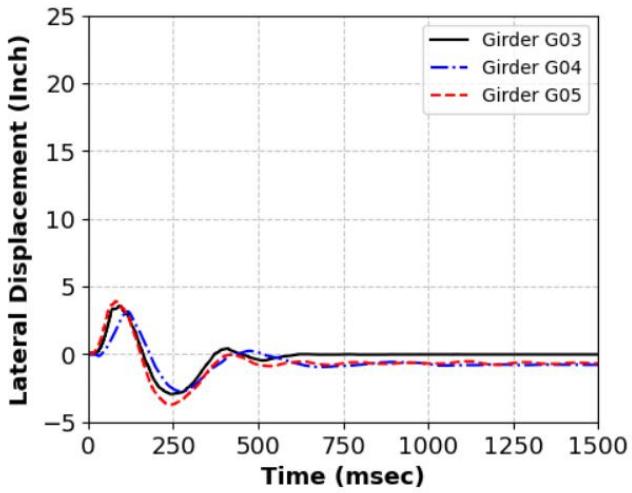

Figure 4-16. The dynamic response of Girders G03, G04, and G05

4.3.4 Severe damage

In Figure 4-17a, Girder G01 served as the control girder in the impact test matrix. It was reinforced with 12 prestressing strands as flexural reinforcement and shared identical boundary conditions with Girder G02. The girder was subjected to the highest kinetic energy from the impact bogie, resulting in severe damage. A plastic hinge formed at the mid-span at the point of impact, compromising six strands—four on the impact face and two on the rear—equivalent to

50% of the total strands. The strands displayed sagging, unbundling, and nicking caused by direct impact forces and excessive lateral deflection.

Concrete spalling was extensive, with 52% of the cross-sectional area lost at the top flange, web, and bottom flange. The bottom flange experienced spalling due to concrete crushing, with the impactor penetrating three inches into the girder. Excessive lateral deflection contributed to additional spalling at the web and top flange (Figure 4-17a). Cracking on the impact side extended 17 feet, covering 80% of the span, with inclined shear and torsional cracks ranging from hairline to 0.1 inches in width, decreasing in size further from the impact point. On the rear side, cracks dispersed over a length of six feet, approximately 14% shorter than on the impact side, suggesting plastic shear hinge formation and punching shear failure caused by high shear and inertia forces.

The girder experienced a maximum lateral displacement of 16.3 inches and a residual drift of 2%, along with a vertical residual displacement of 3.5 inches (Figure 4-18). The lateral deflection was the primary cause of strand yielding and concrete spalling. Meanwhile, the increased vertical residual displacement (camber) was a secondary effect resulting from the loss of the concrete section. Based on Harries et al.'s (2012) classification, the damage level was categorized as Severe IV, as the strand loss exceeded 35% and the vertical deflection surpassed 0.5%.

In Figure 4-17d, Girder G06, reinforced with 16 prestressing strands, exhibited a 33% increase in flexural strength compared to Girder G01. Despite this, the girder sustained significant damage under impact, with five out of 16 strands (31%) severely compromised but not ruptured. The strands exhibited sagging, unbundling, and nicking due to direct impact and lateral deflection.

Concrete spalling affected 35% of the cross-sectional area at the impact site, involving the top flange, web, and bottom flange. Spalling at the bottom flange resulted from a 5-inch penetration by the impactor while spalling at the web and top flange was due to excessive lateral deflection. Additionally, the bottom flange exhibited severe cracking and delamination (Figure 4-17d).

Cracking on the front face, where the girder faced the impact bogie, extended 15 feet on either side, covering 73% of the span. These cracks included inclined shear and torsional patterns that diminished in width from 0.1 inches to hairline cracks (less than 0.005 inches) as they radiated from the impact point at a 45-degree angle. The rear face displayed similar crack patterns but with reduced severity (Figure 4-17d).

Girder G06 exhibited a maximum lateral displacement of 15.9 inches and a residual displacement of 5.5 inches, corresponding to a 2.1% lateral drift (Figure 4-18). Excessive deflection was the primary cause of strand damage and concrete spalling. Based on Harries et al.'s classification, the damage to G6 was categorized as Severe III, with strand loss exceeding 25% but remaining below 35%, and vertical deflection exceeding 0.5%.

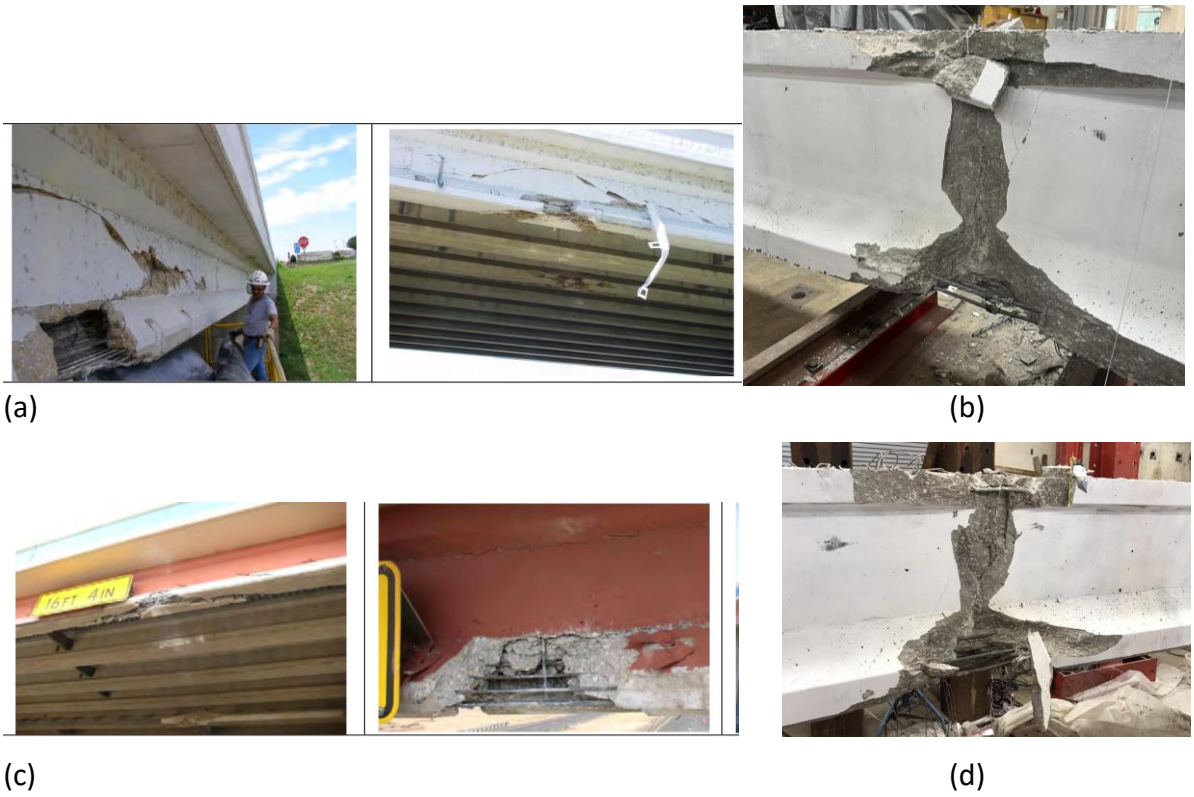

Figure 4-17. (a) Bridge over US 67, (b) Girder G01, (c) FM 1788 over IH20 AASHTO I-girder, Texas (d) Girder G06 (The photographs were reproduced after NCHRP 20-07/Task 307)

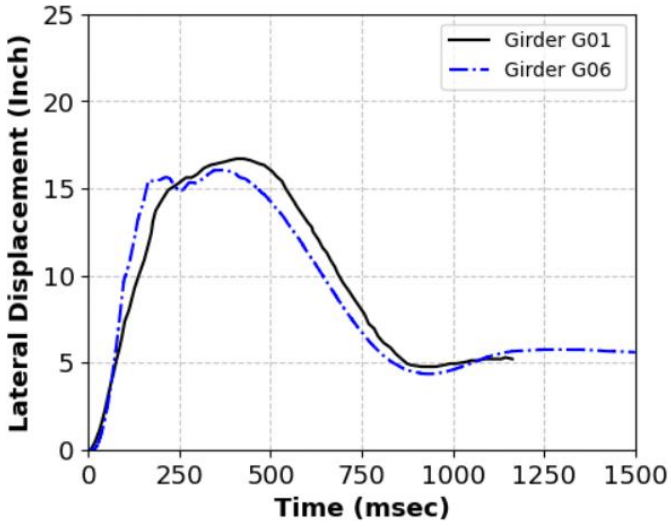

Figure 4-18. The dynamic response of Girders G01 and G06

4.4 Flexural residual strength of the damaged girders

4.4.1 Material characterization

To accurately evaluate the performance of the girders, material tests were conducted on various components, including the beam concrete, prestressing strands, reinforcement bars, and repair materials. All material testing adhered to the standards established by the American Society for Testing and Materials (ASTM).

4.4.2 Girder concrete

Table 4-2 presents a comprehensive overview of the compressive strength data for the fabricated girders. The girders were transported to the laboratory in sets of three. Concrete strength evaluation was conducted using standard 4-inch diameter by 8-inch height cylindrical specimens**.**

The test was performed using a universal testing machine according to the ASTM C39/C39M standard test method for the compressive strength of cylindrical concrete specimens. The table includes individual compressive strength results for each sample tested, as well as the calculated average compressive strength across all specimens. This data provides crucial information on the concrete's structural capacity and uniformity across the girder batches. Refer to Appendix D for pictures of testing.

Table 4-2. Concrete girder compressive strength

Girder	Test	Compressive strength (psi)	Average compressive strength (psi)
Girder G01-G02-G03	Test #1	10959	10556
Girder G01-G02-G03	Test #2	11135	
Girder G01-G02-G03	Test #3	9575	
Girder G04-G05-G06	Test #1	10660	11018
Girder G04-G05-G06	Test #2	11814	
Girder G04-G05-G06	Test #3	10581	
Girder G07-G08-G09	Test #1	11770	11257
Girder G07-G08-G09	Test #2	10997	
Girder G07-G08-G09	Test #3	11005	
Girder G10-G11-G12	Test #1	11795	11455
Girder G10-G11-G12	Test #2	11338	
Girder G10-G11-G12	Test #3	11231	
Girder G13-G14	Test #1	9678	10538
Girder G13-G14	Test #2	10916	
Girder G13-G14	Test #3	11021	

4.4.3 Concrete compressive strength of patch material

Table 4-3 summarizes the experimental results from concrete crushing tests conducted on a patch material specimen. This specimen utilized Sika Grout 428 FS, a high-performance, rapid-strength cementitious grout, to restore the damaged concrete cross-section effectively.

To evaluate the mechanical properties of the patch material, 2 × 2-inch cube specimens were prepared from the same mortar batch and tested under compressive loading per ASTM C109 standards**.** These tests, conducted seven days after casting, determined the material's ultimate compressive strength. Refer to Appendix D for pictures of testing.

Table 4-3. Compressive strength test results for Sika grout 428 FS

Test #	Strength, psi
1	9684
2	10159
3	10745
Average f'_c, psi	10196

4.4.4 Prestressing strand

Specimens of Prestressing strands were taken out form the tested girder for conducting uniaxial tensile testing. Table 4-4 summarizes the results of uniaxial tensile tests conducted on three 0.5-inch Grade 270 prestressing strand specimens to determine their mechanical properties. The analysis revealed an average tensile strength of 267.86 ksi across all specimens.

Strand specimens were securely gripped using specialized prestressing chuck assemblies to ensure proper load transfer and eliminate slip during testing. This procedure adhered to the ASTM A416/416M standard**,** which governs testing for seven-wire steel strands used in prestressed concrete.

The stress-strain relationships derived from the tests, highlight the strands' elastic response, yield point, and ultimate strength, offering critical insights into their mechanical performance. Refer to Appendix D for pictures of testing.

Table 4-4. Tensile capacity of prestressing strands

Strand test	Load, kips	Yield, ksi	Average yield stress, ksi	Ultimate strength, ksi	Average strength, ksi
1	41.6	254.6	247.1	271.5	274.8
2	41.3	252.5		270.2	
3	40.2	230.5		261.9	
4	42.5	249.0		276.7	
5	45.1	248.7		293.7	

Table 4-5 presents the results of direct uniaxial tensile testing for three spliced strands, which with an average failure strength of 251 ksi, approximately 93% of the ultimate strength of the original strand. The failure mode observed was consistent with findings reported in the literature, whereas the failure strength exceeded values documented by (Zobel, 1996) by 8%. The failure occurred in the prestressing strand itself, with no compromise in the integrity of the splice chuck. This indicates that the splice chuck possesses sufficient strength to endure loads exceeding the ultimate capacity of the connected prestressing strands, emphasizing its reliability under extreme tensile loads. Refer to Appendix D for pictures of testing.

Table 4-5. Spliced strand uniaxial tensile test

Strand Test	Load, kips	Stress, ksi	Failure mode
1	37.0	241.8	Strand fracture near end wedge anchorage
2	38.3	250.3	Strand fracture near end wedge anchorage
3	40.3	263.4	Strand fracture near end wedge anchorage
	Average strength, ksi	251.8	

4.4.5 Carbon fiber-reinforced polymer (CFRP)

Table 4-6 summarizes the mechanical properties of the tested fabric material obtained through tensile testing of three coupon specimens, conducted according to ASTM D3039M**.** The material exhibited an average maximum tensile strength of 85.5 ksi and an elastic modulus of 40,124 ksi**.**

Table 4-6. Tensile properties of FRP specimens

Sample ID	Average width, in	Average thickness, in	Area, in^2	Average stress, ksi	Modulus of elasticity, ksi	Ultimate strain, %
Specimen 1	0.94	0.11	0.10	95.22	5393.5	0.55%
Specimen 2	0.98	0.12	0.12	60.31	39860.7	0.42%
Specimen 3	0.99	0.12	0.12	100.94	75118.3	0.82%

Chapter 5. Assessment of the Residual Flexural Strength of the Damaged Girders

5.1 Introduction

Two methods were employed to evaluate the residual flexural strength of damaged prestressed girders. The first method involved flexural testing of girder G3 after a 25% loss of strands and girder G4 after a 50% loss of strands. Additionally, girder G2 underwent flexural testing following impact loading with no strand loss, while girder G6 underwent flexural testing in its as-built condition. The second method utilized non-destructive testing to evaluate the residual prestress in girder G6.

5.2 Flexural testing for residual flexural strength of PC girders

5.2.1 Test setup and instrumentation

The structural assessment involved subjecting Girders G02, G03, and G04 to four-point flexural testing (Figure 5-1). The test setup featured a 44 ft simply supported span with a 15 ft constant moment zone. Load application was achieved using two 500-kips hydraulic cylinders, with forces measured through load cells attached to each cylinder (Figure 5-2). An electronic data acquisition system captured real-time data throughout the testing process.

The loading protocol consisted of incremental steps of approximately 20, 40, and 60 kips. At each increment, the loading was temporarily halted to allow for crack mapping. To monitor potential horizontal movement, LVDTs were positioned at the beam ends and foundation supports. Additionally, string potentiometers were installed at three locations on each beam: beneath each load point and at the midspan.

Before casting the girders, strain gauges were mounted on the prestressing strands and shear reinforcement of each beam. These gauges were connected to the data acquisition system, enabling continuous monitoring of strain during the testing process.

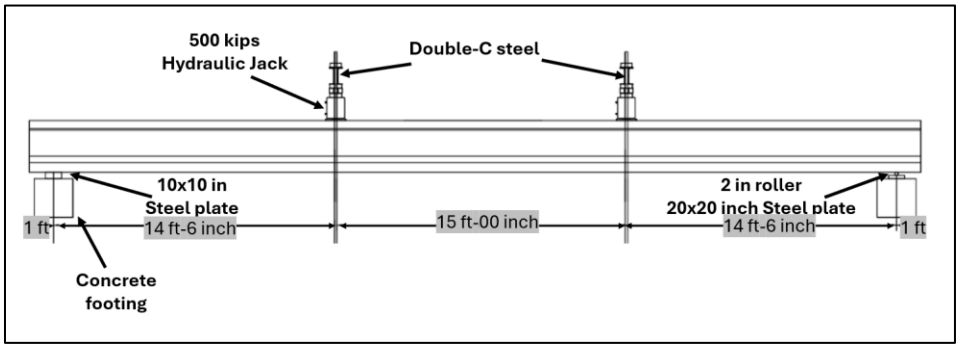

Figure 5-1. Elevation of the four-point test setup

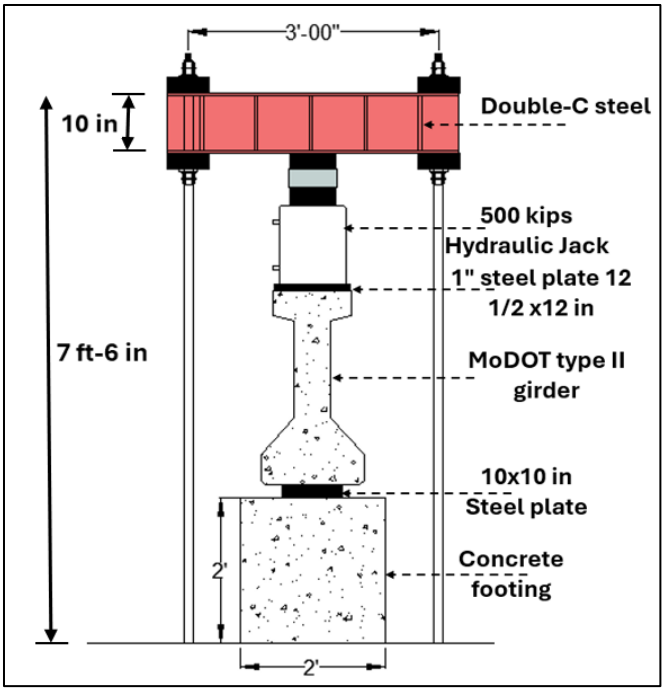

(b)

Figure 5-2. Cross-section of experimental test setup configuration

5.2.2 Girder G02

Post-impact testing of girder G02 revealed no visible strand exposure, with concrete damage limited to slight spalling of the bottom flange's concrete cover. Diagonal shear cracks were observed on both sides of the girder, with crack widths ranging from 0.005 inches (very fine) to 0.01 inches. Additionally, the girder exhibited a net upward camber of 1.25 inches, attributed to the reduction in the concrete cross-section caused by the impact. Using the NCHRP damage classification criteria (refer to Table 2-1, Chapter 2), the damage was categorized as minor. Consequently, this girder was selected for testing to estimate the flexural strength of this set of girders (Figure 5-3).

During the flexural test, initial cracking was observed at 118 kips which corresponds to a cracking moment of 855.5 kips. ft, occurring primarily in the constant moment zone and near the right load point. With increasing load, additional flexural cracks developed along the girder, predominantly within the constant moment region. These cracks propagated to the top of the girder at 148 kips, just before failure. Shear cracks were noted outside the constant moment zone at 135 kips. Significant deflections exceeding L/100 (where L represents the girder span) were recorded at approximately 152 kips. Testing was conducted until a deflection of 6.4 inches was reached (Figure 5-4a), at which point the load stabilized, and the girder split in two at the right load point (Figure 5-4b).

Figure 5-3. Photograph from the lab of the damaged Girder G02

(a)

(b)

Figure 5-4. Testing and failure of the control girder (a) Deformed shape during testing, (b) Failure of the girder

The ultimate failure load reached 158 kips, which corresponded to a bending moment of 1118 kips-ft (Figure 5-4c). The flexural capacity exceeded the AASHTO LRFD estimate by 6.2%. The failure mode was flexural, with cracks initiating at the soffit of the girder and progressively propagating vertically through the web and into the top flange. Shear cracks were observed outside the constant bending moment region, indicating localized stress concentrations. The failure occurred at the harping points, where higher tensile stresses were concentrated. This led to the yielding and subsequent failure of the harped strands, followed by the failure of the straight strands, emphasizing the critical role of tensile stress distribution in the girder's structural behavior.

5.2.3 Girder G03

Despite the absence of visible damage, such as exposed reinforcement or concrete deterioration, strain gauge data from the impact test on Girder G03 revealed that three prestressing strands had either significantly lost their prestress force or exceeded their yield point. To eliminate structural contributions from the compromised strands, these strands—located on one side of the girder—were severed at the impact location (Figure 5-5).

Post-impact, the measured camber was 1.25 inches, which decreased to 0.75 inches after severing the strands, representing a 40% reduction in camber. During the subsequent flexural test, initial cracking was observed at 65 kips in the constant moment region, which corresponds to a cracking moment of 471 kips.ft, extending beyond pre-existing impact-induced cracks. As the load increased, additional flexural cracks propagated, concentrated primarily in the constant moment region. At 112 kips, these cracks reached the top flange, signaling imminent failure.

Shear cracks developed outside the constant moment zone at 108 kips, reflecting significant shear stress. Testing continued until a deflection of 4.27 inches, at which point the load dropped suddenly. The girder ultimately failed in a brittle manner, splitting at midspan. Vertical cracks widened due to the loss of prestress, leaving the concrete to bear tensile stresses alone. The ultimate failure load was recorded at 118 kips, corresponding to a failure moment of 855 kips-ft (Figure 5-6). The flexural capacity was almost equal to the AASHTO LRFD estimate (Table 5-1).

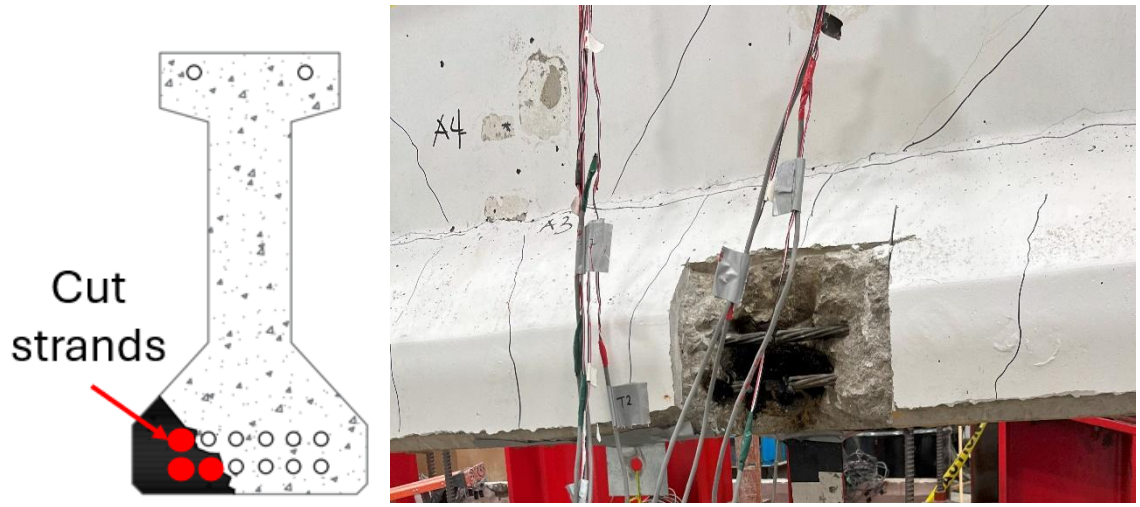

(a) (b)

Figure 5-5. Girder G03 strands cut, (a) Cross section showing loss of strands, (b) The section along the girder where strands were cut (before the flexural test)

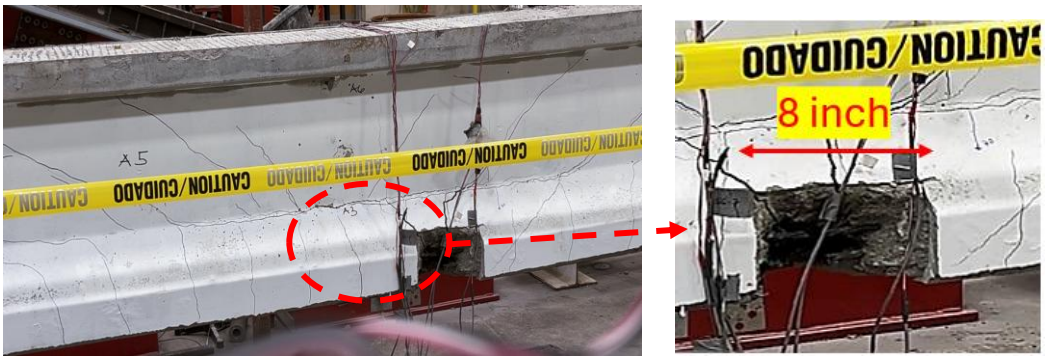

(a)

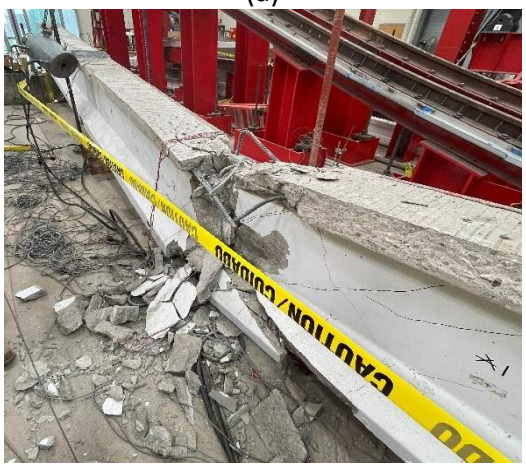

(b)

Figure 5-6. Girder G03 (a) The testing of the girder, (b) Failure of the girder.

5.2.4 Girder G04

The girder, designated as Girder G04 during the impact test, exhibited significant damage to its prestressing strands, as indicated by internal strain gage data. The collision caused three of the twelve prestressing strands to either reach their yield strength or lose a substantial portion of their initial tension. To achieve the target damage level of 50%, an additional three strands were severed, bringing the total to six severed strands, all located on the same side of the girder (Figure 5-7).

Following the impact test and subsequent strand cutting, the girder retained a camber of 1.38 inches, with minimal lateral (out-of-plane) displacement of 0.125 inches. During the flexural test, initial cracking occurred at a 30-kips load within the constant moment region, which corresponds to a cracking moment of 217.5 kips. ft, extending beyond the fractures induced by the impact. As the load increased, additional bending-related cracks developed, primarily within the constant moment area. These cracks extended into the upper flange at a load of 68 kips, signaling imminent failure.

Diagonal shear cracks formed outside the constant moment region at 63 kips, marking the onset of combined flexural-shear failure. The test progressed until the girder deflected 2.1

inches, at which point the load plateaued. At this stage, the combined flexural-shear cracks widened beyond 0.1 inches. Unlike previous specimens, G4 exhibited increased ductility, eventually failing due to out-of-plane deformation caused by eccentric prestressing forces. The girder ultimately failed at a load of 73 kips, corresponding to a maximum moment capacity of 526 kips-ft (Figure 5-8). The flexural capacity was 6.9% lower than the AASHTO LRFD estimate.

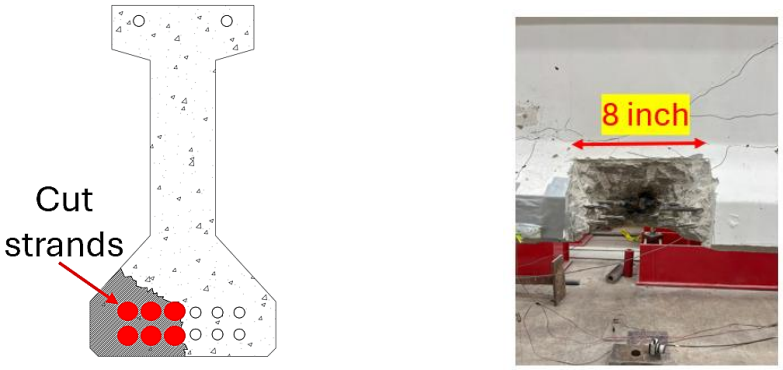

(a) (b)

Figure 5-7. Girder G04, (a) Cross section showing loss of strands, (b) The section along the girder where strands were cut before the flexural test

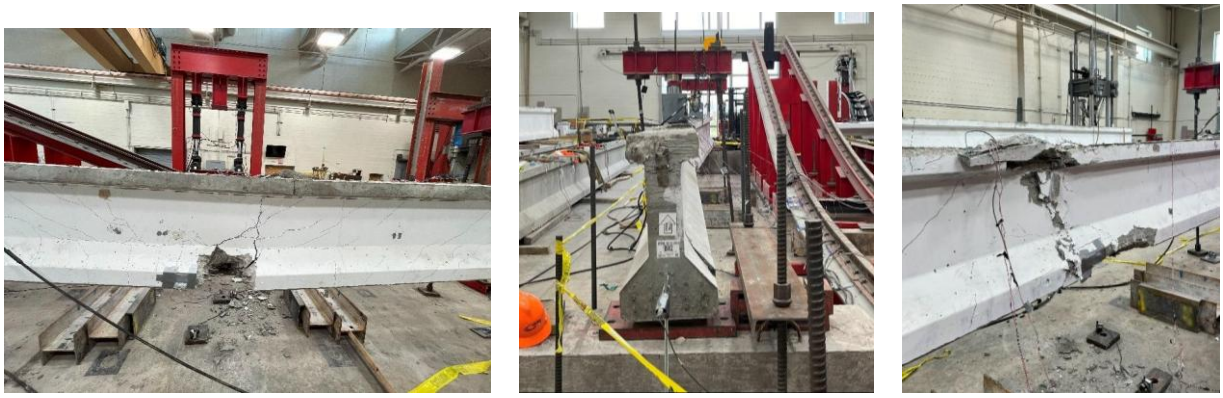

(a) (b) (c)

Figure 5-8. Failure of the Girder G04 (a) Cracks widening at 70 kips, (b) Out of plane deflection, (c) Failure of the girder

5.2.5 Girder G06

The girder, identified as G6 during the impact test, sustained substantial damage to its prestressing strands. Visual inspection revealed that the collision caused at least seven of the sixteen prestressing strands to either reach their yield strength or experience a significant reduction in initial tension. To evaluate the extent of prestress loss and estimate the girder's flexural strength, nondestructive testing (NDT) was conducted on each strand individually. Details of this testing procedure are outlined in subsequent sections.

Following the NDT, the damaged areas in the bottom flange, web, and top flange were repaired using non-shrink, high-strength grout to restore the section of concrete that was lost (Figure 5-9a). The epoxy injection was then employed to seal the cracks, using a low-viscosity epoxy resin applied under pressure. The crack injection was used to mitigate the degradation in the stiffness of the girder. Subsequently, a four-point flexural test was performed to assess the residual flexural strength of the girder and compare it with the NDT results. Initial cracking in the bottom flange was observed at a 25-kips load within the constant moment region. As the applied load increased, additional bending-related cracks developed, predominantly in the constant moment area.

At a load of 68 kips, these cracks propagated into the upper flange, indicating imminent failure. By 70 kips, vertical cracks widened and deepened, marking the onset of failure. The test continued until the girder deflected by 0.5 inches, at which point the load dropped abruptly to 75 kips due to the crushing of the top flange (Figure 5-9c). The failure applied load corresponds to a bending moment of 521 kips-ft. The girder's flexural capacity exceeded the AASHTO LRFD estimate by 9.4%, based on the measured residual prestress forces in the strands, as described in Section 5.3.

(a)

(b)

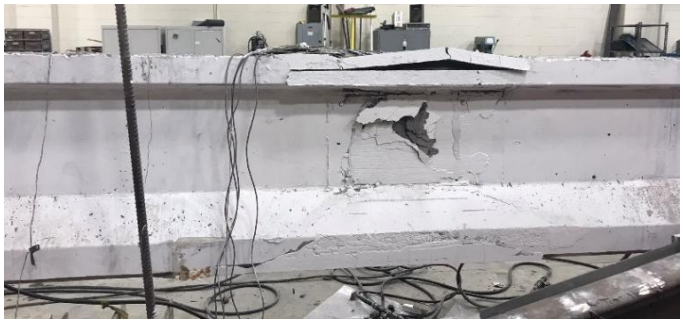

(c)

(d)

Figure 5-9. Girder G06 (a) Formwork and concrete patching before testing, (b) Crushing of the top flange at 75 kips, (c) Complete failure of the girder

5.2.6 Girder G14

The girder designated as Girder G14 was as built and was not subjected to impact. The girder had 16 prestressing strands. Flexural testing was conducted to estimate the flexural capacity of the girder to compare it with the previous results of G06 and the non-destructive test estimate (Figure 5-10a).

During the flexural test, initial cracking occurred at a 76-kips load, which corresponds to a cracking moment of 551 kips. ft, within the constant moment region (Figure 5-10b). As the load increased, additional bending-related cracks developed, primarily within the constant moment area. These cracks extended into the web at a load of 105 kips.

Diagonal shear cracks formed outside the constant moment region at 155 kips marking the onset of combined flexural-shear failure. The test progressed until the girder deflected 4.3 inches, at which the girder failed. The girder ultimately failed at a load of 190 kips, which corresponds to a cracking moment of 1377 kips. ft. The test flexural capacity of the girder exceeded by 8.4% the estimate by the AASHTO LRFD. The failure mode and location were almost identical to Girder G02, where the failure occurred at the location of the harping point which aligned with the location of the hydraulic jack.

(a)

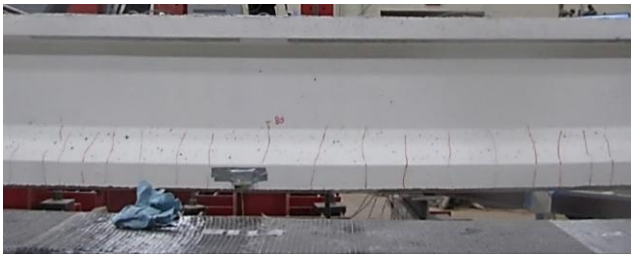

(b)

Figure 5-10. Girder G06 (a) Test setup, (b) Cracking at 80 kips

5.2.7 Summary of residual flexural strength tests

Figure 5-11 presents the force-deflection curves for all girders analyzed in this chapter. Girder G2 demonstrated a flexural strength of 1,146 kips-ft, whereas Girder G14, designed with an increased number of prestressing strands, achieved a significantly higher flexural capacity of 1,377 kips-ft (refer to Table 5-1). This corresponds to a 20% increase in flexural strength,

attributed to a 33% enhancement in prestressing force. Notably, the AASHTO specifications underestimated the strength of both girders by an average of 8.6%.

For the girders with reduced prestressing strands, Girder G03 showed a flexural strength of 854 kip-ft after the removal of 25% of its prestressing strands, reflecting a 25.4% reduction in flexural capacity. Similarly, Girder G04, with 50% of its prestressing strands removed, exhibited a further decline in flexural strength to 562 kips-ft, equating to a 49% reduction. Girder G14's flexural strength was 8.4% higher than the AASHTO prediction, a value closely matching the 6.2% margin observed for Girder G02. For the impact-damaged Girder G6, the residual flexural strength closely aligned with the nondestructive testing estimates, achieving an accuracy error of approximately 9.4%, as elaborated in the subsequent section.

These findings reveal an almost linear correlation between the reduction in prestressing strands and the corresponding decline in flexural strength, underscoring the proportional relationship between these parameters (Figure 5-12). A comprehensive summary of the flexural strength results, including the error defined as the ratio of experimental to calculated flexural strength per AASHTO LRFD, is provided in Table 5-1**.**

Table 5-1. Summary of the residual strength results

Girder Number	Girder test	Girder compressive strength, f'_c (ksi)	Flexural strength (kip. ft) AASHTO LRFD	Flexural strength (kip. ft) Test	Test/AASHTO
Girder G02	As built 12	10.24	1053	1118	106.2%
Girder G14	As built 16	10.53	1270	1377	108.4%
Girder G03	Residual-12-25%	10.56	852	855	100 %
Girder G04	Residual-12-50%	11.00	565	526	93.1%
Girder G06	Residual-16-63%	11.4	476	521	109.4%

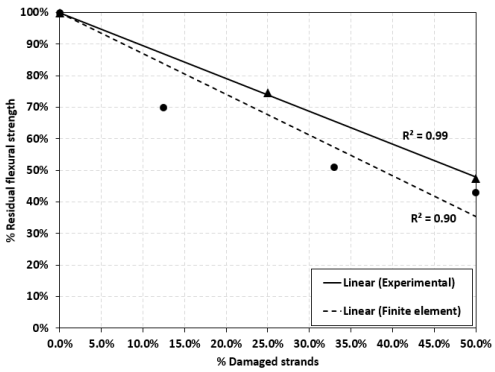

Figure 5-11. Relationship between residual flexural strength and damaged strands from both experimental and finite element analysis

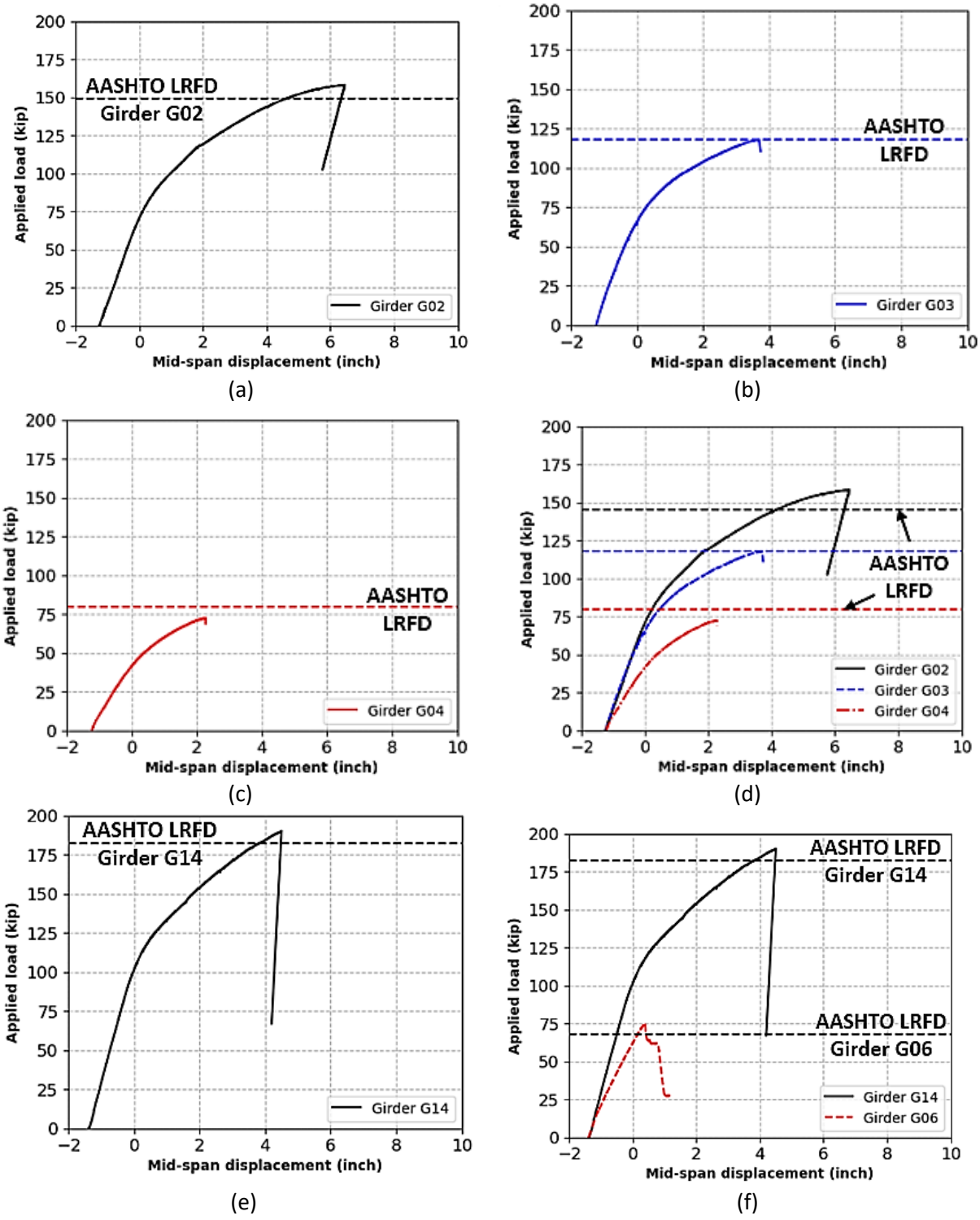

Figure 5-12. Flexural testing force-deflection curve for tested girders (a) Girder G02, (b) Girder G03, (c) Girder G04, (d) Comparison of Girders G02, G03 and G04, (e) Girder G14, (f) Girder G14 and Girder G06

5.3 Non-destructive testing for flexural strength of PC girders

5.3.1 Measuring prestress losses

A field technique for measuring residual prestress losses has been developed, requiring no specialized devices, data acquisition systems, or skilled technicians. This method is based on the principles of the cable general theorem (Leet and Gilbert, 4th edition). Figure 5-13 illustrates the theorem; the prestressing strands are modeled as cables that carry axial loads without significant flexural stiffness. According to the theorem, at any point along the cable subjected to vertical loads, the product of the cable sag (or vertical deflection, Δ) and the horizontal component (*h*) of the cable tension equals the bending moment at the same point in a simply supported beam subjected to the same load (Equation 5-2).

$$M = h \cdot \Delta \qquad \text{Equation 5-1}$$

$$M = \frac{P \,.\, l}{4} \qquad \text{Equation 5-2}$$

$$T = h = \frac{P \,.\, l}{4 \,.\, \Delta} \qquad \text{Equation 5-3}$$

$$T = h \cdot \cos\theta \approx h, \text{ (for small deflections)} \qquad \text{Equation 5-4}$$

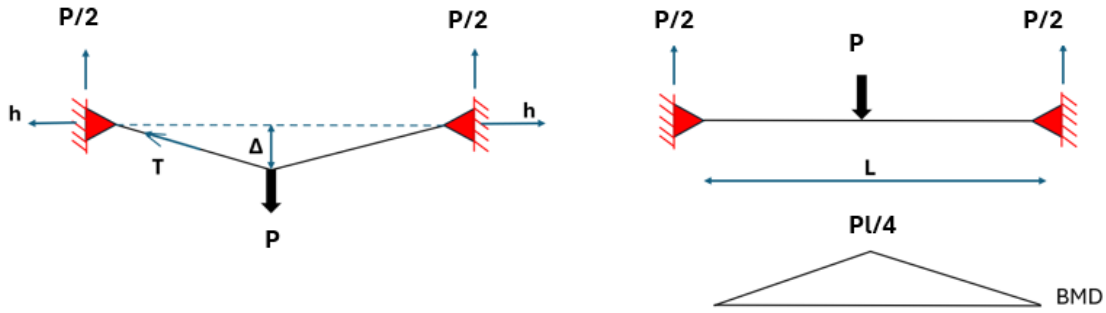

Figure 5-13. General cable theorem illustration

The technique leverages small-deflection and general cable theories, ensuring that it is non-destructive and does not require inducing large deflections in the stressed strands. The horizontal component of the tension can therefore be equated to the tension in the strand. Given that the strand cross-section is uniform, this tension remains consistent across the length of the exposed strand. The boundary conditions assume that both ends of the strand are hinged, based on three considerations: (1) the strand's lack of flexural rigidity means it cannot provide lateral stiffness when exposed, (2) the strand is bonded to the concrete, allowing the ends to rotate freely and linearly relative to the point of load application, and (3) the applied

vertical load is small, resulting in minimal deflection even if the strand has experienced significant stress loss.

To accurately estimate the flexural strength, determining the effective prestress using a non-destructive testing (NDT) method was essential. The research team devised a technique involving the suspension of a 24.5-lb. weight at the midpoint of each exposed strand, using a scale for precise application. The exact lengths of the strands were measured, and a dial indicator with a precision of 1/10,000 of an inch was used to monitor the resulting deflection, as illustrated in Figure 5-13. By modeling the strand endpoints as hinges under simply supported conditions, the effective prestress force (T) was calculated using the relationship among the sag (Δ), the applied weight (P), and the strand length (L).

Table 5-2 summarizes the NDT measurements and prestress loss calculations. Figure 5-14 shows the number and location of each strand that was assessed using the deflection method. Figure 5-15 shows the implementation of the deflection method for the damaged Girder G06. According to AASHTO LRFD (section 5.9.5.4.2c) the stress in prestressing strands immediately after the transfer is taken not less than 0.55 f_{py} (55% of the strand yield strength).

The ratio of the measured effective prestress to the minimum code requirement was evaluated. Using a binary criterion, strands with ratios above 1 are considered to have sufficient effective prestress force to contribute to the flexural strength, and ratios less than 1.0 were excluded from flexural strength calculations (Table 5-3). Measurements revealed that only six out of 16 strands met this criterion. Consequently, the flexural strength was estimated based on these six strands, reflecting the reduced contribution to the girder's overall capacity. The failure load reached 74.5 kips, corresponding to a bending moment of 521 kips-ft. The residual flexural strength, estimated through non-destructive testing and assessment of prestress losses, was calculated to be 475 kips-ft, which corresponds to five strands.

The test-to-calculated strength ratio was found to be 9.6%. The increased strength can be attributed to the enhanced compressive strength of the patched area, which likely improved the overall load-carrying capacity. Another contributing factor was the conservative assumption that only five strands were functional out of 16, based on the minimum effective prestress limit as a threshold. However, one additional strand, identified as Strand 9, exhibited a measured effective prestress ratio of 0.9. While this value fell slightly below the threshold, it likely contributed to the flexural strength, suggesting the conservative criteria may have underestimated the strand's contribution, although it is practical to apply the conservative criteria to ensure safe design.

Table 5-2. Summary of the measurement of the NDT

1	24.5	18.75	0.1330	114.8	863.49	0.86
2	24.5	16.75	0.0330	102.6	3108.90	3.11
3	24.5	14.25	0.1030	87.30	847.39	0.85
4	24.5	15.75	0.0360	96.50	2679.69	2.68
5	24.5	18.00	0.0120	110.3	9187.50	9.19
6	24.5	19.50	0.0630	119.4	1895.83	1.90
7	24.5	19.75	0.2280	121.0	530.56	0.53
8	24.5	14.375	0.0210	88.00	4192.71	4.19
9	24.5	11.5	0.0038	70.40	18536.18	18.54
10	24.5	14.00	0.0035	85.80	24500.00	24.50
11	24.5	16.75	0.0040	102.6	25648.44	25.65
12	24.5	20.00	0.2560	122.5	478.52	0.48
13	24.5	13.50	0.0525	82.70	1575.00	1.58
14	24.5	10.25	0.0020	62.80	31390.63	31.39
15	24.5	12.38	0.0038	75.80	19946.55	19.95
16	24.5	16.13	0.0040	98.80	24691.41	24.69

w: Vertical Weight; l: Strand exposed length; Δ : Vertical Deflection; M: Bending moment, P_e: Prestress force

Table 5-3. Summary of meeting the AASHTO LRFD Minimum Effective Prestress Compliance

1	20.45	0.86	0.0	x
2	20.45	3.11	0.2	x
3	20.45	0.85	0.0	x
4	20.45	2.68	0.1	x
5	20.45	9.19	0.4	x
6	20.45	1.90	0.1	x
7	20.45	0.53	0.0	x
8	20.45	4.19	0.2	x
9	20.45	18.54	0.9	x
10	20.45	24.50	1.2	✓
11	20.45	25.65	1.3	✓
12	20.45	0.48	0.0	x
13	20.45	1.58	0.1	x
14	20.45	31.39	1.5	✓
15	20.45	19.95	1.0	✓
16	20.45	24.69	1.2	✓

$\mathbf{P}_{e,\,min}$: Minimum effective prestress; ✓: Pass; x: Fail

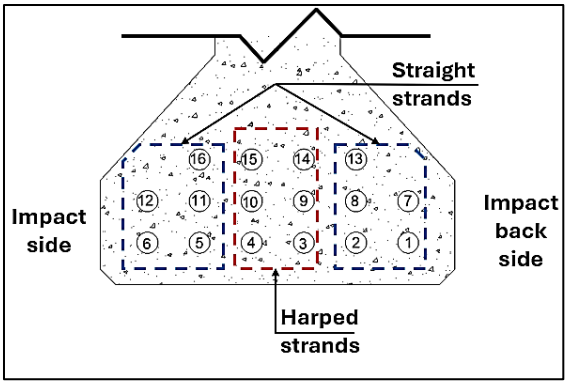

Figure 5-14. Layout of the strand numbers

Figure 5-15. Implementation of deflection method (a) Setup, (a) Dial gage, (c) Weight scale

Chapter 6. Experimental Evaluation of Repair Techniques

6.1 Introduction

This chapter investigates the repair of damaged girders using two distinct methods: the mechanical strand splicing technique and externally bonded CFRP composites, Figure 6-1. The primary objective was to restore the girder's flexural strength.

(a) (b)

Figure 6-1. Methods used for structural repair (a) Mechanical strand splicing (b) CFRP composite

6.2 Mechanical splicing repair

The mechanical splicing method, utilizing the commercially available Grabb-It system, is relatively easy to install. However, limited research has been conducted on its performance, and existing studies have not reached a consensus on its efficiency. Current literature recommends limiting the splicing to 15% of the prestressing strands due to the lack of experimental data beyond this ratio.

An experimental program was conducted to investigate the flexural behavior of four girders repaired using mechanical splicing–Girders G05, G10, G11, and G12. Before repair, the girders experienced strand losses ranging from 17% to 33%. The repaired girders were subjected to four-point bending tests in a simply supported configuration.

6.2.1 Surface preparation of the damaged area

Loose and damaged concrete was removed using a jackhammer, exposing the damaged strands and surrounding material. The exposed area ranged from 4 to 7 feet long, depending on the extent of the damage and the number of spliced strands required to allow for staggered splices. The repair section should be preloaded as needed to ensure live load tensile stresses do not exceed those of the original section (NCHRP 280).

6.2.2 Application of the Grabb-It strand splicing technique

The Grabb-It mechanical splice utilizes a turnbuckle mechanism consisting of two threaded rods housed within a threaded coupler in the middle. This system applies tension to the strands on both sides through strand chucks at each end. The manufacturer provides a method for monitoring strand tension by measuring slippage at both ends and comparing the original and

post-tension thread lengths within the splice. This enables the calculation of elongation and tension, as specified in the manufacturer's installation guidelines. During the tensioning process, the research team installed strain gauges to capture real-time strain data.

Each spliced strand was tensioned to a prestress force of 26 kips, representing 70% of the specified yield strength (f_{py}), in accordance with AASHTO LRFD Bridge Design Specifications for effective prestress after losses, refer to Appendix F. This ensured that the spliced strands achieved a prestress level equivalent to the original undamaged strands to ensure uniform stress distribution.

To optimize stress distribution and mitigate stress concentrations, strand splices were staggered per established engineering guidelines. Visual inspections were performed during and after installation to verify proper alignment and tensioning, ensuring the reliability and effectiveness of the repair strategy.

6.2.3 Grout patching

Following the splicing and tensioning of the strands, the damaged concrete areas were repaired using Sika 48 FS, a non-shrink, high-strength grout. Formwork was constructed around the spliced region to provide support during the repair process. To ensure quality control, two-inch cube samples were taken from the grout mixture on the day of casting. The cubes were then tested after three and seven days to determine the compressive strength.

While preloading is typically used to apply prestress to the patched area and prevent cracking under service loads, the focus of this study was on evaluating the girder's flexural capacity rather than its performance under service conditions. As a result, preloading was not implemented in this experimental program. The flexural testing was specifically designed to continue until the ultimate failure state, to assess the girder's behavior at its maximum load capacity.

6.2.4 Crack injection

Following the high-strength grout casting and initial curing, a detailed inspection was conducted to identify any cracks resulting from the impact test. Identified cracks were carefully opened and chased using specialized tools to widen their surface and expose their full extent. The cracks were then thoroughly cleaned to remove debris and loose material, ensuring a clean and sound surface for effective treatment, as recommended by ACI PRC-224-01(ACI 224). A Simpson strong-tie low-viscosity epoxy resin was applied under pressure to seal the identified cracks. The process for the mechanical splicing is summarized in Figure 6-2.

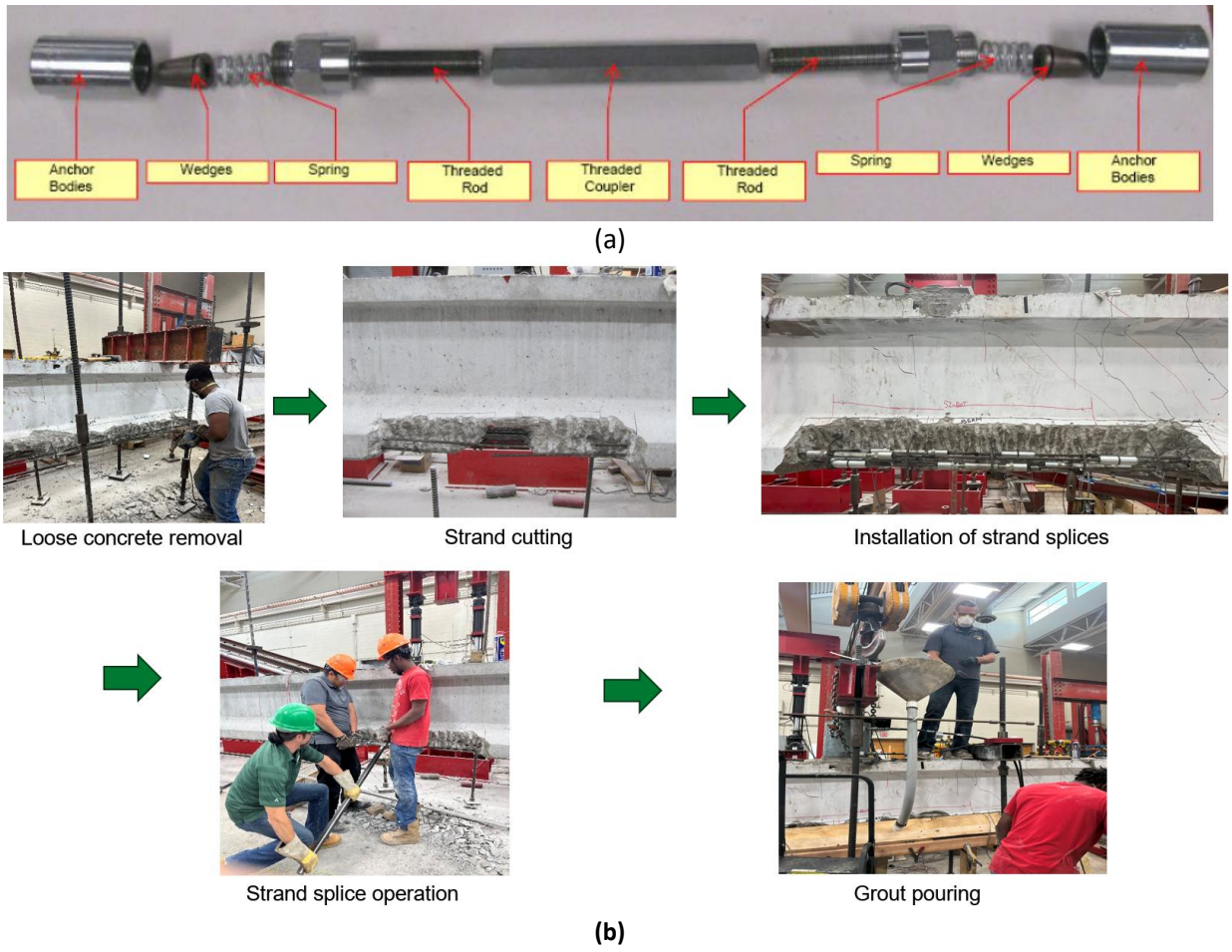

Figure 6-2. (a) GRABB-IT overview (Source: https://www.prestresssupply.com/), (b) Strand splicing repair steps

6.2.5 Test setup and instrumentation

The experimental setup was designed to evaluate the flexural performance of the repaired prestressed girders. The test featured a 44-foot simply supported span, with loads applied symmetrically 14.5 feet from each support. This configuration created a 15-foot constant moment zone at the center of the beam (Figure 6-3). The load was applied using two 500-kips hydraulic cylinders equipped with precision load cells, ensuring accurate force measurement throughout the test.

A data acquisition system continuously monitored the girder's response. Linear variable differential transformers (LVDTs) installed at the girder ends and supports measured horizontal displacements. String potentiometers positioned beneath each load point and at the midspan recorded vertical deflections. Additionally, strain gauges were mounted on the prestressing strands before concrete casting to monitor strain behavior throughout the test.

Figure 6-3. Test setup configuration

6.2.6 Girder G10 – spliced 17% of strands

This girder was not subjected to impact loading. Instead, intentional cutting was performed on two out of twelve strands, representing a 17% strand damage level. The cutting was carried out using an electric grinder. After the removal of concrete and cutting of the strands, the girder exhibited a camber of 1.8 inches. The girder was repaired using strand splicing, following the steps outlined earlier. After the repair, the camber increased to 1.99 inches, indicating a successful reintroduction of prestress into the damaged strands.

Following the repair, the girder underwent four-point flexural testing as described previously. An initial crack was observed in the constant moment region at a load of 91 kips. As the load increased, additional flexural cracks appeared, predominantly within the constant moment zone, extending vertically to the top flange at a load of 132 kips.

At 138 kips, diagonal shear cracks began to form beyond the constant moment region. Testing continued until the girder experienced a significant deflection of 6.06 inches, demonstrating substantial ductility. At this stage, the load plateaued, with flexural-shear crack widths reaching approximately 0.1 inches. Audible popping noises were noted at 144 kips, followed by the sound of concrete crushing at 149 kips. The girder ultimately reached a maximum load of 150.7 kips, corresponding to a moment capacity of 1064.7 ft-kips (Figure 6-4).

The force versus mid-span displacement curve is shown in Figure 6-5, indicating that the spliced girder exhibited initial stiffness comparable to that of the control girder (Girder G02). This confirmed the effectiveness of the splicing, concrete patching, and crack injection techniques.

Table 6-1 summarizes the strengths of the repaired girders compared to the tested control girder and the AASHTO LRFD theoretical flexural strength of the control girder. The spliced girder regained 95.2% of the control girder's strength and exceeded the theoretical capacity by 1.1%, highlighting the success of the restoration methods.

Figure 6-6 presents the strain-force curve for the spliced girder. In Figure 6-6a, the spliced strands S1 and S2, which were straight, demonstrated behavior nearly identical to that of the undamaged strands, with strain increasing proportionally to the applied bending moment. In addition, although the mode of failure of the repaired girder was similar to that of the control girder, the spliced strands peaked at a strain of 0.007 corresponding to the applied load of 120 kips, approximately 80% of the girder's maximum capacity. This force corresponds to a displacement of 3.6 inches (Figure 6-7).

(a)

(b)

Figure 6-4. Girder G10 (a) Overall view of the girder at failure, (b) Close-up view of the girder at failure

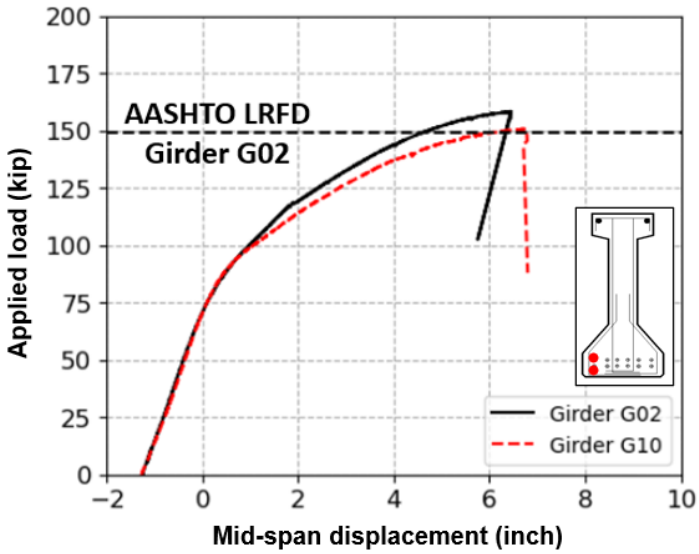

Figure 6-5. Force-displacement spliced girder 17% - Girder G10

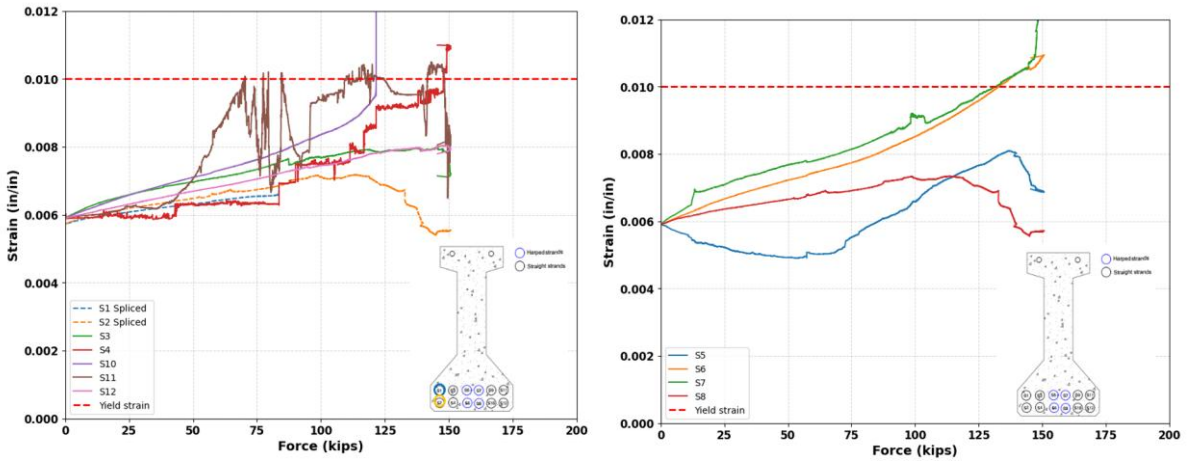

(a) (b)

Figure 6-6. Strain-force relationship of prestressing strands of Girder G10, (a) Straight strands, (b) Harped strands

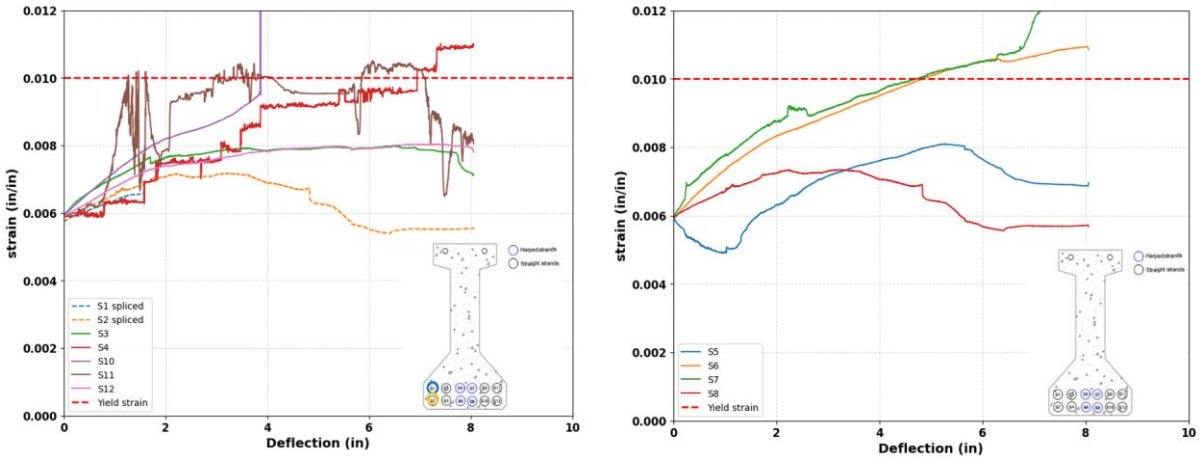

(a) (b)

Figure 6-7. Strain-deflection relationship of prestressing strands of Girder G10 (a) Straight strands, (b) Harped strands

6.2.7 Girder G11 – spliced 25% of strands

Similar to Girders G10, G11 was not subjected to impact loading. Three out of twelve strands were intentionally cut, using an electric grinder, simulating a 25% strand damage level. Following the removal of concrete and cutting of the strands, girder G11 exhibited a camber of 1.7 inches. The spliced strands were installed in a staggered configuration (Figure 6-8).

Once repaired and cured, the girder was subjected to four-point flexural testing. The failure mode of the girder exhibited typical flexural behavior, characterized by vertical cracks

originating from the soffit of the girder and propagating upward as the load increased until failure. Flexural shear cracks were also observed outside the constant bending region, particularly beneath the hydraulic jacks.

The first crack was observed in the constant moment region at a load of 74 kips. As loading continued, additional bending-related cracks appeared, primarily concentrated within the constant moment zone. Vertical cracks extended to the beam's top flange at a load of 112 kips.

At 118 kips, diagonal shear cracks began to form beyond the constant moment region, near the applied load. Testing proceeded until the girder reached a significant deflection of 5.8 inches. Audible popping sounds were heard at 128 kips, followed by the sound of concrete crushing at 132 kips. The girder reached its structural limit at 132.9 kips, corresponding to a maximum moment of 939 ft-kips (Figure 6-9).

Unlike Girder G10, where the failure occurred at the harping point away from the spliced strands, the failure of Girder G11 occurred at the spliced strand location. This suggests that the failure was initiated by the inability of the spliced strands to sustain the applied load (Figure 6-9a).

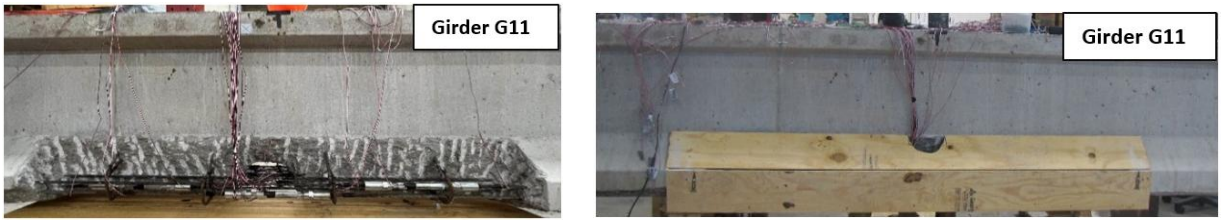

(a) (b)

Figure 6-8. Girder G11 with 25% strand damage (a) Strand splicing configuration, (b) Formwork used for splicing repair

(a) (b)

Figure 6-9. Girder G11 (a) Deflection of the girder during testing, (b) Failure of the girder

Figure 6-10 illustrates the force versus midspan displacement curve, demonstrating that the spliced girder effectively restored the initial stiffness of the Girder G02 up to an applied load of 25 kips, equivalent to 19% of the flexural capacity of the girder. Furthermore, the repaired girder (Girder G11) recovered 84% of Girder G02 strength and restored 89.2% of its theoretical

capacity (Table 6-1). The increased number of spliced strands reduced the efficiency of the repair. This is further evidenced by the shift in the failure location to the spliced strands rather than the harping point, as observed in both the Girder G02 and Girder G10.

Figure 6-11 presents the strain gauge data for the spliced girder. In Figure 6-11a, spliced strands S2 and S4, both straight strands, exhibited behavior nearly identical to the undamaged strands, with strain increasing proportionally to the applied force and bending moment. However, the strain gauge on strand S1 appeared defective, likely due to damage during the grout casting process. Furthermore, strand S4, an interior strand, demonstrated superior performance compared to S2, an exterior strand. S4 continued to display tension until the girder's failure, while S2 stopped at a force of 89 kips, corresponding to 67% of the girder's capacity—lower than the capacity achieved by the same strand in Girder G10. This force also corresponds to a displacement of 1.9 inches (Figure 6-12).

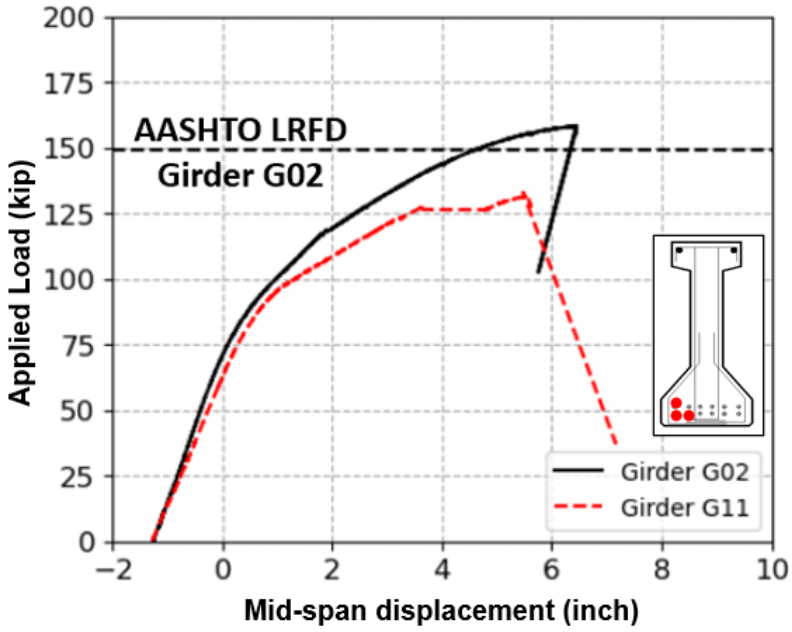

Figure 6-10. Force displacement curve of Girder G11

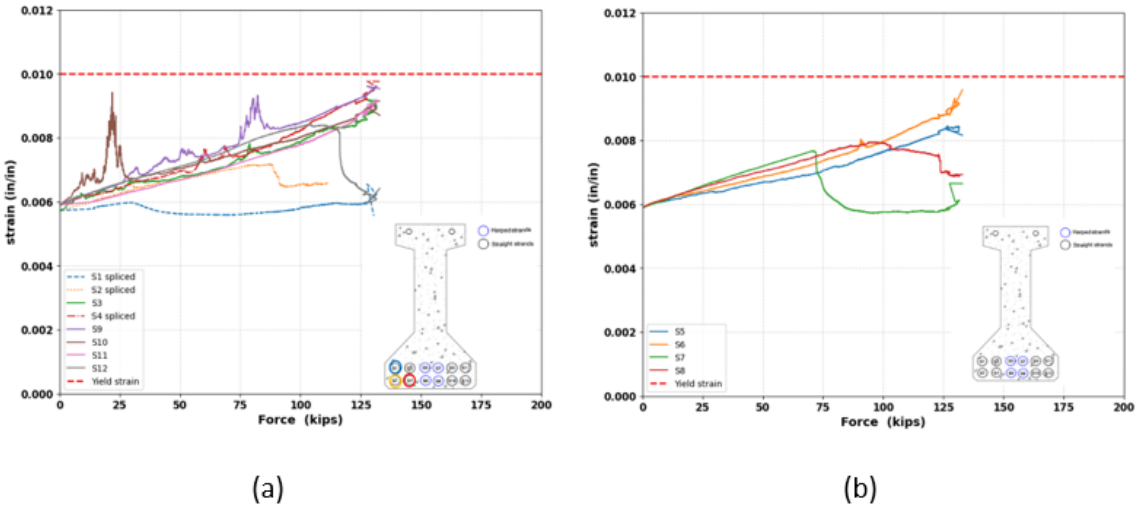

Figure 6-11. Strain-force relationship of prestressing strands of Girder G11 (a) Straight strands, (b) Harped strands

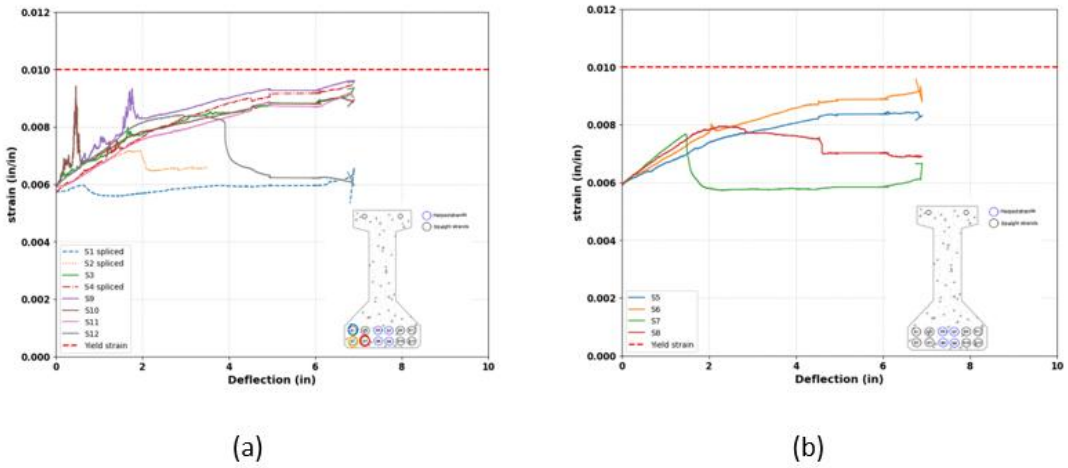

Figure 6-12. Strain-deflection relationship of prestressing strands of Girder G11 (a) Straight strands, (b) Harped strands

6.2.8 Girder G05 – spliced 33% of strands

Girder G5 underwent two impacts at maximum intensity, as described in Chapter 4. Analysis of internal strain gage data revealed the severity of the collisions, with four prestressing cables either reaching their yield strength or experiencing significant tension loss, resulting in a damage level of 33%. Following the impact tests and the severance of strands, the girder exhibited a camber of 1.375 inches and an out-of-plane lateral displacement of 0.3125 inches. Four of the twelve strands were spliced (Figure 6-13). After applying prestress, the camber increased to 1.625 inches, partially restoring the girder's pre-tensioned state.

After the repair and curing, the girder underwent four-point flexural testing. During testing, initial cracking was observed at a load of 61 kips, with cracks originating in the constant moment region and extending beyond the pre-existing impact-induced fractures. As the load increased, additional bending cracks developed, concentrated mainly within the constant moment region. Testing continued until the girder reached a deflection of 2.31 inches. At this point, the load remained approximately constant, and flexural-shear cracks widened to over 0.1 inches.

The girder ultimately failed at the location of the spliced strands. The force-deflection curve (Figure 6-15) indicates that the girder achieved a maximum load of 95 kips, which corresponds to a bending moment of 671.2 kips.ft which is 60% of the tested girder's original capacity and 63.7% of its theoretical flexural capacity. However, the initial stiffness was significantly reduced due to the damage sustained during multiple impact stages.

The repair did not fully restore the girder's flexural strength, primarily for two reasons. First, as observed in girders G10 and G11, the restored strength is influenced by the percentage of spliced strands, with a higher ratio of spliced strands leading to a lower efficiency of the splicing. Second, only the four exposed strands with severe damage were spliced, while the remaining strands embedded in the concrete were assumed fully functional. Undetected deterioration in these embedded strands likely contributed to the reduced overall capacity.

Figure 6-14c highlights stress concentrations at the ends of the strand splice chuck area. These localized stress concentrations caused bulging and spalling of the concrete cover, which may have led to the premature failure of the spliced strands.

(a) (b)

Figure 6-13. Girder G05 with 33% strand damage (a) Strand splicing configuration, (b) Formwork used for splicing repair

(a) (b)

(c)

Figure 6-14. Girder G05 failure (a) Failure at the splicing location, (b) Close-up to the splicing after concrete removal, (c) Splice chuck causing a horizontal crack

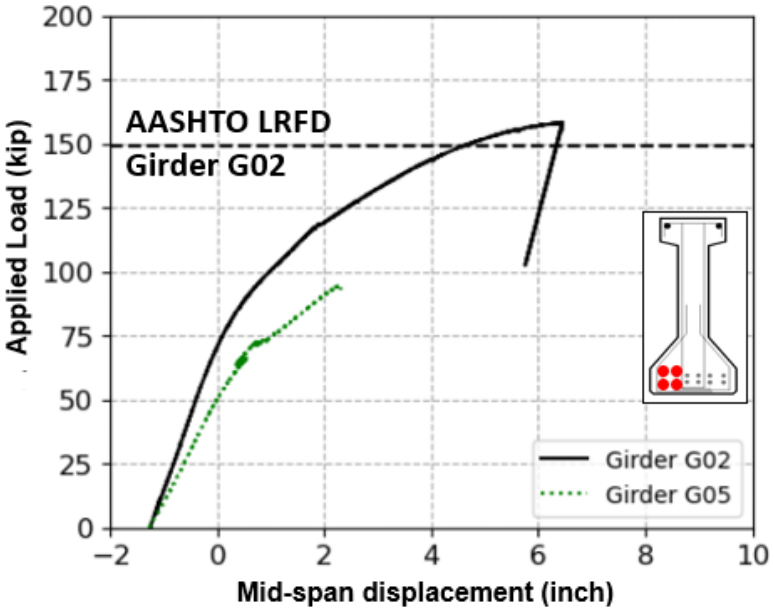

Figure 6-15. Girder G05 force-deflection curve of spliced girder 33%

6.2.9 Girder G12 – spliced 33% of strands

This girder was not subjected to impact damage; instead, four out of twelve prestressing strands were intentionally severed. To achieve this, concrete was removed from one side over a 7-foot length at mid-span, allowing access to cut the four strands using a steel grinder, resulting in a 33% strand loss. The girder had an initial camber of 1.5625 inches.

The primary objective of testing this girder was to evaluate mechanical splicing by replicating the repair at 33% strand loss while eliminating uncertainties observed in the previous test. Strain data and observations from the prior test indicated that the outer spliced strands were not fully utilized and tended to fail prematurely.

To address this issue, the two outermost spliced strands in this girder were confined using #4 rectilinear rebars, spaced every five inches along the splice length (Figure 6-16). These reinforcement elements were embedded in the concrete using epoxy, ensuring sufficient development length. The primary purpose of these rectilinear reinforcements was to provide additional lateral support to the longitudinal spliced strands, improving their effectiveness and mitigating premature failure.

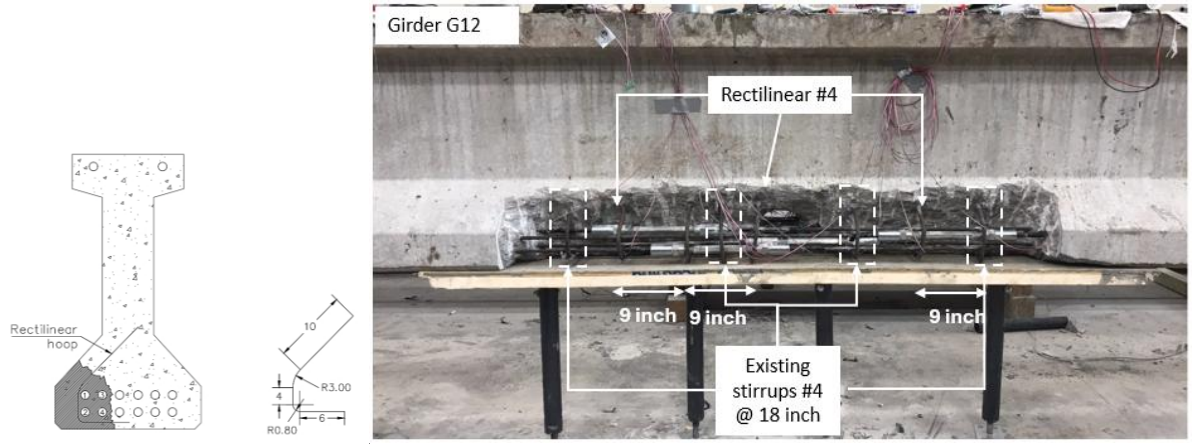

(a) (b)

Figure 6-16. (a) Illustration of the confining of the splice, (b) Photograph from the lab

Initial cracking occurred at 44 kips in the constant moment region, with subsequent bending cracks concentrating in this zone. At 120.35 kips, cracks extended vertically to the upper flange, approaching ultimate capacity. Diagonal shear cracks emerged beyond the constant moment area at 131 kips.

The beam exhibited significant ductility with crack redistribution along the length of the girder and reached a maximum deflection of 6.23 inches. Popping sounds were heard at 98 kips, followed by concrete crushing at 141 kips. Pronounced vertical cracking resulted from reduced

prestress in the repaired section. As shown in Figure 6-15, the girder reached its structural limit at 145 kips, achieving a maximum moment capacity of 1024.4 ft-kips (Figure 6-17).

(a)

(b)

Figure 6-17. Photographs of G12 showing (a) Failure of 33% damage repaired girder at midspan (b) Close-up view of girder failure

Figure 6-18 presents force versus midspan-displacement data that reveals the spliced girder effectively regained the initial stiffness of Girder G02 up to 15 kips of jacking force, which represents 10.34% of total girder capacity.

Strength comparisons between the repaired girders and AASHTO LRFD theoretical values are documented in Table 6-1. The data shows impressive recovery, with the spliced girder achieving 91.6% of the control girder's strength and 98% of the theoretical capacity.

Figure 6-19 documents strain gage measurements from the spliced girder testing. As shown in Figure 6-19a, straight spliced strands S2 and S3 performed similarly to undamaged strands, showing proportional strain increases with both jacking force and bending moment. There were two exceptions: strand S4 reached yield at approximately 125 kips, and strand S1's strain gauge failed after 25 kips of loading. The comparable behavior between spliced strands S2 and S3 and the existing (not spliced) strands can be attributed to the enhanced confinement design using rectilinear hoops, as shown in Figure 6-19,20. This response indicates that the confinement system successfully integrated the spliced strands into the repaired structure up to higher applied loads while maintaining overall performance.

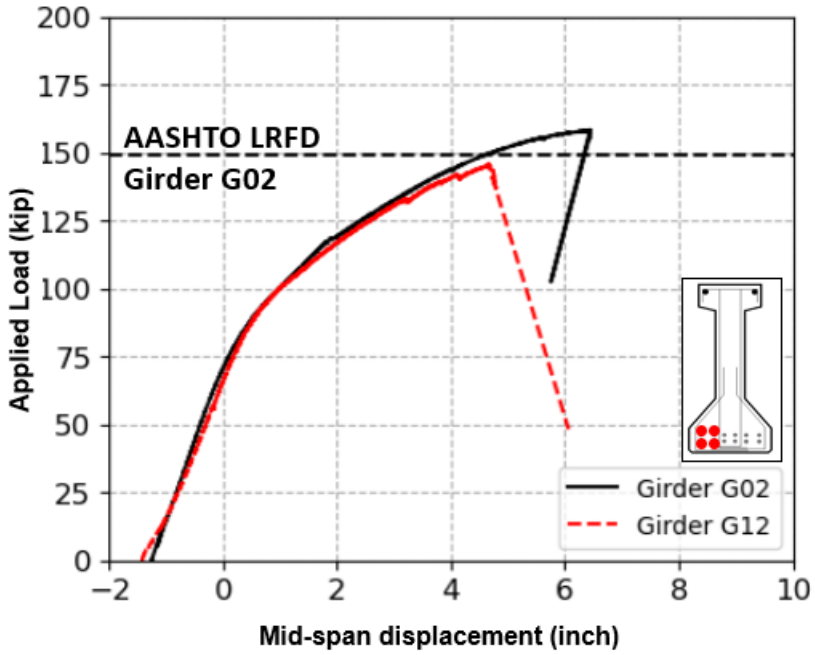

Figure 6-18. Force deflection curve for Girder G12

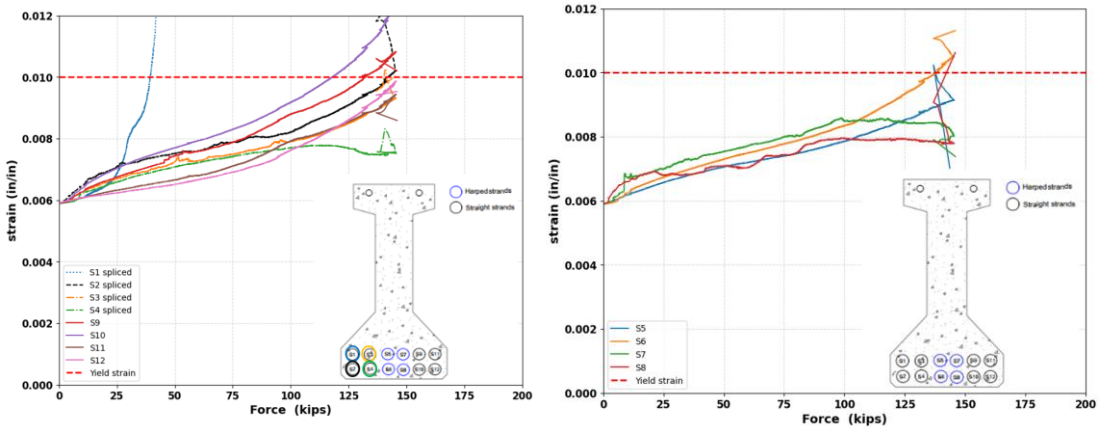

(a) (b)

Figure 6-19. Strain-force relationship of prestressing strands for Girder G12 (a) Straight strands (b) Harped strands

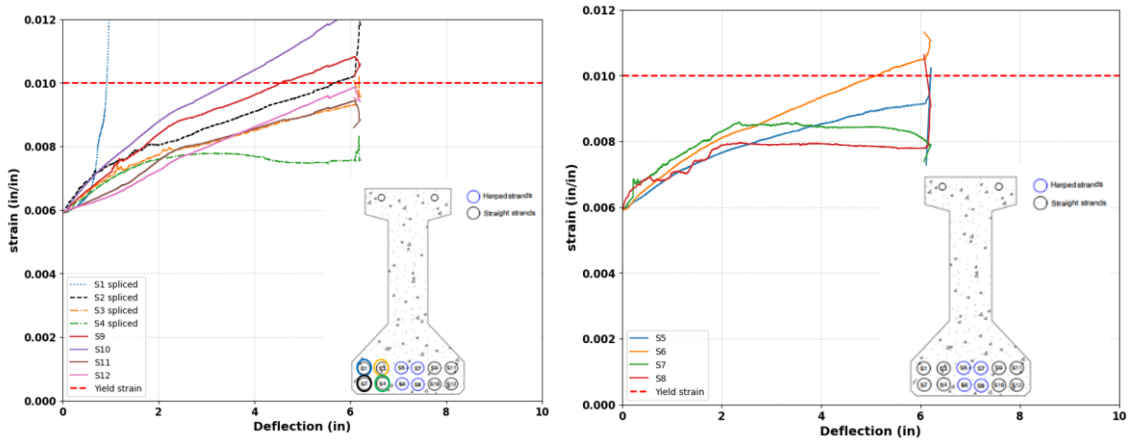

(a) (b)

Figure 6-20. Strain-deflection relationship of prestressing strands for Girder G12 (a) Straight strands (b) Harped strands

Table 6-1. Summary of the spliced girder testing results

Girder	Peak applied load (kips)	Bending moment (kips.ft)	Max. displacement (inch) at peak load	Repair/Girder G02-test	Repair/ Girder G02-AASHTO LRFD
Girder G02	158.3	1118.0	6.44	-	-
Girder G10	150.7	1064.7	6.60	95.2%	101.1%
Girder G11	132.9	939.0	5.80	84.0%	89.2%
Girder G05	95.0	671.2	2.30	60.0%	63.7%
Girder G12	145.0	1024.4	6.23	91.60%	97.3%

6.2.10 Calibration of the Grabb-It torque measurement technique

For this study, the research team installed strain gauges during the tensioning process of the splices. Table 6-2 compares the strain values derived from the manufacturer's procedure with those obtained from the strain gauges. The manufacturer's method was found to overestimate strain and tension by 18% compared to the actual strain measurements.

Table 6-2. Strain data from GRABB-IT specs and strain gage instrumentation

S1 from Girder G10	0.0055	0.0067	0.82
S1 from Girder G11	0.0057	0.00835	0.680
S2 from Girder G11	0.00536	0.0077	0.69
S4 from Girder G11	0.0059	0.0074	0.79
S1 from Girder G05	0.006	0.0059	1.01
S2 from Girder G05	0.006	0.0061	0.98
S3 from Girder G05	0.0065	0.0065	1.00
S4 from Girder G05	0.0054	0.0088	0.61
		Absolute mean error	0.82

6.3 Externally bonded-CFRP

Externally bonded CFRP (Carbon Fiber Reinforced Polymer) composites have been widely used for repairing damaged girders without the need for splicing severed strands or reapplying prestressing forces. There were two primary objectives in implementing this method in the current research. First, the study aimed to evaluate the efficiency of CFRP repair in cases of severe damage, with a loss of prestressing strands of up to 33%. This represents a significant extension of prior research, which predominantly focused on lower levels of damage severity, typically up to 25% strand loss. Second, the research sought to compare the performance of CFRP-repaired girders with those repaired using strand splicing. This comparative analysis is critical to understanding how the two methods perform in terms of strength and ductility under varying levels of damage severity, providing valuable insights into their respective advantages and limitations.

Carbon fiber reinforced polymer (CFRP) composites were applied to two girders with two levels (17% and 33%) of flexural strength loss to compare the behavior of the spliced girders. Externally bonded CFRP with the wet-layup system was selected for the repair. The number of plies was designed in accordance with the guidelines of the ACI 440.2-R11. The design was essentially for determining the required number of longitudinal plies that would be installed on the soffit of the girder. The design strain of the CFRP system was calculated according to (Equation 6-1). An Anchorage system consisting of CFRP U-wraps was provided along the length of the longitudinal plies to delay the debonding strain.

$$\varepsilon_{fd} = 0.083\sqrt{\frac{f_c'}{n E_f t_f}} \leq 0.9\varepsilon_{fu}\ (in.lb)$$ Equation 6-1

Where ε_{fd} is the design strain of FRP, f_c' is the compressive strength of concrete in ksi, n is the number of longitudinal FRP plies, E_f is the modulus of elasticity of FRP, and t_f is the thickness of the longitudinal FRP ply.

The CFRP fabric used was CSS-CUCF44, a unidirectional carbon fiber material. The material properties are summarized in Table 6-3.

Table 6-3. Dry fiber material properties of CFRP

Material property	Value
Tensile strength (ksi)	670
Tensile modulus (ksi)	37000
Nominal dry thickness (inch)	0.0324
Elongation at failure	1.9%
Dry fabric density (lb./in^3)	0.065

6.3.1 Girder G07 - externally bonded-CFRP 17%

Girder G07 was repaired using externally bonded Carbon Fiber Reinforced Polymer (CFRP) composites with the manual wet lay-up system. The girder had two strands out of twelve removed from one side, corresponding to a 17% loss of prestressing strands (Figure 6-21). Two longitudinal CFRP plies, following ACI 440.2R-17 guidelines, were applied to the girder's soffit.

The design estimated a debonding strain of 0.57% for the two CFRP plies (Equation 6-1). The strain at the soffit was adjusted for the preloading required to straighten the girder before CFRP installation. The goal was to restore the girder's nominal capacity. The longitudinal plies were 33 feet long, with the cutoff length extending after the span at which the bending moment is less than the cracking moment with a value of development length, as per ACI 440 guidelines. The first ply was terminated six inches beyond the second layer. U-wraps were spaced at 16 inches, with 5-inch spacing at both ends for proper anchorage. Flexural strengthening details are illustrated in Figure 6-21.

Girder G07 suffered lateral damage due to impact, causing significant cracking. A low-viscosity epoxy resin was injected into the damaged area to seal the cracks and restore structural integrity. Concrete was removed from the bottom flange to access the damaged strands, which were cut and restored with formwork and high-strength non-shrink grout (Sika 428 FS). Concrete cubes were tested at three and five days to confirm strength. Shear dowels (#4 rebar) were used to bond the new concrete to the existing structure.

Surface preparation was crucial for optimal CFRP adhesion (Figure 6-22a). After curing, all corners were rounded to ¾ inch radius using concrete grinders to reduce stress concentrations. The surface was roughened to CSP level 3 with a concrete scarifier. A high-modulus epoxy paste

was applied before CFRP installation for surface leveling and to ensure a flat surface for the application of the longitudinal plies. The CFRP fabric was impregnated with resin and applied to the girder's soffit, with U-wraps installed afterward (Figure 6-22b).

A witness panel was installed during the CFRP application to conduct a pull-off test following ASTM D5722 (Figure 6-23). The test was performed after 72 hours on four specimens, yielding an average failure normal stress of 378 psi—significantly exceeding the ASTM D5722 minimum requirement of 150 psi. The failure occurred in the concrete substrate, which is the preferred failure mode, as shown in Figure 6-23b.

The girder was rotated 180 degrees, allowing hydraulic jacks to apply force from below, to allow sufficient access to the girder soffit for proper surface preparation and FRP application. During testing, no cracks were observed as the jacking force increased, though noticeable upward deflection occurred. The failure was sudden and brittle, characterized by the rupture of the U-wrap, followed by the debonding of the longitudinal plies (Figure 6-22c). Figure 6-24 shows the force-deflection curve of the repaired girder. The flexural strength of the girder reached 194.9 kips which corresponds to 1375 kips.ft and exceeded the Girder G02 test by 23% and the AASHTO LRFD estimate of Girder G02 by 30.5%. Table 6-3 summarizes the breaking force of the repaired girder compared to Girder G02 and the design.

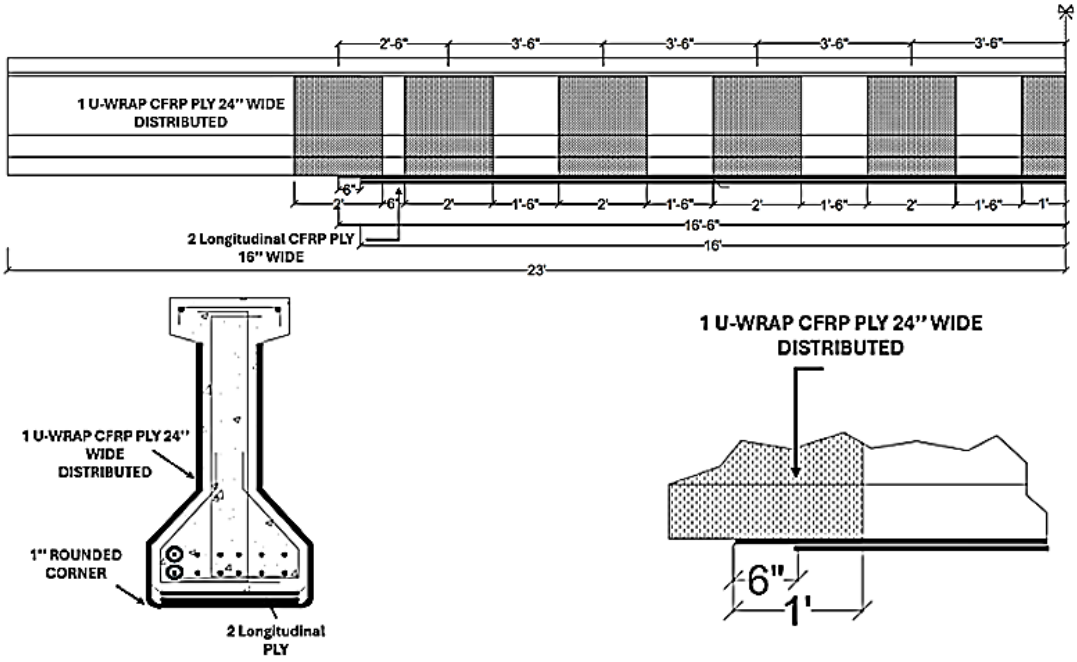

Figure 6-21. Elevation of repair of Girder G07, cross-section and CFRP U-wrap details, and termination details for longitudinal CFRP

(a) (b)

(c)

Figure 6-22. (a) Surface preparation, (b) CFRP curing, (c) Failure of the girder

(a) (b)

Figure 6-23. (a) Witness panel for pull-off test, (b) Pull-off test specimens' failure

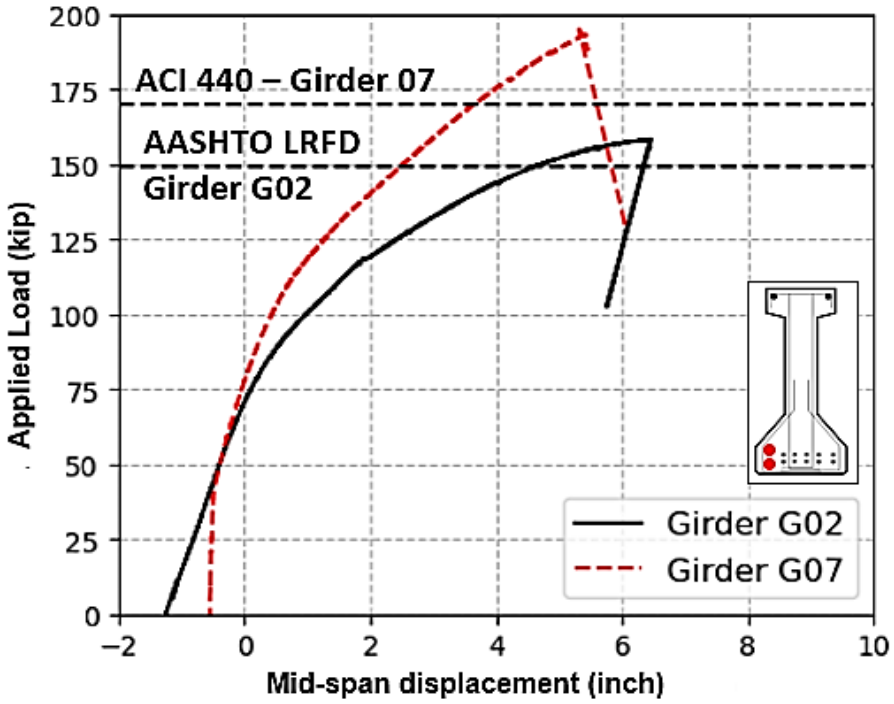

Figure 6-24. Force deflection curve of repaired Girder G07

6.3.2 Girder G08 - externally bonded-CFRP 33%

Similar to Girder G07, Girder G08 was repaired using externally bonded CFRP using the manual wet lay-up system. The girder had three strands out of twelve removed from one side, corresponding to a 33% loss of prestressing strands (Figure 6-25). One additional ply was added, for a total of three longitudinal CFRP plies, and all were applied to the girder's soffit following ACI 440.2R-17 guidelines. The same CFRP fabric from the previous repair was used for consistency and fair comparison.

The design estimated a debonding strain of 0.46% for the three CFRP plies. The strain at the soffit was adjusted for the preloading required to straighten the girder before CFRP installation. The goal was to restore the girder's nominal capacity. The same CFRP configuration of the previous repair was implemented in this repair. The longitudinal plies were 33 feet long, with the cutoff length extending after the span at which the bending moment is less than the cracking moment with a value of development length, as per ACI 440 guidelines. The longitudinal plies were terminated six inches from each other (Figure 6-25). U-wraps were spaced at 16 inches, with 5-inch spacing at both ends for proper anchorage. Flexural strengthening details are in illustrated Figure 6-25.

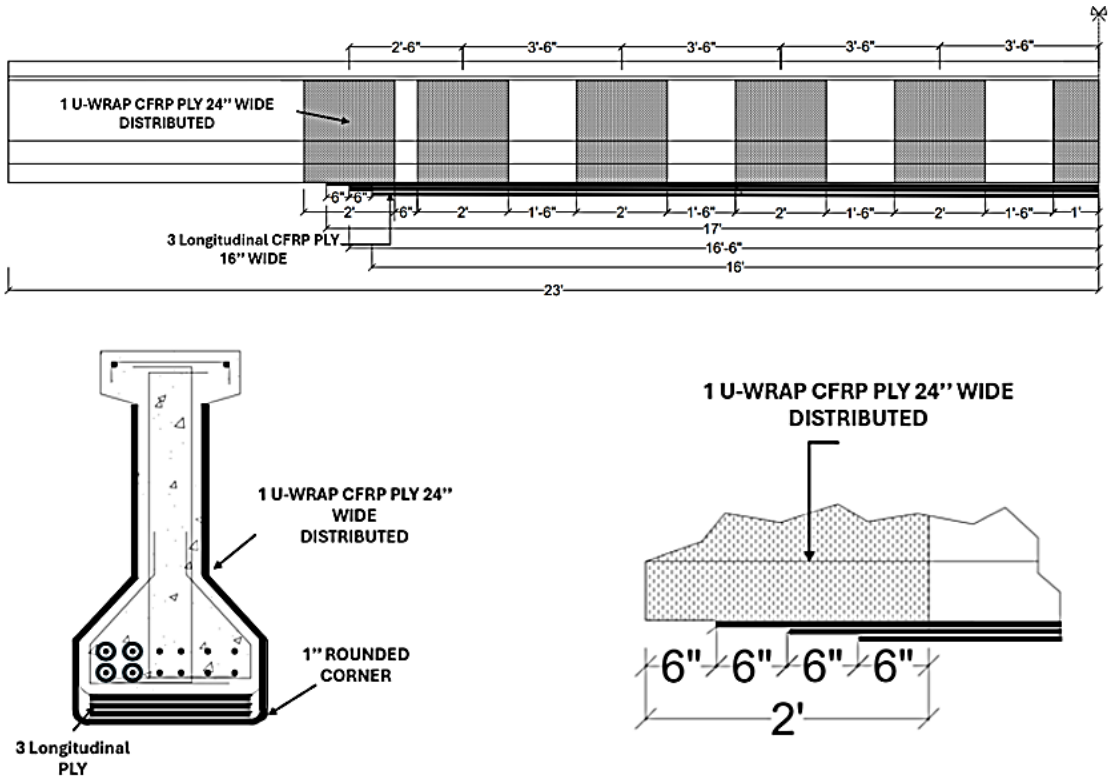

Figure 6-25. (a) Elevation of repair of Girder G08, cross-section and CFRP U-wrap details, and termination details for longitudinal CFRP

Girder G08 also suffered lateral damage due to impact, causing significant cracking. A low-viscosity epoxy resin was injected to seal the cracks and restore structural integrity. Concrete was removed from the bottom flange to access the damaged strands, which were cut and restored with formwork and high-strength non-shrink grout (Sika 428 FS). Concrete cubes were tested at three and five days to confirm strength. Shear dowels (#4 rebar) were used to bond the new concrete to the existing structure.

Surface preparation was crucial for optimal CFRP adhesion (Figure 6-26). After curing, all corners were rounded to ¾ inch radius using concrete grinders to reduce stress concentrations. The surface was roughened to CSP level 3 with a concrete scarifier. A high-modulus epoxy paste was applied before CFRP installation for surface leveling. The CFRP fabric was impregnated with resin and applied to the girder's soffit, with U-wraps installed afterward (Figure 6-26).

A witness panel was installed during the FRP application to conduct a pull-off test in accordance with ASTM D5722 (Figure 6-27). The test was performed after 72 hours on four specimens, yielding an average failure normal stress of 218 psi—exceeding the ASTM D5722 minimum requirement of 150 psi. The failure occurred in the concrete substrate, which is the preferred failure mode, as shown in Figure 6-22.

Similar to the previous repair, the girder was rotated 180 degrees, allowing hydraulic jacks to apply force from below, to allow sufficient access to the girder soffit for proper surface preparation and CFRP application. During testing, no cracks were observed as the jacking force increased, though noticeable upward deflection occurred. The failure was sudden and brittle, characterized by the rupture of the U-wrap, followed by the debonding of the longitudinal plies (Figure 6-26c). The flexural strength of the girder reached 184.1 kips which corresponds to 1296 kips.ft and exceeded Girder G02 test by 16% and the AASHTO LRFD estimate of Girder G02 by 23% (Figure 6-28). Table 6-4 summarizes the breaking force of the repaired girder compared to the G2 and the design. The weight of the girder at the location of the hydraulic jacks was subtracted from the estimation of the peak applied load.

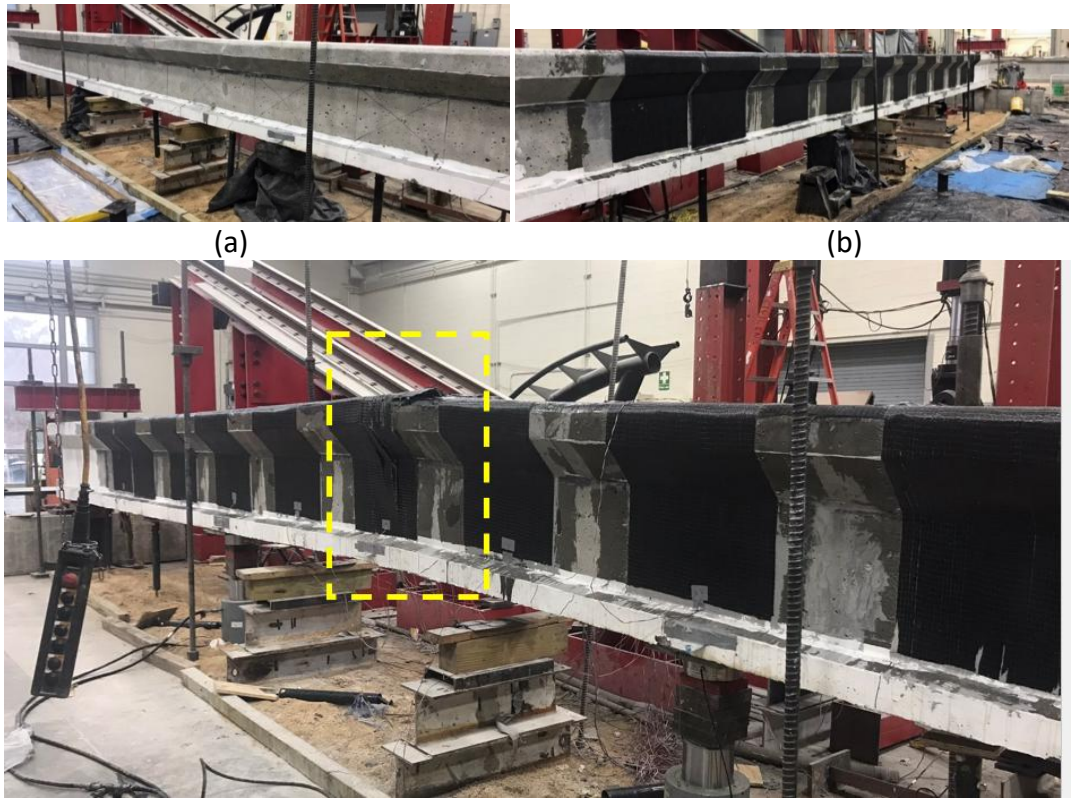

Figure 6-26. (a) Surface preparation, (b) CFRP curing, (c) Failure of the girder

(a) (b)

Figure 6-27. (a) Witness panel for pull-off test, (b) Pull-off test specimens' failure

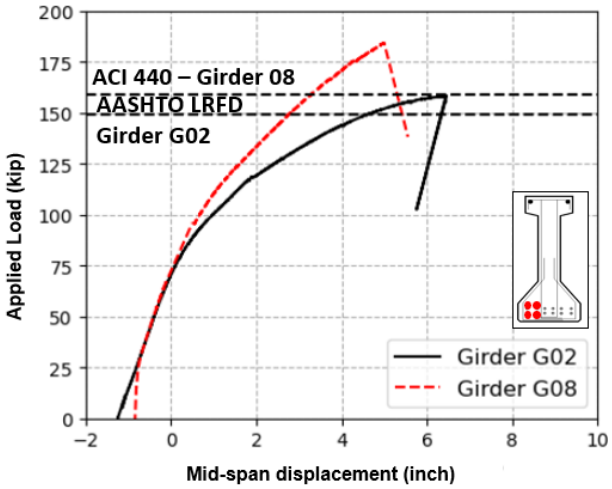

Figure 6-28. Force deflection curve of repaired Girder G08

Table 6-4. Summary of the FRP girder testing results

Girder	Peak applied load (kips)	Bending moment (kips. ft)	Max. displacement (inch) at peak load	Repair/ Girder G02-test	Repair/ Girder G02-AASHTO LRFD
Girder G02	158.3	1118	6.44	-	-
Girder G07	194.9	1375	5.70	123%	130.5%
Girder G08	184.1	1296	4.96	116%	123%

6.4 Hybrid repair system

6.4.1 Girder G13 - spliced 50% of strands

This girder was not subjected to impact damage; instead, six out of twelve prestressing strands were intentionally severed. To achieve this, concrete was removed from two sides over a 7-foot length at mid-span, allowing access to cut the six strands three from either side using a steel grinder, resulting in a 50% strand loss. The girder had an initial camber of 1.375 inches. The primary objective of testing this girder was to evaluate the effectiveness of hybrid repair in a 50% loss of strands. Mechanical strand splice was used internally to reconnect broken strands and induce prestress force, while externally bonded CFRP was used in only a U-wrap configuration as a confinement for the repaired section.

The U-wrap was applied continuously over the entire repair area with a 6-inch overlap to ensure complete confinement. Proper surface preparation was essential for maximizing CFRP bond performance. A concrete scarifier was used to ensure that by creating a CSP-3 surface roughness profile. All corners were rounded to a ¾-inch radius with concrete grinders to eliminate stress concentration points.

Before applying the CFRP system, high-modulus epoxy paste was applied to level the concrete surface. The CFRP fabric was saturated with epoxy resin and installed in a U-wrap configuration around the repair zone (Figure 6-29). To verify installation quality, a witness panel was created during the CFRP application process. Following ASTM D5722 guidelines, pull-off testing was conducted after a 72-hour cure period on four specimens. The testing revealed an average failure stress of 528 psi, almost 3.5 times the minimum 150 psi requirement specified by ASTM D5722. The failure mode occurred within the concrete substrate, which is the desired failure mode, confirming optimal bond development.

(a) (b)

Figure 6-29. (a) Girder being repaired with mechanical strand splice, (b) Photograph of completely repaired girder (hybrid system) with CFRP U-wraps as confinement

For the experimental setup, the girder was inverted 180 degrees to permit the application of hydraulic jacking forces from beneath. This configuration provided essential access to the girder soffit, facilitating proper surface preparation and CFRP application procedures. As loading

progressed during testing, the girder exhibited significant upward deflection, though notably, no visible cracking patterns developed despite increasing force application. The failure sequence began with audible popping sounds emanating from the CFRP system, followed by the ultimate failure mechanism by debonding of the U-wrap in the central section of the repair (Figure 6-30). Figure 6-31 shows the force-deflection curve where the maximum failure applied load was 121 kips which corresponds to 877.3 kips.ft which represents 75% of the Girder G02 test and 80% of the AASHTO LRFD flexural capacity estimate for Girder G02.

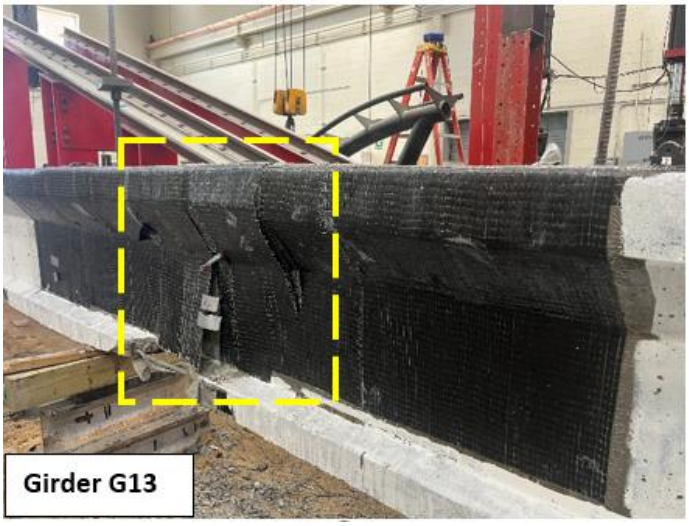

(a)

(b)

Figure 6-30. Photographs of Girder G13 showing (a) Failure of 50% damage repaired girder at midspan (b) A view of concrete damage behind the u-wrap system

Figure 6-32 shows strain measurements from six spliced strands (labeled S1 through S6) and two additional monitoring points (S8 and S12). All strain measurements initially show a relatively linear response as force increases from 0 to approximately 75 kips, with strains ranging from about 0.006 to 0.007 in/in. As loading continues beyond 75 kips, the strain response becomes increasingly nonlinear, with all instrumented elements showing accelerated development with each increment of force. This nonlinearity indicates the onset of inelastic behavior in the structural system. Several gauges exhibit sudden strain drops or jumps near the failure point (around 121 kips), particularly visible in the red trace, suggesting localized failures or stress redistributions occurring in specific strands.

The strain pattern demonstrates that all spliced strands participated in carrying load, though with some variation in their strain responses, particularly as the system approached failure. The relatively consistent strain behavior across multiple measurement points indicates effective load distribution among the spliced strands in the repair system until reaching ultimate capacity.

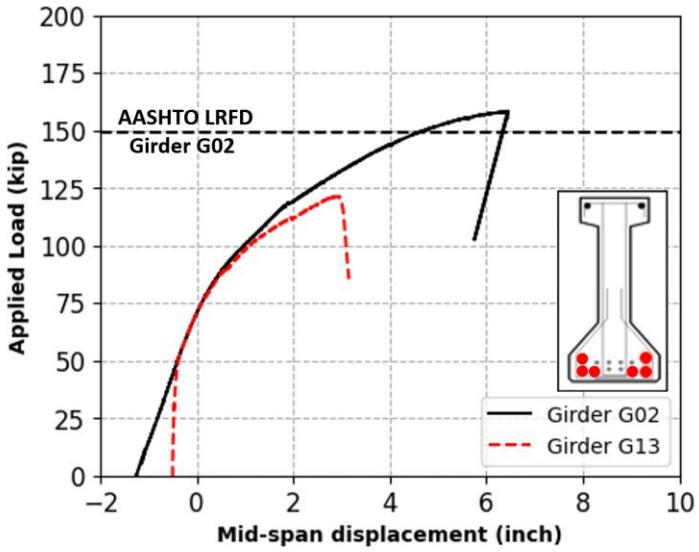

Figure 6-31. Force deflection curve for Girder G13

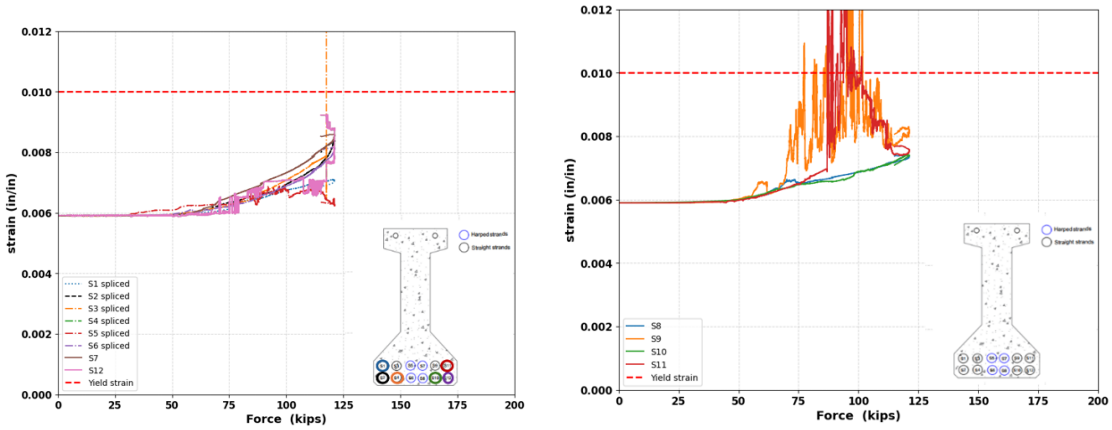

(a) (b)

Figure 6-32. Strain-force relationship of prestressing strands for Girder G13 (a) Straight strands (b) Harped strands

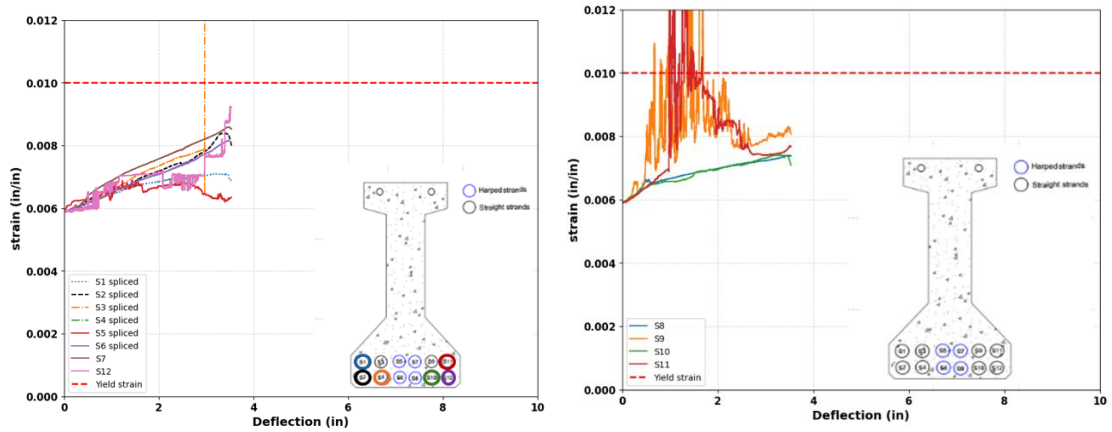

(a) (b)

Figure 6-33. Strain-deflection relationship of prestressing strands for Girder G13 (a) Straight strands (b) Harped strands

Chapter 7. Findings, Conclusions, and Design Recommendations

This study evaluates the performance of prestressed concrete bridge girders subjected to lateral collision forces, with a particular focus on over-height vehicle impacts. The investigation commenced with the development of comprehensive finite element models, which were utilized to design the test specimens. These models were calibrated using data from 13 experimental girders reported in the literature.

The validated models were further employed to conduct two parametric studies, simulating both dynamic and static damage scenarios. These simulations encompassed collisions involving semi-tractor trailers traveling at speeds of up to 90 mph and carrying trailer loads of up to 80 kips. Additionally, the scenarios examined the complex biaxial bending stresses induced by accidental lateral eccentricity.

The study also presents findings from an extensive experimental program, which involved 23 tests conducted on 14 full-scale, 46-foot MoDOT Type II bridge girders. This experimental effort investigated impact dynamics, the residual flexural strength of girders experiencing up to 50% prestressing strand loss, and the efficacy of two repair techniques: mechanical splicing and externally bonded carbon fiber-reinforced polymer (CFRP). These repair methods were assessed for their effectiveness in restoring flexural strength following strand losses ranging from 17% to 33%.

7.1 Key findings and conclusions

- Failure Mode: Shear plug failure was identified as the predominant failure mode in impacted girders, as confirmed through both experimental testing and numerical analysis.
- Realistic Damage Simulation: The damage observed in experimental impact tests closely mirrored real-world bridge girder-vehicle collision scenarios, validating the experimental program's ability to replicate practical damage mechanisms effectively.
- Residual Strength: Girders with 25% to 50% strand loss exhibited significant reductions in load ratings. A linear relationship between the loss of prestressing strands and flexural strength was found as follows:
    - For 25% strand loss, the flexural strength was reduced by 23.5% from the Girder G02 test capacity.
    - For 50% strand loss the flexural strength was reduced by 52.9% from Girder G02 test capacity.
- Non-Destructive Testing (NDT): A practical field technique, the cable deflection method, was developed to estimate prestress losses in strands without requiring specialized equipment or skilled technicians. The method requires exposing the strands up to 20 inches in length, with proper shoring to ensure structural ductility. Flexural

strength estimates derived from this technique were validated against four-point flexural tests, with a conservative error margin of 9.4%.

- Stiffness Degradation: The loss of up to 50% of prestressing strands led to approximately a 60% reduction in stiffness. When both prestressing strand loss and concrete section reduction ranged from 17% to 50%, the initial stiffness degradation varied between 25% and 54%, respectively.
- Mechanical Splicing: The efficiency of mechanical strand splicing varied based on the level of strand loss:
    - 17% strand loss: 95.2% original flexural strength recovery was achieved and was 101.1% of the Girder G02 AASHTO LRFD estimate.
    - 25% strand loss: 84% recovery was observed and was 89.1% of the AASHTO LRFD of Girder G02.
    - 33% strand loss: Splicing was ineffective, as no significant recovery occurred due to premature failure caused by the bulging of spliced strands in the outer layer, despite proper installation. However, by providing confinement of the spliced strands internally using steel rectilinear, 91.6% of recovery was achieved which corresponds to 97.3% of the AASHTO LRFD estimate of Girder G02.
    - 50% strand loss: 78.4% of recovery was achieved by providing external confinement of the concrete by CFRP U-wraps which was equivalent to 83.3% of the AASHTO LRFD estimate of Girder G02.
    - A simplified linear equation was proposed to calculate the residual flexural strength based on the ratio of spliced strands based on literature and the current research results from up to 50% strand loss.
    - The confinement of both internal and external for the spliced strands was found to add approximately 8.5%.
- Externally Bonded CFRP: CFRP repairs were highly effective, fully restoring 100% of the flexural strength for girders with up to 33% strand loss. Additionally, CFRP repairs provided a flexural strength reserve of 16% of the original strength enhancing the overall structural performance.

Table 7-1. Summary of the flexural strength increase/reduction of the tested girders

Girder Number	Girder test	Calculated Flexural strength (kips. ft)			Test/Calculated	Repair test capacity /Girder G02 AASHTO
		AASHTO LRFD	ACI 440-2R.17	Test		
Girder G02	As built 12	1053.0	-	1118.0	106.2%	-
Girder G14	As built 16	1270.0	-	1377.0	108.4%	-
Girder G03	Residual-12-25%	852	-	855.0	100%	-
Girder G04	Residual-12-50%	565.0	-	526.0	93.0%	-
Girder G06	Residual-16-63%	476.0	-	521.0	109.4%	-
Girder G10	Spliced 17%	-	-	1064.7	-	101.1%
Girder G11	Spliced 25%	-	-	939.0	-	89.1%
Girder G05	Spliced 33%	-	-	671.2	-	63.7%
Girder G12	Spliced 33%	-	-	1024.4	-	97.3%
Girder G07	CFRP 17%	-	1191	1375.0	115.4%	130.5%
Girder G08	CFRP 33%	-	1117	1296.0	116.0%	123.0%
Girder G13	Hybrid 50%	-	-	877.2	-	83.3%

7.2 Design recommendations

The primary design recommendations derived from this study are as follows:

- Equivalent Static Force (ESF): The numerical models proposed an ESF of 135 kips (600 kN), which closely aligns with the Eurocode (EN-1991.1.7.2006) ESF of 112 kips (500 kN) for bridge superstructures collisions. Following the EN-1991 (section 4.3.2), the equivalent load should be applied as a concentrated load over an area of 10 inches by 10 inches. The load factor can be taken following AASHTO LRFD Table 3.4.1-1 as 1.0 for Extreme Event II state.

- Accidental Lateral Eccentricity: The flexural strength of girders experiencing asymmetric strand loss due to vehicle impacts can be estimated using AASHTO LRFD guidelines with an additional 15% reduction factor to account for the eccentricity resulting from the asymmetric loss of prestressing strands and concrete.
- Preloading Considerations: Preloading is not necessary when using mechanical splicing for flexural strength recovery. However, it may be needed for EB-CFRP repair in cases where excessive camber is present.
- Mechanical splicing was tensioned up to the effective prestress force, demonstrating the capability to restore up to 25% of ruptured strands with an efficiency rate of 84% without confinement. When internal confinement was applied, splicing repair of 33% strand loss achieved a 91.6% recovery of flexural strength. Therefore, for optimal recovery of flexural strength, the use of internal or external confinement of the spliced strands is strongly recommended. However, in cases where mechanical splicing is applied without appropriate confinement — as indicated in the report — and more than 25% strand loss occurs, it should not be used as the sole repair method. Under such circumstances, alternative repair approaches or girder replacement are recommended to ensure structural integrity and safety.
- Externally Bonded CFRP: In accordance with ACI 440 design guidelines, the application of three plies of externally bonded Carbon Fiber Reinforced Polymer (CFRP) can fully restore 100% of the flexural strength of girders experiencing up to 33% strand loss, with an additional reserve of 16%. The use of distributed CFRP-U wraps as an anchorage system proved effective in delaying debonding and maximizing the strain capacity of the longitudinal plies, even without the use of mechanical anchorage. However, when strand loss exceeds 33%, CFRP should not be used as the sole repair method. In such cases, supplementary repair strategies such as mechanical splicing or girder replacement are recommended to ensure structural performance and safety.

7.3 Future research recommendations

Based on the findings of this study, several areas require further investigation to enhance the understanding of impact damage on prestressed concrete girders and refine repair strategies. Future research should focus on the following aspects:

- Impact intensity: Investigate the effect of higher impact velocities experimentally on the damage of the prestressed concrete girders.
- Confinement for mechanical splicing: Investigate the effects of additional reinforcement confinement on the girder repaired using mechanical strand splicing.
- Preloading effects on repair performance: Assess the influence of preloading before patching concrete repairs, particularly in scenarios where significant camber exists, to determine its impact on long-term performance and crack mitigation.

- Design impact forces: Further refine the equivalent static force (ESF) for bridge superstructures by incorporating additional real-world collision scenarios and field data, ensuring improved accuracy in design impact loads.
- Hybrid repair techniques: Investigate the combined use of mechanical splicing and externally bonded CFRP repairs to optimize the recovery of flexural strength in girders with extensive damage.
- CFRP configurations: Examine the effectiveness of distributed versus continuous CFRP repairs, particularly for cases where fully wrapped repairs may induce premature failure, ensuring optimal strengthening strategies.
- Fatigue performance and long-term durability: Conduct fatigue life studies to evaluate the long-term performance of repaired girders under cyclic loading conditions, addressing concerns related to material degradation and structural resilience.

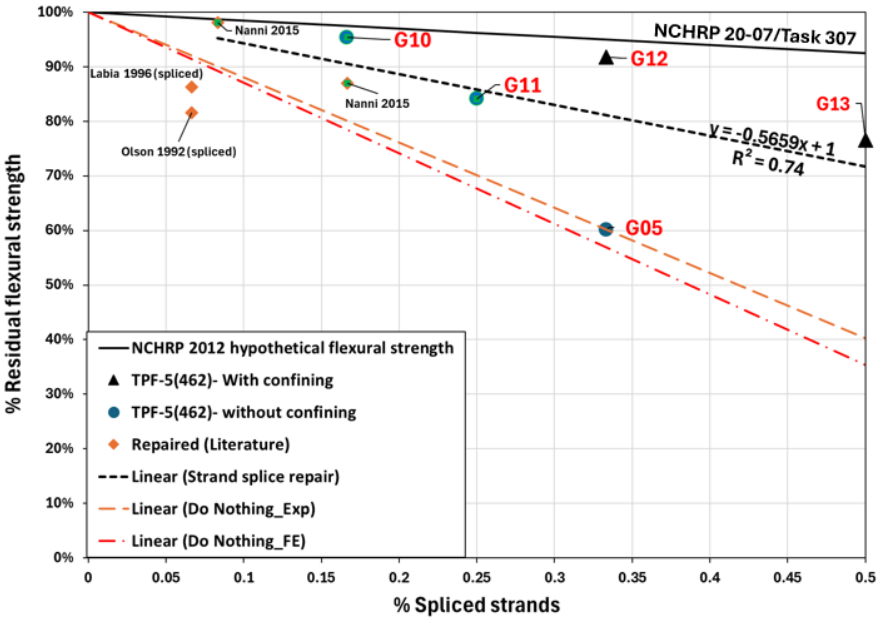

Figure 7-1. Relationship between the loss of strands and the flexural strength

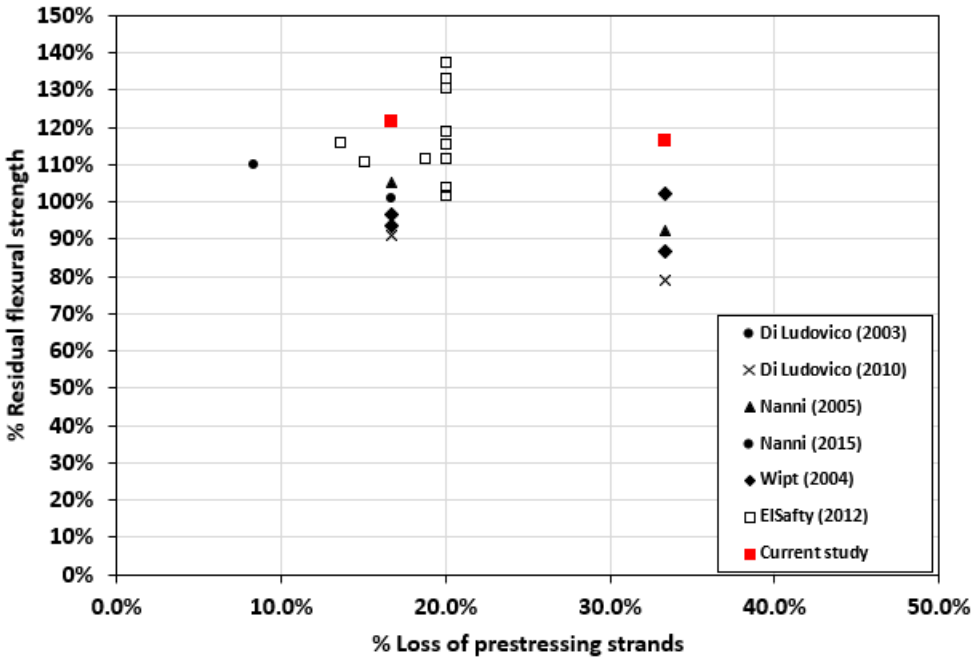

Figure 7-2. Relationship between the loss of strands and the restored flexural strength

Chapter 8. References

Abendroth, Robert E, B O Andrawes, F S Fanous, and others. 2004. “Steel Diaphragms in Prestressed Concrete Girder Bridges.”

Abendroth, Robert E, F Wayne Klaiber, and Mark W Shafer. 1991. “Lateral Load Resistance of Diaphragms in Prestressed Concrete Girder Bridges.”

AASHTO. 2015. “Load and Resistance Factor Design for Highway Bridge Superstructures.” *Reference Manual* 18 (3): 74–82.

Adhikary, Satadru, Bing Li, and Kazunori Fujikake. 2015. “Low Velocity Impact Response of Reinforced Concrete Beams: Experimental and Numerical Investigation.” *International Journal of Protective Structures* 6 (1): 81–111. https://doi.org/10.1260/2041-4196.6.1.81.

Agrawal, A.K. 2011. *Bridge Vehicle Impact Assessment*.

Agredo Chávez, Angélica, Jaime Gonzalez-Libreros, Gabriel Sas, Lennart Elfgren, Silvia Bianchi, Fabio Biondini, and Brian Kukay. 2022. “Available Tests to Evaluate Residual Prestressing Forces in Concrete Bridges.” In , 1123–31. Prague, Czech Republic. https://doi.org/10.2749/prague.2022.1123.

Azizinamini, Atorod. 2020. “Accelerated Bridge Construction.” *Journal of Bridge Engineering* 25 (12): 02020002. https://doi.org/10.1061/(ASCE)BE.1943-5592.0001643.

Azizinamini, Atorod, Bruce J. Keeler, John Rohde, and Armin B. Mehrabi. 1996. “Application of a New Nondestructive Evaluation Technique to a 25-Year-Old Prestressed Concrete Girder.” *PCI Journal* 41 (3): 82–95. https://doi.org/10.15554/pcij.05011996.82.95.

Cao, Ran, Anil Kumar Agrawal, Sherif El-Tawil, and Waider Wong. 2021. “Overheight Impact on Bridges: A Computational Case Study of the Skagit River Bridge Collapse.” *Engineering Structures* 237 (June 2020): 112215. https://doi.org/10.1016/j.engstruct.2021.112215.

Chehab, Alaa I., Christopher D. Eamon, Gustavo J. Parra-Montesinos, and Thai X. Dam. 2018. “Shear Testing and Modeling of AASHTO Type II Prestressed Concrete Bridge Girders.” *ACI Structural Journal* 115 (3): 801–12. https://doi.org/10.14359/51701917.

Civjan, Scott A., James O. Jirsa, Ramon L. Carrasquillo, and David W. Fowler. 1998. “Instrument to Evaluate Remaining Prestress in Damaged Prestressed Concrete Bridge Girders.” *PCI Journal* 43 (2): 62–71. https://doi.org/10.15554/pcij.03011998.62.71.

Cook, Wesley, Paul J. Barr, and Marvin W. Halling. 2015. “Bridge Failure Rate.” *Journal of Performance of Constructed Facilities* 29 (3): 04014080. https://doi.org/10.1061/(ASCE)CF.1943-5509.0000571.

Czaderski, Christoph, and Engineer Fh. n.d. “Determining the Remaining Tendon Force of a Large- Scale, 38-Year-Old Prestressed Concrete Bridge Girder.”

Deng, Linzhong, Michel Ghosn, Ales Znidaric, and Joan R. Casas. 2001. “Nonlinear Flexural Behavior of Prestressed Concrete Girder Bridges.” *Journal of Bridge Engineering* 6 (4): 276–84. https://doi.org/10.1061/(ASCE)1084-0702(2001)6:4(276).

Dunne, Richard, and Eric, Thorkildsen. 2020. “Case Study: Response to Bridge Impacts – An Overview of State Practices.” Dunne, R., & Thorkildsen, E. (2020). Case Study: Response to Bridge Impacts–An Overview of State Practices (No. FHWA-HIF-20-087).

Fu, Yingqian, Xinlu Yu, Xinlong Dong, Fenghua Zhou, Jianguo Ning, Ping Li, and Yuxuan Zheng. 2020. “Investigating the Failure Behaviors of RC Beams without Stirrups under Impact Loading.” *International Journal of Impact Engineering* 137:103432. https://doi.org/10.1016/j.ijimpeng.2019.103432.

Fujikake, Kazunori, Bing Li, and Sam Soeun. 2009. “Impact Response of Reinforced Concrete Beam and Its Analytical Evaluation.” *Journal of Structural Engineering* 135 (8): 938–50. https://doi.org/10.1061/(asce)st.1943-541x.0000039.

Garber, David B., José M. Gallardo, Dean J. Deschenes, and Oguzhan Bayrak. 2015. “Experimental Investigation of Prestress Losses in Full-Scale Bridge Girders.” *ACI Structural Journal* 112 (5): 553–64. https://doi.org/10.14359/51687909.

Griffin, Alex. 2014. “Shear Behavior of High Strength Self-Consolidating Concrete in Nu Bridge Girders,” 190 pp.

Hao, Hong, Tung T. Tran, Huawei Li, Thong M. Pham, and Wensu Chen. 2021. “On the Accuracy, Reliability and Controllability of Impact Tests of RC Beams.” *International Journal of Impact Engineering* 157 (July): 103979. https://doi.org/10.1016/j.ijimpeng.2021.103979.

Harries, Kent A., Jarret Kasan, Richard Miller, and Ryan Brinkman. 2012. “Updated Research for Collision Damage and Repair of Prestressed Concrete Beams.” *NCHRP Project 20-07, Task 307, Final Rep*, no. May.

Helal, J, M Sofi, and P Mendis. 2015. “Non-Destructive Testing of Concrete : A Review of Methods,” no. September 2017.

Higgs, Arek, Paul J. Barr, and Marvin W. Halling. 2015. “Comparison of Measured and AASHTO LRFD-Predicted Residual Prestress Forces, Shear and Flexural Capacities of High-Strength Prestressed-Concrete Bridge Girders.” *Journal of Bridge Engineering* 20 (1): 1–9. https://doi.org/10.1061/(asce)be.1943-5592.0000646.

Jia, Junfeng, Longguan Zhang, Jinping Ou, and Xize Chen. 2023. “Nondestructive Testing and Health Monitoring Techniques for Structural Effective Prestress.” Edited by Ka-Veng

Yuen. *Structural Control and Health Monitoring* 2023 (September):1–30. https://doi.org/10.1155/2023/8940008.

Jing, Yuan, Zhongguo John Ma, and David B. Clarke. 2016. “Full-Scale Lateral Impact Testing of Prestressed Concrete Girder.” *Structural Concrete* 17 (6): 947–58. https://doi.org/10.1002/suco.201500224.

Kishi, N., H. Konno, K. Ikeda, and K. G. Matsuoka. 2002. “Prototype Impact Tests on Ultimate Impact Resistance of PC Rock-Sheds.” *International Journal of Impact Engineering* 27 (9): 969–85. https://doi.org/10.1016/S0734-743X(02)00019-2.

Kishi, N., H. Mikami, K. G. Matsuoka, and T. Ando. 2002. “Impact Behavior of Shear-Failure-Type RC Beams without Shear Rebar.” *International Journal of Impact Engineering* 27 (9): 955–68. https://doi.org/10.1016/S0734-743X(01)00149-X.

Kishi, N., T. Ohno, H. Konno, and A. Q. Bhatti. 2006. “Dynamic Response Analysis for a Large-Scale RC Girder under a Falling-Weight Impact Loading.” *Solid Mechanics and Its Applications* 140:99–109. https://doi.org/10.1007/1-4020-4891-2_8.

Kishi, Norimitsu. 2019. “Numerical Simulation of Reinforced Concrete Structures under Impact Loading.” *Materialwissenschaft Und Werkstofftechnik* 50 (5): 599–610. https://doi.org/10.1002/mawe.201800181.

Labia, Yolanda, and Bruce Douglas. 1997. “Full-Scale Testing And Analysis of 20-Year Old Pretensioned Cocnrete Boc Girders.”

Li, Huawei, Wensu Chen, and Hong Hao. 2019. “Dynamic Response of Precast Concrete Beam with Wet Connection Subjected to Impact Loads.” *Engineering Structures* 191 (April): 247–63. https://doi.org/10.1016/j.engstruct.2019.04.051.

Ludovico. 2005. “Repair of Bridge Girders with Composites: Experimental and Analytical Validation.” *ACI Structural Journal* 102 (5). https://doi.org/10.14359/14659.

Nanni, Gangi and. 2018. “Evaluation of Repair Techniques for Impact-Damaged Prestressed Beams.”

Olsen, Steven A. 1992. “Reusability and Impact Damage Repair of Twenty-Year-Old AASHTO Type III Girders.”

Oppong, Kofi, Dikshant Saini, and Behrouz Shafei. 2021a. “Characterization of Impact-Induced Forces and Damage to Bridge Superstructures Due to over-Height Collision.” *Engineering Structures* 236 (June):112014. https://doi.org/10.1016/j.engstruct.2021.112014.

Oppong, 2021b. “Ultrahigh-Performance Concrete for Improving Impact Resistance of Bridge Superstructures to Overheight Collision.” *Journal of Bridge Engineering* 26 (9): 04021060. https://doi.org/10.1061/(asce)be.1943-5592.0001736.

Pham, Thong M., and Hong Hao. 2017. “Effect of the Plastic Hinge and Boundary Conditions on the Impact Behavior of Reinforced Concrete Beams.” *International Journal of Impact Engineering* 102:74–85. https://doi.org/10.1016/j.ijimpeng.2016.12.005.

Pham, Thong M., and Hong Hao. "Influence of global stiffness and equivalent model on prediction of impact response of RC beams." International Journal of Impact Engineering 113 (2018): 88-97.Pham, Thong M., Yifei Hao, and Hong Hao. 2018. “Sensitivity of Impact Behaviour of RC Beams to Contact Stiffness.” International Journal of Impact Engineering 112:155–64. https://doi.org/10.1016/j.ijimpeng.2017.09.015.

Radlinska, A., J. MacCarthy, L. Matzke, and F. Nagel. 2012. “Coatings and Treatments for Beam Ends.” *Pennsylvania Department of Transportation: Villanova, PA, USA*.

Saatci, Selcuk, and Frank J. Vecchio. 2009. “Effects of Shear Mechanisms on Impact Behavior of Reinforced Concrete Beams.” *ACI Structural Journal* 106 (1): 78–86. https://doi.org/10.14359/56286.

Schwer, L E, and Y D Murray. 2002. “Continuous Surface Cap Model for Geomaterial Modeling: A New LS-DYNA Material Type.” *7th International LSDYNA Users Conference*, no. 2, 35–50.

Shahawy, Mohsen A., and Barrington deV Batchelor. 1996. “Shear Behavior of Full-Scale Prestressed Concrete Girders: Comparison Between AASHTO Specifications and LRFD Code.” *PCI Journal* 41 (3): 48–62. https://doi.org/10.15554/pcij.05011996.48.62.

Shanafelt, G. O., and W. B. Horn. 1980. *Damage Evaluation and Repair Methods for Prestressed Concrete Bridge Members*. National Cooperative Highway Research Program 226. Washington, D.C.

Shanafelt, George O., and Willis B. Horn. "Guidelines for evaluation and repair of prestressed concrete bridge members." NCHRP report 280 (1985)Tabatabai, Habib, and Azam Nabizadeh. 2019. “Strength and Serviceability of Damaged Prestressed Girders,” no. 0092.

Wei, Jie, Jun Li, Chengqing Wu, Zhong xian Liu, and Jie Li. 2021. “Hybrid Fibre Reinforced Ultra-High Performance Concrete Beams under Static and Impact Loads.” *Engineering Structures* 245 (February): 112921. https://doi.org/10.1016/j.engstruct.2021.112921.

Wight, J.K., and J.G. MacGregor. 2012. *Reinforced Concrete: Mechanics and Design.*

Wilden, Helmuth, ed. 2010. *PCI Design Handbook: Precast and Prestressed Concrete*. 7th ed. Chicago: Precast/Prestressed Concrete Institute.

Wu, Youcai, and John E. Crawford. 2015. "Numerical Modeling of Concrete Using a Partially Associative Plasticity Model." *Journal of Engineering Mechanics* 141 (12): 04015051. https://doi.org/10.1061/(asce)em.1943-7889.0000952.

Wu, Youcai, John E Crawford, and Joseph M Magallanes. n.d. "Performance of LS-DYNA® Concrete Constitutive Models."

Xu, L. J., X. Z. Lu, S. T. Smith, and S. T. He. 2012. "Scaled Model Test for Collision between Over-Height Truck and Bridge Superstructure." *International Journal of Impact Engineering* 49:31–42. https://doi.org/10.1016/j.ijimpeng.2012.05.003.

Yoo, Doo-Yeol, Nemkumar Banthia, and Young-Soo Yoon. 2017. "Impact Resistance of Reinforced Ultra-High-Performance Concrete Beams with Different Steel Fibers." *ACI Structural Journal* 114 (1). https://doi.org/10.14359/51689430.

Zhan, Tingbian, Zhihua Wang, and Jianguo Ning. 2015. "Failure Behaviors of Reinforced Concrete Beams Subjected to High Impact Loading." *Engineering Failure Analysis* 56 (February): 233–43. https://doi.org/10.1016/j.engfailanal.2015.02.006.

Zhao, De Bo, Wei Jian Yi, and Sashi K. Kunnath. 2018. "Numerical Simulation and Shear Resistance of Reinforced Concrete Beams under Impact." *Engineering Structures* 166 (March): 387–401. https://doi.org/10.1016/j.engstruct.2018.03.072.

Zhao, Wuchao, Jiang Qian, and Pengzhao Jia. 2019. "Peak Response Prediction for RC Beams under Impact Loading." *Shock and Vibration* 2019. https://doi.org/10.1155/2019/6813693.

Zobel, Robert Steven. *Evaluation and repair of impact damaged pre-stressed concrete bridge girders*. The University of Texas at Austin, 1996.

Appendix A- Numerical Parametric Studies

A.1 Dynamic response of girder under impact loads

Over-height truck impacts in the United States frequently involve tractor-semi-trailers. This study utilized a validated finite element (FE) model of a tractor semi-trailer, developed based on Texas Transportation Institute Test 7069-13 (Figure A-1). The model simulated a 1992 Freightliner FLD120 with an integral sleeper cabin. Additionally, the validated model of a prestressed concrete girder, previously developed and discussed, was integrated with the tractor semi-trailer model.

The integrated model was employed to analyze nine crash scenarios, which included both full bridge structures (Figure A-2a) and isolated girders with three different cross-section types (Figure A-2b, c, d). Table A-1 shows the properties of each selected girder. Table A-2 shows the investigated parameters, such as truck speed, mass, and girder span, which were determined through a combination of machine learning analysis and an extensive literature review conducted during the early stages of the project.

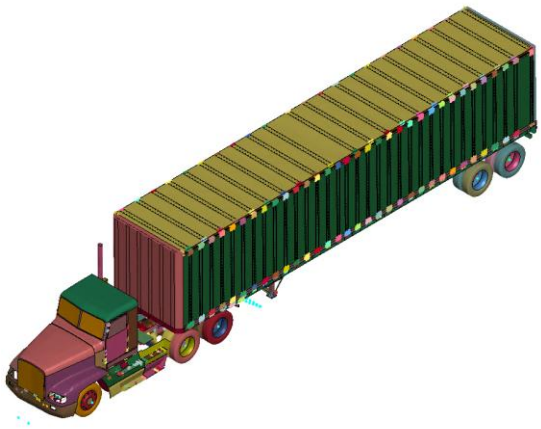

Figure A-3. Full finite element model for Texas Transportation Institute Test 7069-13

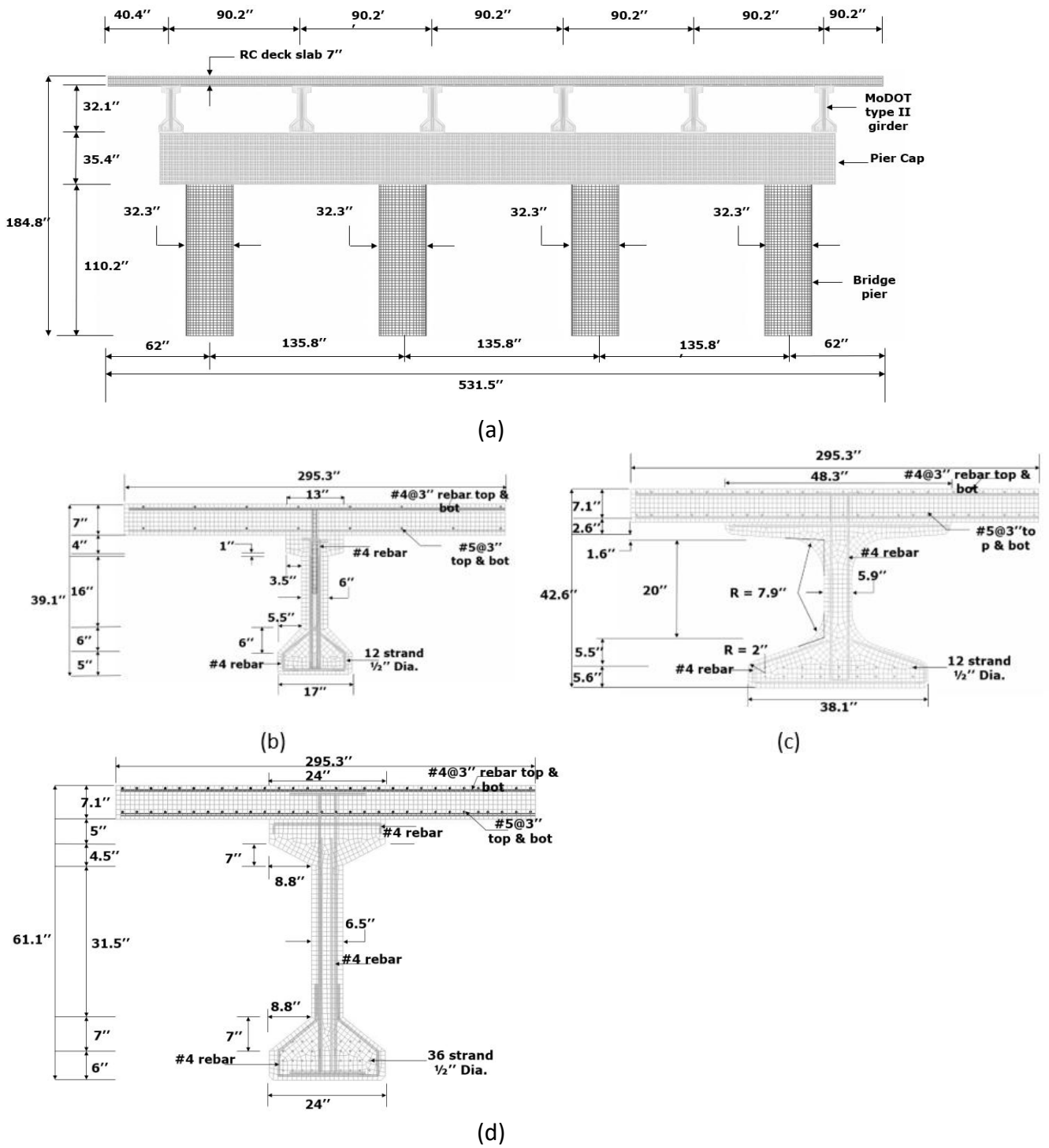

Figure A-4. FE models, (a) Full bridge of MoDOT type 2, isolated girders with composite deck slab, (b) MoDOT type 2, (c) MoDOT type 6, (d) MoDOT type NU 35 girder

Table A-2. Girder description and geometric summary

Description	MoDOT I-type 2	MoDOT I- type 6	MoDOT NU 35
Girder concrete strength (ksi)	7.00	7.00	7.00
Deck concrete strength (ksi)	5.00	5.00	5.00
Number of 0.5” strands	12	36	12
Deck depth (inch)	7.00	7.00	7.00
Deck effective width (inch)	30	30	30
Strand type	Low relaxation 270 ksi	Low relaxation 270 ksi	Low relaxation 270 ksi
Mild steel tensile strength (ksi)	60	60	60

Table A-3. FE study parameters

Model number	Truck speed (Mph)	Truck mass (kips)	Span (feet)	Bridge deck condition	Effect studied
01-M2-L50-S50-M55	50	55	50	Isolated girder	Reduced model
02-M2-L50-F50-M55	50	55	50	Full bridge	Reduced model
03-M2-L50-S30-M55	30	55	50	Isolated girder	Truck speed
04-M2-L50-S70-M55	70	55	50	Isolated girder	Truck speed
05-M2-L50-S90-M55	90	55	50	Isolated girder	Truck speed
06-M6-L50-S50-M55	50	55	50	Isolated girder	Girder span & cross-section
07-M6-L90-S50-M55	50	55	90	Isolated girder	Girder span & cross-section
08-NU35-L50-S50-M55	50	55	50	Isolated girder	Girder span & cross-section
09-M2-L50-S50-M80	50	80	50	Isolated girder	Truck mass

A.1.1 Comparison between isolated girders and full bridge

The study compares the impact response of three scenarios, a full bridge, an isolated girder with a composite deck, and an isolated girder without a composite deck, all subjected to a truck traveling at 50 Mph with a mass of 55 kips. The boundary conditions varied to restrain the girder’s top flange in translation, rotation, or both as shown in Figure A-3. Reducing the modeling of a full bridge to an isolated girder can significantly reduce the computation time which allows for performing more analyses.

Figure A-4 displays the impact force time history for both the full bridge (02-M2-L50-F50-M55) and the isolated girder (01-M2-L15.24-S80-M24.9). Multiple peaks of impact force were observed in the full bridge's impact time history, in contrast to the isolated girder. This phenomenon can be attributed to the sequential folding of the trailer roof against the girder in the case of the full bridge. This was a result of the relatively high lateral stiffness of the full bridge, which prevented the composite deck from undergoing out-of-plane rotation. The

impact time history for both cases primarily represented the impact of the tractor-semitrailer with the front girder only without any interaction with the interior girders. The full bridge peak impact force of 227 kips had an increase of 11.5% against the isolated girder of 201 kips. Also, the collision duration was four times longer than the isolated girder. This difference was attributed to the stress wave propagation through a medium as shown in (Figure A-6a).

Figure A-3 depicts three scenarios involving a full bridge (Figure A-3a), an isolated girder with a composite deck (Figure A-3b), and an isolated girder without a composite deck (Figure A-3c) under impact load. These scenarios were subjected to the same truck speed of 50 Mph and a truck mass of 55 kips, assuming three different restraint conditions of the top flange of the PC girder. The imposed restrained conditions either restrained the top flange of the girder in translation and rotation, only translation, or only rotation. Figure A-5 presents a comparison of the lateral deflection of the top flange of the impacted girder at the extreme fiber illustrated for each case. The scenario of the isolated girder with a composite deck, with all translation and rotation degrees of freedom restrained, exhibits similarity to the impact on a girder in a full bridge in terms of lateral displacement at the interface between the girder and deck.

Figure A-6 exhibits the stress contours for both the simulation of the full bridge (Figure A-2a) and the girder with composite deck slab (Figure A-2b). The longitudinal stress waves had to travel a longer distance from the impact region through the concrete medium before hitting the boundary and reflecting its source, thus prolonging the collision time as shown in (Figure A-4). The damage is more substantial for the isolated girder (01-M2-L50-S50-M55) than the full bridge due to the increase of deck lateral stiffness and the absence of the remaining bridge girders' contribution (Figure A-6b). However, overall girder response and failure modes for both cases were relatively similar. Thus, a reduced model of an isolated girder with a composite deck was chosen for the remaining analyses to save the computation cost.

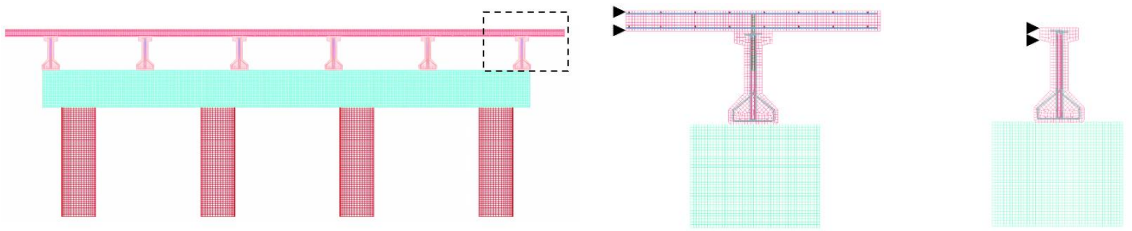

(a) (b) (c)

Figure A-5. FE 3D view (a) Full bridge (02-M2-L50-F50-M55), (b) Isolated girder with composite deck (01-M2-L50-S50-M55), (c) Isolated girder without composite deck

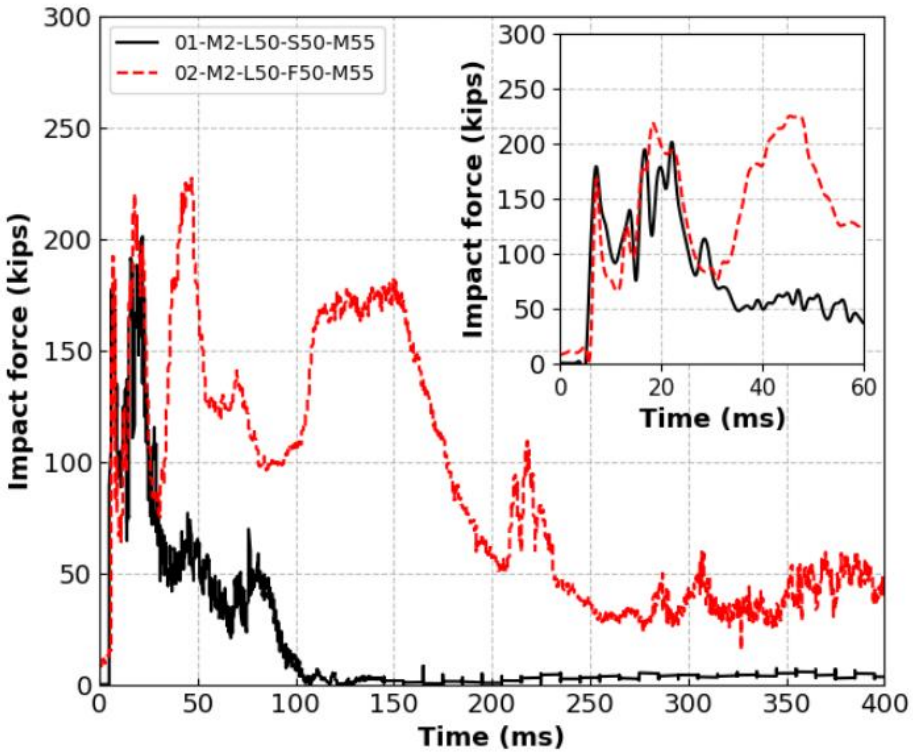

Figure A-6. Comparison of the impact time history between the full bridge and composite girder

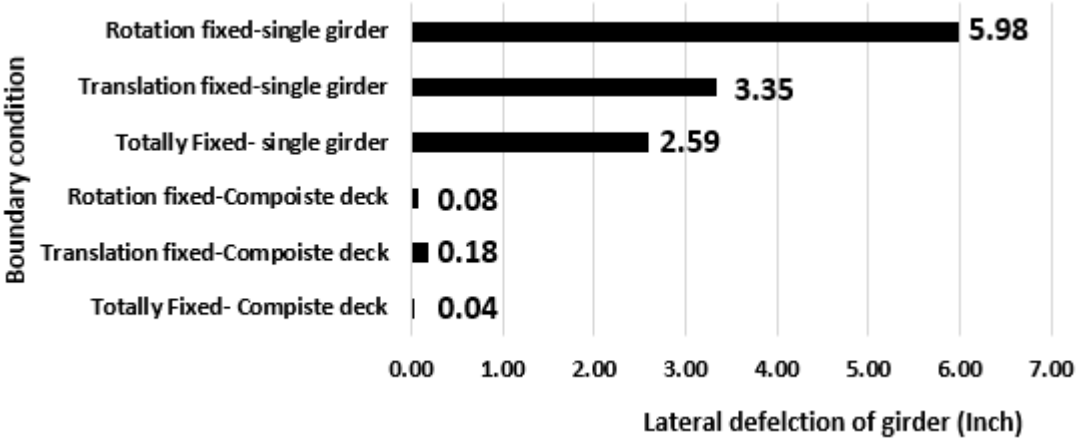

Figure A-7. Lateral deflection in mm of the top flange of the girder

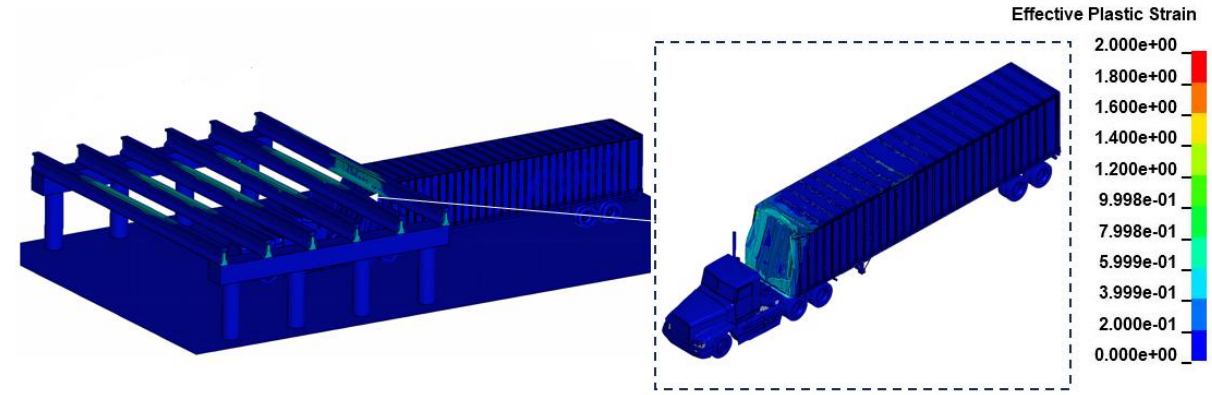

(a)

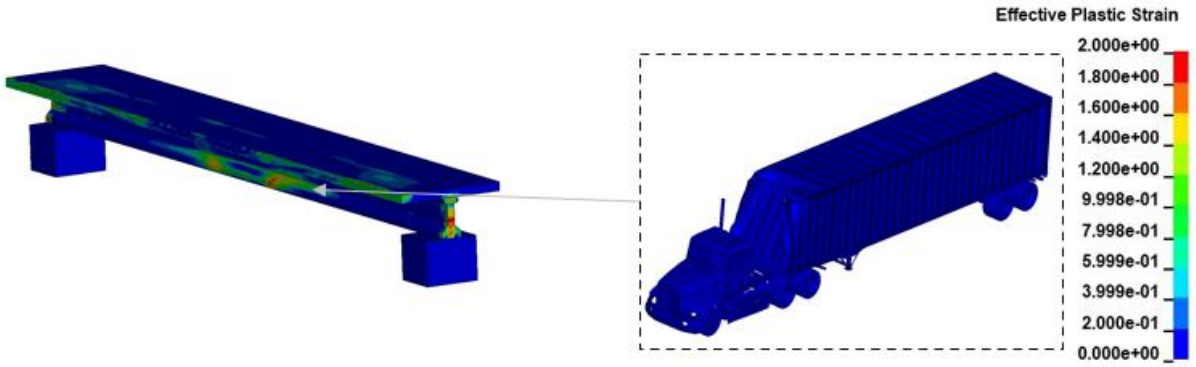

(b)

Figure A-8. Stress contours (a) Full bridge (02-M2-L50-F50-M55), (b) Isolated girder (01-M2-L50-S50-M55)

A.1.2 Peak impact forces

The dynamic peak impact forces for all isolated girders and full bridge models ranged from 170-341 kips (Table A-3). A 25-millisecond moving average filter was applied to all impact time histories to extract the equivalent static force. The moving average filter functions by attenuating high-frequency fluctuations in the impact force data over a sliding time window of 25 milliseconds. This process mitigates transient oscillations and isolates the sustained force component, providing a more representative measure of the load experienced by the structure.

A.1.3 Equivalent static forces

Figure A-7 illustrates the impact time histories for model 01-M2-L50-S50-M55, comparing the original impact force data with the filtered results using the 25-millisecond moving average. The application of this filter reduced the peak impact force from 201 to 128 kips, representing a 36% reduction.

The moving average was applied across all scenarios to quantify the equivalent static force (ESF), which represents the quasi-static load that produces the same structural effects as the transient dynamic impact. This approach is critical because dynamic forces, characterized by brief but intense peaks, can be disproportionately higher than the forces sustained over longer durations. The equivalent static force thus provides a scientifically robust basis for assessing the structural response to impact conditions.

Figure A-8 illustrates the distribution of the equivalent static force (ESF) values derived from the simulated models. The mean ESF was found to be 128 kips, with a standard deviation of 25 kips. Notably, the normal distribution of the ESF values reveals that the Eurocode-specified collision force of 112 kips for bridge superstructures falls within the range defined by two standard deviations of the mean. Furthermore, the mean ESF exceeds the Eurocode limit by 18.6%. In the absence of a collision force estimate for bridge girders in the AASHTO LRFD specifications, this study highlights the credibility and applicability of the Eurocode collision force provision for bridge superstructures.

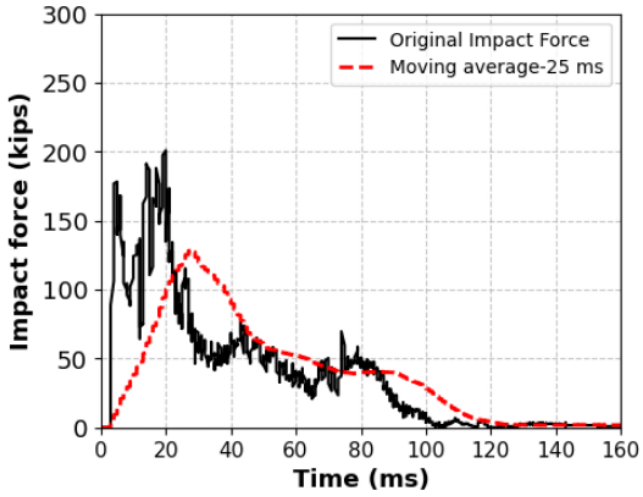

Figure A-9. Original impact force of model 01 (01-M2-L15.24-S80-M24.90) and its moving average filter 25 ms

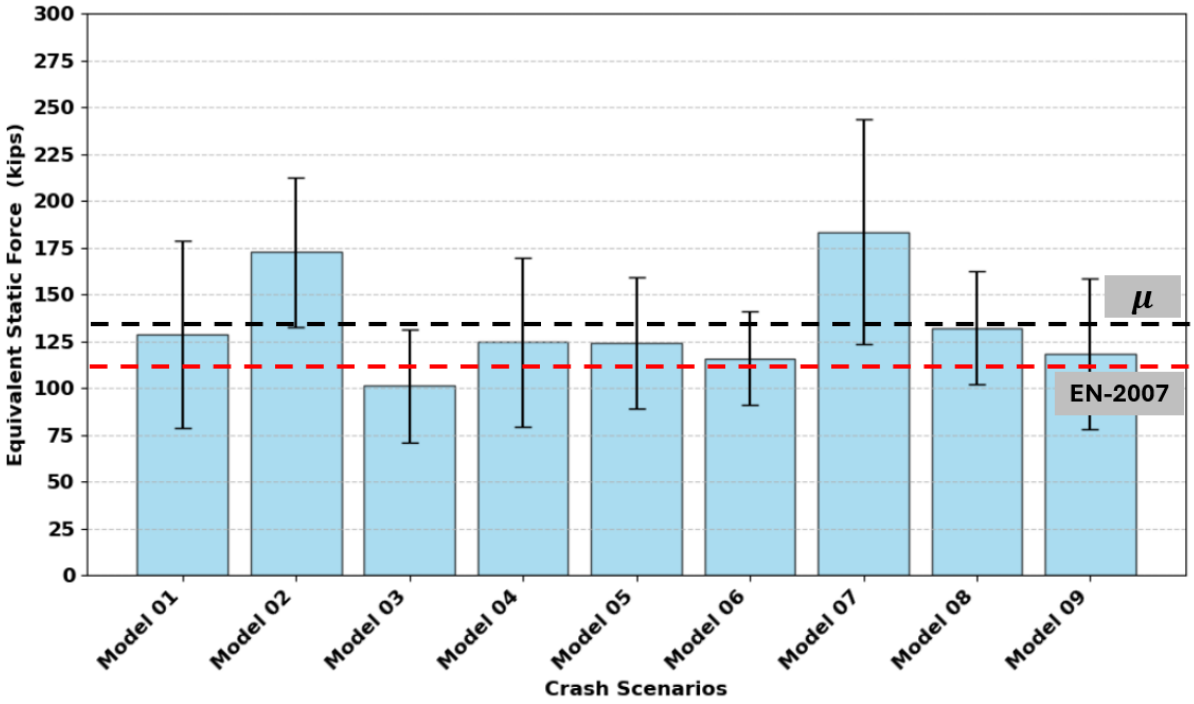

Figure A-10. Equivalent static forces

Table A-4. Summary of the dynamic and equivalent static forces

01-M2-L50-S50-M55	201	129
02-M2-L50-F50-M55	227	173
03-M2-L50-S30-M55	173	102
04-M2-L50-S70-M55	283	125
05-M2-L50-S90-M55	341	125
06-M6-L50-S50-M55	170	116
07-M6-L90-S50-M55	268	183
08-NU35-L50-S50-M55	215	132
09-M2-L50-S50-M80	225	118

A.2 Biaxial bending effect on residual flexural strength

A.2.1 Introduction

These over-height vehicle collisions often cause severe damage, including accidental asymmetric loss of prestressing strands and sections of concrete (Figure A-9), leading to biaxial bending moments. Such effects compromise the girders' flexural resistance, a vital factor for structural safety and bridge serviceability.

Current design standards, such as AASHTO LRFD, do not adequately address the complexities of biaxial bending caused by lateral eccentricities resulting from asymmetric strand loss on girders. This shortage leaves a significant knowledge gap, as the residual flexural capacity can be overestimated, potentially risking reliable assessment of the girder residual capacity following such collisions.

(a) (b)

Figure A-11. Photographs of over-height vehicle collisions with bridge prestressed girders (a) Galloway road over I-84 (Courtesy of IDAHO DOT), and (b) Bridge over US 50 East (Courtesy of Missouri DOT)

A.2.2 Main objective

The primary objective of this study is to evaluate the residual flexural strength of bridge girders subjected to asymmetric losses prestressing strands and concrete sections. By addressing the limitations in existing design standards such as AASHTO LRFD and PCI, the study aims to propose a reduction factor that accounts for the accidental biaxial bending effects, providing engineers with a practical tool for better structural assessments post-collision.

For this parametric study, a prototype bridge was selected and described. The selected bridge girder served as the basis for conducting a comprehensive analysis, enabling a deeper understanding of the influence of varying damage scenarios on the girder's performance.

A.2.3 Prototype bridge

The bulb-tee girder is one of the most commonly used girder types in bridges across the United States and was therefore selected for this study. Using designs from the PCI Bridge Design Manual, a single-span 120-foot-long bulb-tee (BT-72) with a composite deck was selected as the prototype (Figure A-10 and Table A-4). More details about the bridge design can be found in the PCI Bridge Design Manual (Wilden 2010).

Table A-5. Characteristics of the prototype bridge and girder (PC, 2014)

Description	**AASHTO-PCI Bulb-Tee (BT-72)**
Bridge	Single span with cast-in-place concrete deck
Overall length (ft)	121
Design span (ft)	120
Deck effective flange (ft)	9
Deck depth (Inch)	8
Number of strands	48
Prestressing strand type	270 ksi Low relaxation ½” diameter
Girder compressive strength (ksi)	6.5
Deck compressive strength (ksi)	5
Strand effective stress after losses (ksi)	177
Nominal flexural strength (kips.ft)	6182

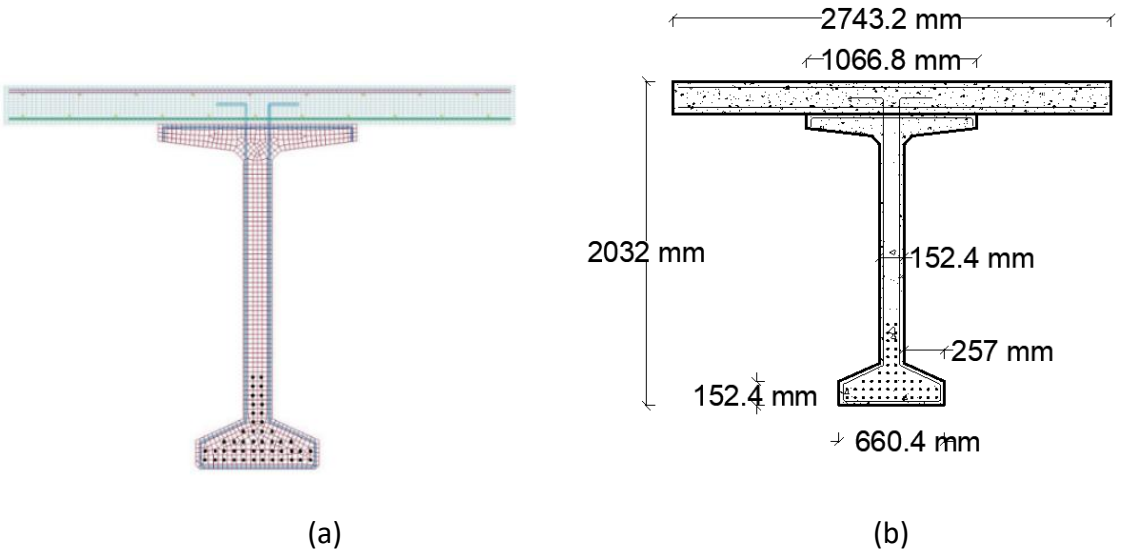

Figure A-12. Bulb tee (BT -72) bridge girder (a) Dimensions , and (b) FE model

A.2.4 Girder models and loading

Seventeen models categorized in two distinct sets of models were developed for this investigation.

- Asymmetric Damage Models: These models represent realistic damage scenarios, such as those caused by truck collisions with girders, and are intended to capture the practical implications of accidental impacts.
- Symmetric Damage Models: Although symmetric damage scenarios are not typical in real-world events, they are crucial for isolating and analyzing the distinct effects of asymmetry versus the effects of damage itself. These models serve as a controlled baseline, enabling a more comprehensive understanding of the structural response under varying conditions.

The inclusion of both sets of models is integral to achieving the study's research objectives. For instance, a girder with a 12.5% strand loss would experience a reduction in strength due to the strand loss itself, as well as an additional reduction attributed to the asymmetry of the damage. The symmetric model is designed to isolate and capture the reduction in strength caused solely by the strand loss, while the asymmetric model quantifies the additional impact due to the asymmetry of the damage. This approach ensures a thorough analysis of the structural behavior under different damage scenarios.

In particular, the models are categorized into five groups to represent various hypothetical damage scenarios (Table A-5). These groups are described as follows:

- Group 1: A reference model with no damage, serving as the control case.
- Group 2: Models with symmetric loss of prestressing strands.

- Group 3: Similar to Group 2 but with asymmetric strand removal while the concrete section remained undamaged. This configuration allowed the uncoupling of the effects of prestressing force loss from concrete damage.
- Group 4: Similar to Group 2, but with symmetric concrete damage in addition to strand loss.
- Group 5: Similar to Group 3, but with asymmetric concrete damage included.

Each group, except Group 1, includes four models representing varying damage levels ranging from Severe II (12.5% strand loss) to Severe IV (50% strand loss) as defined by Harries et al. (2012). Each model was designated as Sym (symmetric) or Asym (asymmetric) based on the strand loss pattern, followed by the letter S to denote strands and the percentage of strand loss. This was further followed by the letter C to denote concrete and the corresponding percentage of concrete damage. For example, a model with 12.5% asymmetric strand loss and 0% concrete damage is designated as Asym-S12.5%-C0%.

An interior girder was selected to eliminate torsional effects caused by the deck slab overhang and barrier weights. This ensured a fair comparison between symmetric and asymmetric strand loss scenarios and focused the analysis on prestressing losses' impact on girder behavior.

Strand removal was performed selectively according to the prescribed damage level. Only the strands within the damaged mid-span region, spanning 5.97 ft (representing 5% of the total span length), were removed, while strands outside this zone were left continuous to simulate bonded strands extending beyond the collision zone realistically (Figure A-11d). Figures A-12-A15 illustrate the removed strands and cross-section regions in all the simulated cases.

Figure A-11 illustrates the methodology for idealizing the damage. Simulating the extent of concrete damage in specimens presents significant challenges due to the random and variable nature of impact-induced damage. Nevertheless, observations from multiple real-world accidents reveal that damage predominantly concentrates on the bottom flange and, to a lesser extent, on the web. To replicate these patterns, an idealized damage model was developed, removing portions of the bottom flange and/or web along the central 5.97 ft to simulate concrete spalling (Figure A-11d).

It is important to note that this idealization does not aim to replicate a specific damage scenario. Instead, its purpose is to understand the influence of such damage on girder performance, enabling the development of general conclusions about the effects of impact damage rather than modeling a specific real-world case. Once finalized, each model was subjected to a four-point bending load. The load was applied in a monolithic manner until the model could no longer sustain additional loading. The total applied load (P) and the corresponding mid-span deflection were recorded and are discussed in the following sections.

Table A-6. Summary of the FE models

Group #	Model designation	Condition	Severity	% loss	Removed	% Concrete section loss
1	Control	--	--	--	--	--
2	Sym-S12.5%-C0%	Symmetric	II	12.5	6	0.0
2	Sym-S20.8%-C0%	Symmetric	III	20.8	10	0.0
2	Sym-S33%-C0%	Symmetric	III	33.0	16	0.0
2	Sym-S50%-C0%	Symmetric	IV	50.0	24	0.0
3	Asym-S12.5%-C0%	Asymmetric	II	12.5	6	0.0
3	Asym-S20.8%-C0%	Asymmetric	III	20.8	10	0.0
3	Asym-S33%-C0%	Asymmetric	III	33.0	16	0.0
3	Asym-S50%-C0%	Asymmetric	IV	50.0	24	0.0
4	Sym-S12.5%-C12.5%	Symmetric	II	12.5	6	12.5
4	Sym-S20.8%-C22%	Symmetric	III	20.8	10	22.0
4	Sym -S33%-C28%	Symmetric	IV	33.0	16	28.0
4	Sym -S50%-C56%	Symmetric	IV	50.0	24	56.0
5	Asym -S12.5%-C12.5%	Asymmetric	II	12.5	6	12.5
5	Asym -S20.8%-C22%	Asymmetric	III	20.8	10	22.0
5	Asym -S33%-C28%	Asymmetric	IV	33.0	16	28.0
5	Asym -S50%-C56%	Asymmetric	IV	50.0	24	56.0

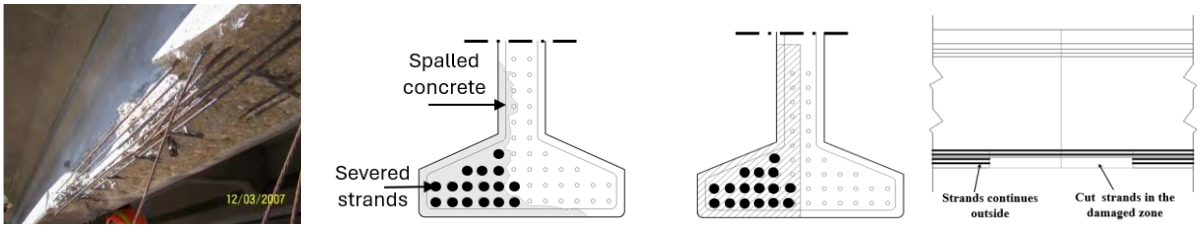

(a) (b) (c) (d)

Figure A-13. Idealization process of the real-life girders damaged by over-height collision. (a) Photograph from bridge girder damage (Harries et al. 2012), (b) Non-uniform loss of concrete cross-section, (c), Idealization of the strands and concrete cross-section shape, (d) Removal of the strand

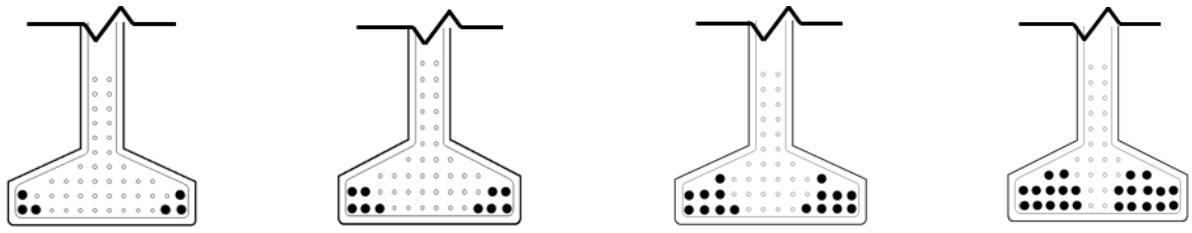

(a) (b) (c) (d)

Figure A-14. Symmetric loss of strands configuration (a) S12.5%-C0%, (b) S20.80%-C0%, (c) S33% -C0%, and (d) S50%-C0%

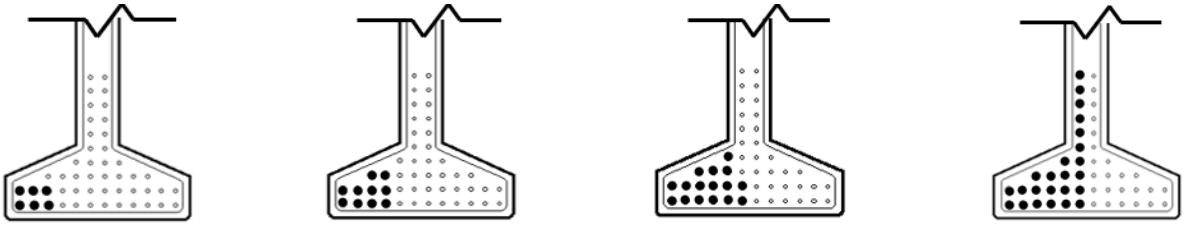

(a) (b) (c) (d)

Figure A-15. Asymmetric loss of strands configuration (a) S12.5%-C0%, (b) S20.80%-C 0%, (c) S33%-C0%, and (d) S50%-C0%

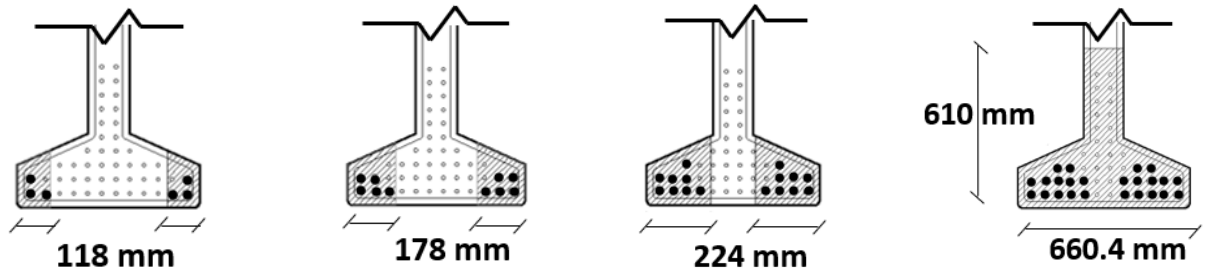

(a) (b) (c) (d)

Figure A-16. Symmetric loss of strands with concrete loss configurations (a) S12.5%-C12.5%, (b) S20.8%-C22%,(c) S33%-C28%, and (d) S50%-C56%

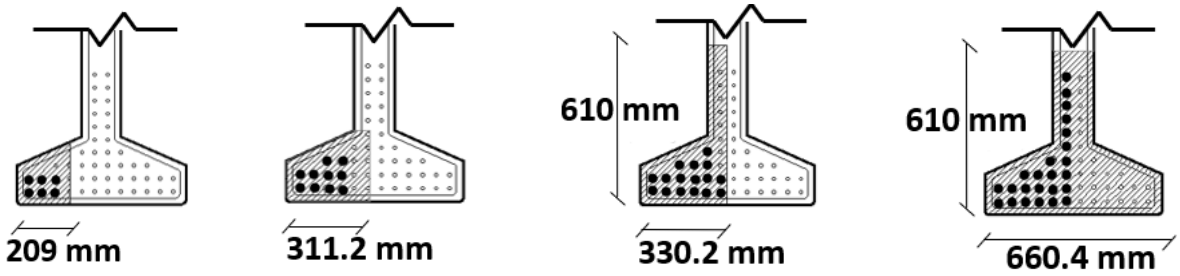

(a) (b) (c) (d)

Figure A-17. Asymmetric loss of strands configuration (a) S12.5%-C12.5%, (b) S20.8%-C22%, (c) S33%-C28%, and (d) S50%-C56%

A.2.5 Ultimate strength of the girders

Figures A-16 and A-17 display the relationship between the bending moment with the mid-span deflection for all models with loss of strands alone and combined loss of strands and concrete damage, respectively. In the control scenario with no loss of prestressing strands, the FE model exhibited a peak bending moment capacity of 17,875 kN.m (13183 kips. Ft), with a mid-span deflection of 445 mm (17.5 inch). This capacity exceeded the AASHTO LRFD flexural strength prediction of 15,398 kN.m (11357 kips. ft) by 16%. The observed increase is attributed to the incorporation of nonlinear material behavior and the enhanced contributions from the composite section. These factors result in a higher load-carrying capacity compared to the AASHTO LRFD provisions, which are based on Navier-Bernoulli assumptions, including linear approximations and the premise that plane sections remain plane. Furthermore, such assumptions may not fully account for the complex composite interaction between the girder and deck.

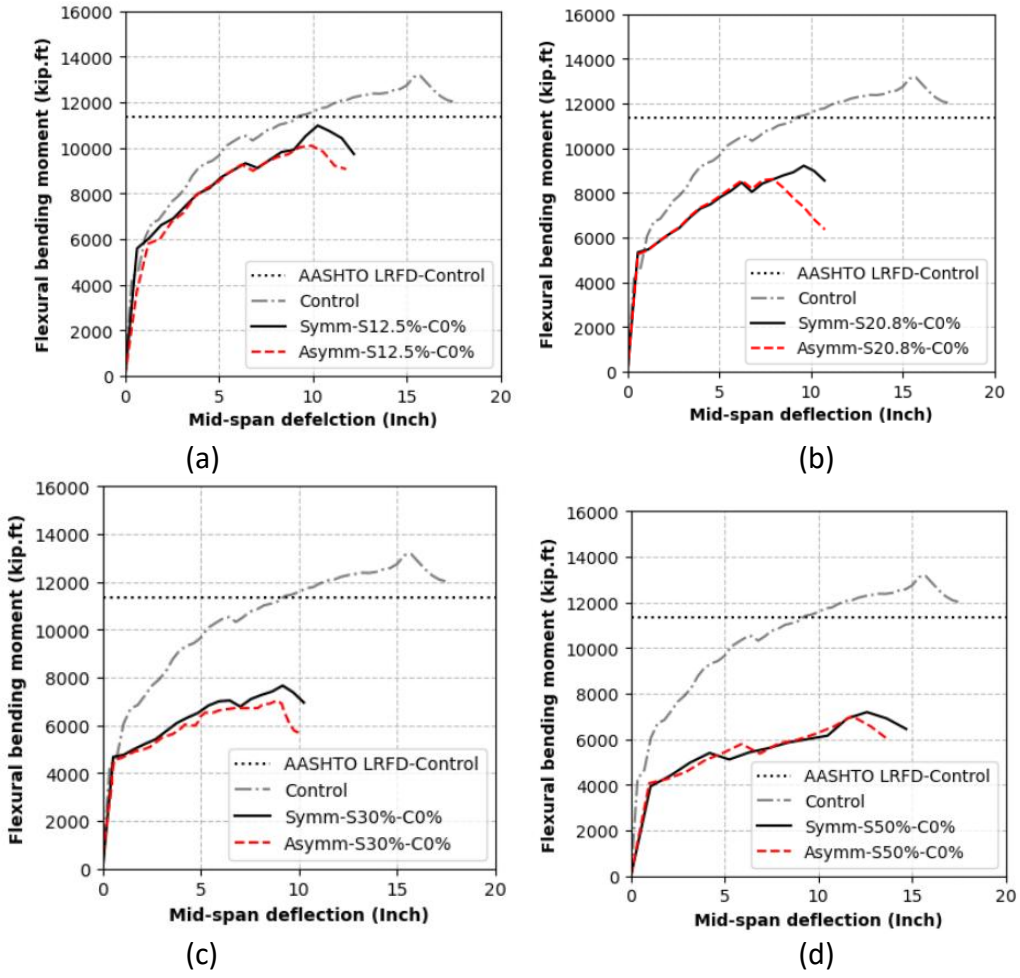

Figure A-18. The residual flexural capacity of specimens having loss of strands (a) S12.5%-C0%, (b) S20.8%-C0%, (c) S33%-C0%, and (d) S50%-C0%

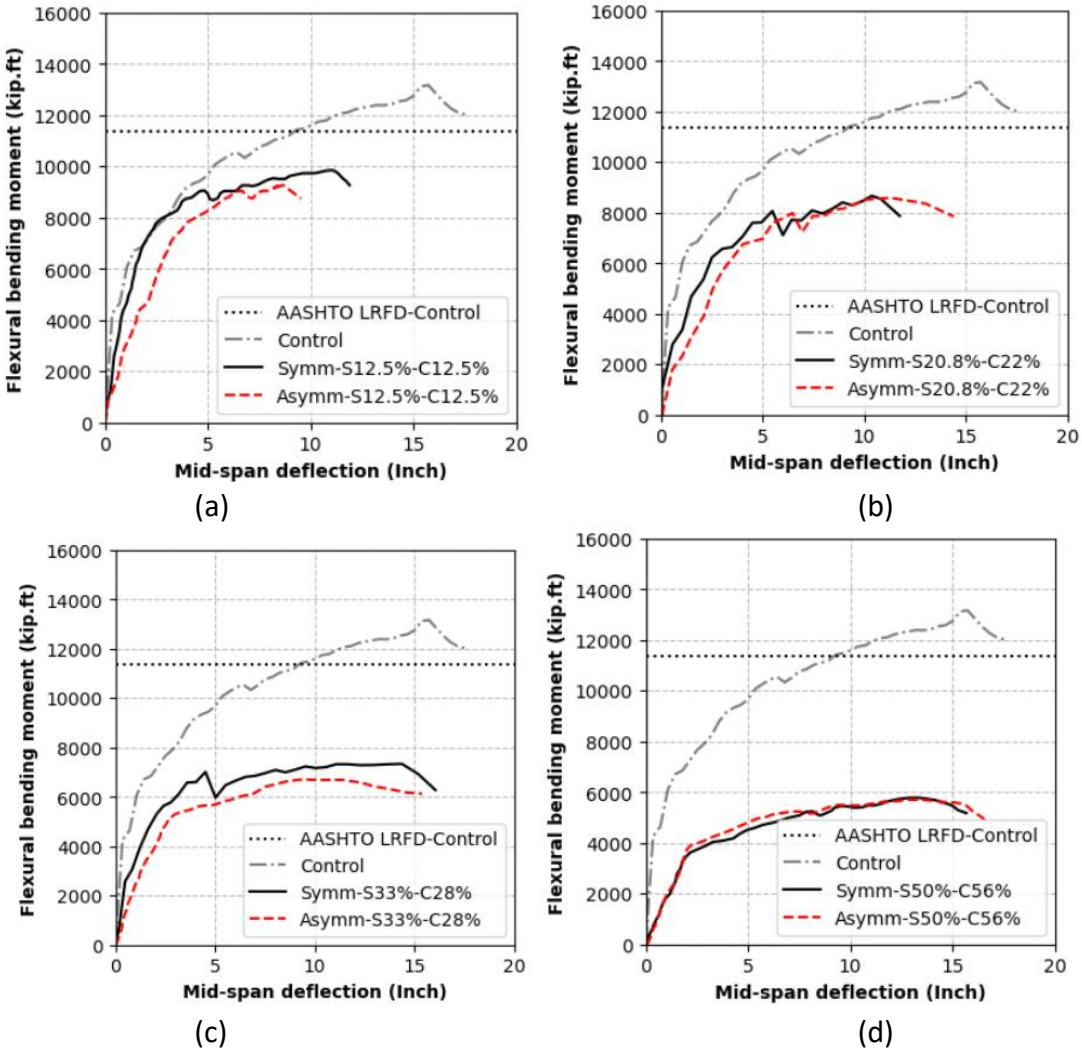

Figure A-19. The residual flexural capacity of specimens having loss of strands and concrete damage (a) S12.5%-C12.5%, (b) S33%-C28%, (d) S20.8%-C22%, and (d) S50%-C56%

A.2.6 Initial stiffness of the girders

For cases of strand loss alone (without concurrent cross-section damage), the force-deflection curves (Figures A-16) showed only a minor reduction in initial stiffness ranging from 2% to 10% strand loss (Table A-6), with a more pronounced decline in flexural strength. This suggests that while the initial stiffness remains somewhat resilient to strand losses, the ultimate flexural capacity deteriorates due to the altered internal force distribution and neutral axis depth (c). For cases of combined concrete cross-section and strand loss, the initial stiffness reduction becomes more pronounced, ranging from 9% to 77% (Table A-8). That was mainly due to the concrete section loss, which decreased the girder's moment of inertia which caused more deflection. Furthermore, the initial stiffness of the asymmetric cases represents 88% to 43% of

that of the symmetric cases, for scenarios involving strand loss alone and combined strand and concrete cross-section loss, respectively.

A.2.7 Strain energy and ductility

The area under the deflection-flexural strength curve represents the strain energy, which quantifies the energy absorbed by a structural member during loading. Figure A-18a illustrates the relationship between the normalized absorbed energy by the control value for the symmetric and asymmetric configurations. The absorbed energy exhibited a significant decrease as the number of strand losses increased beyond 20% loss of strands, ranging from 46% to 67% for strand losses of 12.5% to 50%. When strand loss with a reduction in the concrete cross-section, the reduction in energy absorption was slightly changed, ranging from 45% to 63% for the same range of strand losses (12.5% to 50%) as depicted in Figure A-18b.

The forced displacement for each beam was idealized as elastoplastic using the initial stiffness and ultimate strength. The ultimate displacement from the idealized curve divided by the yield displacement is defined as the displacement ductility. Figure A-18b shows the normalized displacement ductility index by the control value of all specimens ranging from 4.4 to 10. The ductility exhibited a slight decrease as the number of strand losses increased, ranging from 6.6 to 7.5 for strand losses of 12.5% to 50% (Table A-7). When strand loss was combined with a reduction in the concrete cross-section, the reduction in displacement ductility became more pronounced, increasing to 4.4 to 5.5 for the same range of strand losses of 12.5% to 50% (Table A-9).

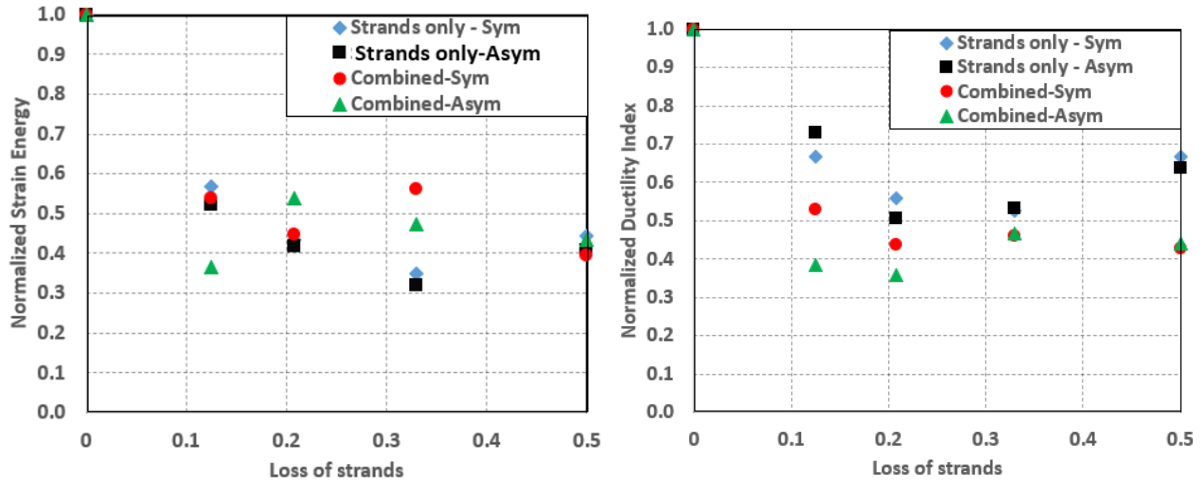

Figure A-20. Normalized measures by the control value for the symmetric and asymmetric configurations (a) Strain energy, (b) Ductility index

Table A-7. Strength and initial stiffness ratios for specimens with loss of strands only

Case	FS – Sym (kips.ft)	IS – Sym (kips/ft)	FS – Asym (kips.ft)	IS - Asym (kips/ft)	Normalized FS – Sym	Normalized IS – Sym	Normalized FS - Asym	Normalized IS – Asym
Control	13184	8791	13184	8791	1.00	1.00	1.00	1.00
S12.5%-C0%	10971	8904	10090	8134	0.83	0.95	0.77	0.93
S20.8%-C0%	9207	8301	8618	8301	0.70	0.94	0.65	0.94
S33%-C0%	7650	6964	6782	6329	0.58	0.79	0.51	0.72
S50%-C0%	7183	6574	7007	6685	0.54	0.75	0.53	0.76

FS: Flexural strength; IS: Initial stiffness; Sym: Symmetric; Asym: Asymmetric

Table A-8. Ductility and strain energy ratios with loss of strands only

Case	DI – Sym (Inch/ Inch)	SE – Sym (kips.ft)	DI – Asym (Inch/ Inch)	SE – Asym (kips.ft)	DI - Normalized Sym	SE - Normalized Sym	DI - Normalized Asym	SE - Normalized Asym
Control	10.35	4641	10.35	4641	1.00	1.000	1.00	1.00
S12.5%-C0%	6.89	2636	7.54	2419	0.67	0.57	0.73	0.52
S20.8%-C0%	5.77	2018	5.24	1935	0.56	0.43	0.51	0.42
S33%-C0%	5.45	1614	5.51	1492	0.53	0.35	0.53	0.32
S50%-C0%	6.91	2056	6.60	1892	0.67	0.44	0.64	0.41

DI: Ductility Index; SE: Strain Energy; Sym: Symmetric; Asym: Asymmetric

Table A-9. Strength and initial stiffness ratios for specimens with loss of strands and concrete section

Case	FS – Sym (kips.ft)	IS – Sym (kips/ft)	FS – Asym (kips.ft)	IS – Asym (kips/ft)	FS – Normalized Sym	IS – Normalized Sym	FS – Normalized Asym	IS - Normalized Asym
Control	13184	8791	13184	8791	1.00	1.00	1.00	1.00
S12.5%-C12.5%	9835	2785	9270	1582	0.75	0.32	0.70	0.18
S20.8%-C22%	8662	1437	8589	1114	0.66	0.16	0.65	0.13
S33%-C28%	7337	1470	6706	1237	0.56	0.17	0.51	0.14
S50%-C56%	5779	1159	5702	1070	0.44	0.13	0.43	0.12

FS: Flexural strength; IS: Initial stiffness; Sym: Symmetric; Asym: Asymmetric

Table A-10. Ductility and absorbed energy ratios for specimens with loss of strands and concrete section

Case	DI – Sym (Inch/ Inch)	SE – Sym (kips/ft)	DI – Asym (Inch/ Inch)	SE – Asym (kips/ft)	DI – Normalized Sym	SE - Normalized Sym	DI - Normalized Asym	SE Normalized Asym
Control	10.35	4641	10.35	4641	1.00	1.000	1.00	1.00
S12.5%-C12.5%	5.50	2509	3.97	1699	0.53	0.54	0.38	0.37
S20.8%-C22%	4.50	1769	3.70	2514	0.44	0.38	0.36	0.54
S33%-C28%	4.80	2609	4.85	2202	0.46	0.56	0.47	0.47
S50%-C56%	4.40	1842	4.55	2017	0.43	0.40	0.44	0.43

DI: Ductility Index; SE: Strain Energy; Sym: Symmetric; Asym: Asymmetric

Figure A-19 illustrates the correlation between strand loss and the ratio of residual flexural strength relative to the undamaged girder (control) strength. For all cases, there was an approximately linear decrease in ultimate flexural strength with increasing the number of severed strands. However, the flexural strength loss is generally higher in the case of combined loss of concrete cross-section and strands. Also, the loss is slightly larger in the cases of asymmetric compared to the symmetric cases. For the strand loss alone, the losses ranged from 17% – 46% and 23%- 47% for loss of prestressing strands in symmetric and asymmetric cases, respectively (Figure A-19a). For loss of strands and concrete cross-section loss combined, the losses ranged from 25% – 56% and 30%- 57% for loss of prestressing strands in symmetric and asymmetric cases, respectively (Figure A-19b).

Trendlines were developed for each set of models. Coefficient of determination (R^2) values were found to be 0.91 and 0.82 for symmetric and asymmetric strand loss cases, respectively, in scenarios without cross-section loss. When both strand and cross-section losses were combined, the R^2 values changed to 0.94 and 0.80 for symmetric and asymmetric cases, respectively. These relatively high R^2 values indicate that even complex damage scenarios can be effectively approximated using linear relationships, which could prove valuable for initial damage assessment procedures.

The ratio of flexural strength between symmetric and asymmetric cases ranged from 3% to 13% for strand loss alone and from 1% to 9% for combined strand and concrete losses (Tables A-6 and A-8). The higher ratios observed for strand loss alone compared to the combined case indicate that lateral bending effects are less pronounced when concrete section loss is present.

This can be attributed to the lack of strain compatibility between the strands and the concrete, which reduces lateral bending.

As strand losses increase, lateral eccentricity also increases, intensifying the effects of lateral bending. This results in an inclined neutral axis that deviates from being perpendicular to the section's vertical axis. In other words, plane sections no longer remain plane after bending, as section warping disrupts the fundamental assumptions of beam theory. Additionally, cross-sectional losses further weaken flexural strength due to compatibility issues between the undamaged strands and the surrounding concrete. These mismatches hinder uniform load transfer, leading to a reduction in the overall flexural strength of the prestressed concrete (PC) girder. As strand losses increase, the neutral axis depth (c) shifts upward toward the top fiber of the compression flange. This upward shift reduces the prestressing strand stress at failure (f_{ps}), as calculated in Equation A-1 in accordance with AASHTO LRFD (5.7.3.1.1-1).

$$f_{ps} = f_{pu}(1 - k\frac{c}{d_p})$$

Equation A-1

Where f_{pu} is the ultimate strength of prestressing steel, and d_p is the distance from the extreme compression fiber to the centroid of prestressing steel. This decrease in f_{ps} with increasing neutral axis depth underlines the diminishing contribution of prestressing strands to the girder's residual strength, as the stress distribution becomes less favorable.

The flexural strength of each girder was calculated using the AASHTO LRFD flexural strength provisions (Equation A-1 and A-2, AASHTO 5.7.3.2.2-1). Utilizing the cross-sectional area of the remaining (undamaged) strands, A_{ps}, the flexural strength can be determined while neglecting the damage to the concrete section and the asymmetric effects on strength.

$$M_n = A_{ps}f_{ps}\left(d_p - \frac{a}{2}\right) + A_s f_s\left(d_s - \frac{a}{2}\right) - A_s' f_s'(d_s' - \frac{a}{2}) + 0.85\, f_c'(b - b_w)h_f(\frac{a}{2} - \frac{h_f}{2})$$

Equation A-2

Where M_n is the nominal flexural capacity, A_{ps} is the area of prestressing strands, fps is the prestressing strand stress at failure, d_p is the effective depth, a is the compression stress block depth, A_s and A_s' are the non-prestressed steel areas on tension and compression sides, respectively, f_s and f_s' are the yield strengths of non-prestressed steel on tension and compression sides, respectively, d_s' is a distance of the non-prestressed steel at compression to the top fiber, f_c' is the concrete compressive strength, b is the girder top flange width, b_w is the girders' web width, and h_f is the girder top flange depth.

Figure A-19 illustrates the relationship between the ratio of residual flexural strength to the ultimate flexural strength of an undamaged girder and the loss of prestressing strands for all cases. At the extreme case of 50% loss of prestressing strands, the AASHTO approach overestimated the flexural strength compared to the FE flexural analysis by 11% and 18% for the strand loss alone and the combined strand and concrete cross-section loss cases,

respectively. This occurred because the FE analysis accounts for asymmetry and section and material nonlinearity, resulting in more accurate predictions of flexural strength.

Given the complexity and time-consuming nature of FE analyses, this study proposes a versatile reduction factor that can be integrated into the AASHTO LRFD procedure to account for asymmetric strand loss. Following incidents such as bridge-truck collisions, the number of severed strands can be determined, the area of the remaining undamaged prestressing strands, $A_{ps,}$ can be determined, and the residual flexural strength can be estimated using Equation A-3. Subsequently, an asymmetric reduction factor, Ψ_{IM}, is applied as follows:

$$M_r = \Psi_{IM} M_n$$

Equation A-3

Based on the FE analysis, a Ψ_{IM} value of 0.85 is proposed, representing the maximum reduction observed in this study. It is anticipated that as more data become available, this factor may be refined further.

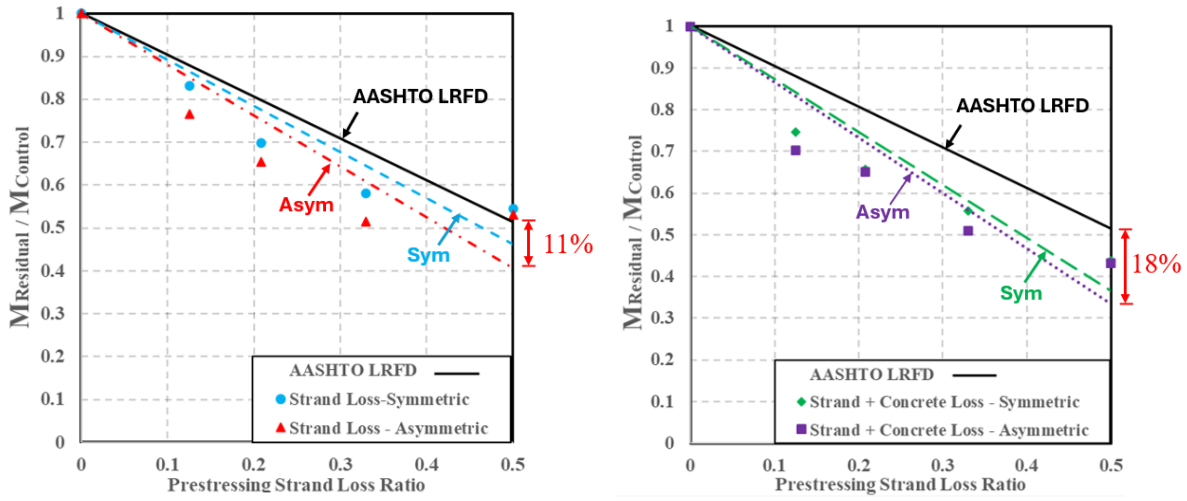

(a) (b)

Figure A-21. Estimation error of the sectional flexural resistance due to the biaxial bending moment (a) Loss of strands only (b) Combined loss of strands and concrete section

Appendix B. Impact Simulator Setup

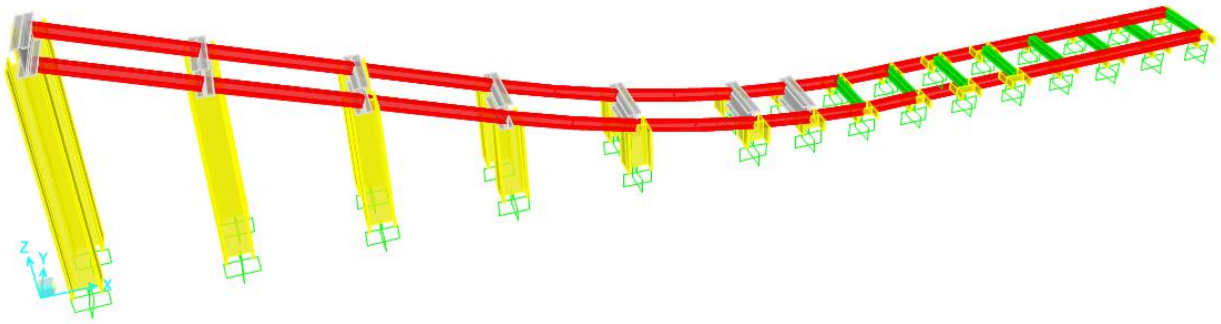

3D Model of the track system in Sap2000

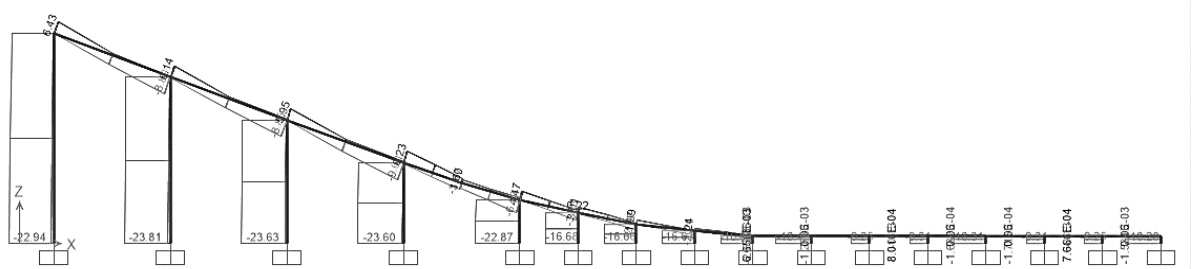

Track system maximum axial forces

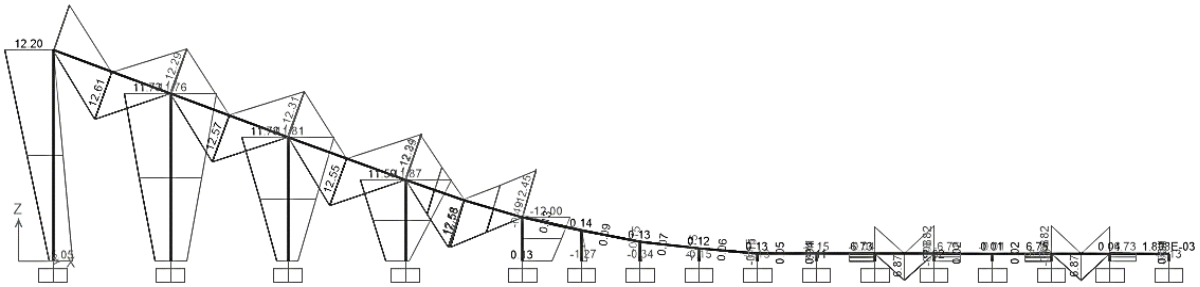

Track system maximum bending moments

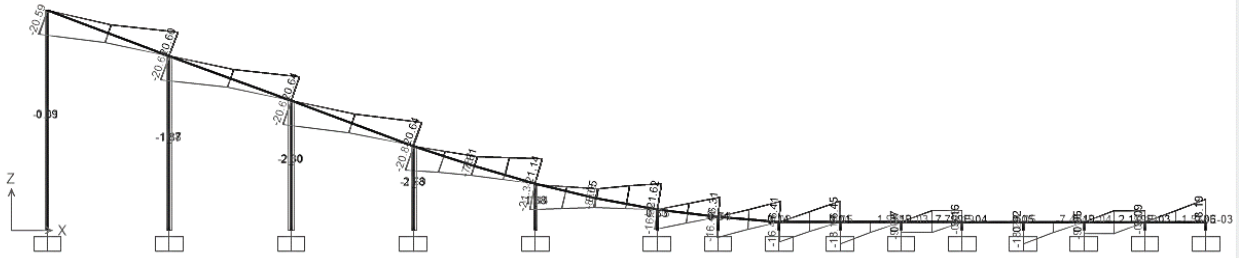

Track system maximum frame shear forces

Figure B-22. Structural analysis modeling of the track system using CSI SAP 2000

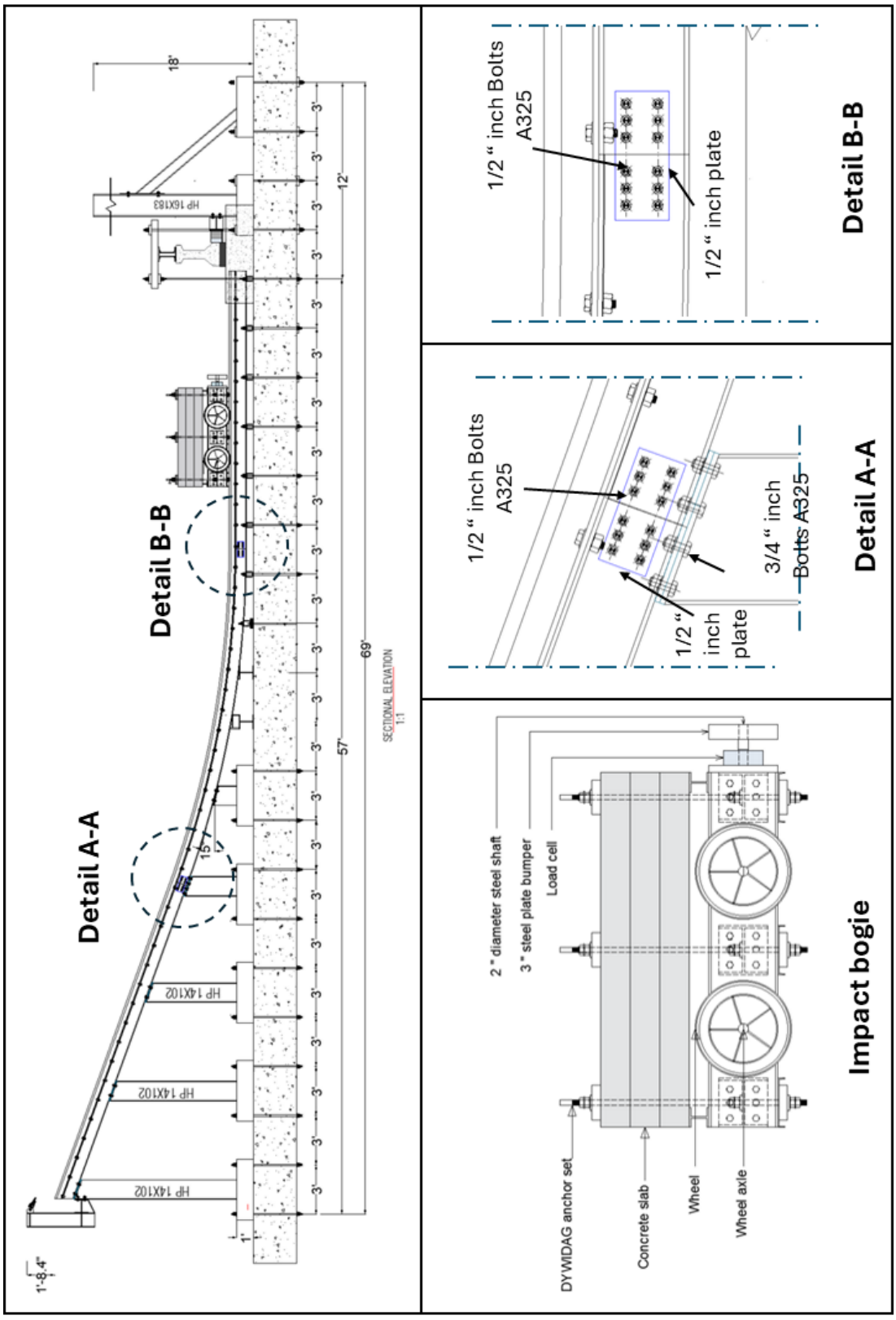

Figure B-23. Design details of the track and impact bogie

B.1 Impact simulator preparations

(a)

(b)

(c)

(d)

Figure B-24. (a) West lateral reaction frame, (b) East lateral reaction frame, (c) Cutting track supporting beam for bending, (d) Cutting track rail beam for bending

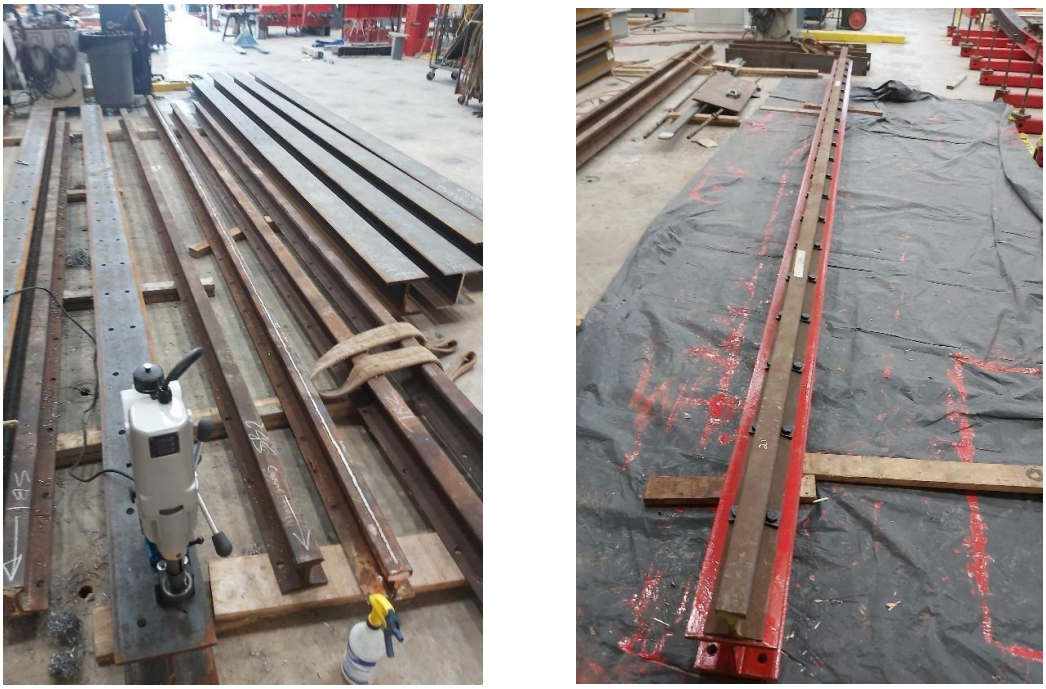

(a) (b)

Figure B-25. (a) Drilling the supporting beams of the track, (b) Installing the rail to the track on the ground before assembly with the track

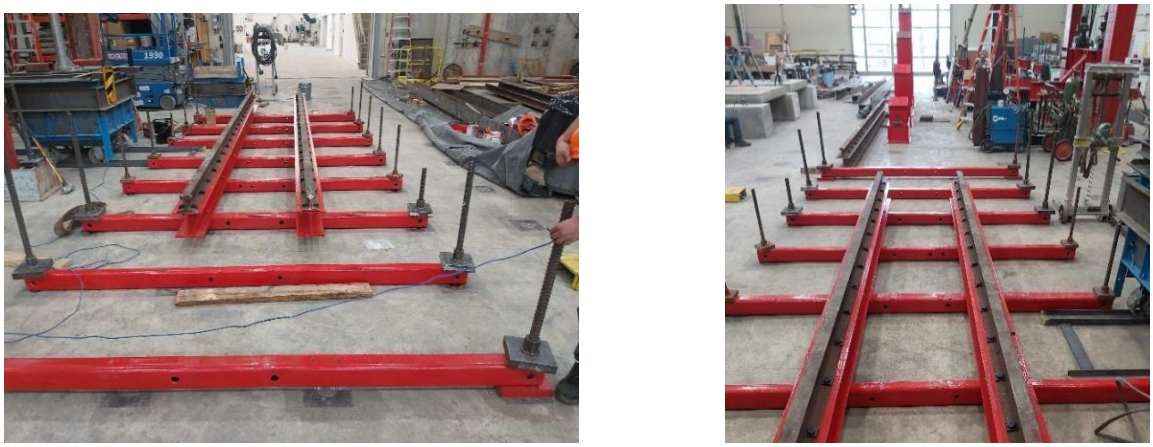

(a) (b)

Figure B-26. (a) Assembly of the horizontal track, (b) Installing the columns of the elevated track

Figure B-27. Completing installing the curved supporting beams from two sides

(a)

(b)

Figure B-28. (a) Drilling and installation of connecting steel plates, (b) Installing the rail to the track supporting beams

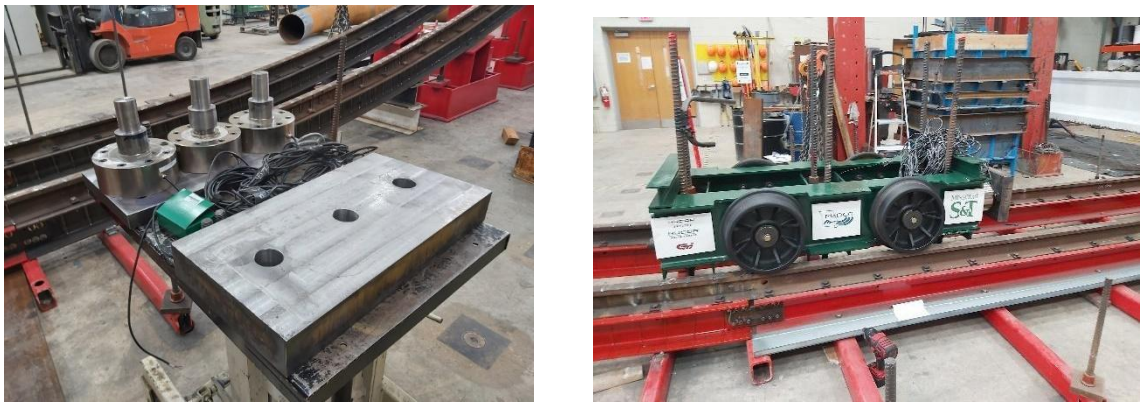

(a) (b)

Figure B-29. The impactor head and load cells (a) Impactor head elements, (b) Impactor head mounting on the bogie

(a) (b) (c)

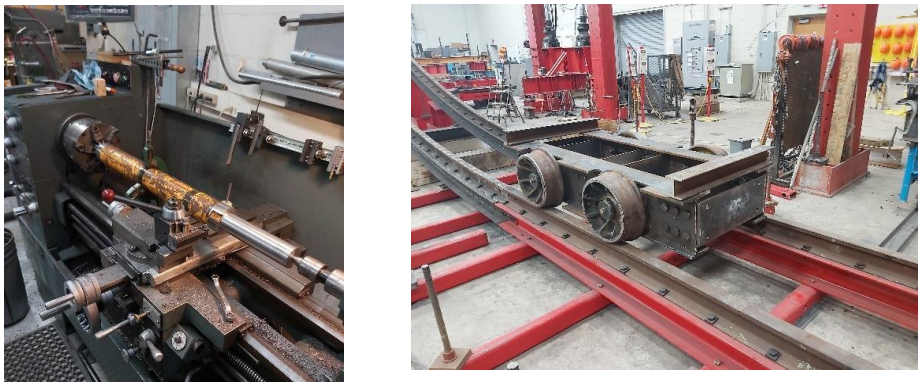

(d) (e)

Figure B-30. Impact bogie fabrication (a) Axle bearing plate, (b) Bogie main frame, (c) Machining the bogie wheels, (d) Machining the axle, (e) Bogie and wheels assembly

(a)

(b)

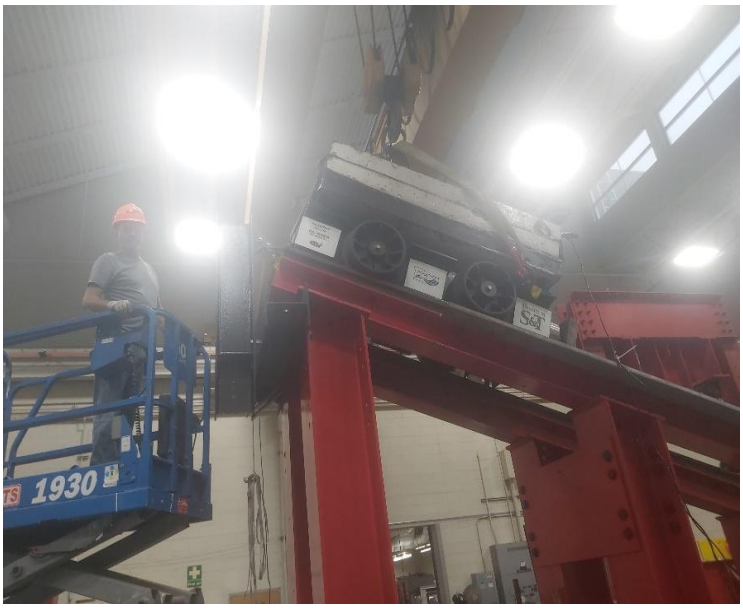

(c) (d)

Figure B-31. Release system of the impact bogie (a) Toggle release, (b) Installing the release cantilever, (c) Installing the toggle release with the cantilever, (d) Lifting the bogie for a trial test of the release system

Figure B-32. Installing strain gages at the girder fabrication phase

Figure B-33. Delivery of the girders to the structural laboratory at Missouri S&T

B.2 Girder setup

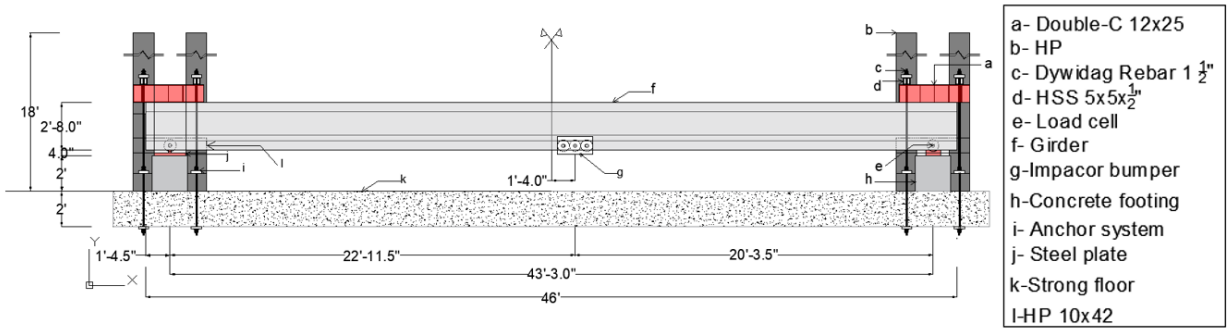

Figure B-34. Girder test setup illustration

(a)

Figure B-35. Placing the girder in the test setup

Appendix C. Impact Testing Results

C.1 Damage of impacted beams

C.1.1 Girder G01

(a)

(b)

Figure C-36. Damaged photographs of Girder G01 impact (a) Impact side, (b) Back side

C.1.2 Girder G02

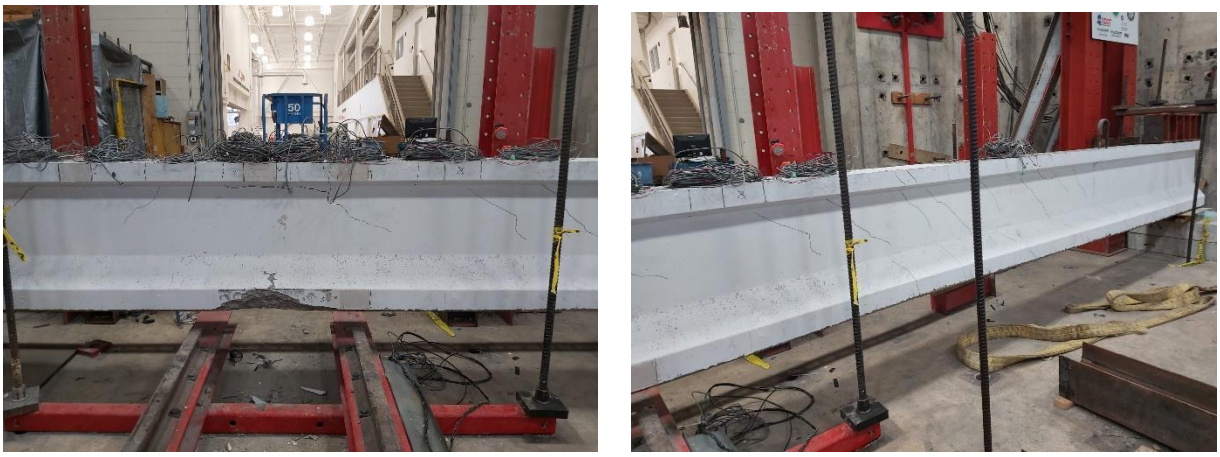

(a)

(b)

Figure C-37. Damage photographs of Girder G02 impact (a) Impact side, (b) Back side

C.1.3 Girder G03

(a)

(b)

Figure C-38. Damage photographs of Girder G03 (a) Impact side, (b) Back side

Figure C-39. Test setup for Girders G03-G04-G05

Figure C-40. Cracking of the girder after impact

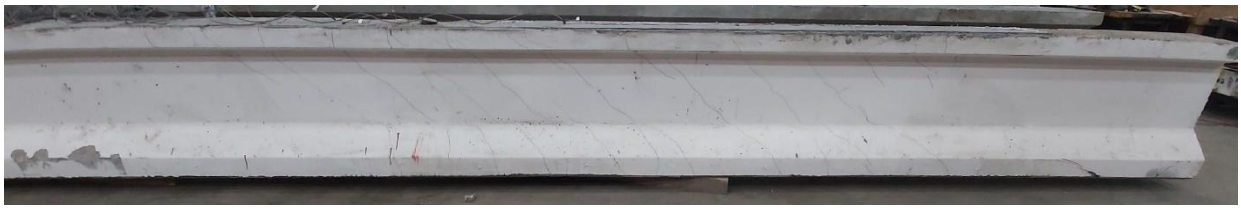

Figure C-41. Girder damage

C.1.4 Girder G04

(a)

(b)

Figure C-42. Damage photographs of Girder G04 (a) Impact side, (b) Back side

C.1.5 Girder G05

(a)

(b)

Figure C-43. Damage photographs of Girder G05-first impact (a) Impact side, (b) Back side

(a)

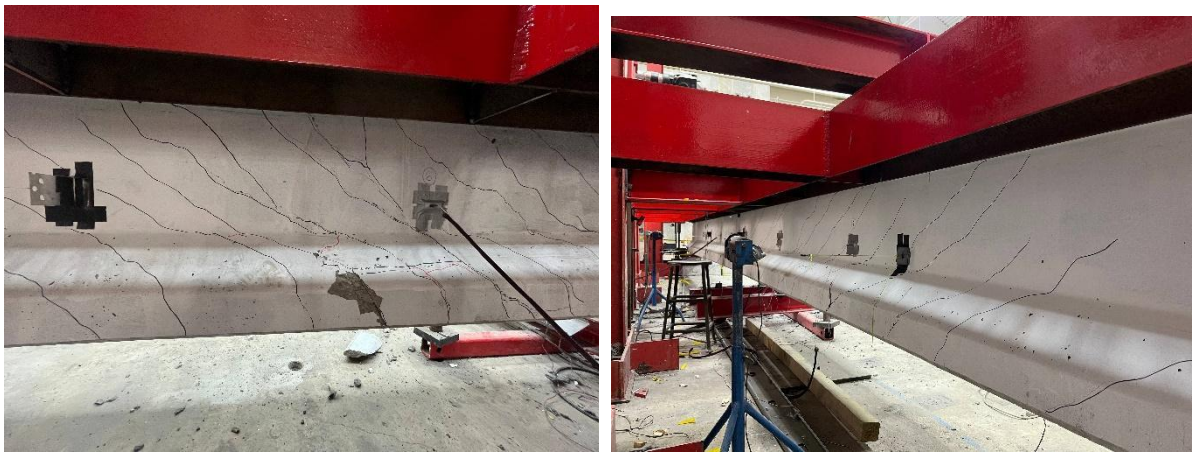

(b)

Figure C-44. Damage photographs of Girder G05-second impact (a) Impact side, (b) Back side

C.1.6 Girder G06

(a)

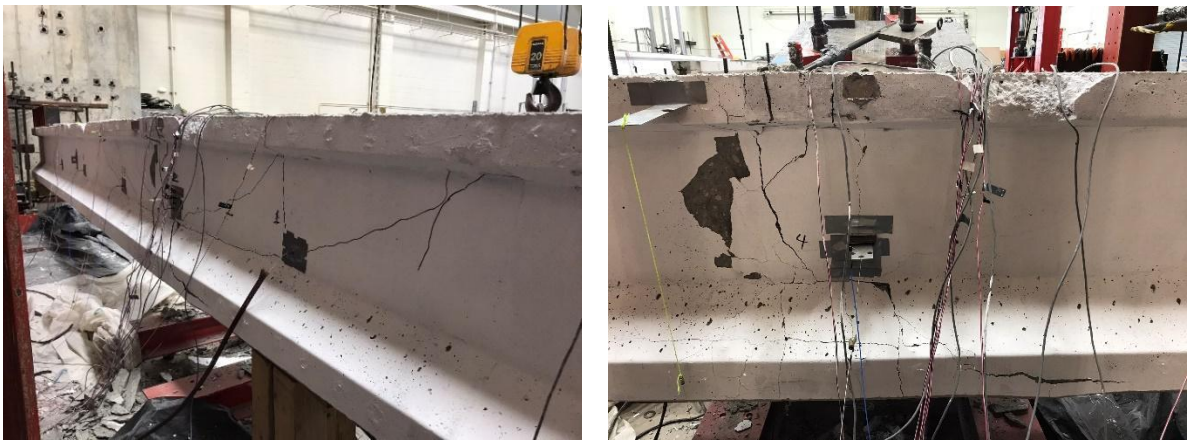

(b)

Figure C-45. Damage photographs of Girder G06-second impact (a) Impact side, (b) Back side

C.1.7 Girder G07

(a)

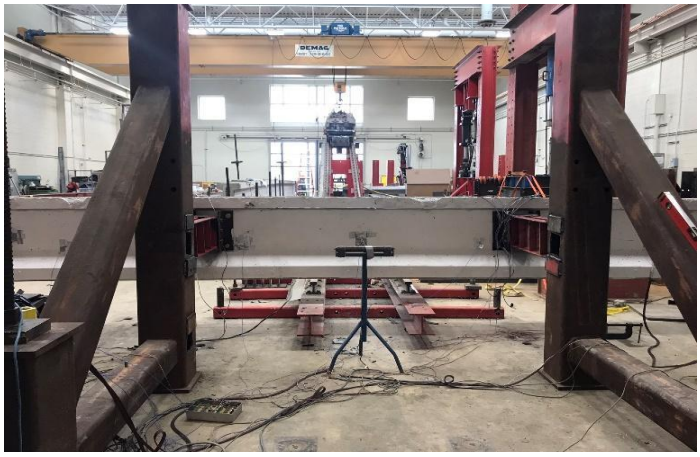

(b)

Figure C-46. Damage photographs of Girder G07 with the additional stirrups and intermediate steel diaphragms (a) Impact side, (b) Back side

C.1.8 Girder G08

(a)

(b)

Figure C-47. Damage photographs of Girder G08 with intermediate steel diaphragms (a) Impact side, (b) Back side

C.2 Impact time comparisons histories

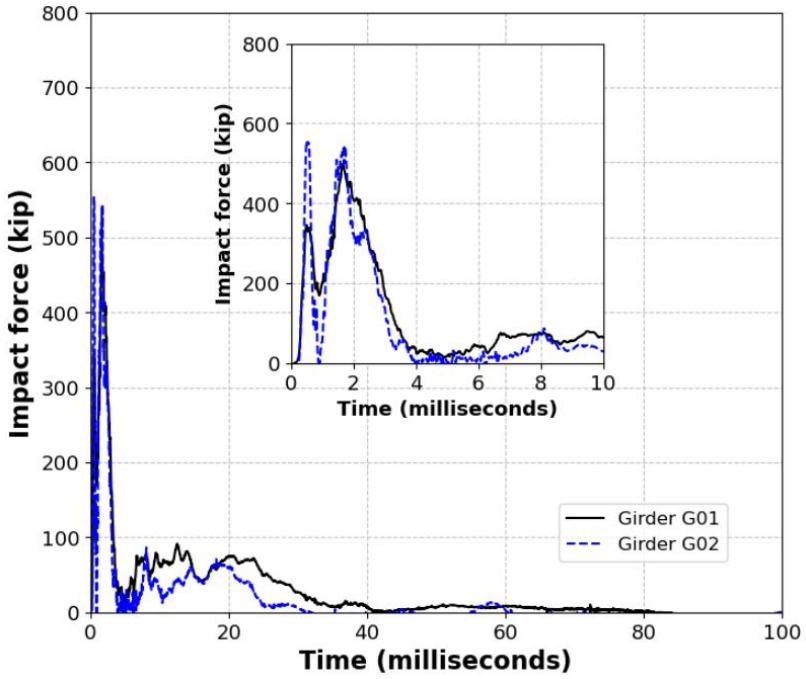

Figure C-48. Effect of mass on the impact time history (Girders G01-G02)

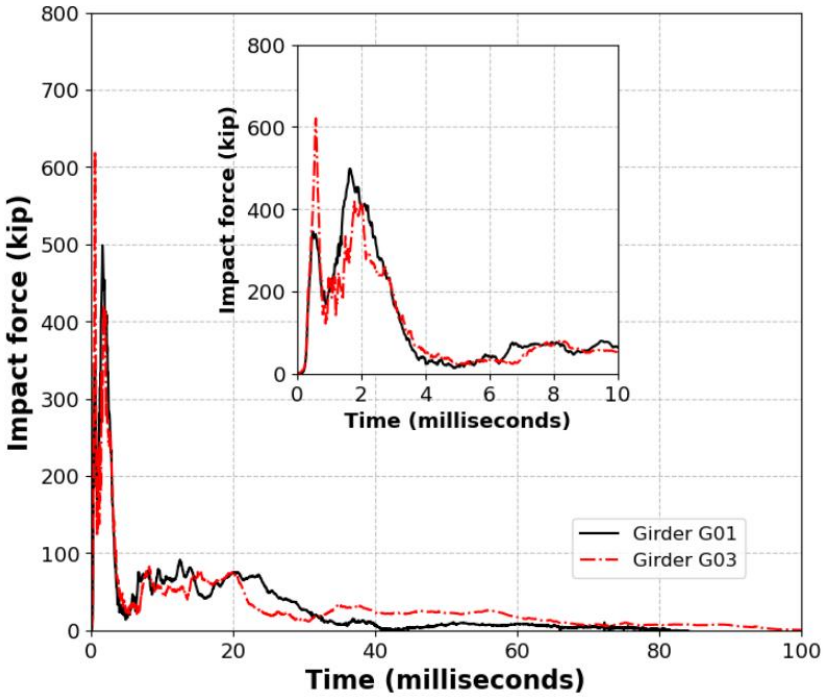

Figure C-49. Effect of top flange restrained (Girders G01-G03)

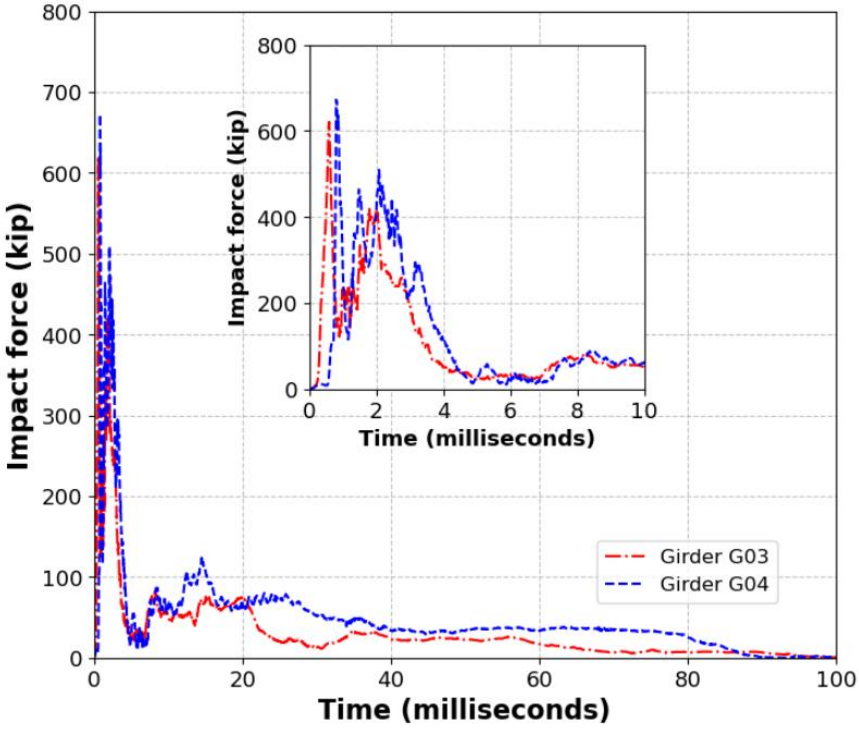

Figure C-50. Effect of impact contact area (Girders G03 and G04)

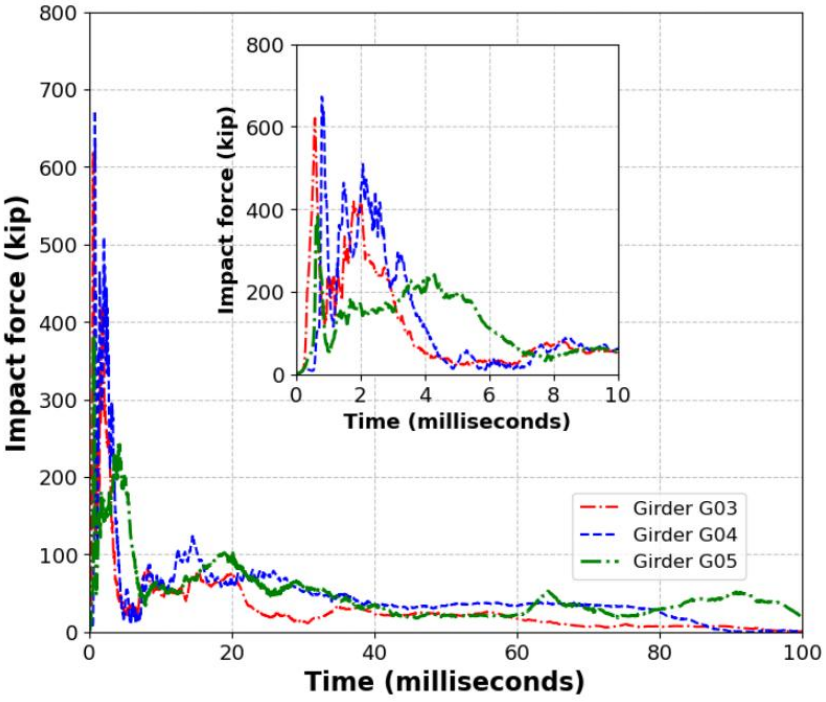

Figure C-51. Effect of multiple impacts (Girders G03-G04-G05)

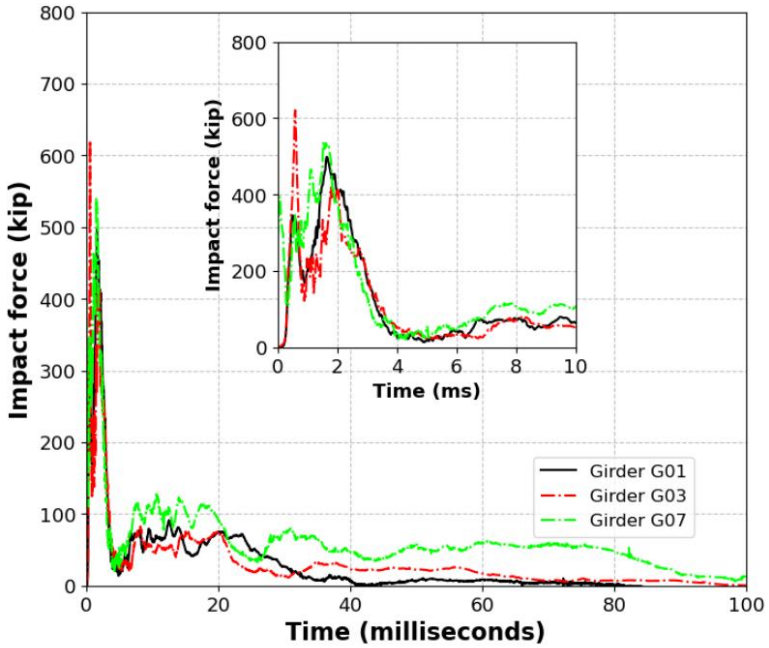

Figure C-52. Effect of increasing the girder flexural strength (Girders G01-G03-G07)

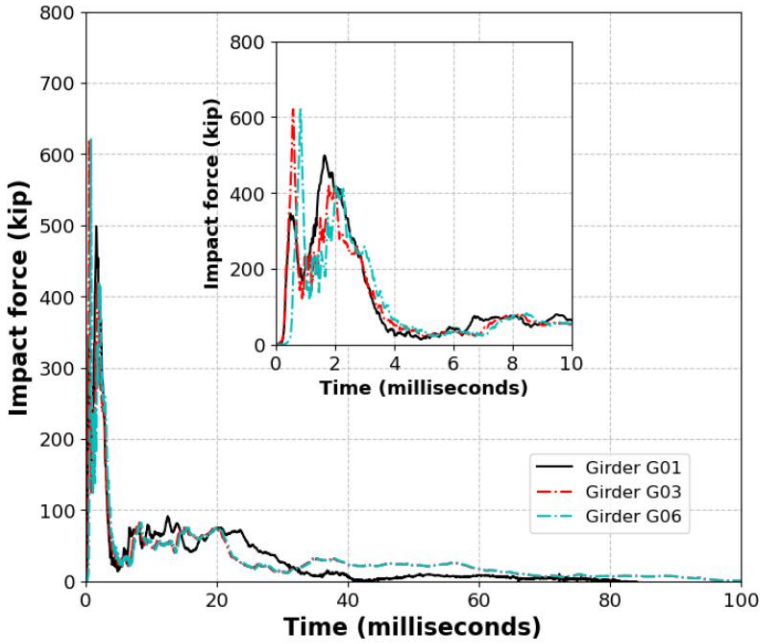

Figure C-53. Effect of increasing the girder flexural strength (Girders G01-G03-G06)

C.3 Strain of prestressing strands

C.3.1 Girder G01

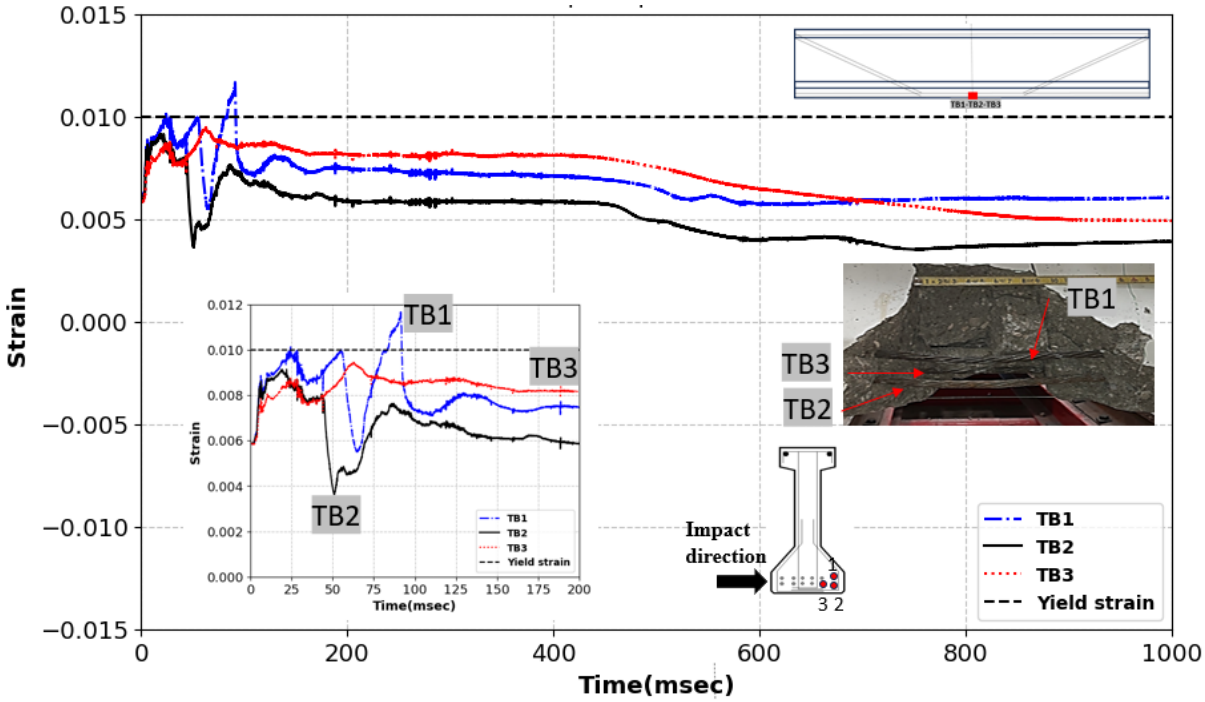

Figure C-54. Back strain gages of Girder G01

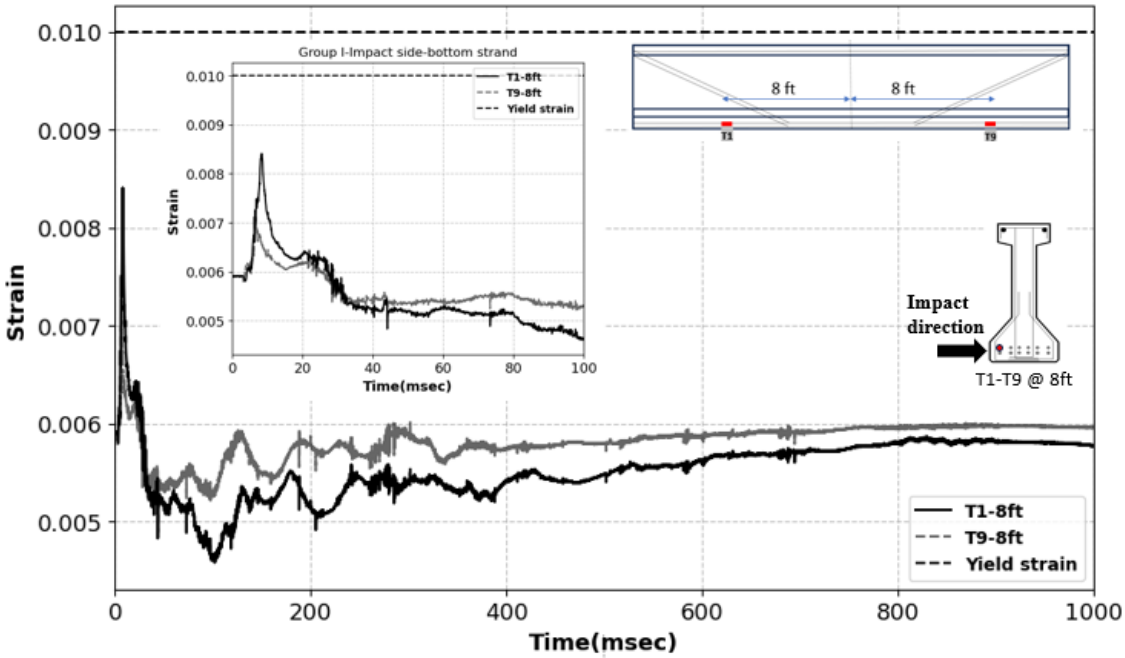

Figure C-55. Impact side strain gages of Girder G01

C.3.2 Girder G02

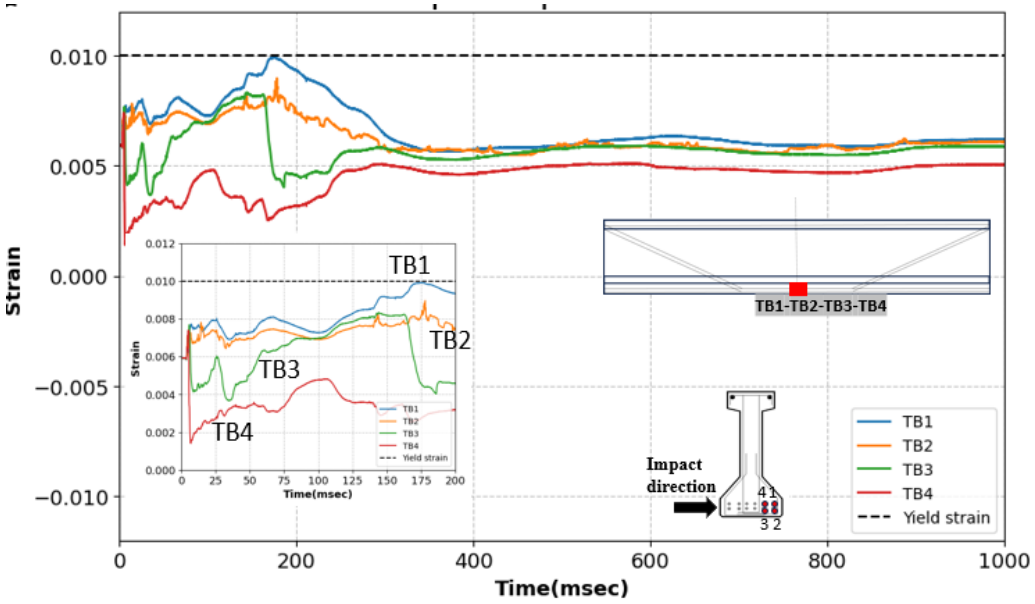

Figure C-56. Back side strain gages of Girder G02

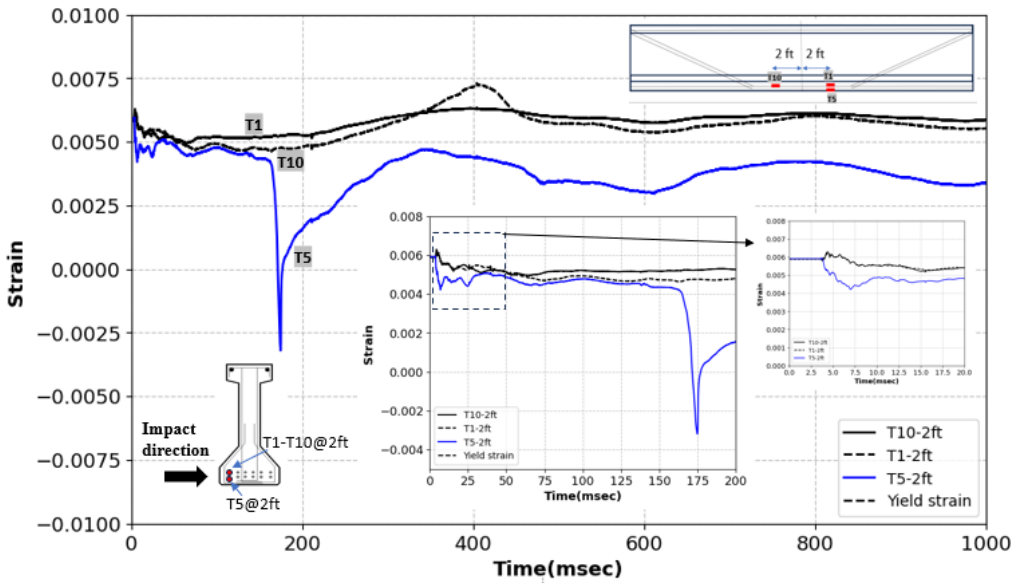

Figure C-57. Impact side strain gages of Girder G02

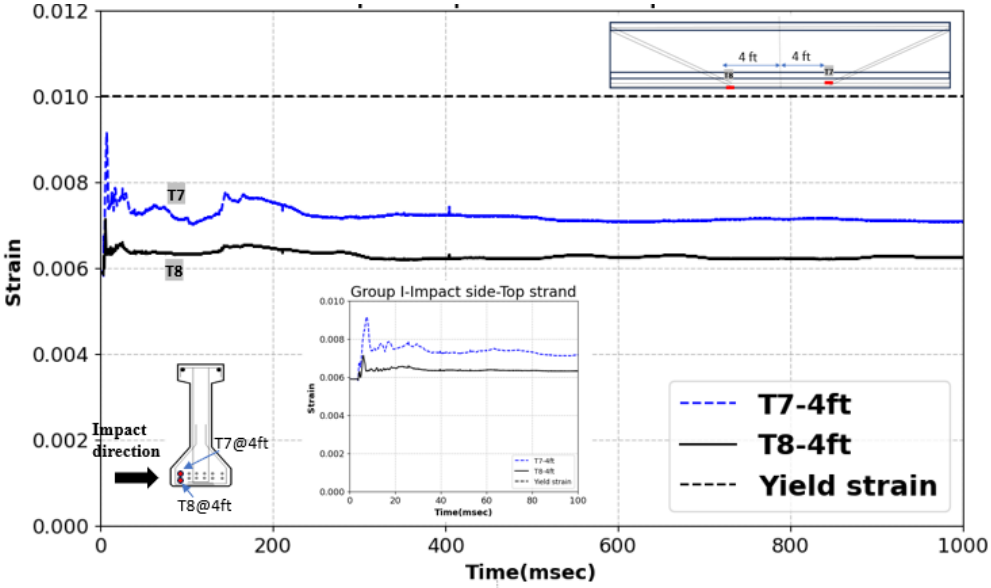

Figure C-58. Impact side strain gages of Girder G02

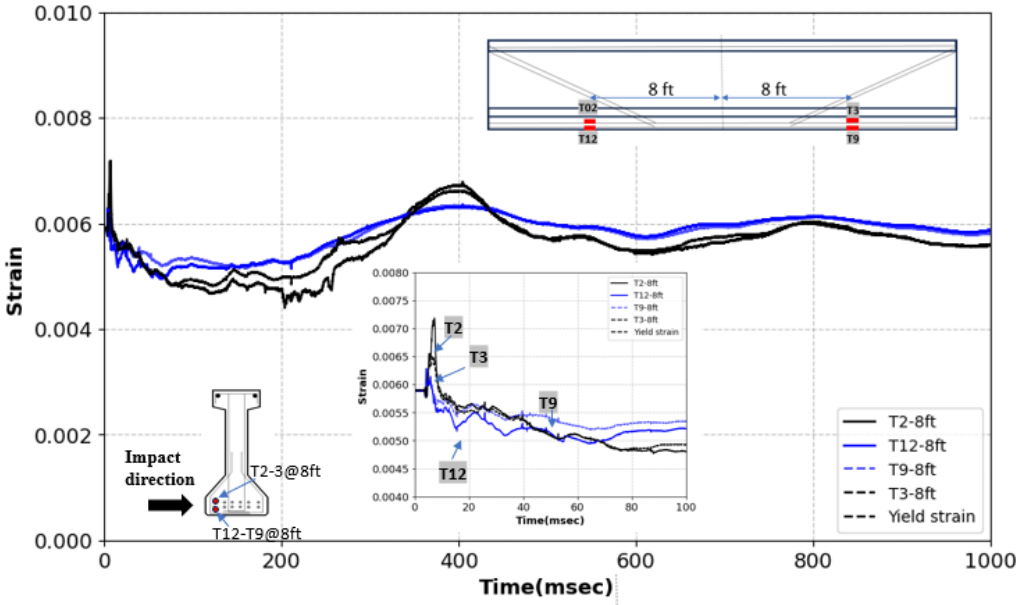

Figure C-59. Impact side strain gages of Girder G02

C.3.3 Girder G03

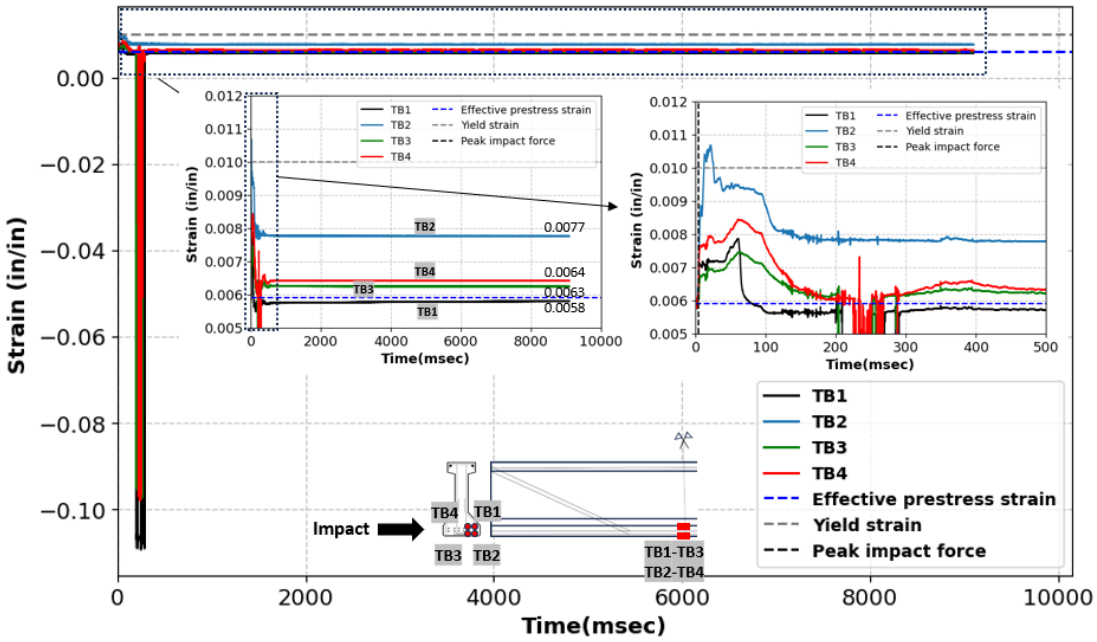

Figure C-60. Back side strain gages of Girder G03

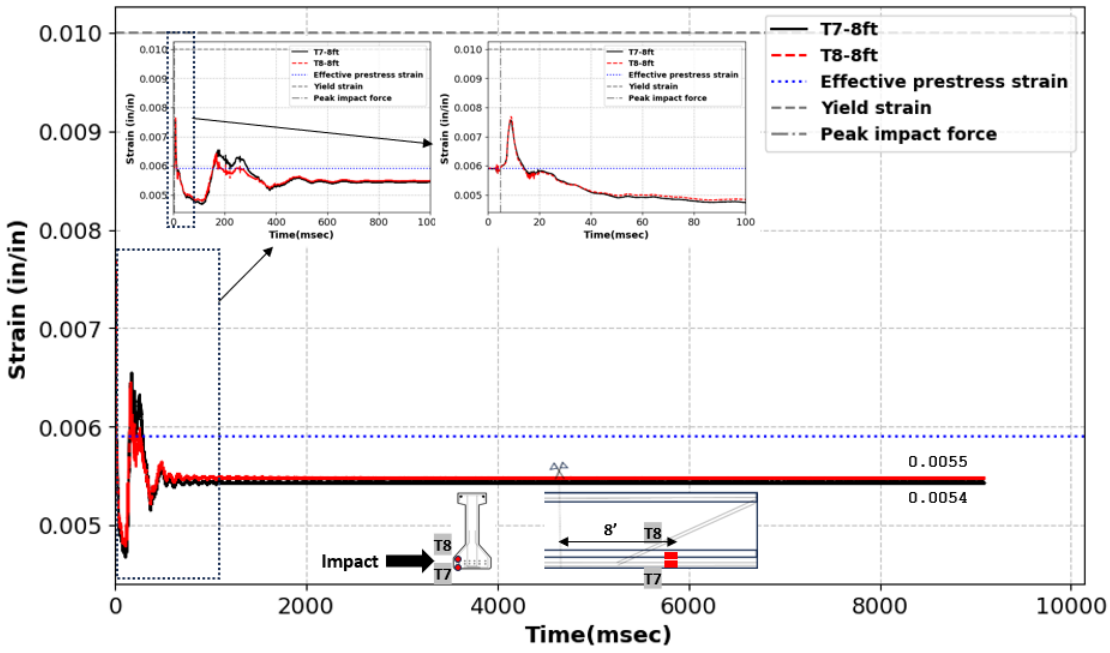

Figure C-61. Impact side strain gages of Girder G03

C.3.4 Girder G04

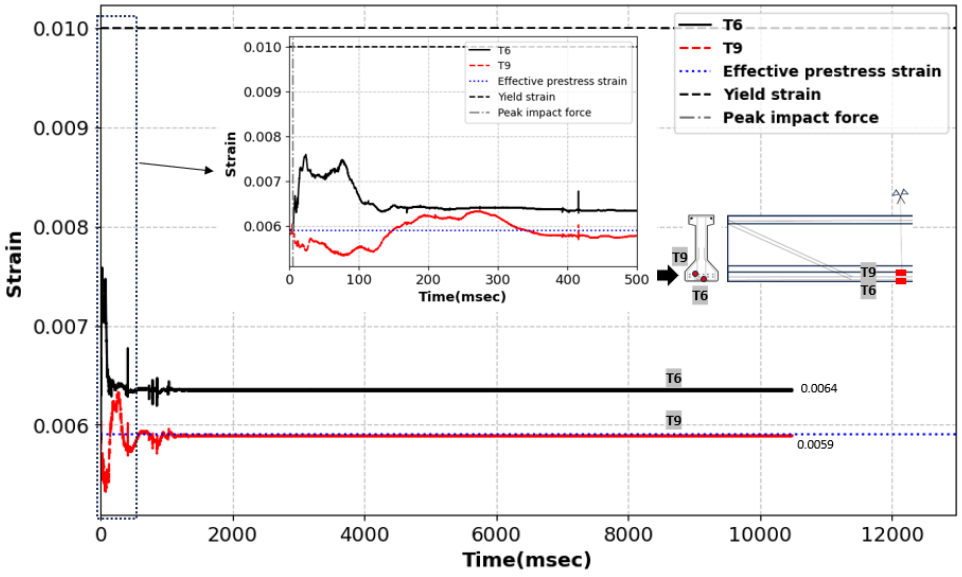

Figure C-62. Back side strain gages of Girder G04

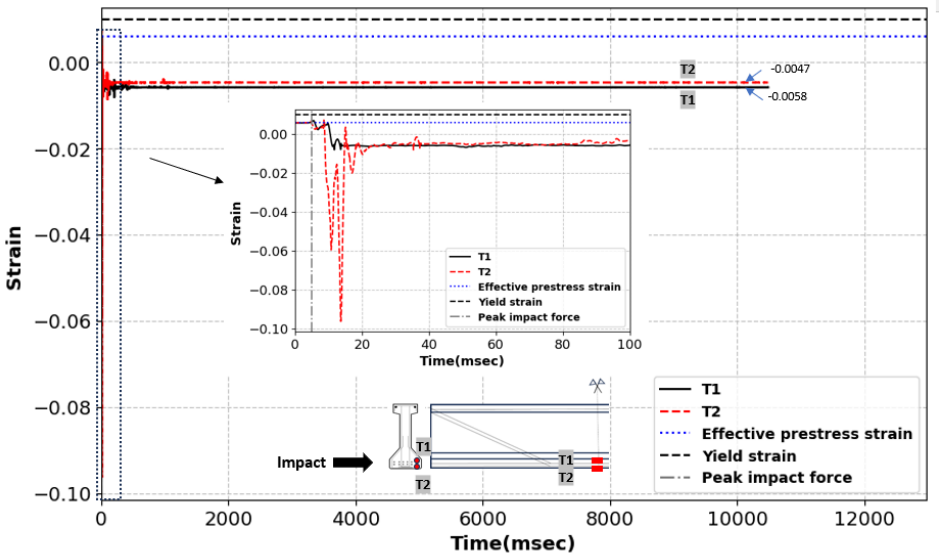

Figure C-63. Impact side and cross-section center strain gages of Girder G04

C.3.5 Girder G05

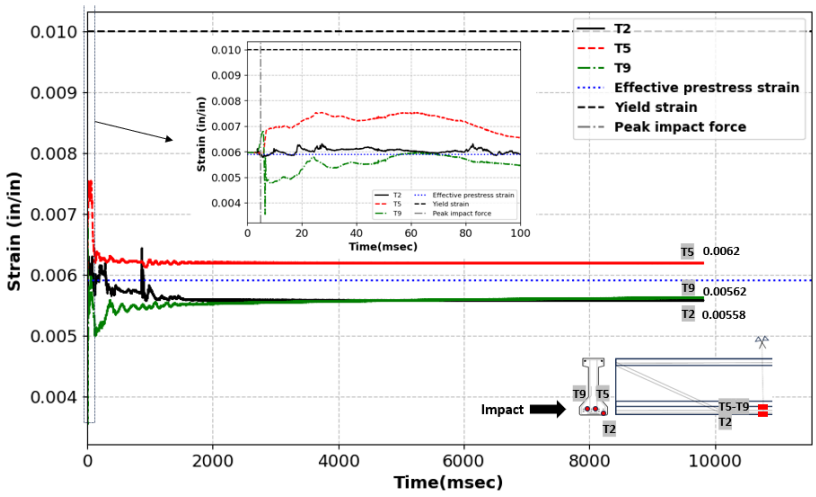

Figure C-29. Cross-section center and back side strain gages of Girder G05-first impact

C.4 High-speed camera for Girder G01

Figure C-33 presents an aerial view captured by the high-speed camera, providing a detailed visualization of the significant progressive damage observed on girder G1 during the impact event. The sequence of events is summarized as follows.

At 5 ms**,** the flat plate made full contact with the bottom flange of the girder, initiating the peak impact force, as detailed in Figure C-33 This marked the beginning of the damage progression.

By 250 ms, the top flange began to exhibit cracking, primarily due to the lateral bending moment induced by the applied impact force. These cracks signified the early stages of structural compromise in the girder.

At 330 ms**,** noticeable lateral deflection was observed in the girder, accompanied by the formation of additional cracks. This deflection caused further distress in the concrete, which began to spall as the material exceeded its tensile strength.

By 700 ms**,** the girder experienced its maximum lateral deflection of 16.7 inches, a critical point in the structural response where the combined effects of bending and shear became most pronounced.

Following this peak deflection, the girder exhibited elastic rebound. By 1165 ms**,** it completed the rebound phase, leaving a permanent lateral deflection of 4.5 inches. This residual deformation highlighted the extent of the inelastic behavior of the girder under the given impact conditions.

Additionally, global shear cracks were observed on both the front and rear faces of the girder, underscoring the severity of the impact forces. These shear cracks contributed to the overall

damage pattern and emphasized the combined effects of lateral deflection and shear stresses on the girder's structural integrity.

The observed behavior demonstrates the dynamic response and failure mechanisms of prestressed concrete girders subjected to high-impact loading, offering valuable insights into their performance under extreme conditions.

Impact moment = 5 ms

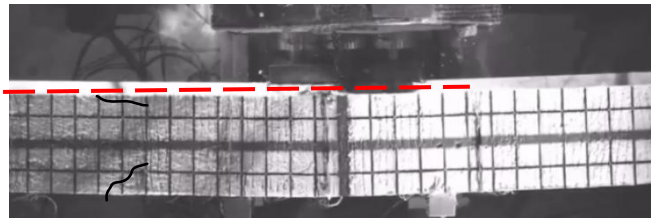

Time 250 ms

Time 330 ms

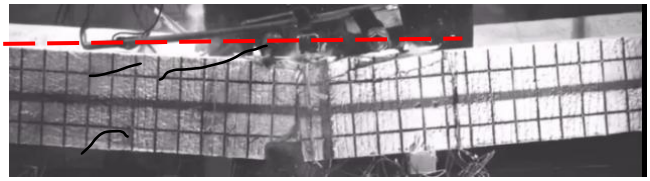

Time 415 ms (max deflection)

Time 1165 ms (end of rebound)

Figure C-30. High speed camera of Girder G01 top view footage

Appendix D. Material Testing Properties

D.1 Girder concrete

Figure D-31. Compression standard cylinder test (a) Compression testing configuration of a 4x8 inch cylindrical specimen under uniaxial loading (b) Failure of specimen

D.2 Concrete compressive strength of patch material

Figure D-32. Grout mortar cube testing; (a) 2X 2in cube compressive test; (b) 2-inch cube specimen of Sika Grout 428 FS after compression testing

D.3 Prestressing strand

Seven-wire prestressing strand tensile test setup

Failure of seven-wire prestressing strand specimen after tensile testing.

Figure D-33. Uniaxial tension testing of prestressing strand

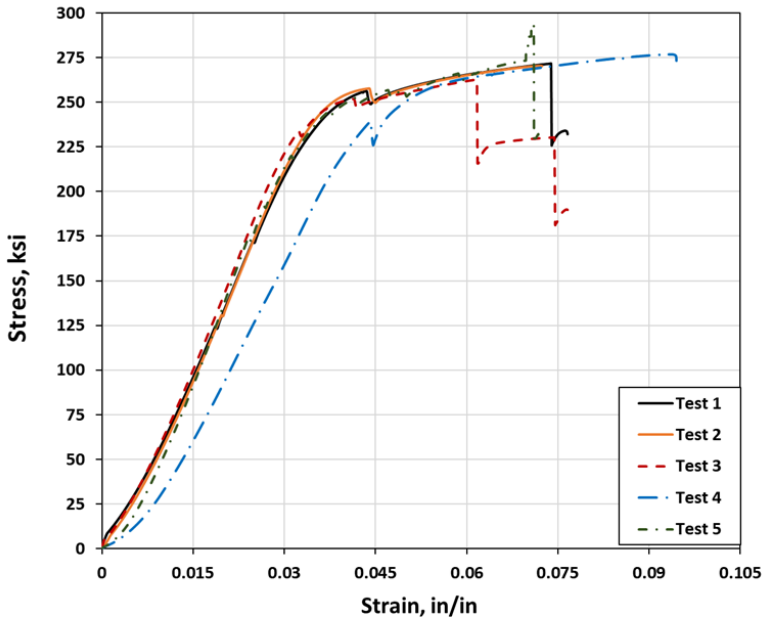

Figure D-34. Stress-strain curve of tested specimens of prestressing strands

D.4 Tensile testing of strand splice

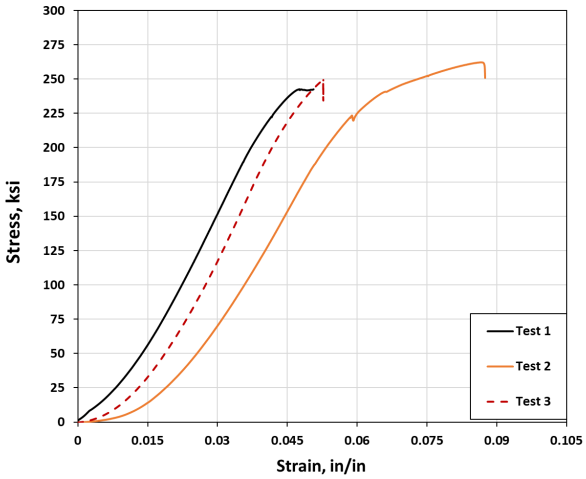

Figure D-35. Stress-strain curve of spliced strand uniaxial tensile test

(a) (b) (c)

Figure D-36. (a) MTS testing apparatus for uniaxial tensile test, (b) Failure of the strand near end wedge anchorage

D.5 Fiber-reinforced polymer

(a) (b)

Figure D-37. Uniaxial testing of the FRP composite, (a) FRP specimen under uniaxial tension, (b) FRP specimen exhibiting longitudinal splitting failure after tensile testing

Appendix E. Experimental Lateral Static Loading

E.1 Estimate of the out-of-plane flexural strength

In this analysis, the effect of torsion caused by the eccentric lateral force from the centroid of the girder is neglected for simplicity. The approach relies on the fundamental assumptions of Bernoulli beam theory, which includes:

- Strain Compatibility: The strain in the concrete and steel is compatible, meaning both materials deform together under loading.
- Plane Sections Remain Plane: Cross-sections of the beam remain planar before and after bending, a key assumption in linear elasticity.
- Equilibrium of Internal Forces: The internal forces within the section, including the compressive force in the concrete, the compressive force in the compression reinforcement, and the tensile force in the tension reinforcement, are in equilibrium with the applied external loads.

The analysis procedure follows a standard method for doubly reinforced concrete sections. Initially, a neutral axis depth (c) is assumed. The neutral axis separates the compression and tension zones of the section, and its position influences the distribution of stresses within the beam. The effective flange width of the compression flange is then estimated by dividing the area of the compression concrete by the total area of the compression flange (Equation E-1).

To ensure the equilibrium of internal forces, an iterative process is employed (Equation E-2). This involves adjusting the assumed neutral axis depth and recalculating the associated forces until the sum of the compressive forces (from the concrete and compression reinforcement) equals the tensile force from the tension reinforcement. This iterative approach ensures that the neutral axis depth accurately reflects the true stress state of the section under the applied loading. Once the neutral axis depth is determined, the flexural resistance of the section can be calculated. This step involves computing the moment contribution from the compressive forces (Equations E-4 and E-5), and the tensile force (Equation E-3) considering their lever arms relative to the neutral axis. By adopting this systematic procedure, the analysis captures the key structural behaviors of the doubly reinforced concrete section while adhering to the fundamental principles of mechanics and material compatibility as illustrated in Figure E-1. Table E-1 summarizes all the calculations and parameters required for the analysis.

$$b_{eff} = \frac{A_1}{\sum_n A} b = \frac{C-3.63}{C} x\ h$$

Equation E-4

$$T = C_s + C_c$$

Equation E-5

$$T = A_{ps} f_{pu}$$

Equation E-6

$$C_s = A'_{ps} f_{pu}$$

Equation E-7

$$C_c = 0.85 f'_c (A_c - A'_{ps})$$

Equation E-8

Table E-11. Parameters and values of the flexural resistance of the asymmetric section

Parameters	**Values**
Prestressing strands at the compression fiber, A_{ps}' (in^2)	0.612
Prestressing strands at the tension fiber, A_{ps}' (in^2)	1.224
Ultimate strength of strands, f_{pu} (ksi)	270
Unconfined compressive strength of concrete, f'_c (ksi)	5.00
Effective depth at the compression fiber, d (in)	3.50
Effective depth at the tension fiber, d (in)	11.00
Neutral axis depth, c (in)	4.625
Compression force in concrete block, Cc (kips)	184.60
Compression force in compression prestressing strands, C_s(kips)	145.70
Tension force in tension prestressing strands, Cs(kips)	330.48
Prestressing strand stress at ultimate, f_{ps} (ksi)	238.20
Tension prestressing strand strain, ε_t	0.0041
Flexural resistance, M_r (kips. ft)	230.7
Flexural failure force, P_r (kips)	21.21

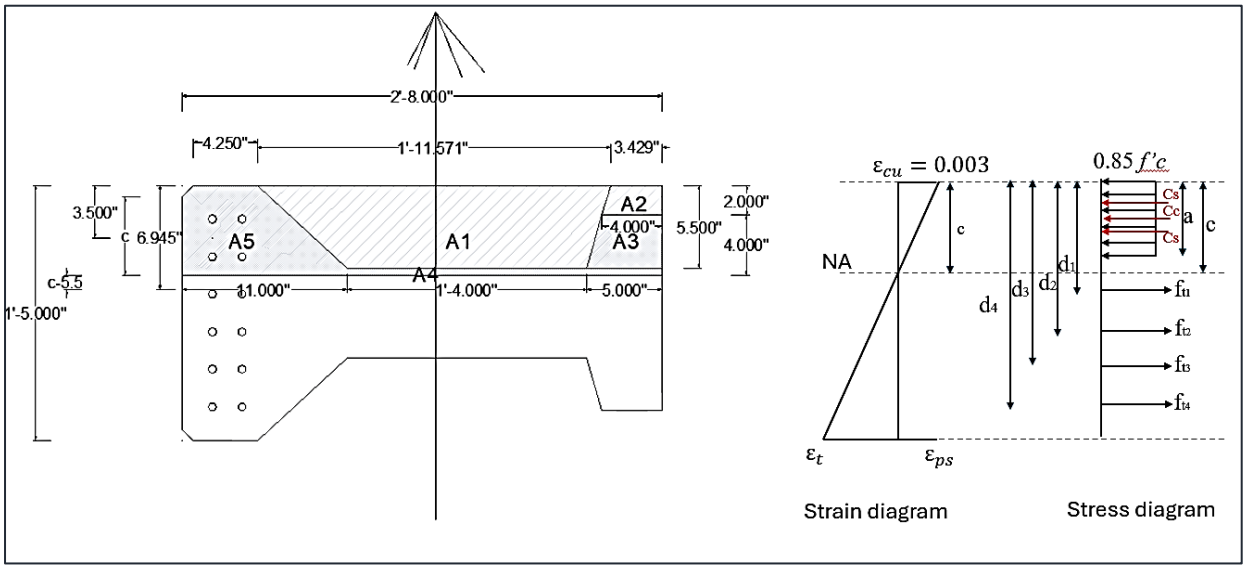

Figure E-38. Illustration of the strain compatibility of the flexural strength

E.2 Test setup and failure mode

Figure E-2. Test setup of Girder G09 of lateral static testing

(a)

(b)

(c)

Figure E-3. Damage photographs of Girder G09 from lateral static testing (a) Loading side, (b) Back side of loading, (c) Back side after unloading

Appendix F. Residual Flexural Strength and Load Rating

F.1 Experimental testing of residual flexural strength

F.1.1 Girder G02

(a)

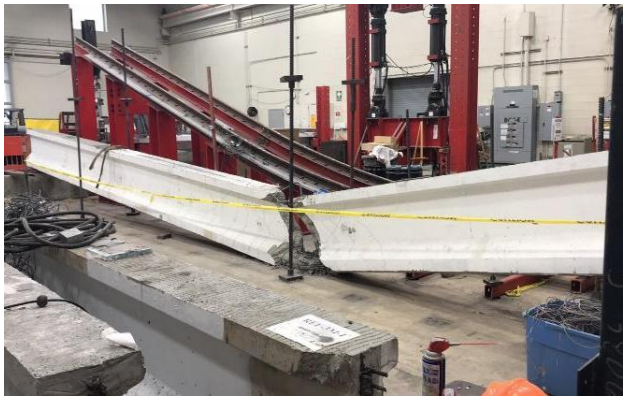

(b)

(c)

Figure F-3. (a) Deflection of the girder during testing, (b) Failure of girder (c) Close up to the strands at failure

F.1.2 Girder G14

(a)

(b)

Figure F-4. (a) Cracking of the girder during testing, (b) Failure of the girder

F.1.3 Girder G03

(a)

(b)

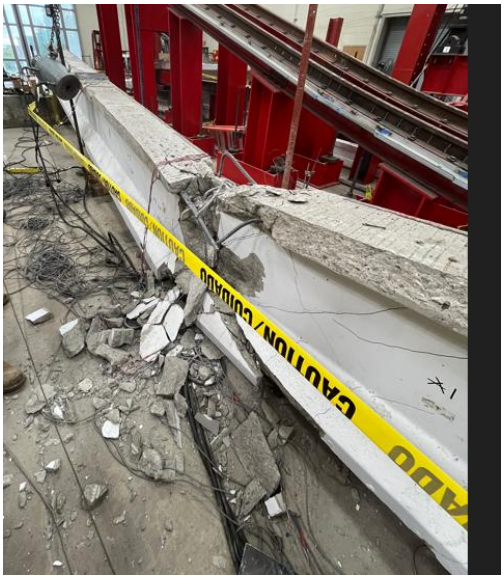

(c)

Figure F-5. Photographs of the girder 25% residual strength (a) Cutting the strands, (b) Flexural vertical cracking during testing, (c) Failure of the girder

F.1.4 Girder G04

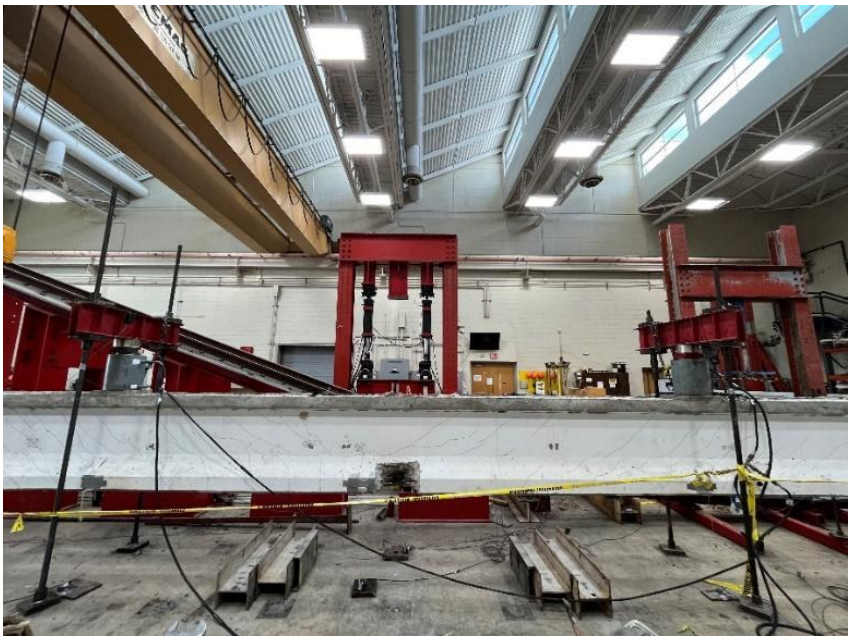

(a)

(b)

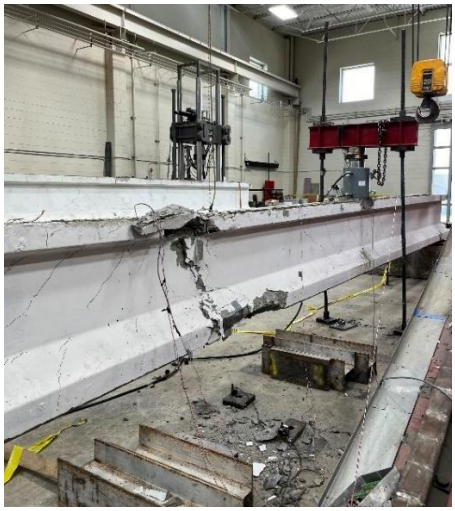

(c)

Figure F-6. Residual strength 50% flexural twelve strands (a) Deflection during testing, (b) Severe cracking just before failure, (c) Crushing of the top flange at failure

F.2 Calculation of the hypothetical bridge

Calculation of the control girder and the damaged girder flexural capacities are done in accordance with *AASHTO LRFD Bridge Specifications 9th.*

Interior effective flange width calculation of the bridge (AASHTO LRFD 4.6.2.6.1):

Effective width is the least of

= 0.25 * effective span length = 0.25 * (0.75 * 43.5 ft * 12") = 97.87 inches

= 12 * average slab thickness + the greater of the web thickness = 12*6" + 6" = 78"

= 12 * average slab thickness +0.5 * width of the girder's top flange = 12*6+ 0.5 * 13" = 78.5"

= Average spacing of adjacent girders = 7.5 ft * 12 = 90"

Final effective width of interior girder = 78 inch = 6 ft and 6 inches

Exterior girder effective flange width (AASHTO LRFD 4.6.2.6.1):

The effective flange width of the exterior girder is half of the adjacent girder's effective width + the least of the following

= 1/8 * effective span length = 1/8 * 0.75*43.5*12 = 48.9"

= 6 * average slab thickness + the greater of the web thickness = 6*6" + 6" = 42"

= 6* average slab thickness +0.25 * width of the girder's top flange = 6*6+ 0.25 * 13" = 39.25"

= the width of the overhang = 2.0ft *12" = 24"

= $b_{\text{effective interior}}$ / 2 + least of (48.9, 42, 39.25, 24") =78/2 + 24 = 63" = 5 ft 3 inches

Final effective width of exterior girder = 78 inch = 5 ft and 3 inches

Prestress losses AASHTO LRFD 5.9.5.1:

Prestressing strands shall be Grade 270 uncoated, low relaxation, seven-wire strands in accordance with AASHTO M 203 with the following design properties.

Ultimate tensile strength, f_{pu} = 270 ksi

Yield strength, $f_{py} = 0.9 f_{pu}$ = 243 ksi

Maximum allowed force per strand, $f_{pbt} A_{ps}$ = 30.98 kips (1/2-inch strands)

1/2-inch strand: diameter, d_{ps} = 0.5 in. and area, A_{ps} = 0.153 in.^{2}

Modulus of elasticity, E_p = 28,500 ksi

$$E_{Ci} = 57000\sqrt{f_c'} = 57000\sqrt{10240} = 3823676\ Psi = 5767\ ksi$$

Maximum allowed stress prior to transfer, f_{pbt} = 0.75f_{pu} = 202.5 ksi

270 ksi low-relaxation 12 strands, 0.5" dia

A_{ps} = 12 * 0.153 in^2 = 1.836 in^2

$$\Delta f_{pT} = \Delta f_{pES} + \Delta f_{pSR} + \Delta f_{pCR} + \Delta f_{pR2}$$

Equation F-9

Initial stress in tendons immediately prior to transfer (AASHTO LRFD 5.9.5.3)

$f_{p+}\Delta f_{pES} = 0.75 f_{pu}$

= 0.75 * 270 = 202.5 Ksi

<u>Elastic shortening losses 5.9.5.2.3a-1</u>

$$\Delta f_{pES} = \frac{A_{ps} f_{ps}\left(I_g + e_c^2 A_g\right) - e_c M_g A_g}{A_{ps}\left(I_g + e_c^2 A_g\right) + \frac{A_g I_g E_{ci}}{E_p}}$$

Equation F-10

M_g = Girder midspan moment due to member self-weight

Girder self-weight = 0.313 kips/ft

Mg = 0.313 * (44)^2 / 8 = 75.7 kips.ft = 909 Kips. in

e_c = average eccentricity of stands at mid-span = 14.08-3 = 11.0 in

$$\Delta f_{pES} = \frac{1.836\ in2 * 0.75 * 270\ ksi(33{,}974 + 11^2 * 310.9) - 11 * 909 * 310.9}{1.836\ (33{,}974 + 11^2 * 310.9) + \frac{310.9 * 33{,}974 * 5767 Ksi}{28500\ Ksi}} = 10.36\ Ksi$$

<u>Prestressing stress at transfer</u>

f_{pt} = stress immediately before transfer - Δf_{pES}

= 202.5 – 10.36 =192.1 Ksi

$P_t = N_{strands} A_{ps} f_{pt}$ = 12 * 0.153 * 192.1 = 352.7 Kips

Initial prestress loss = 1-192.1/202.5 = 5.1 %

Shrinkage losses (S5.9.5.4.2)

$$\Delta f_{pSER} = (117\text{-}1.03H) \text{ Mpa}$$

Equation F-11

Where H is the average annual ambient relative humidity % = 70%

Δf_{pSR} = (117-1.03*70) = 44.9 (MPa) = **6.51 Ksi**

Creep losses (S5.9.4.3-1)

$$\Delta f_{pCR} = 12\, f_{cgp} - 7.0\, \Delta f_{cdp} \text{ Mpa} \quad \geq 0$$

Equation F-12

Where f_{cgp} is the concrete stress at the c.g. of the prestressing strands at transfer. Δf_{cdp} is a change in concrete stress at c.g. of prestressing strands due to permanent loads. It depends on the effect of the weight of the deck, diaphragm, haunch and parapet.

$$f_{cgp} = \frac{\frac{A_{ps} f_{ps}}{A_g}\left(1 + \frac{e_c^2 A_g}{I_g}\right) - \frac{e_c M_g}{I_g}}{1 + \frac{A_{ps}}{A_g}\left(\frac{E_c}{E_p}\right)\left(1 + \frac{e_c^2 A_g}{I_g}\right)}$$

Equation F-13

$$f_{cgp} = \frac{\frac{1.836 * 0.75 * 270}{310.9}\left(1 + \frac{11^2 * 310.9}{33974}\right) - \frac{11 * 909}{33974}}{1 + \frac{1.836}{310.9}\left(\frac{5767}{28500}\right)\left(1 + \frac{11^2 * 310.9}{33974}\right)} = 2.48\, Ksi$$

$$\Delta f_{cdp} = [(M_{dia} + M_{slab})\, e\,] / I_g + [(M_{parpet} + M_{wearing}) * (y_{b,\,NC} - PS_{cg}) / I_C$$

Equation F-14

Δf_{pCR} = 12*1.56 *6.89 Ksi/MPa - 7.0 *0.15*1.56 *6.89 Ksi/MPa = 117 Mpa = 17 Ksi

Relaxation losses (S5.9.5.4.4c) for stress-relieved strands

$$\Delta f_{pR2} = 138 - 0.4\, \Delta f_{pES} - 0.2\, (\Delta f_{pSR} + \Delta f_{pCR}) \text{ (MPa)}$$

Equation F-15

= 138 - 0.4 * 23.05*6.89 – 0.2*(6.51*6.89 +17*6.89) = 42 Mpa = 6.1 Ksi

Relaxation losses (S5.9.5.4.4c) for low-relaxation strands (30% of the stress-relieved)

Δf_{pR2}= 0.3 * 6.1 = 1.83 Ksi

Total loss after transfer

$$\Delta f_{pT} = \Delta f_{pES} + \Delta f_{pSR} + \Delta f_{pCR} + \Delta f_{pR2}$$

Equation F-16

= 10.36 + 6.89 + 17 + 1.83 = 36 Ksi

Final effective prestress after all losses

Max f_{pe} = 0.8 f_{py} = 0.8 * 0.9 *270 =194.4 Ksi

Min f_{pe} = 0.55 f_{py} = 0.5 * 0.9 *270 =121.5 Ksi

f_{pe} = 0.75 f_{pu} - Δf_{pT} = 0.75*270 – 36 = 166.4 Ksi < Max f_{pe} (194.4 Ksi) Ok

> Min f_{py} (121.5 Ksi) Ok

Effective force in prestressing P_{pf} = A_p f_{pe} = 0.153 in2 * 166.4 = 25.5 kips = **26 kips**

F.3 The flexural strength of the non-composite section (without effective flange width)

No. of strands = 12

A_{ps} = 12*0.153 = 1.836 in^2

$f_{ps} = f_{pu}\left(1 - k(c/d_p)\right)$

For low-relaxation strands, k= 0.28

d_p = h – distance from the bottom of the beam to location pf Ps steel force

d_p = 32” – 3” = 29”

Flanged girders are considered T-section behavior regarding flexural stresses (5.7.3.1.1-3)

For compressive strength of 10.24 ksi of girder concrete,

β_1 = 0.85-0.05(f’c-4 ksi) = 0.85 – 0.05*(10.24-4) = 0.53 < 0.65, = 0.65

$$c = \frac{A_{ps}f_{pu} + A_s f_y - A_s^{'} f_y^{'} - 0.85\beta_1 f^{'}(b - b_w)h_f}{0.85 f^{'}\beta_1 b + kA_{ps}f_{pu}/d_p}$$

Equation F-17

Assume a rectangular section and check if c exceeds the structural slab thickness 5”, with 2 # 4 mild steel at the tension zone.

$$c = \frac{A_{ps}f_{pu} - A_s^{'}f_y^{'}}{0.85f'c\ b\beta_1 + kA_{ps}f_{pu}/d_p}$$

Equation F-18

$neutral\ axis\ depth\ (c) = \frac{1.836*270-2*0.2*60}{0.85*10.24*0.65*13+0.28*1.836*\frac{270}{29}}$ =6.02 " > 5

The assumption of rectangular behavior is not valid; the neutral axis is not within the top flange depth. Calculate neutral axis depth c as T-section (5.7.3.1.1-3)

$$c = \frac{A_{ps}f_{pu} + A_sf_y - A_s^{'}f_y^{'} - 0.85f^{'}(b - b_w)h_f}{0.85fc^{'}\beta_1 b_w + kA_{ps}f_{pu}/d_p}$$

Equation F-19

$= \frac{1.836*270+0-2*0.2*60-0.85*10.24(13-6)*5}{0.85*10.24*0.65*6+0.28*1.836*\frac{270}{29}} =$ 4.31 inch

(Stress block height) a = β_1 c = 0.65 * 4.31= 2.8 inch

f_{ps} = 270 (1 – 0.28(4.31/29)) = 258.7 Ksi

$$M_n = A_{ps}f_{ps}\left(d_p - \frac{a}{2}\right) + 0.85f^{'}{}_c\left(b_f - b_w\right) * h_f\left(\frac{a}{2} - \frac{h_f}{2}\right)$$

Equation F-20

$= 1.836 * 258.7\left(29 - \frac{2.8}{2}\right) + 0.85 * 10.24\ (13 - 6) * 5\left(\frac{2.8}{2} - \frac{5}{2}\right)$ = 12774 kips.in = **<u>1064 kips. ft</u>**

Check maximum reinforcement. LRFD 5.7.2.1

$$\frac{\varepsilon_c}{c} = \left(\frac{\varepsilon_t}{d_p - c}\right)$$

Equation F-21

$= \frac{0.003}{4.31} = \left(\frac{\varepsilon_t}{29-4.31}\right),\ \varepsilon_t =$ 0.017>ε_{TC}) = 0.005

All prestressed RFT: $\varepsilon_{ty} = 0.002$ (steel yield strain)

$$\varepsilon_{TC\ (Tension-controlled)} = 0.002 + 0.003 = 0.005$$

Flexural failure and section is tension controlled

ϕ = 1 for flexural

Factored flexural resistance (M_r) = ϕ M_n = 1 x 1081 = ***<u>1064 kips. ft</u>***

F.4 The control girder with effective flange width

No. of strands = 12

A_{ps} = 12*0.153 = 1.836 in2

$f_{ps} = f_{pu}\,(1 - k(c/d_p))$

For low-relaxation strands, k= 0.28

d_p = h – distance from the bottom of the beam to location pf Ps steel force (PS c.g.)

d_p = 32+6 – 3" = 35"

For 6 ksi of deck slab concrete, β_1 = 0.85-0.05(f'c-4 ksi) = 0.85 – 0.05*(6-4) = 0.75 > 0.65

$neutral\ axis\ depth\ (c) = \frac{1.836*270 - 2*0.199*in2*60}{0.85*6*0.75*69+0.28*1.836*\frac{270}{35}} = \frac{471.84}{267.9}$= 1.76 "< 5

a = β_1 c = 0.75 * 1.76= 1.32 inch

f_{ps} = 270 (1 – 0.28(1.32/35)) = 267.1 Ksi

$M_n = A_{ps} f_{ps} \left(d_p - \frac{a}{2}\right)$

$= 1.836 * 267.1 \left(35 - \frac{1.32}{2}\right)$ = 16840 kips. In = **1403 kips. Ft**

Check maximum reinforcement. LRFD 5.7.2.1

$$\frac{\varepsilon_c}{c} = \left(\frac{\varepsilon_t}{d_p - c}\right) = \frac{0.003}{1.93} = \left(\frac{\varepsilon_t}{35 - 1.92}\right), \qquad \varepsilon_t = 0.051 > \varepsilon_{TC} 0.005$$

Design flexural resistance (M_r) = ϕ M_n = 1 x 1399 = **1399 kips. ft**

The contribution of the deck slab to the flexural strength = 1399 – 1081 = 318 kips.ft

F.5 Dead and live load calculations

Dead structural and non-structural components (DC)

Girder self-weight

= (310.9/144) * 145 lb./ft^3 = 313 lb./ft = **0.313 kip/ft**

Deck slab weight

Slab width = overhang width +0.5 * girder spacing

= 2 ft + 0.5 *7.5’ = 5.75 ft

W_{slab} = t_{slab} *W_{slab} * 0.145 K/ft^3 = (6”/12 in) x5.75x 0.145kips/ft^3 = **0.41 kip/ft**

Assume no concrete diaphragm located in the girder span.

Parapet (Barrier) weight

Parapet unit weight = 625.1 in2

The parapet weight may be distributed equally to all girders in cross section:

$W_{parapet}$ = 625.1 (Parpet cross-section) *(1/12^2) * 0.16 kips/ft^3 = 0.69 kips/ft

= 0.69/ 5 girders = 0.139 kips/ft per girder for one parapet

= 0.139 kips/ft *2 Parapet = **0.277 kips/ft per one girder**

Total DC = 0.313 + 0.41 + 0.27 = 0.993 kips/ft

M_{DC} = 0.993 * 43.8^2 / 8 = 238.1 kips. ft at mid-span

Wearing weight (DC)

$W_{wearing}$ = (1.5 in/12) x 0.14 kips/ft^3 x 32.25 ft = 0.56 k/ft

= 0.56 / 5 = **0.11-kips/ft/ girder**

Moment due to DW = wl^2/8 = 0.11 * 43.8^2/ 8 = 26.37 kips. ft at mid-span

Live load analysis

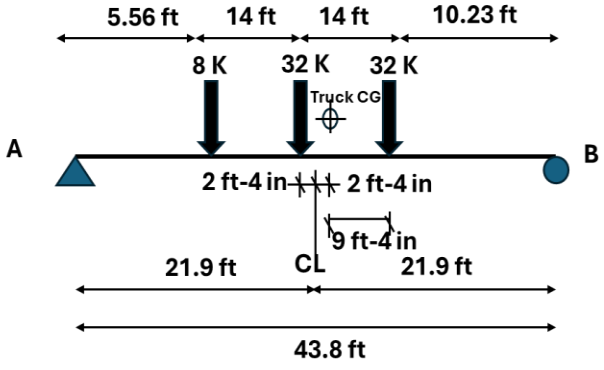

Figure F-7. HS20 vehicle loads on the mid-span of the girder

The HL-93 is a theoretical live load model employed in the design of bridges and other structures. It integrates three primary components:

- Design Truck: Based on the HS20 load configuration, featuring a total vehicle weight of 72 kips.
- Design Tandem: Consists of two axles arranged in series, connected to a single truck, with a total weight of 50 kips.
- Design Lane Load**:** A uniformly distributed load of 0.64 klf is applied along the longitudinal direction.

The HL-93 model is designed to account for the worst-case loading scenario. The term "HL-93" stands for "highway load," reflecting its development year, 1993.

This model is utilized to determine the live vehicular loads acting on bridges and roadways. By adopting the HL-93 model, bridge owners can ensure that a bridge meets satisfactory load ratings for all AASHTO-designated legal loads.

Near-Midspan Maximum Moment Location (x = L/2 - 2.33’ = 19.567’):

$R_{A =}$ 8 K * (14+14+10.23)/43.8 + 32 K * (10.23+14)/43.8 + 32K * (10.23)/43.8

= 8 K * 0.87 + 32 K * 0.553 +32 K * 0.233= 32.11 Kips

$M_{near\ mid\text{-}span,\ truck}$ = 32.11 * (21.9-2.33) – 8 *(14)= 516.4 kips. ft

$M_{near\ mid\text{-}span\ ,\ lane}$ = 0.64/2 [(43.8)(19.566) – (19.566)^2]= 151.73 kft

$M_{LL\ near\ midspan}$ = 516.4 * 1.33 + 151.73= 838.5 k.ft

Midspan Maximum Moment (x = L/2 = 21.9’ with the 8kips @ 5.567’, 32kips @ 19.567’ and 33.567’ from R A end):

R_A = 8 K * (14+14+7.9)/43.8 + 32 K * (14+7.9)/43.8 + 32 K * (7.9)/43.8 = 28.33 kips

Mtruck @ midspan = 28.33 * (21.9) - 8 * (14) = 508.42 kips-ft

Mlane @ midspan = 0.64 * 43.8^2 / 8 = 153.48 kips-ft

MLL @ midspan = 508.42 * 1.33 + 153.48 = 829.68 kips-ft

Live load distribution factor = 0.647

$M_{LL\ midspan}$ = 0.647 x 829.68 = 536.8 kft

Moment design for midspan at service loads

Mu = 1.25 DC + 1.5 DW + 1.75 LL (1+ IM)

= 1.25 x 254 + 1.5 x26.49 + 1.75 x 536.8 = 1296.6 k.ft < M_n (1399 kips. Ft)

F.6 Load rating of exterior beams

ɣ factors for both inventory and operating levels

Inventory; $ɣ_{DC}$ = 1.25, $ɣ_{DW}$ = 1.50, $ɣ_{LL+IM}$ = 1.75

Operating; $ɣ_{DC}$ = 1.25, $ɣ_{DW}$ = 1.50, $ɣ_{LL+IM}$ = 1.35

P = 0

F.6.1 Design load rating

F.6.1.1 Inventory level

DC = 238 kips. ft

DW= 26.37 kips. ft

Strength limit states, C = $\emptyset c \emptyset s \emptyset Rn$ (6A.4.2.1-2)

Rn=Nominal member resistance (as inspected)

P = Permanent loads other than dead loads

$$RF = \frac{\varphi C - ɣ_{DC} DC - ɣ_{DW} DW \pm ɣ_P P}{ɣ_{LL}(LL + IM)}$$

$$RF = \frac{1399 - 1.25*238 - 1.5*26.37 \pm 0}{1.75*(536.8)} = \frac{1061.9}{939.4} = 1.13 > 1$$

F.6.1.2 Operating

RF = 1.13 *(1.75 / 1.35) = 1.46> 1 OK

F.7 Load rating and repair/replacement decision

F.7.1 Residual flexural strength and load rating calculations

For cases involving prestressing losses, the following steps are typically taken:

- Residual strength estimation: Calculate the remaining flexural capacity of the girder, accounting for reduced prestressing forces.

- Load rating analysis: Perform a load rating to determine if the girder can still support the intended service loads safely.

F.7.2 Case scenarios

The control case involves the design of a prototype overpass bridge per AASHTO LRFD Bridge Design Specifications. The bridge design features five MoDOT Type II prestressed concrete girders, each incorporating 12 prestressing strands (Figure F-6). The bridge has a total width of 32.25 feet, with girders spaced 7.5 feet apart (center-to-center). The overall length of the bridge is 46 feet, classifying it as a short-span structure. Key details of the designed bridge, including its dimensions, materials, and other relevant parameters, are summarized in Table F-1.

To assess the structural capacity and performance of the bridge, load rating calculations were performed in accordance with the Manual for Bridge Evaluation (MBE). These calculations provided an accurate evaluation of the bridge's ability to withstand vehicular loads under both inventory and operating conditions.

Table F-1. Properties of the selected bridge and girder

Description	**MoDOT type II**
Bridge	Single span with cast-in-place concrete deck
Design span (ft)	46
Deck depth (inch)	7
Number of strands	12
Prestressing strand type	270 MPa Low relaxation 0.5 inch
Girder compressive strength (ksi)	10.5
Deck compressive strength (ksi)	6
Deck reinforcement	#4 Top mat / #5 Bottom mat
Strand effective stress after losses (ksi)	170
Nominal flexural strength (kips. ft)	1441

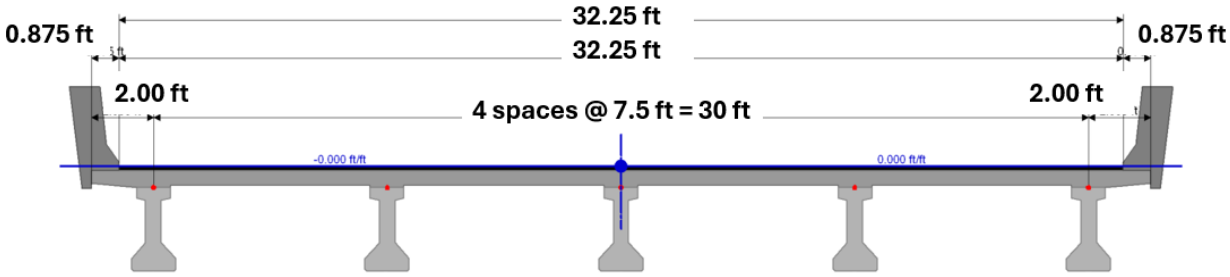

(a)

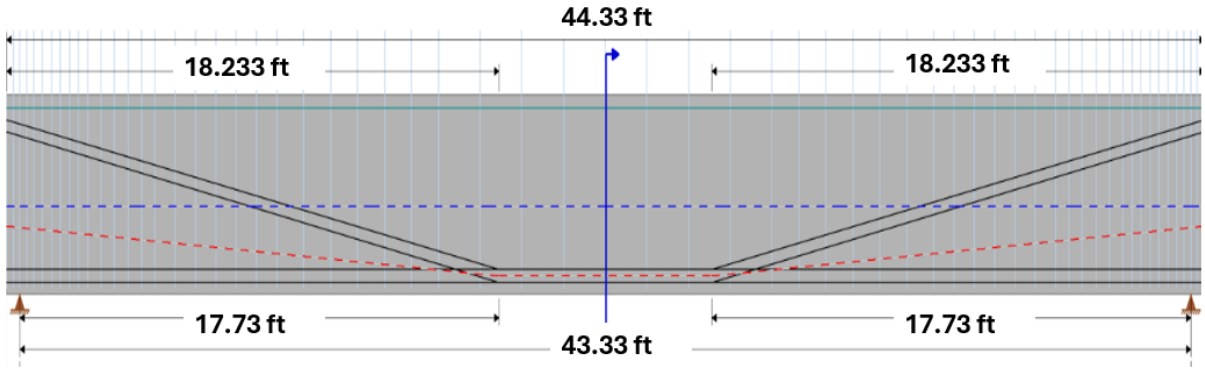

(b)

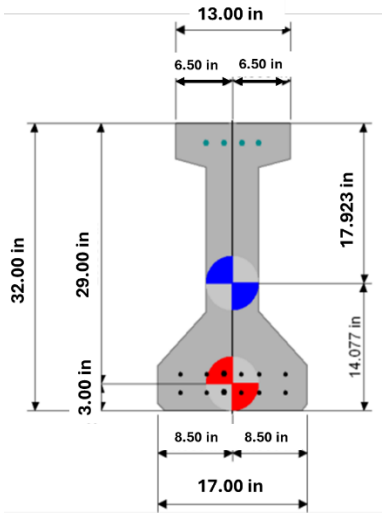

(c)

Figure F-8. Bridge layout, (a) Girder reinforcement, (b) Typical girder cross section at mid-span, and (c) Cross-section of girder

F.7.3 Load rating and safety evaluation for bridge structures

Ensuring public safety is the primary responsibility of structural engineers. The National Bridge Inspection Standards (NBIS) Subpart C stipulates that every bridge must be evaluated for its load-carrying capacity in accordance with the AASHTO Manual Bridge Evaluation (MBE). This

evaluation process employs the Load and Resistance Factor Rating (LRFR) method to assess whether a bridge can safely carry expected loads. In the context of bridge girder adequacy, two load ratings are considered: design load rating and legal load rating**.**

F.7.3.1 Design load rating

The design load rating provides an initial assessment of a bridge's capacity to carry loads and is divided into two levels. Equation F-1 can be used to calculate these levels.

1. Inventory Level**:** This represents the maximum load a bridge can carry over its lifespan without causing significant deterioration or damage. It is typically considered the "safe" load level for repetitive use such as HL-20 and HL-93 (Table F-2).
2. Operating Level**:** This is the maximum load a bridge can bear for short durations without immediate failure, though it may cause accelerated deterioration over time.

F.7.3.2 Legal load Rating

Legal load ratings assess a bridge's ability to handle state-regulated vehicles that are authorized for normal travel on public roads. These trucks, such as Type 3, 3S3, 3-3, and emergency vehicles (EV2, EV3), are used to verify a bridge's capacity under typical highway conditions (Table F-2). These legal loads are essential for evaluating whether a bridge can accommodate routine legal vehicles without exceeding safe limits.

F.7.4 Importance of load rating in bridge safety

The load rating serves as the basis for making decisions on whether a bridge can safely accommodate traffic. It helps engineers determine the need for load postings (limiting vehicle weights), bridge strengthening**,** or decisions related to overweight vehicle permits.

The design load rating evaluates the bridge for typical loads, using design vehicles such as the HL-93 and HS-20, which are specified in AASHTO LRFD guidelines (Table F-2). This assessment is done at the strength limit state, taking into account the bridge's ability to handle maximum design loads. The rating includes both inventory and operating levels, and if both levels exceed unity (RF > 1), the bridge is considered safe for all inventory**,** operating**,** and legal loads.

F.7.5 Legal load rating process

If a bridge fails to meet the operating level rating (RF < 1), a legal load rating assessment is conducted. This second-level assessment evaluates the bridge's ability to carry specific legal loads defined by state regulations, including standard trucks (such as Type 3**,** 3S2, 3-3) and emergency vehicles which include heavier trucks using equation F-1. The legal load rating helps determine whether the bridge requires any modifications, such as load posting or strengthening to ensure its continued safe use. This assessment is critical for ensuring the bridge's capacity to handle not only normal traffic but also specialized and emergency vehicles.

$$RF = \frac{C - \gamma_{DC}DC - \gamma_{DW}DW \pm \gamma_P P}{\gamma_{LL}(LL + IM)}$$

Equation F-1

$$C = \phi_c \phi_s \phi R_n$$

Equation F-2

Where RF is the load rating C is the factored capacity; γ_{DC} is the load factor for structural components; γ_{DW} is the load factor for wearing surfaces and utilities; γ_{LL} is the evaluation live load factor; γ_p is the load factor for permanent loads; DC is dead load effect due to structural components; DW is dead load due to wearing surfaces and utilities; LL is live load effect; IM id the dynamic load allowance.

F.7.6 Impact of prestressing strand loss on load rating

In scenarios where a bridge has sustained damage, such as the loss of prestressing strands due to an impact, the load rating may need to be recalculated. The reduction in prestressing strands directly impacts the flexural strength of the bridge girder, particularly at the mid-span, where the maximum bending moment occurs. For this analytical analysis, load ratings were evaluated for different levels of prestress loss, ranging from 17% to 50%. These scenarios simulate realistic conditions, such as collision damage where the strands were removed from one side of the girder.

F.7.7 Load rating results

Figure F-7 illustrates the relationship between the load rating factor and the prestressing strand loss for the prototype bridge, as discussed in section F.7.5. As previously mentioned, the first level of evaluation according to the Load and Resistance Factor Rating (LRFR) involves the design load rating, which consists of two levels: Inventory and Operating.

At approximately 15% prestressing strand loss, the Inventory level maintains a load rating factor greater than 1, which also satisfies all other levels. From 17% to 25% strand loss, load ratings for inventory, operating, legal-truck NRL, and legal-truck Type EV3 cross below RF equals 1.0. It is worth noting that standard AASHTO legal loads, truck types 3, 3S2, and 3-3, still meet the requirement with RF greater than 1. However, heavy trucks from emergency vehicle categories, such as NRL and EV3, fail to meet the necessary rating. At this point, the bridge may require either restricting access to emergency vehicles (i.e., posting a load limit) or retrofitting to restore its strength.

In conclusion, the load rating assessment reveals that girders experiencing flexural strength reductions between 15% and 25% necessitate retrofitting to restore their flexural capacity. The conservative threshold of 15% prioritizes safety and ensures the structural integrity of the bridge, while the upper threshold of 25% emphasizes the urgency of repairs to prevent severe structural inadequacy. These thresholds serve as the basis for retrofitting protocols aimed at maintaining the bridge's operational and legal load-carrying capacity. Table F-3 summarizes the load ratings for varying damage severity levels.

Table F-2. MBE standard truck weights for load rating

Truck Type	Inventory Level (kips)	Operating Level (kips)	Legal Level (kips)
HS-20	72	72	NA
HL-93 Truck	72	72	NA
H-20 Tandem	50	50	NA
Type 3	46	46	46
Type 3S2	82	82	82
Type 3-3	60	60	60
Emergency vehicle (EV2)	57.5	57.5	57.5
Emergency vehicle (EV3)	86	86	86
Notional Rating Load (NRL)	80	80	80

Table F-3. Load rating values for different flexural strength loss

Strand loss	M_r (kips. ft)		Rating Factor (RF)							
					(AASHTO Legal loads)					
	AASHTO	PCI	I	O	Type 3	Type 3S2	Type 3-3	NRL	EV2	EV3
Control-0%	1403	1445	1.18	1.53	2.05	2.21	2.46	1.34	2.13	1.41
17%	1182	1214	0.93	1.2	1.64	1.77	1.97	1.07	1.72	1.13
25%	1060	1094	0.80	1.03	1.42	1.53	1.70	0.92	1.48	0.97
33%	956	981	0.68	0.88	1.21	1.31	1.46	0.79	1.27	0.84
41%	835	860	0.53	0.69	0.98	1.06	1.18	0.64	1.04	0.68
50%	721	739	0.36	0.47	0.69	0.75	0.84	0.45	0.79	0.51

Inventory: I; Operation: O

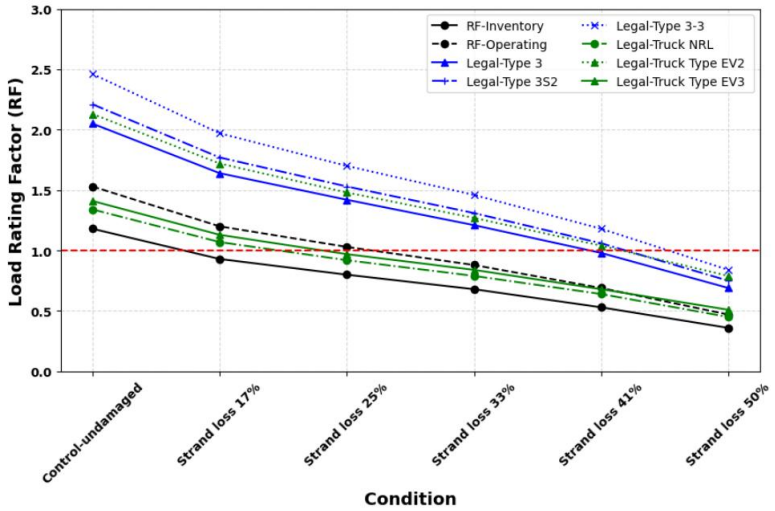

Figure F-7. Load rating relationship with flexural strength loss

Appendix G. Experimental Testing of Repaired Girders

G.1 Girder G10

Figure G-9. Splicing and formwork of spliced girder 17% (Girder G10)

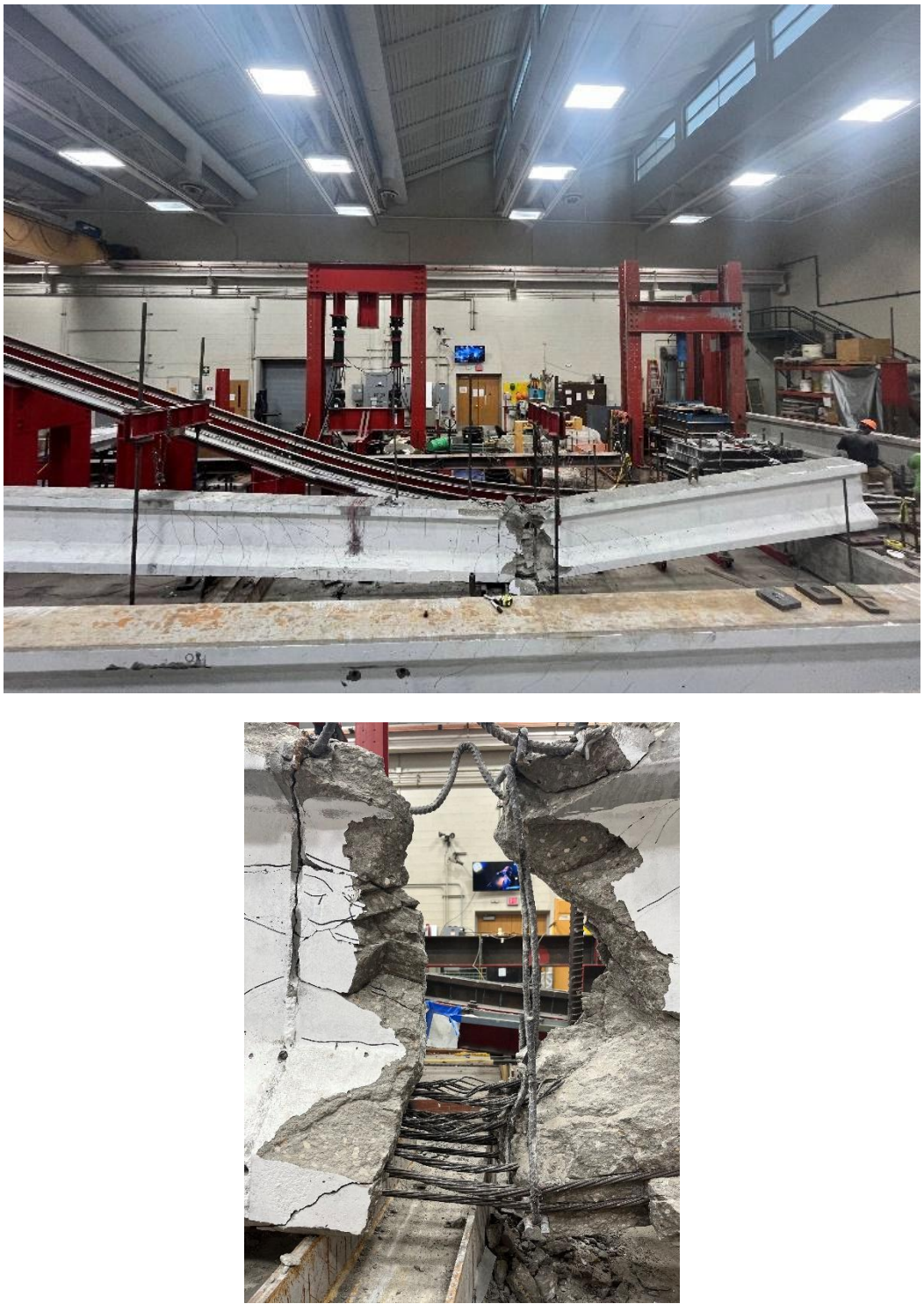

Figure G-10. Testing and failure of Girder G10

G.2 Girder G11

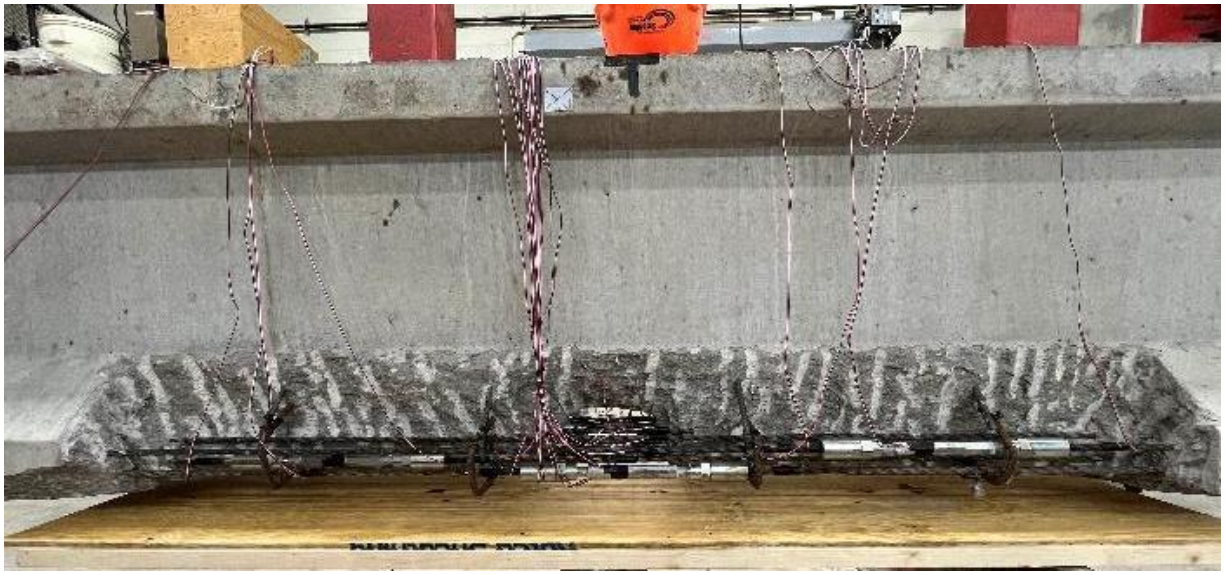

Figure G-11. Splicing and formwork of the spliced 25% (Girder G11)

G.3 Girder G05

Figure G-12. Strands severed from the second impact of Girder G05 before splicing

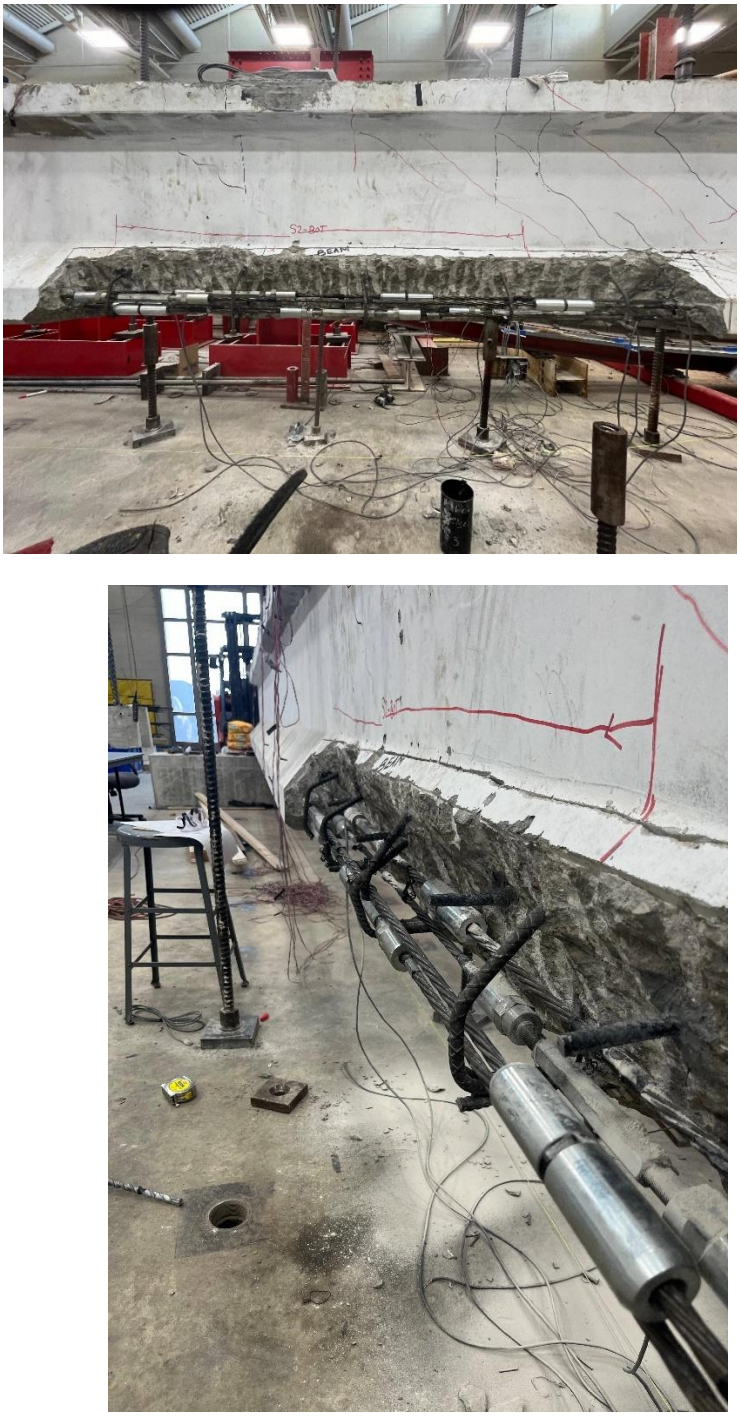

Figure G-13. Splicing the strands and planting shear dowels to connect the patched area

Figure G-14. Formwork and casting grout of the patched area

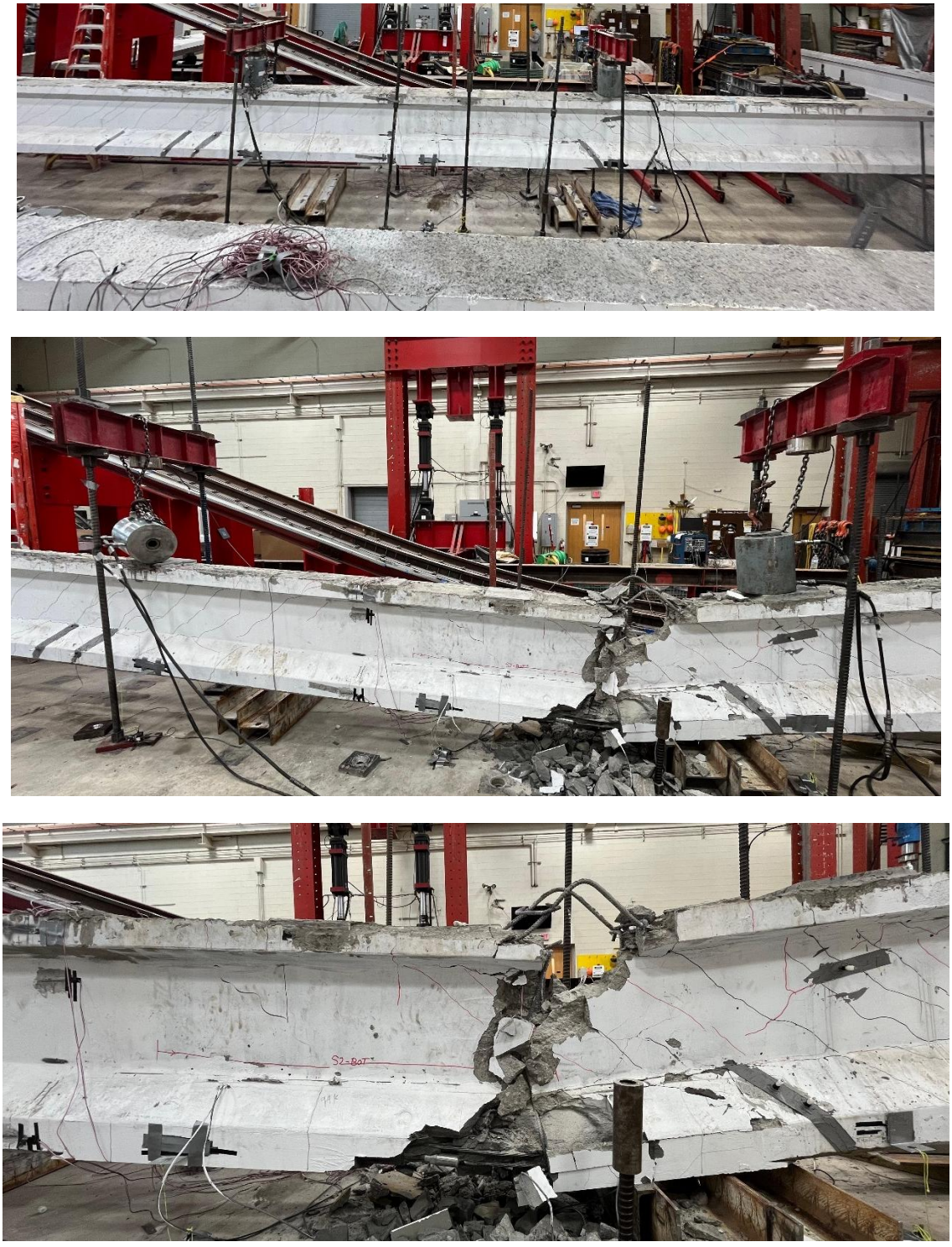

Figure G-15. Testing and failure of the spliced girder

G.4 Girder G12

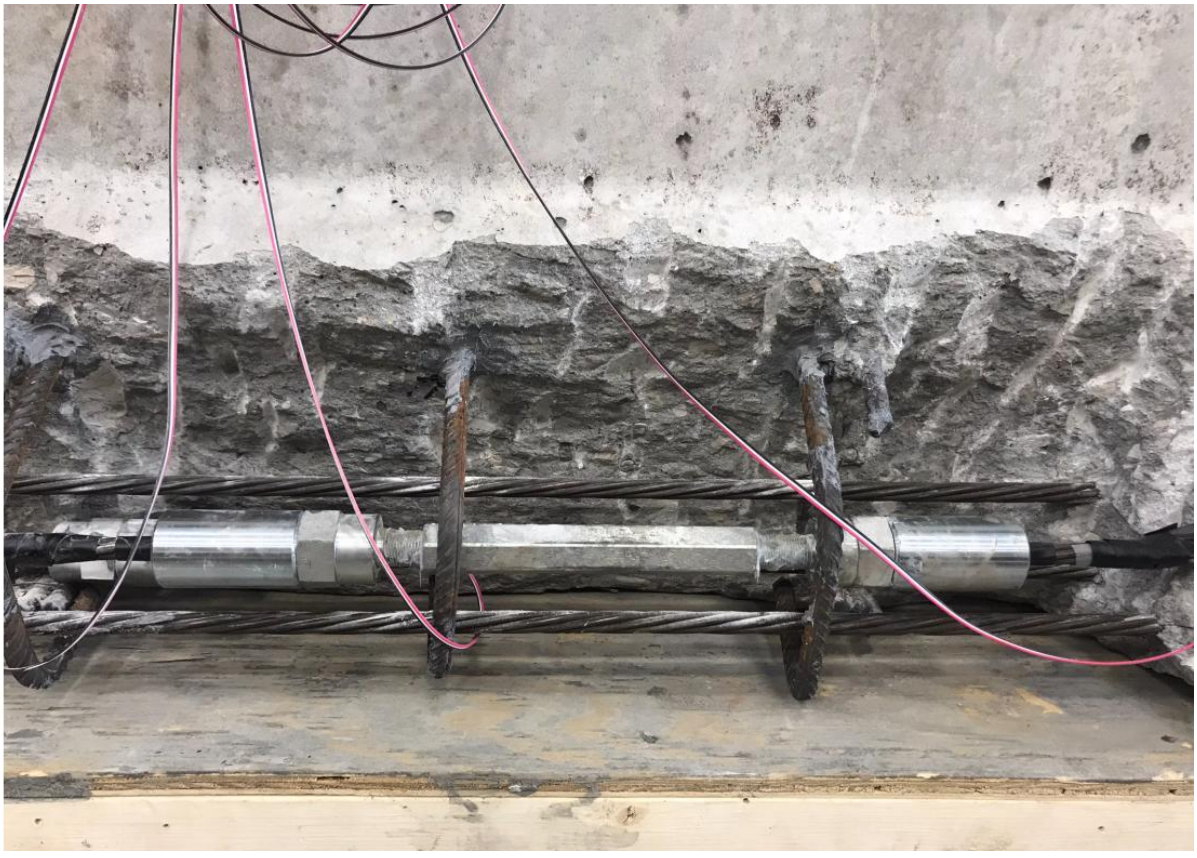

Figure G-16. Installation of the splices and rectilinear rebar for confining

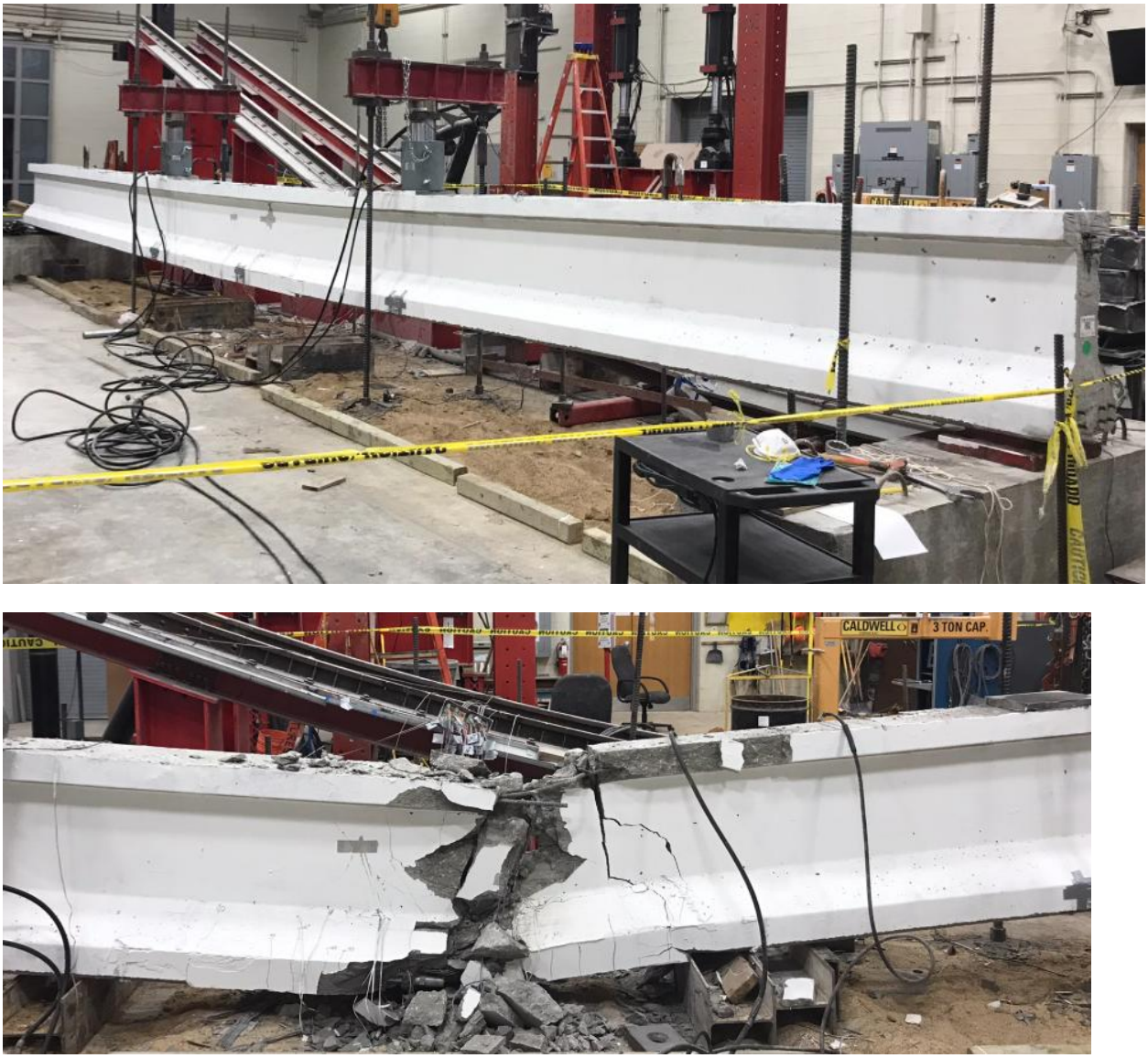

Figure G-17. Testing and failure of the girder

G.5 Girder G07

Figure G-18. Wet layup system of CFRP preparation of the repaired girder

Figure G-19. Girder deflection during testing

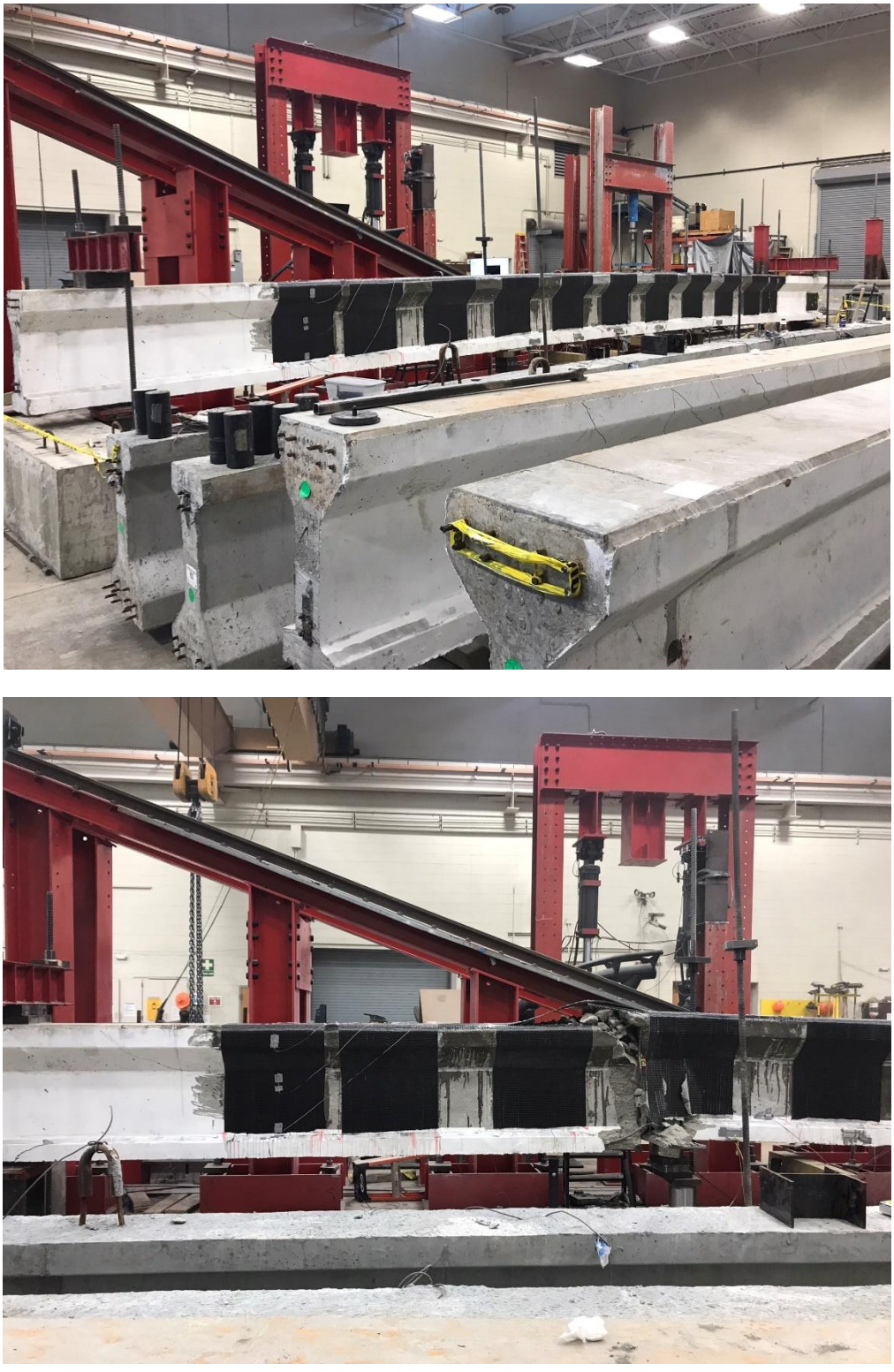

Figure G-20. Girder deflection and failure

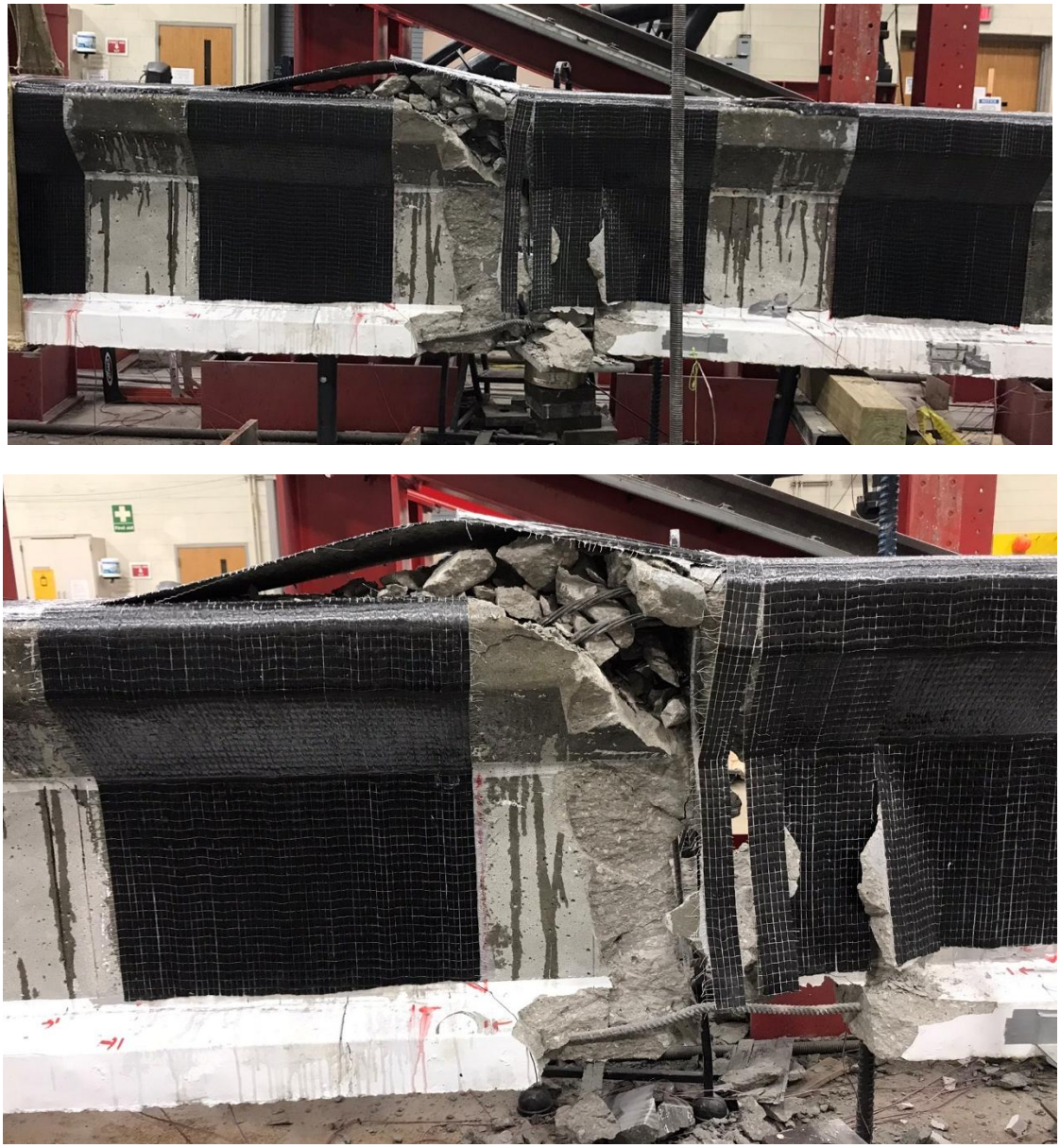

Figure G-21. Rupture of CFRP longitudinal plies

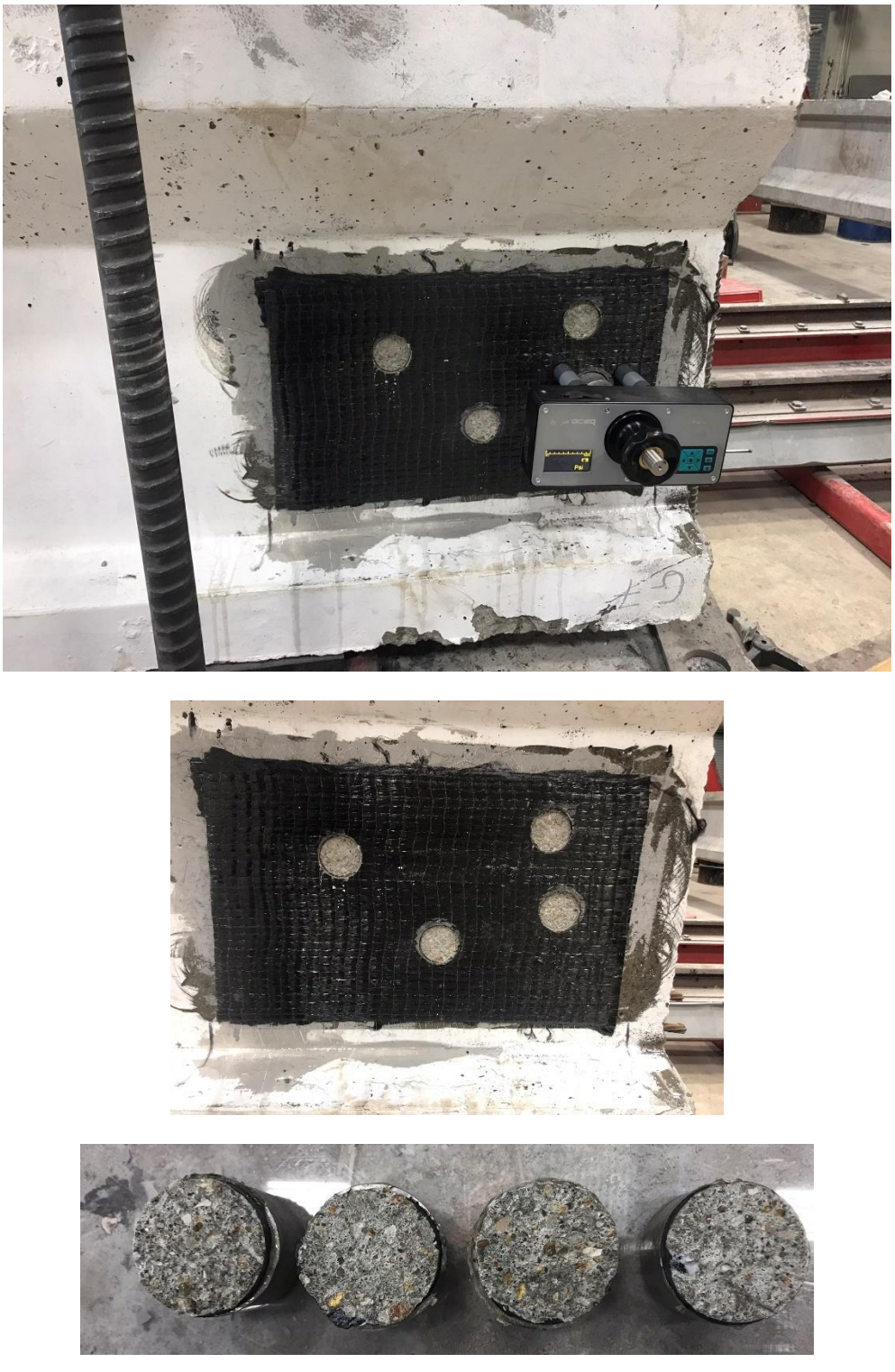

Figure G-22. Pull-off test

G.6 Girder G08

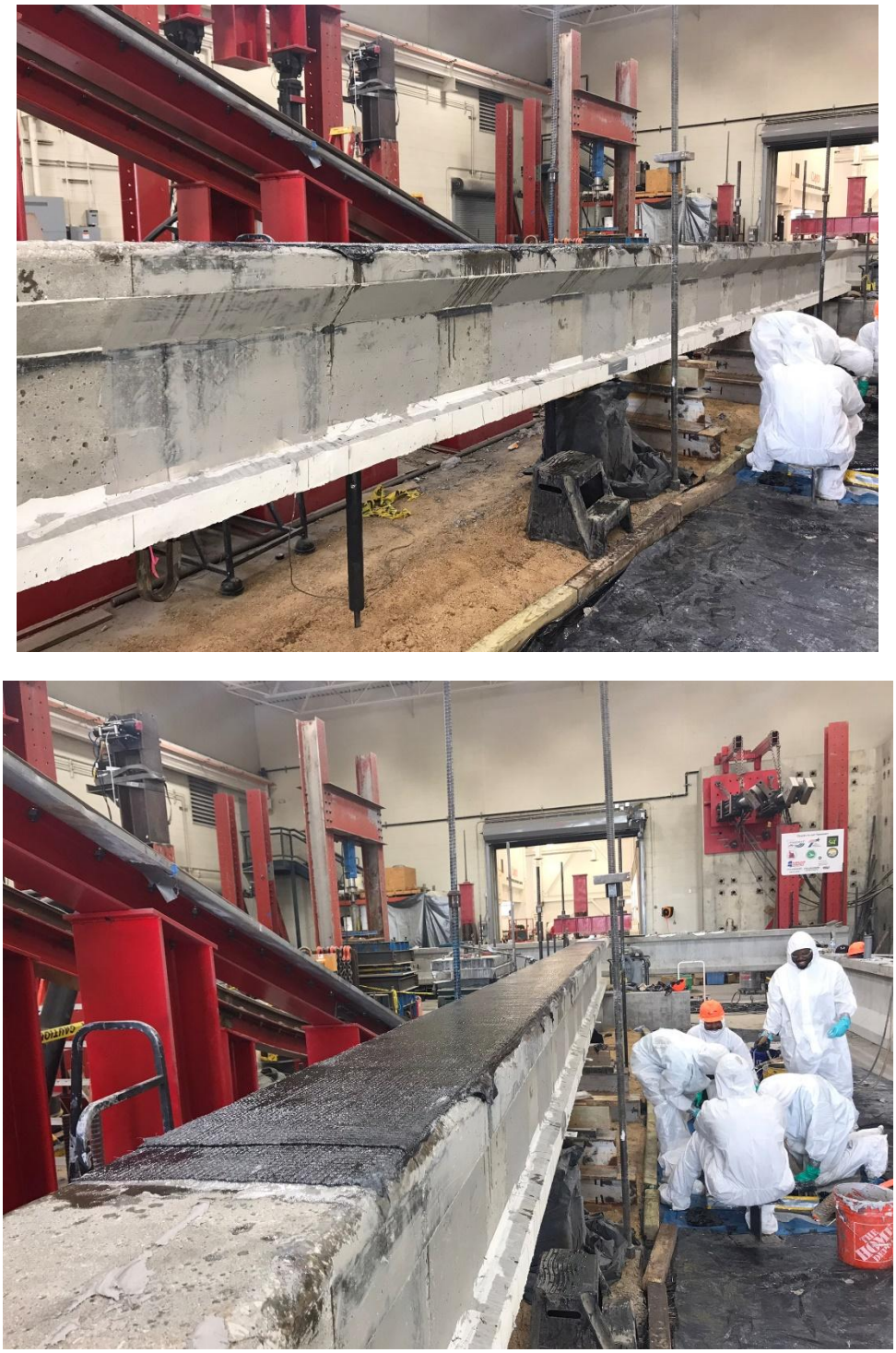

Figure G-23. CFRP wet layup system application to the girder

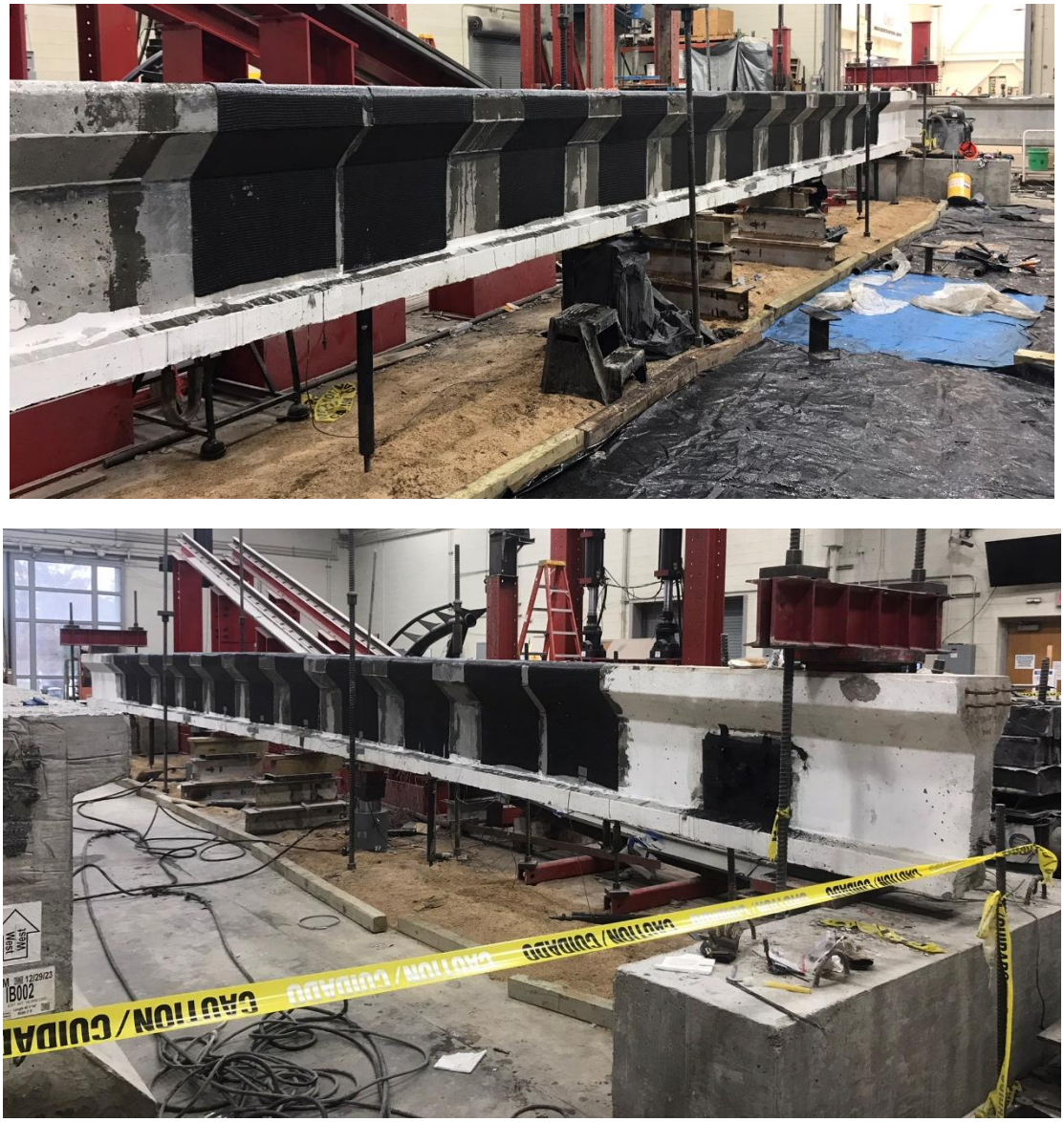

Figure G-24. Testing the repaired girder 33%

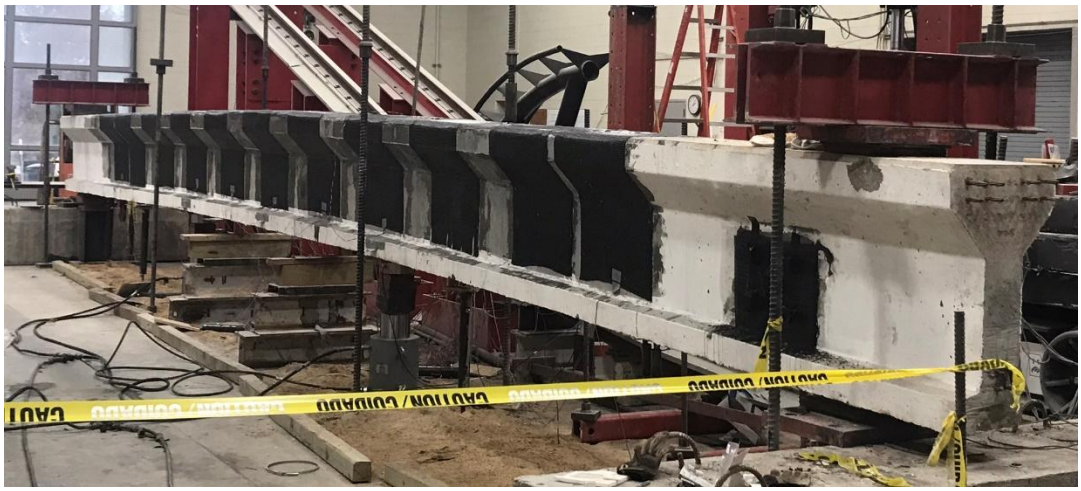

Figure G-25. Testing and failure of the repaired girder

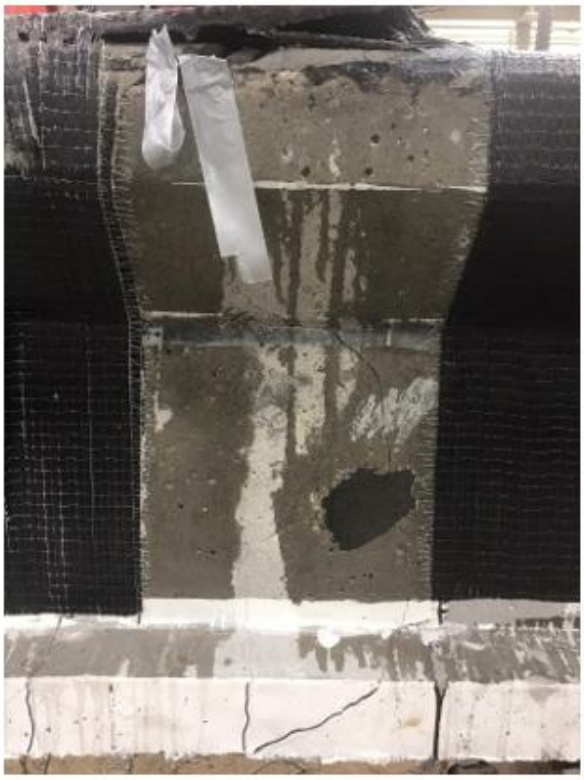

Figure G-26. Failure of the CFRP U-wraps

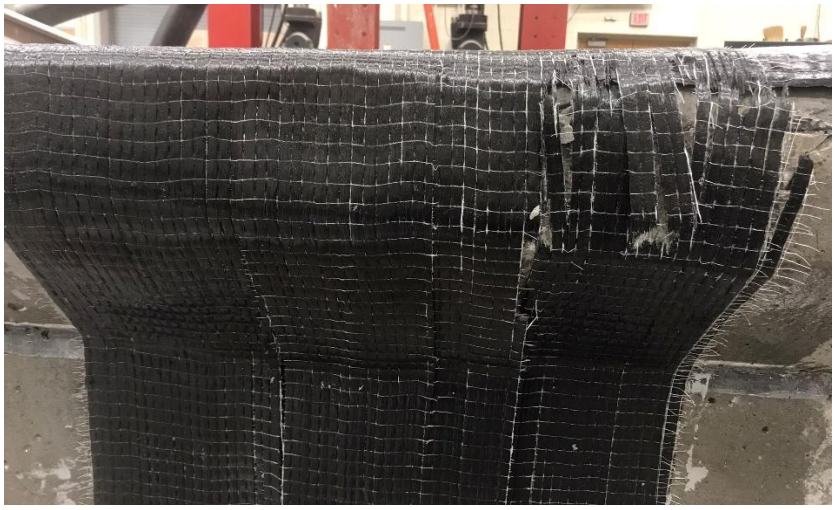

Figure G-27. Rupture of CFRP

Figure G-28. Pull-off test

G.7 CFRP repair design of Girder G08

G.7.1 Flexural strength of undamaged girder

M_n (undamaged) = 1081 kips. ft

G.7.2 Residual strength of damaged Girder G02

f_c' = 11.2 ksi

Residual number of prestressing strands for Girder G02 = 8

A_{ps} = 8 x 0.153 =1.224 in2

d_p = distance from extreme compression fiber to the centroid of the prestressing tendons (in.)

d_p = 32 – 3" = 29"

$\beta_1 = 0.85 - 0.05(f_c^{'} - 4\ ksi)$ AASHTO LRFD 5.7.2.2

$\beta_1 = 0.85 - 0.05(11.2 - 4\ ksi) = 0.49 \geq 0.65$

$$c = \frac{A_{ps}f_{pu} + A_s f_y - A_s^{'} f_y^{'} - 0.85\beta_1 f^{'}(b - b_w)h_f}{0.85 f^{'}\beta_1 b + kA_{ps}f_{pu}/d_p}$$ AASHTO LRFD 5.7.3.1.2-3

Assume a rectangular section and check if c exceeds the structural slab thickness 5

$$c = \frac{A_{ps}f_{pu} - A_s^{'} f_y^{'}}{0.85(fc^{'}, slab)\ b + kA_{ps}f_{pu}/d_p}$$ AASHTO LRFD 5.7.3.1.2-4

4# 5mild steel rebars for the deck slab reinforcement

c = 3.95 inch < 5 inch

The assumption of rectangular behavior is valid, the neutral axis is within the top flange depth

Compression stress block height, a = β_1 c = 0.65 * 3.95 = 2.56inch

$$f_{ps} = f_{pu}\left(1 - k\frac{c}{d_p}\right)$$ AASHTO LRFD 5.7.3.1.1-1

For low-relaxation strands, k= 0.28

$$f_{ps} = 270\left(1 - 0.28\frac{3.95}{29}\right) = 259.7\ ksi$$ AASHTO LRFD 5.7.3.1.1-1

$M_n = A_{ps} f_{ps} \left(d_p - \frac{a}{2}\right) = 1.225 * 259.7(29 - 2.56/2)$ = 8818 kips. in = 734 kips. ft

G.7.3 Design of CFRP composite system

Assume retrofitting is conducted by applying three CFRP plies 16 in. wide strip of CFRP at the girder soffit in accordance with ACI 440.2R-17.

Calculate the FRP system design material properties

$f_{fu} = C_E f_{fu}^* = 0.95 \times 670 = 636.5$ ksi ACI 440-9.4a

$\varepsilon_{fu} = C_E \varepsilon_{fu} = 0.95 \times 1.9/100 = 0.0181$ in/in ACI 440-9.4b

Properties of the concrete

$\beta_1 = 1.05 - 0.05 * 11200 /1000 = 0.49$

$Ec = (57000\sqrt{11200\ psi})/1000 = 6032\ ksi$

$A_{ps} = 8 \times 0.153\ in^2 = 1.224\ in^2$

$A_f = 3$ ply $\times 0.027 \times 15$ in $= 1.215\ in^2$

$y_t = 32 - 14.08 = 17.92$ in.

$I_g = 33{,}974\ in^4$

$$r = \sqrt{\frac{33974}{310.9}} = 10.45\ in.$$

Determine the design strain of the FRP system.

$$\varepsilon_{fd} = 0.083\sqrt{\frac{f_c'}{nE_f t_f}} \leq 0.9\varepsilon_{fu}(in. - lb)$$ ACI 440-10.1.1

$$\varepsilon_{fd} = 0.083\sqrt{\frac{11.2\ ksi}{3 * 37000\ ksi * 0.0324}} = 0.0046 \text{ in.-lb}$$

Determine the state of strain of the girder soffit at the time of FRP installation.

$$\varepsilon_{bi} = \frac{-P_e}{E_c A_{cg}}\left(1 + \frac{e y_b}{r^2}\right) + \frac{M_D y_b}{E_c I_g}$$

Where M_D is the total load on the girder before CFRP application was 435 kips. ft.

Estimate the depth to the neutral axis.

A value of neutral axis depth (c) needs to be assumed, a reasonable starting value is 0.2h, and can be adjusted using iteration based on internal forces equilibrium.

c = 0.2h = 0.2x32 = 6.4 in

Determine the effective level of FRP strain reinforcement

$$\varepsilon_{fe} = 0.003 * \frac{(d_f - c)}{(c)} - \varepsilon_{bi} = 0.0118\ in/in \leq \varepsilon_{fd}$$ ACI 440-10.2.5

Calculate the strain in the existing stress in prestressing strands.

$$\varepsilon_{pnet} = (\varepsilon_{fe} + \varepsilon_{bi})\frac{(d_p - c)}{(d_f - c)} = 0.11\ in/in$$ ACI 440-10.2.10a

Calculate the equivalent stress level in the prestressing steel and CFRP plies.

$$f_{ps} = 270 - \frac{0.04}{\varepsilon_{ps} - 0.007}\ , when\ \varepsilon_{ps} > 0.0086$$

fps = 269.9ksi

$f_{fe} = E_f * \varepsilon_{fe}$ = 37000* 0.0046 = 170.2 ksi ACI 440-10.2.1.10b

Calculate the neutral axis depth

$$\alpha_1 f_c^{'} \beta_1 bc = A_s f_s + A_f f_e$$ ACI 440-10.2.10c

$$c = \frac{1.224 * 269.9 + 1.506 * 170}{0.837 * 11.2 * 0.73 * 13} = 6.59\ in$$

After several iterations, c = 8.69 in

Calculate the flexural strength corresponding to the prestressing steel and FRP.

$$M_n = A_s f_s \left(d - \frac{\beta_1 c}{2}\right) + \Psi_f A_f f_{fe}(d_f - \frac{\beta_1 c}{2})$$

ACI 440-10.2.10d

M_{np} = 1.224 * 261.37 (29-0.73*8.687/2)* 1/12 = 712.4 kips ft

M_{nf} = 1.506 * 170 * (32-0.73*4.98/2) *1/12 = 622.6 kips. Ft

φ = 0.85

M_n = 0.9 (712.4 + 0.85*622.6) = 1117.5 kips.ft > 1081 kips ft

The retrofit design is successful

$$M_n = 1.224x261.4\left(29 - \frac{0.73x8.69}{2}\right) + 0.85x1.51x170(32 - \frac{0.73x8.69}{2})$$

=1117.5 kips.ft > 1081 kips.ft

G.8 Girder G13

Figure G-29. Strand repair and grout patching

Figure G-30. Hybrid girder testing after CFRP installation

Figure G-31. Rupture and delamination of CFRP

Figure G-32. Failure of the girder

Figure G-33. Pull-off test

Appendix H. Failure Analysis of Prestressed Girder Bridges under Over-Height Truck Impact: Numerical Study

H.1 Introduction

The continuous growth of urban areas in recent years has led to a steady increase in urban traffic congestion, resulting in an unprecedented number of overpasses in developing metropolitan areas (X. Xu et al. 2022). Despite the implementation of measures such as height clearance signs, accidents involving over-height trucks or trucks carrying equipment that exceeds the vertical clearance limit continue to occur, causing significant damage to overpasses during their service life.

The United States Department of Transportation (USDOT) conducted a national survey to assess the problem of vehicle-bridge collisions across all 50 states (A K Agrawal, Xu, and Chen 2013; Anil K Agrawal et al. 2011). Each state's Department of Transportation (DOT) was invited to evaluate the severity of the issue. As shown in Figure H-1, the responses indicate that the majority of states perceive bridge strikes as a significant and pressing concern. Over-height trucks were identified as the primary cause of most of these accidents (A K Agrawal, Xu, and Chen 2013; Anil K Agrawal et al. 2011; Cao, Agrawal, and El-Tawil 2021). According to the survey findings, steel and prestressed girder bridges were the most frequently impacted by over-height trucks. A study by (Harries 2009) further highlighted that collisions involving over-height vehicles are the most common cause of damage to prestressed girder bridges.

The increasing height of freight trucks has raised concerns about the growing risk of bridge collisions (Aly and Hoffmann 2022). A notable incident occurred in March 2005, involving the Sgt. Bluff Bridge in Iowa (Harries et al. 2012). In this case, an over-height truck collided with the bridge, causing severe structural damage, including extensive strand cutting and concrete spalling. The destruction was so extensive that the bridge required complete replacement. Beyond the financial implications, this collision also led to traffic congestion, detours, and a temporary bridge closure, illustrating the broad impact of such incidents.

More recently, in 2023, a truck carrying an excavator that exceeded the allowable height clearance collided with the I-10 overpass at I-49 in Lafayette, Louisiana. According to the Louisiana DOT, "three of the eight girders are catastrophically damaged and are no longer viable." This accident also caused falling debris that damaged nearby vehicles and resulted in minor injuries, further demonstrating the far-reaching effects of over-height truck collisions on infrastructure and public safety.

The recurring issue of over-height vehicle collisions with bridges raises several questions among researchers, particularly regarding the performance of prestressed concrete bridges under impact forces. Addressing these questions requires an understanding of the key parameters influencing bridge responses in such scenarios to identify contributors to structural integrity or weaknesses.

Large-scale experimental testing of bridges under vehicle impact is challenging due to the associated costs and complexities, resulting in limited available experimental data. Furthermore, studying individual girders often overlooks the composite effects of the bridge system, which significantly influence its behavior under impact loads. Despite the unpredictable nature of over-height vehicle collisions, computational models have proven effective in accurately simulating bridge-vehicle collision scenarios (Cao, Agrawal, and El-Tawil 2021).

This study examined the failure responses of three common types of bridge superstructures subjected to over-height truck impacts (Berton et al. 2017). Among steel superstructures, the steel box girder bridge was identified as the most resilient due to its ability to localize damage, enhancing structural safety and integrity. In contrast, reinforced concrete beams exhibited extensive damage, with collisions causing numerous cracks along the girder length in addition to localized damage at the impact zone, compromising the bridge's structural integrity. Another study by (L. J. Xu et al. 2012) identified extensive deformation and torsional damage as key factors influencing the risk of collisions, while localized damage was predominantly attributed to punching stresses.

Several scenarios of over-height vehicle impact on prestressed girder bridges were also investigated (Oppong, Saini, and Shafei 2021; Jiang and Chorzepa 2015). The results indicated that higher impact velocities and larger contact areas significantly increased impact forces (Oppong, Saini, and Shafei 2021; Jiang and Chorzepa 2015). Berton et al. (2017) (Saini and Shafei 2019) assessed factors contributing to bridge deck damage caused by over-height truck collisions and found that damage was primarily influenced by impactor mass, speed, beam stiffness, and contact area.

Few studies have explored the behavior of prestressed bridge girders under impact, leading to limited knowledge about the dynamic response of such bridges. To address this gap, this study conducted a comprehensive numerical analysis to investigate the response of prestressed girder bridges under impact loading. Key parameters such as impact speed, impactor mass, impact location, and the presence and type of intermediate diaphragms were systematically evaluated. The primary objective is to develop an in-depth understanding of the complex dynamic behavior associated with over-height truck impacts on prestressed girder bridges.

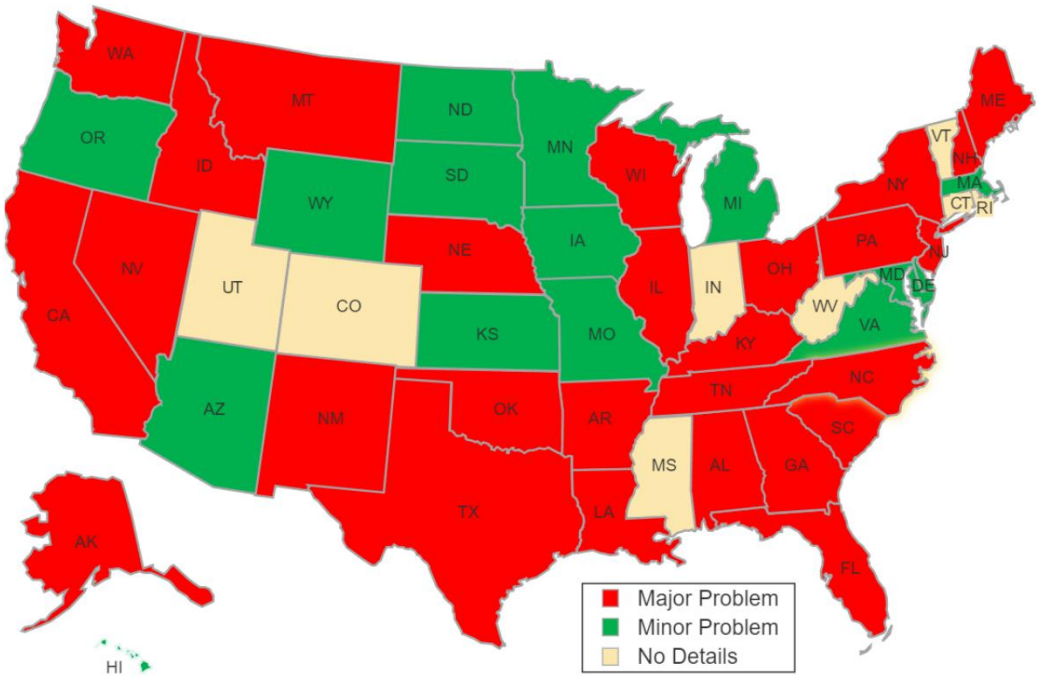

Figure H-34. The severity of the bridge-vehicle collision problem in the different states (A K Agrawal, Xu, and Chen 2013; Anil K Agrawal et al. 2011)

H.2 Finite element analysis

H.2.1 FE bridge model

A comprehensive finite element (FE) model of a large-scale prestressed girder bridge was developed using MoDOT Type II girders previously tested under impact loads. Explicit dynamic analysis was performed using LS-DYNA for all FE models.

The bridge consisted of three 46 ft (14 m) long prestressed concrete girders spaced 6 ft (1.8 m) apart. The dimensions and reinforcement details of the MoDOT Type II girders are shown in Figure H-35. The girders supported an 8 in. (200 mm) thick reinforced concrete deck, with reinforcement details shown in Figure H-36. To enhance structural stability, 8 in. (200 mm) thick reinforced concrete end diaphragms were placed at both ends of the prestressed girders.

The girders were supported by 18 in. (450 mm) thick concrete abutments. Two types of intermediate diaphragms were incorporated into the FE models: An 8 in. (200 mm) thick reinforced concrete diaphragm and a C15×33.9 steel-channel diaphragm, adapted from prior Iowa laboratory bridge testing (Klaiber et al. 1999; Abendroth et al. 2004; Abendroth, Klaiber, and Shafer 1991). The steel channel depth was approximately 50% of the prestressed girder depth and nearly 94% of the girder's web depth. Intermediate diaphragms were modeled at two locations: mid-span and third points of the bridge (Figure H-37). FE models for both types of diaphragms are shown in Figure H-38.

To improve computational efficiency, a rigid cylindrical impactor was used instead of a full vehicle model. The impactor had a diameter of 3.2 ft (1 m), a length of 3.9 ft (1.2 m), and was positioned 1 in. (25 mm) from the girder to ensure a controlled initial state. The impactor velocity was assigned using the *BOUNDARY PRESCRIBED RIGID MOTION keyword (Figure H-39). Although simplified, the rigid impactor model provides a conservative estimate of peak impact forces, assuming all energy is transferred to the girder, representing worst-case scenarios (Do, Pham, and Hao 2019; Gholipour and Billah 2022).

H.2.2 Key modeling elements:

SOLID elements: Represented concrete components, including girders, deck, abutments, end diaphragms, concrete intermediate diaphragms, and the rigid impactor.

- SHELL elements: Modeled the steel channel intermediate diaphragms.
- TRUSS elements: Represented deck reinforcement and girder stirrups.
- BEAM elements: Modeled longitudinal deformed bars and prestressing strands.

A maximum mesh size of 1 in. (25.4 mm) was maintained throughout the FE models. Shared nodes were used between concrete abutments, end diaphragms, girders, and the deck to ensure monolithic behavior. The Lagrange-In-Solid algorithm was employed to transfer stresses between prestressing strands and concrete. *AUTOMATIC SURFACE-TO-SURFACE contact with a friction coefficient of 0.30 was used to simulate interactions between the rigid impactor and the girders (Elshazli et al. 2024; 2025). The FE model of the bridge is shown in Figure H-40.

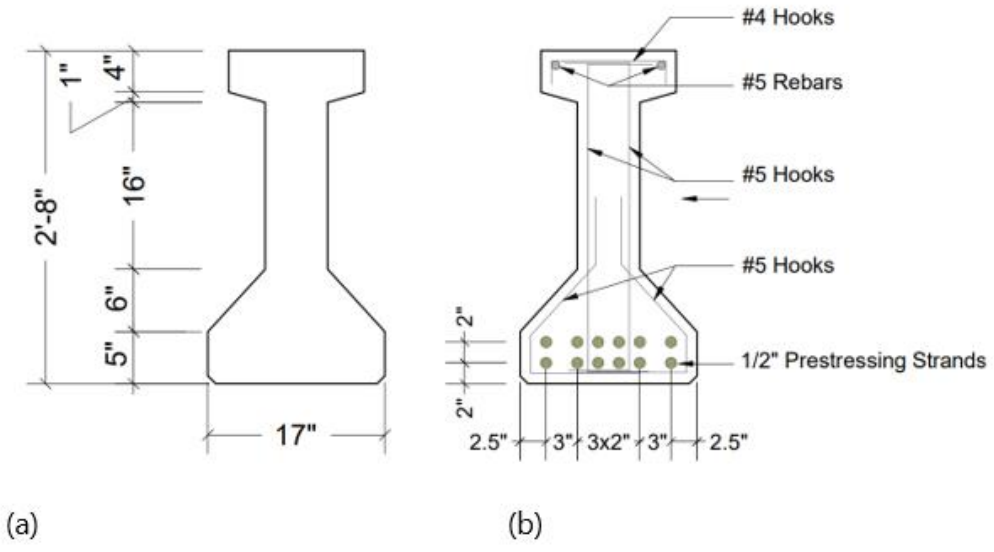

Figure H-35. MoDOT Type II girder details (a) Concrete Dimensions, (b) Reinforcement Details

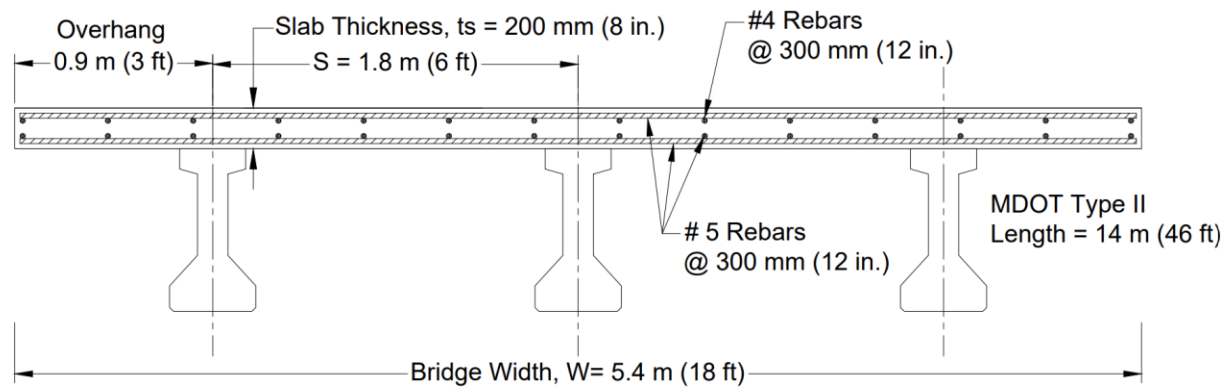

Figure H-36. Selected bridge cross-section view

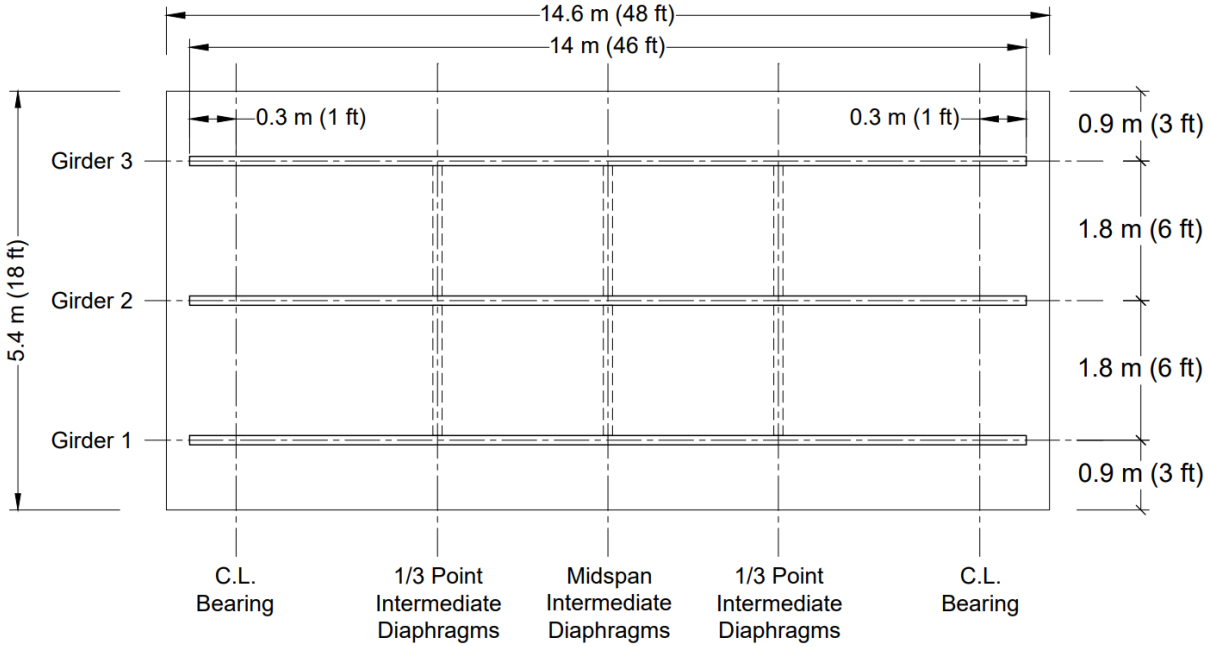

Figure H-37. Bridge layout and intermediate diaphragm's locations

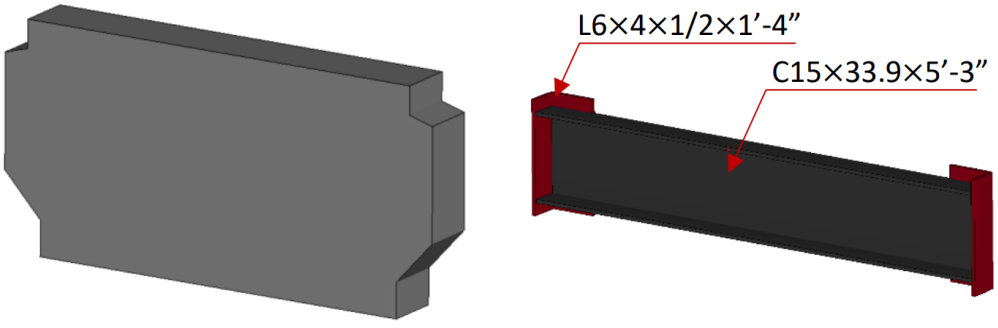

(a) Concrete intermediate diaphragm (b) Steel intermediate diaphragm

Figure H-38. FE intermediate diaphragm models

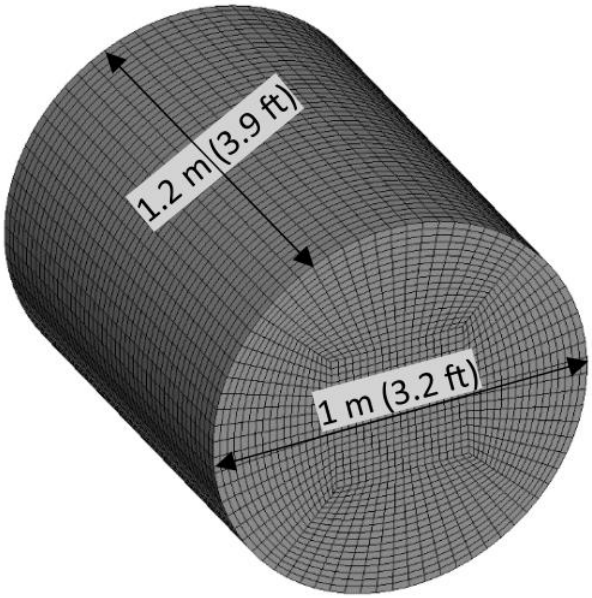

Figure H-39. FE rigid impactor dimensions

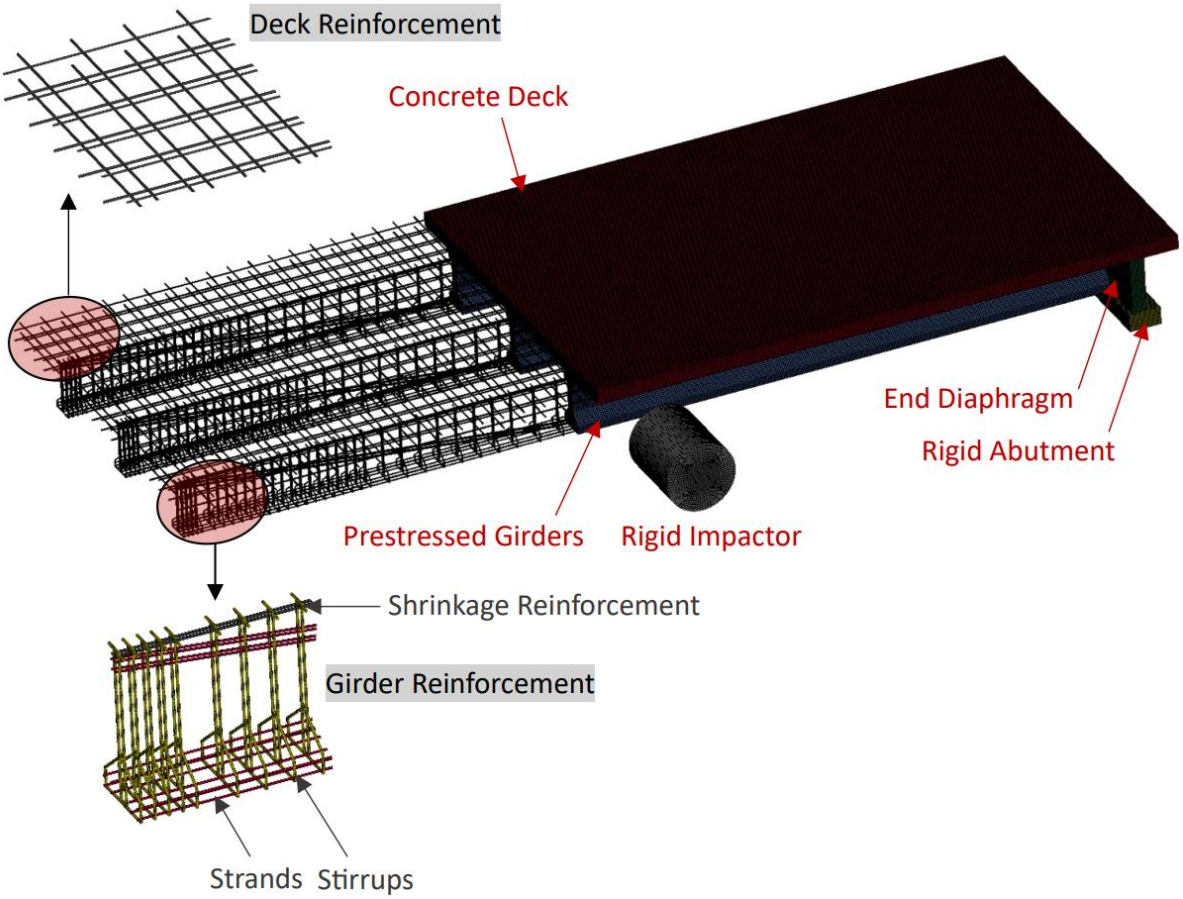

Figure H-40. FE bridge model

H.2.3 Material properties

Concrete

The CSCM material model (*MAT 159) was selected for simulating concrete behavior, based on its robust performance in dynamic loading scenarios as demonstrated previously and supported by prior studies (Gholipour, Zhang, and Mousavi 2018; 2020; 2021; Heng et al. 2021; Zhao, Ye, and Qian 2021; Cao et al. 2019; 2020; Fan et al. 2018; Murray et al. 2007; Murray and others 2007). Key features include:

- Triaxial surfaces: Compression-tension and torsional shear.
- Strain rate effects: Activated using the IRATE flag to simulate increased concrete strength under high strain rates.
- Concrete damage: Modeled using the ERODE parameter, which defines a primary tensile strain threshold for element deletion. For this study, the ERODE value was set at 1.08, representing a maximum primary strain of 8%, as recommended by (Gholipour and Billah 2022).
- Density: 150 pcf (2,400 kg/m³).
- Compressive strength: 8 ksi (55 MPa) for girders; 5 ksi (35 MPa) for the deck and diaphragms.
- Aggregate size: Maximum 0.35 in. (9 mm).

Steel

- Reinforcement bars and prestressing strands were modeled using the *MAT PLASTIC KINEMATIC (MAT 003) model, allowing strain rate effects through the Cowper-Symonds formula. Properties:
- Density: 490 pcf (7,850 kg/m³).
- Elastic modulus: 29,000 ksi (200 GPa) for reinforcement bars; 28,427 ksi (196 GPa) for Grade 270 prestressing strands.
- Yield strength: 66 ksi (460 MPa) for reinforcement bars; and 240 ksi (1,675 MPa) for prestressing strands.
- The *PIECEWISE LINEAR PLASTICITY (MAT 024) model was used for A36 structural steel for the steel channel diaphragms.

H.2.4 Rigid materials

The abutments and rigid impactor were modeled using *MAT RIGID (MAT 020). The impactor's density was adjusted to achieve the desired mass in the parametric study. Boundary conditions constrained the abutment’s vertical movement, while the impactor was free to move in the direction of impact.

H.2.5 Modeling of prestressed concrete

Based on prior evaluations, the temperature-induced shrinkage approach was selected for modeling prestressed concrete. Key details:

- Prestressing strands were modeled using beam elements with 4 integration points.
- Prestressing forces were applied before transient analysis using *DYNAMIC RELAXATION with a tolerance of 1E-03.
- Thermal effects were modeled using *ADD THERMAL COEFFICIENT OF EXPANSION, with temperature vs. time curves defined for dynamic relaxation and transient analysis phases.
- Stress transfer between strands and concrete was handled using the Lagrange-In-Solid constraint, chosen for its efficiency and suitability for large-scale problems with complex reinforcement.

H.3 Study parameters

This research includes an extensive parametric study to investigate the effects of a wide range of parameters on vehicle-prestressed girder bridge collisions. The parametric study matrix is shown in Table 4.2. A rigid impactor, as described in Section 4.2.1, was used to evaluate nine different impact speeds, ranging from 10 mph (16 km/hr.) to 70 mph (113 km/hr.). Additionally, three different impactor masses were considered: 4000 Ibs (2 tons), 8000 Ibs (4 tons), and 12000 Ibs (6 tons). The influence of erosion elements was also analyzed.

Two different impact locations were examined: Full-depth impact: This scenario involved the bottom flange of the girder with a large contact area of 70 in.^{2}, representing the most severe case of maximum force application. Partial-depth impact: This scenario focused on the lower portion of the bottom flange with a significantly reduced contact area of 9 in.^{2}, simulating a situation where the truck grazes the bottom flange of the girder.

In addition to the case without intermediate diaphragms, four alternative intermediate diaphragm configurations were studied: RC.1: A single reinforced concrete diaphragm located at the midspan. RC.2: Two reinforced concrete diaphragms located at the one-third points of the bridge. C.1: A single steel channel diaphragm located at the midspan. C.2: Two steel channel diaphragms located at the one-third points.

This carefully designed parametric study has provided valuable insights into the response of prestressed girder bridges under impact loads, highlighting the influence of key impact parameters. The findings pave the way for enhanced bridge resilience and safety during impact events.

H.4 Finite element model validation

The validation of the finite element (FE) models was carried out through a rigorous process detailed previously. A mesh sensitivity analysis was conducted to ensure that the chosen mesh size produced accurate and reliable simulation results. While mesh sensitivity typically

evaluates numerical solution convergence as the mesh is refined, in explicit analysis, its role is slightly different. Explicit analysis is often used to simulate dynamic events such as impacts, crashes, or explosions, where the structure's response strongly depends on the time evolution of the load and material behavior. The analysis evaluated the effect of varying mesh sizes on result accuracy and stability.

To achieve a balance between computational efficiency and result accuracy, four different mesh sizes were investigated: 1.5 in. (38 mm), 1 in. (25.4 mm), 0.8 in. (20.3 mm), and 0.5 in. (14 mm). As shown in Figure H-41, the sensitivity study results indicate that variations in impact force decreased as the mesh size was reduced from 1.5 in. to 0.6 in. Key findings include:

- Refining the mesh from 1.5 in. to 1 in. led to a 20% increase in impact force.
- Variations in impact force were minimized beyond 1 in., with an increase of less than 4% when the mesh size was further reduced to 0.6 in.
- Displacement variations became negligible after 1 in., with differences of less than 1%.

The computational time was significantly affected by the number of elements:

- Mesh refinement from 1 in. to 0.6 in. resulted in a 620% increase in computational time.
- Due to the size of the erosion elements, changing the mesh size influenced damage visualization. A comparison of damage patterns at different mesh sizes is shown in Figure H-42:
- The 1.5 in. mesh size was insufficient for capturing diagonal cracks.
- The 1 in. and 0.8 in. mesh sizes produced better damage visualization, with closely matching patterns.

Based on these findings, a uniform mesh size of 1 in. was adopted for all FE models to ensure optimal balance between computational efficiency and result accuracy.

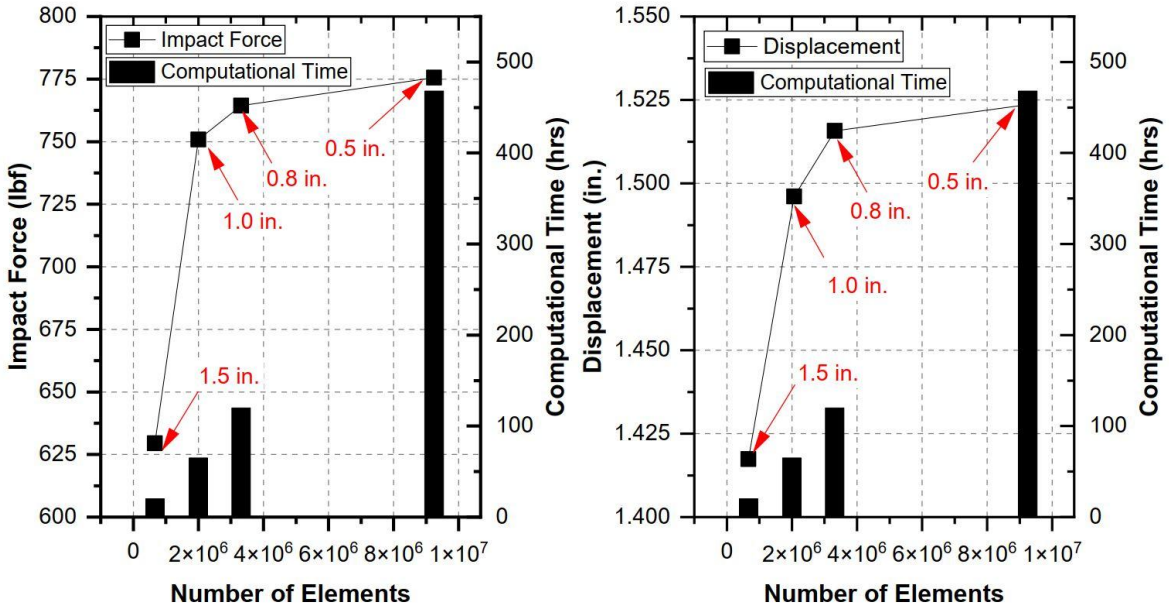

Figure H-41. Mesh sensitivity analysis results

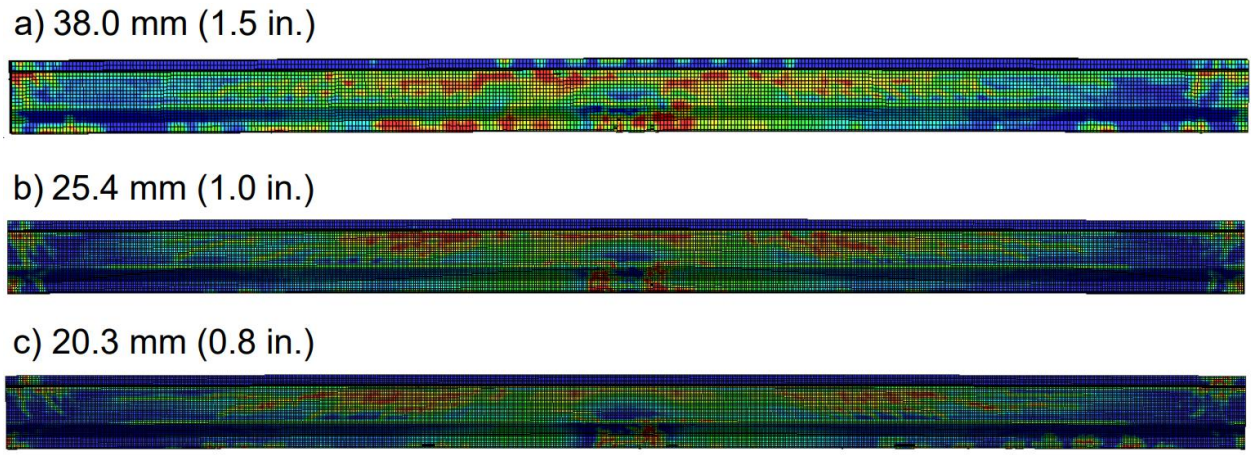

Figure H-42. Damage visualization at different mesh sizes

H.5 Results

H.5.1 Impact speed and mass

The kinetic energy (KE) carried by the impactor is primarily dependent on its speed, leading to a significant increase in KE as the impactor's speed increases. This is particularly evident as the KE experienced a 4800% increase when the impactor speed rose from 10 mph to 70 mph, as shown in Figure H-43.

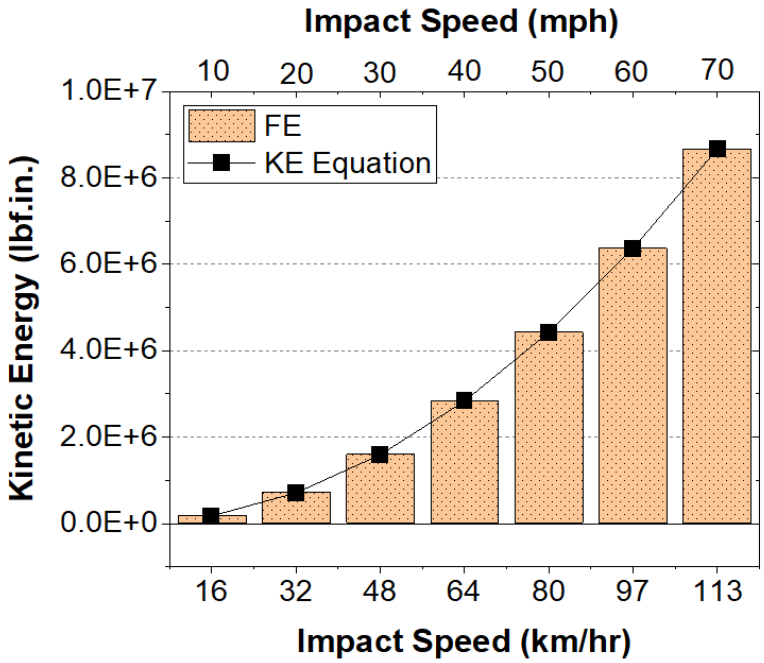

Figure H-43. The kinetic energy of the rigid impactor at different speeds

This proportionate increase in kinetic energy leads to a corresponding rise in impact force. As shown in Figure H-44, the impact force increased from 750 kips at 10 mph to 1366 kips, marking an 80% increase at 60 mph. However, at lower speeds, the structural response exhibited more global behavior with out-of-plane deformation, as indicated by lateral displacements ranging from 1.6 in. at 10 mph to 8.5 in. at 40 mph. Beyond 40 mph, the impact became increasingly localized, resulting in limited displacements. For instance, a lateral displacement of 6.8 in. at 50 mph highlights this transition.

The dynamics of the collision were significantly influenced by the transformation of kinetic energy into internal energy upon contact between the impactor and the girders. This complex process caused structural damage and initiated motion within the impacted girder. As the impactor's velocity increased, the internal energy absorbed by the first girder rose significantly. When the internal energy is insufficient to cause immediate damage at the moment of contact, the kinetic energy of the impactor becomes critical. This imparted kinetic energy increases the girder's internal kinetic energy, leading to greater displacement and permitting the transmission of energy to other bridge components. As shown in Figure H-45, energy transmission between the girders became increasingly restricted as the impact speed increased. The first girder eventually absorbed a larger share of the total internal energy, which rose from 55% at 10 mph to 90% at 60 mph.

Moreover, the peak impact force is influenced by the mass of the impactor. The increased momentum of a heavier impactor results in a higher force exerted on the girder during impact. As illustrated in Figure H-46, the maximum impact force experienced by the girder increased by approximately 5–10% as the impactor mass rose from 4000 Ibs to 8000 Ibs.

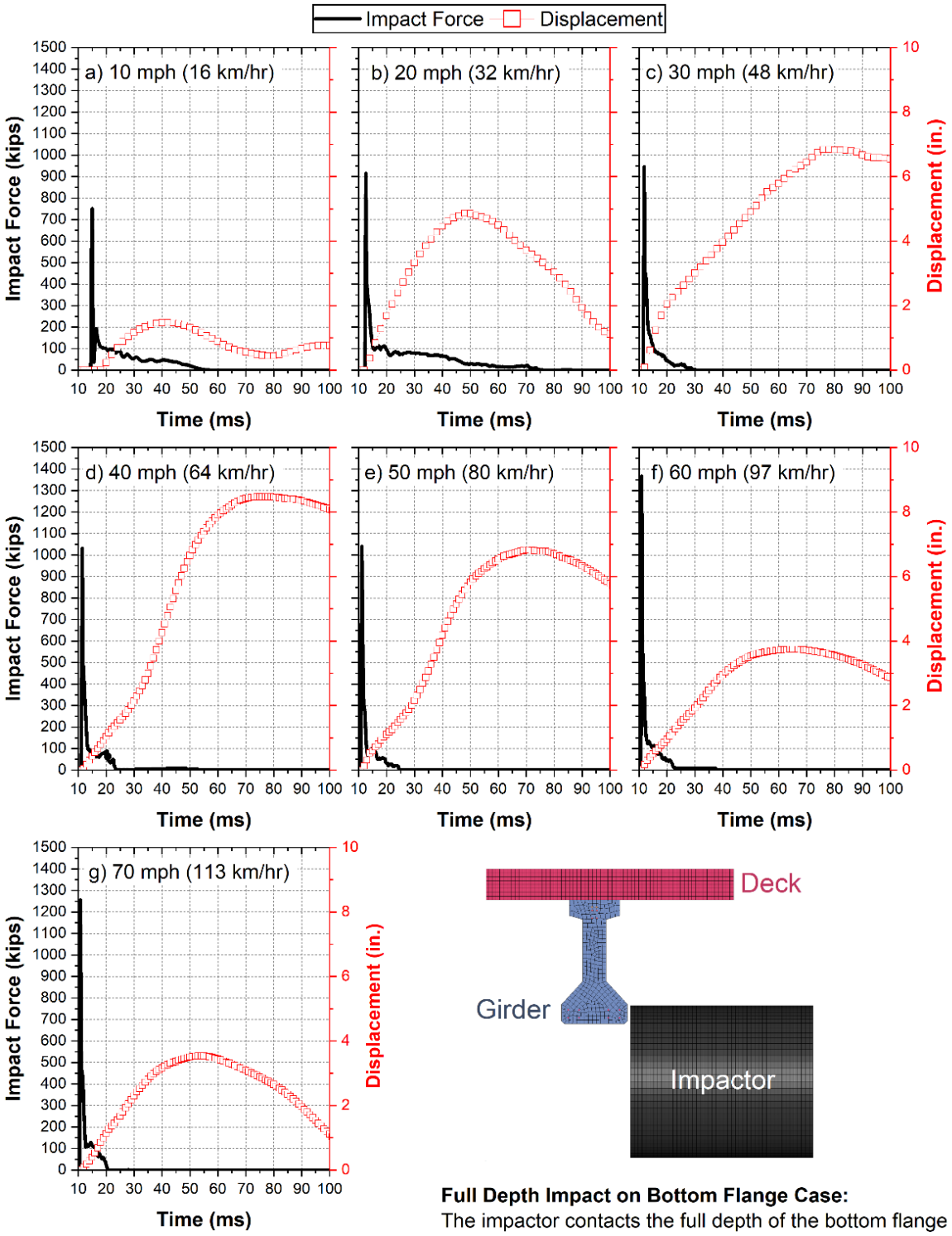

Figure H-44. Impact force and lateral displacements at different impact speeds

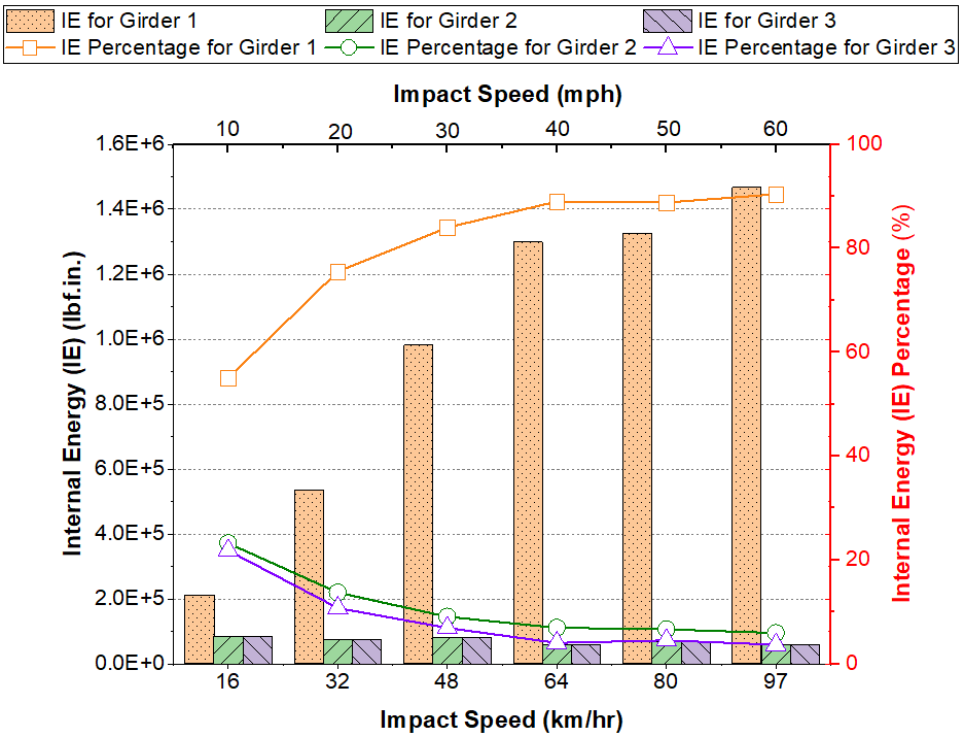

Figure H-45. Internal Energy analysis of the girders at different impact speeds

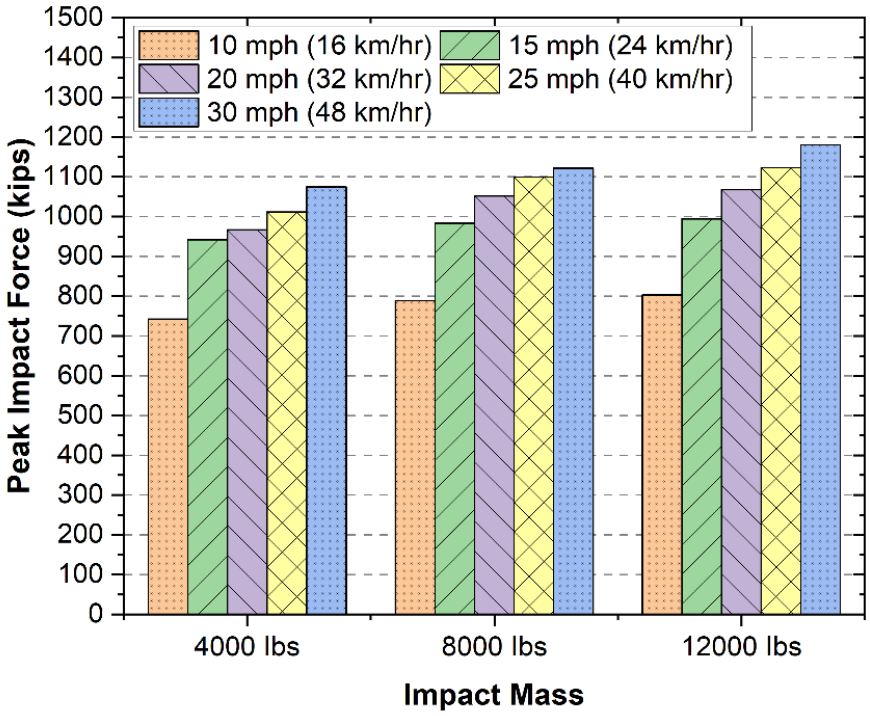

Figure H-46. Internal Energy analysis of the girders at different impact speeds

H.5.2 Use of erosion elements

The use of erosion elements in explicit analysis offers numerous advantages. These features, particularly valuable for dynamic events such as high-velocity impacts, enhance modeling accuracy by realistically depicting the erosion and removal of materials subjected to intense stresses. Erosion features enable a more accurate representation of structural behavior by capturing progressive failure and material removal, especially in scenarios where deformation and failure are critical. Additionally, erosion elements significantly improve computational efficiency in simulations involving short-duration, high-intensity loads by automatically removing unnecessary elements, thereby reducing computational costs.

As part of this research, a comparison was conducted between models with and without erosion elements. As shown in Figure H-47, the findings offer unique insights into the predictive capabilities of these models under various impact conditions. At lower speeds, such as 10 mph, both erosion and non-erosion models predicted similar impact forces and displacements (Figure H-14a). However, as the impact speed and energy increased, a substantial discrepancy emerged. Models without erosion tended to overestimate the impact force at higher speeds. Furthermore, displacement predictions in non-erosion models became increasingly unreliable due to the continued deformation of elements beyond their failure limits (Figure H-47b and c).

Notably, the extensive damage simulated in non-erosion models at high speeds rendered them unsolvable, restricting the investigation to speeds below 30 mph. These findings emphasize the importance of incorporating erosion effects to effectively model and understand the behavior of structures subjected to high-velocity impacts.

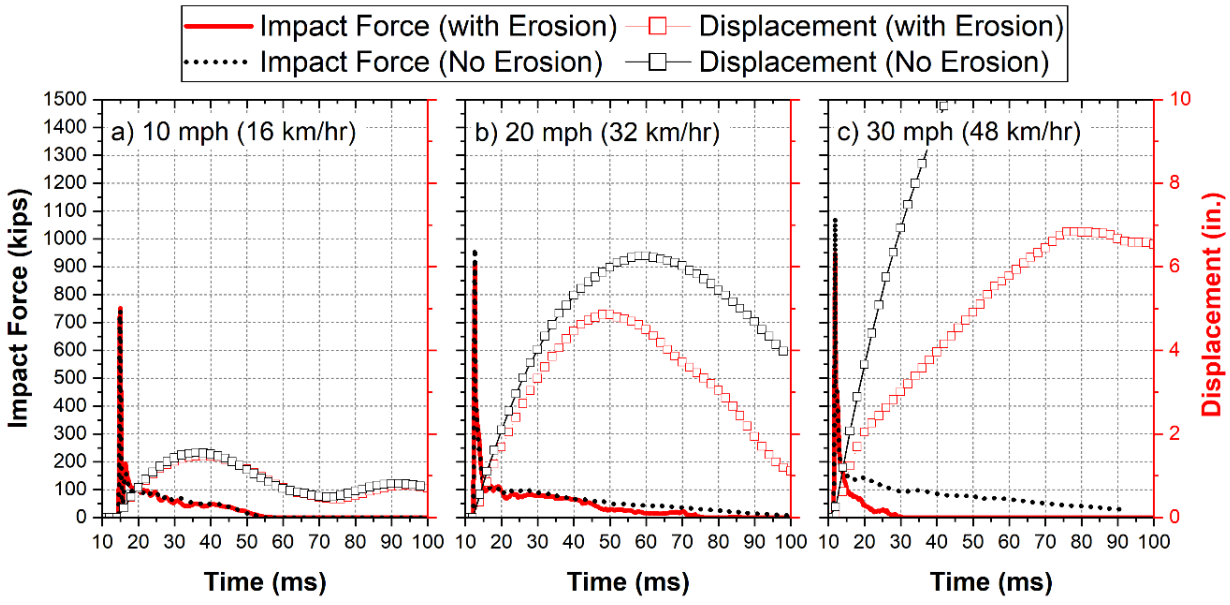

Figure H-47. A comparison between the erosion and non-erosion FE models at different impact speeds

H.5.3 Damage analysis

Local and global damage failures were observed in this study. A frequently observed damage pattern, initially identified by Feldman et al. (1996) [28], is the exterior (fascia) girder torsion-induced shear fracture, commonly associated with side-impact incidents. As illustrated in Figure H-48a, this damage pattern was consistently observed in the finite element (FE) models used in this investigation, with the extent of damage varying according to specific impact conditions. Additionally, as the impact velocity increased, the damage pattern evolved into a more pronounced shear push-out, particularly on the rear side of the girder, as shown in Figure H-48b. Another consistent finding was the occurrence of longitudinal cracking at the connection between the web and the girder flange, as illustrated in Figure H-48c.

The lateral displacement at various points along the girder cross-section was analyzed, as shown in Figure H-49. The greatest displacement occurred at the lowest point of the girder, while the least displacement was observed where the girder connects to the deck. This restraint caused stress concentration, particularly at the top flange, resulting in the formation of both longitudinal and diagonal cracks. Damage patterns on the front and back sides of the bridge girders at different speeds are shown in Figure H-50 and Figure H-51. In addition to the typical diagonal cracks observed in all FE models, direct impacts caused concrete spalling and strand cutting. The extent of concrete spalling increased with impact energy, leading to a greater number of severed strands. The results also highlighted the localization of damage near the impact point, particularly at 40 mph compared to 70 mph. A shear push-out pattern was evident on the rear side of the girders, as shown in Figure H-51, with maximum damage observed at 40 mph, corresponding to localized damage. This damage pattern aligned with the lateral displacement results, which showed the highest displacement at 40 mph, followed by a decrease as speeds increased, consistent with Figure H-44.

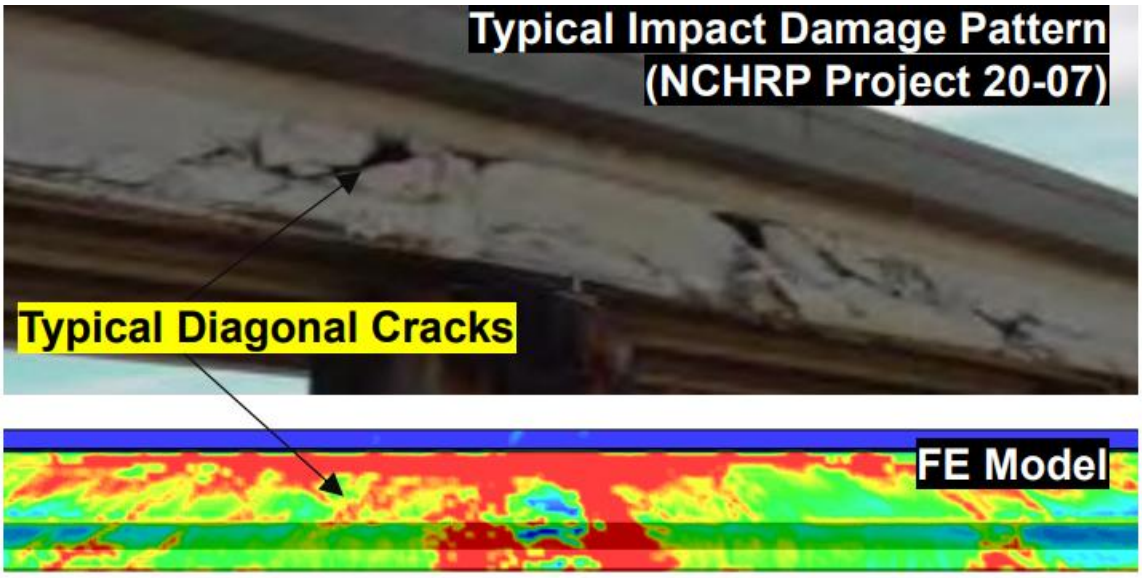

(a) Typical diagonal cracks of the fascia

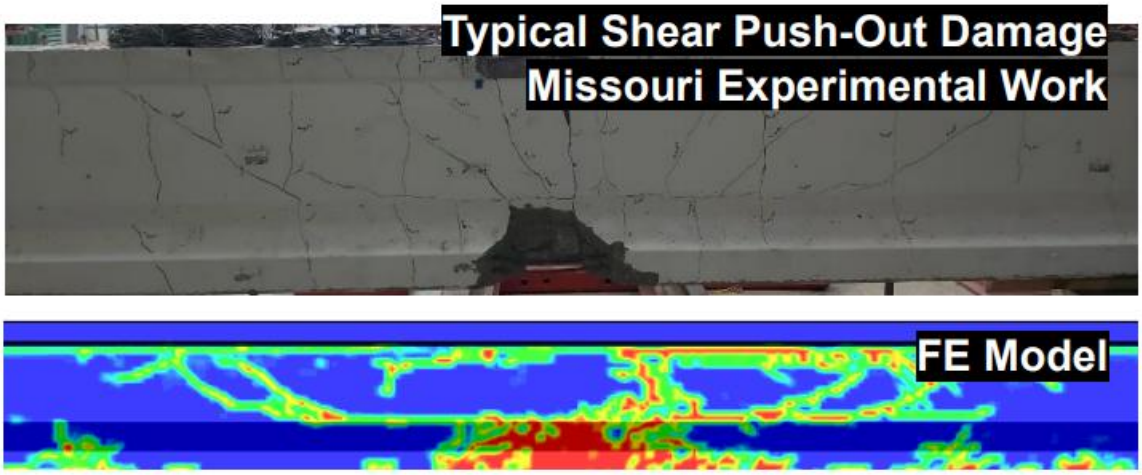

(b) Typical shear push-out damage of the rear side

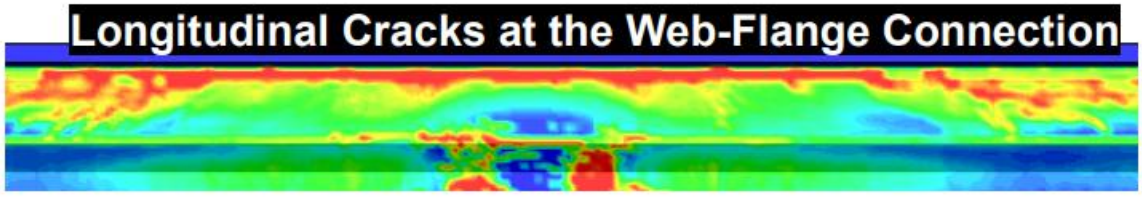

(c) Longitudinal cracks at the web-flange connection

Figure H-48. Typical damage patterns due to lateral impact

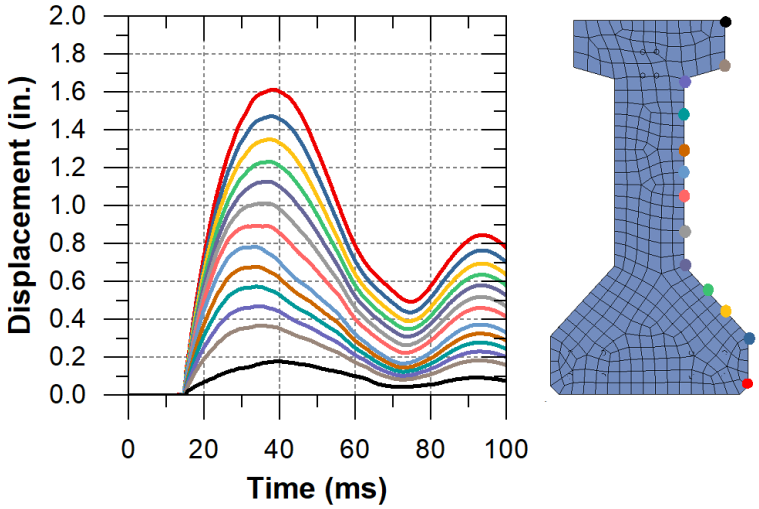

Figure H-49. Lateral displacement of girder at mid-span at different locations during a 10-mph impact

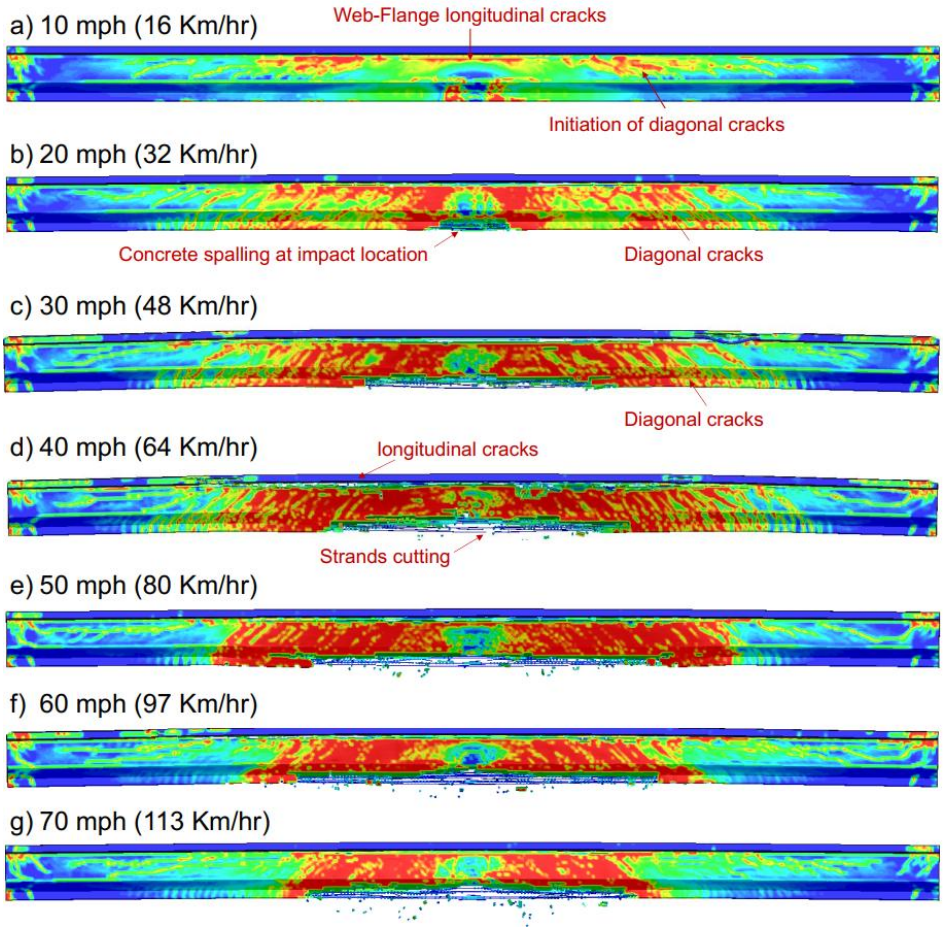

Figure H-50. Damage patterns of the prestressed girders at different impact speeds (front-side view)

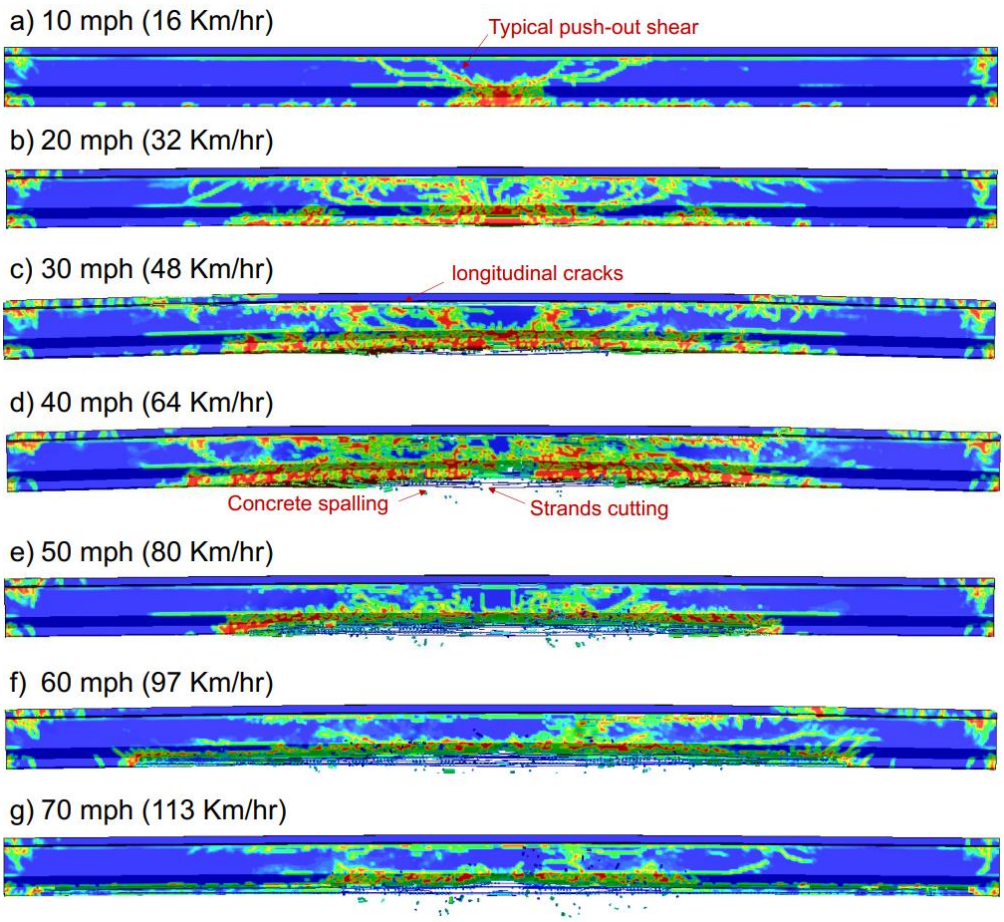

Figure H-51. Damage patterns of the prestressed girders at different impact speeds (backside view)

The FE models provided insights into the response of prestressing strands to impact events. As shown in Figure H-52, strands exhibited varying responses under impact loads:

- Some strands remained unaffected and retained their initial stress.
- Others experienced stress loss due to concrete erosion around the prestressing strands and the lateral displacement caused by the collision.
- Some strands experienced a stress increase within their elastic range, avoiding failure.
- Strands exceeding the yield stress and strain limits were cut, particularly those in direct contact with the impactor, which was severed immediately.

The results showed a significant increase in prestressing strand damage severity as impact energy increased. Figure H-53 classifies strand conditions into three categories: undamaged, up to 40% stress loss, and cut strands. Higher impact speeds corresponded to an increased likelihood of strand cutting and stress loss. Importantly, these findings underscore the need to account for stress loss in strands, as current damage classification methods primarily focus on complete strand cutting (Harries et al. 2012). Even strands appearing to be in good condition may suffer stress loss, compromising the load-bearing capacity of the girders. The results consistently indicated that strand damage was initiated in the first row near the impact location.

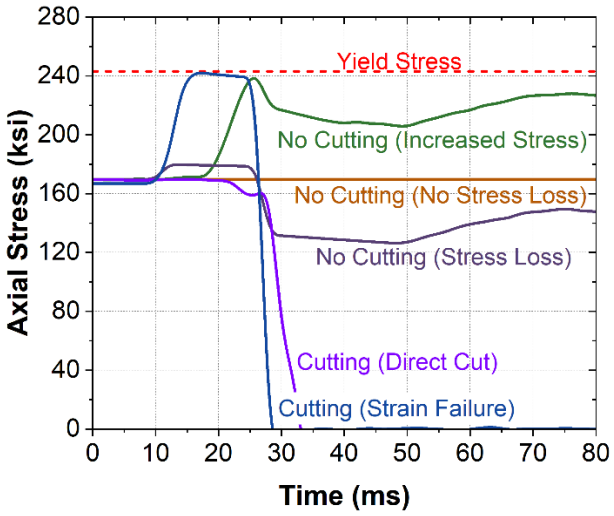

Figure H-52. Response of prestressing strands under impact loads

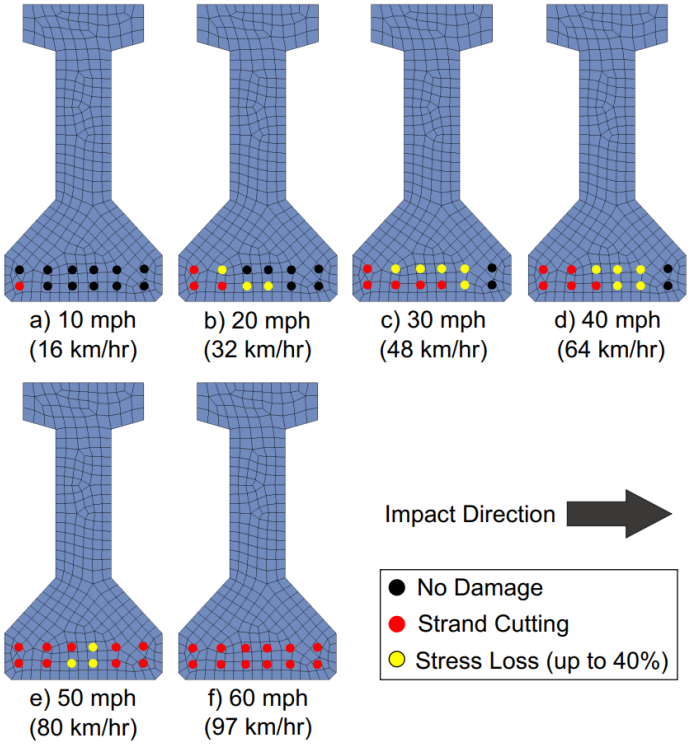

Figure H-53. Prestressing strands damage under impact at different impact speeds

A notable transfer of stresses was observed in the overall response of the bridge to the impact event, particularly at the girder-deck joint contact. The impact load exerted horizontal and vertical load components, both contributing to the formation of longitudinal cracks at the girder-deck joint locations. As the impact energy increased, higher strain magnitudes were transferred to adjacent girders, initiating diagonal cracks, as shown in Figure H-54.

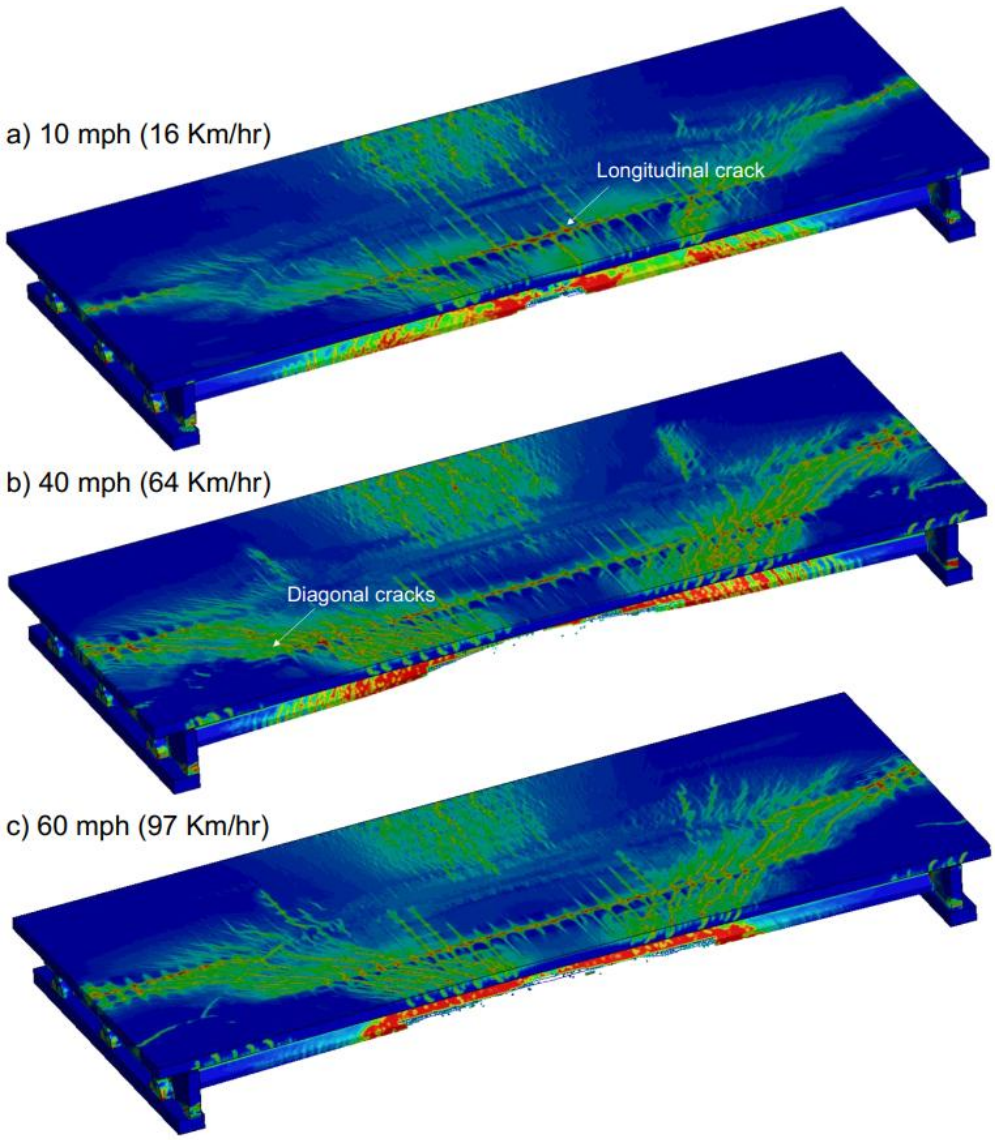

Figure H-54. Overall damage patterns of the prestressed girder bridges at different impact speeds

H.5.4 Impact location

Two impact location scenarios were considered in this study. The first scenario involved a full-depth impact of the bottom flange, with a large contact area of 70 in.², representing the most severe case of maximum force application. The second scenario focused on the impact of the lower portion of the bottom flange, with a significantly reduced contact area of 9 in.², simulating a situation where the truck grazes the bottom flange of the girder.

Figure H-55 compares the impact forces for the full-flange impact case and the partial-flange impact case. The substantial reduction in contact area (approximately 85%) led to a 70–80% reduction in impact forces. Moreover, for the smaller contact area models, the impact force showed minimal variation across different impact speeds. All partial-flange impact models exhibited localized damage, with displacements of less than 0.12 in. The localized damage was

characterized by concrete spalling at the impact location and strand severing, as illustrated in Figure H-56. Additionally, the limited contact area restricted the dissipation of the impactor's kinetic energy by the first girder, causing the impactor to continue moving and impacting subsequent girders.

Changes in strand stresses provided valuable insights into the severity of strand damage under the two impact location scenarios. The full-flange impact scenarios, as shown in Figure H-53, resulted in a significant number of severed strands. In contrast, the partial-flange impact scenarios showed a notable reduction in strand severing, with a maximum of only three severed strands observed in the 70-mph scenario, as shown in Figure H-57.

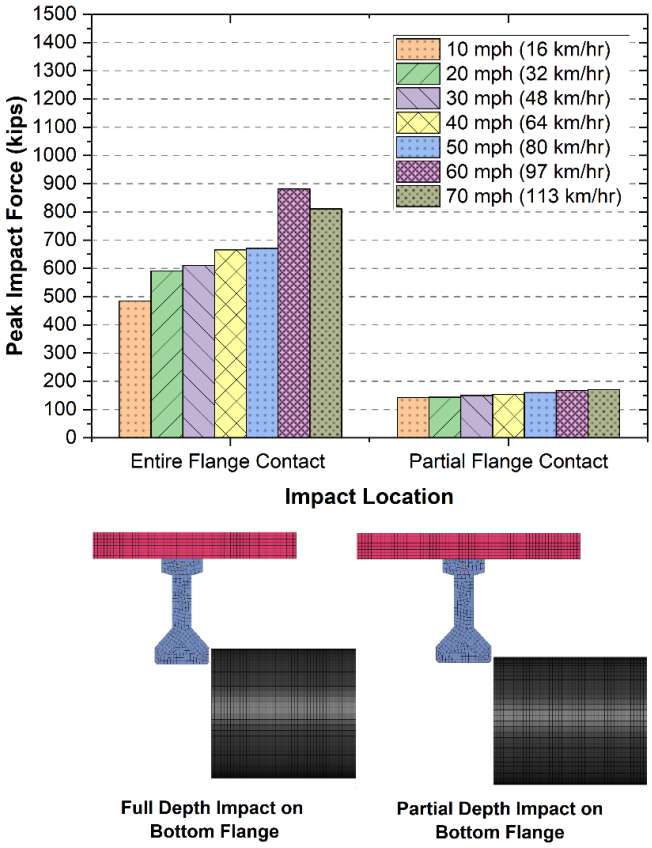

Figure H-55. Effect of impact location on the impact force at different impact speeds

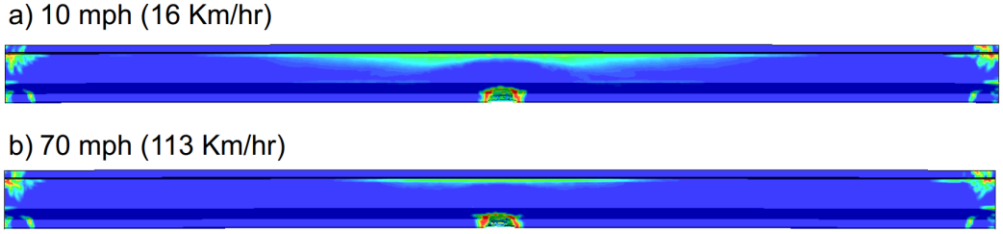

Figure H-56. Damage patterns of the prestressed girders at the partial flange impact scenario (front view)

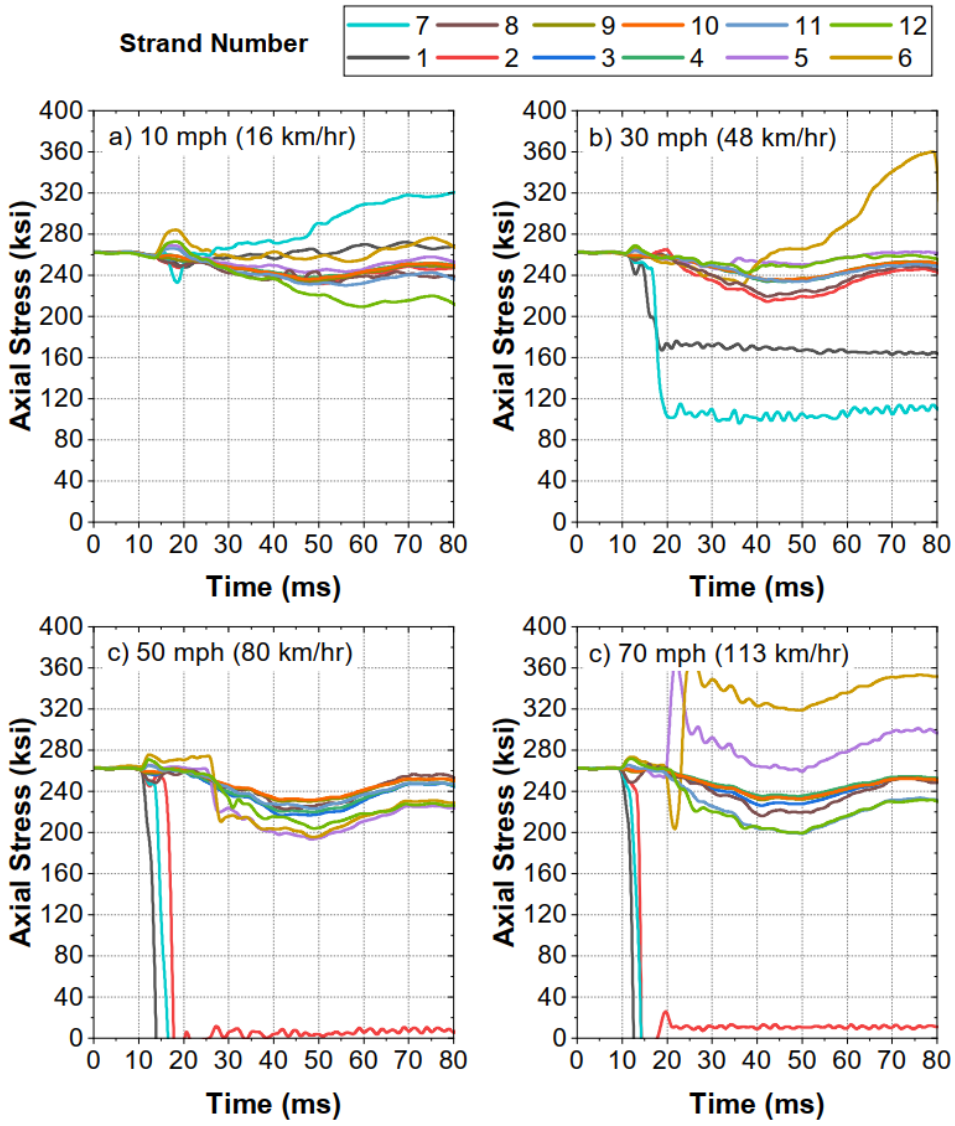

Figure H-57. Variation in the axial stress of the prestressing strands under partial flange impact scenario

H.5.5 Intermediate diaphragms

The use of intermediate diaphragms ensures that the lateral forces are evenly distributed throughout the bridge system. In this study, four intermediate diaphragm cases were investigated and compared to FE models without intermediate diaphragm at different impact speeds, as shown in Figure H-58. While the impact force results showed relatively small variations, the use of a single intermediate diaphragm at the mid-span, specifically at the impact location in our study, resulted in a slight increase in impact force of less than 8%.

The use of intermediate diaphragms played a crucial role in reducing lateral displacement during loading events. The incorporation of a single intermediate diaphragm at the impact location reduced the lateral displacement, in the range of 50- 70%. On the other hand, the use of two intermediate diaphragms reduced the lateral displacements by between 10 and 30%. These findings highlight the importance of intermediate diaphragms in increasing structural

stability and reducing lateral movement during dynamic loading events, contributing to the overall resilience and safety of bridge systems.

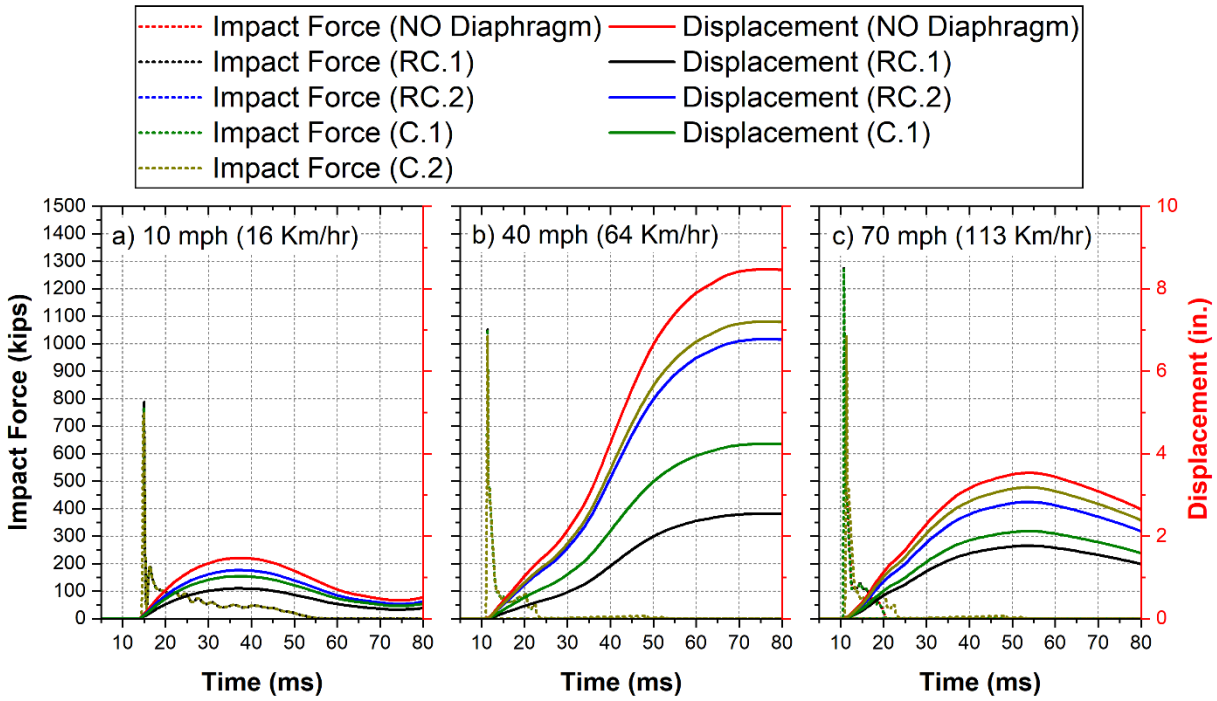

Figure H-58. Effect of using intermediate diaphragms on the impact force and the lateral displacement

H.6 Summary

This study involved high-fidelity finite element (FE) simulations of large-scale prestressed girder bridges under impact loads. An extensive parametric study was conducted, considering various parameters, including impact speed, impactor mass, impact location, and the existence and type of intermediate diaphragms. The primary findings are summarized below:

- Impact Force: Impact force increased from 750 kips at 10 mph to 1366 kips, marking an 80% increase at 60 mph.
- Structural Response: At lower speeds, the structural response exhibited global deformation with out-of-plane displacement, as indicated by lateral displacements ranging from 1.6 in. at 10 mph to 8.5 in. at 40 mph. However, as speeds exceeded 40 mph, the response became localized, resulting in limited displacements. The increased momentum of a heavier impactor led to higher forces being exerted on the girder during impact.
- Energy Absorption: As the impactor's velocity increased, the internal energy absorbed by the first girder rose significantly. When internal energy was insufficient to cause immediate damage, the imparted kinetic energy contributed to increased displacement and allowed for greater energy transmission to other bridge components.

- Damage Responses: Two distinct damage responses were identified: Global damage failures, including longitudinal cracks and diagonal cracks. Local damage failures, such as shear push-out, concrete spalling, and strand cutting.
- Strand Behavior: Strands showed different responses under impact loads. Whereas some strands were substantially unaffected and retained their initial stress, others lost stress at different levels. This loss of stress was attributable mostly to the relaxation caused by concrete erosion around the prestressing strand elements and the lateral displacement caused by the collision. Some strands experienced an increase in the stress within their elastic range and did not reach failure. However, when stress levels exceeded the yield point, accompanied by an increase in strain up to the failure limit, the strands were cut. Furthermore, a subset of strands, particularly those in direct contact with the impactor, were cut directly and immediately.
- Contact Area Reduction: A significant 85% reduction in contact area resulted in a 70–80% decrease in impact forces.
- Intermediate Diaphragms: The inclusion of intermediate diaphragms was critical in reducing lateral displacement during impact events. A single intermediate diaphragm at the impact location reduced lateral displacement by 50–70%.

Appendix I. High Strain Rate Behavior of Low Relaxation

I.1 Introduction

This research work investigates the high strain rate behavior of low relaxation prestressing strands grade 270 in tension. The study aims to fill the gap in understanding the behavior of prestressing strands under high strain rate loadings, which is important for assessing the structural performance of prestressed structures subjected to severe dynamic loadings such as impact and blast. Experimental tests were conducted using the Split Hopkinson Tensile Bar (SHTB) system under strain rates of 400, 800, and 1500 s−1. Each strain rate was applied using three samples, from which the average outcomes were computed. The results showed a significant increase in the material's strength and strain as the strain rate increased. In addition, the results indicated an increase in the dynamic increase factor (DIF), ranging from 5 to 15 percent, as the strain rate increases. The obtained results were used to calibrate two common material constitutive models, Cowper-Symonds and Johnson Cook. The calibrated models can be used to predict the dynamic behavior of materials as a function of strain rate, which is an essential stage in conducting finite element analysis for a variety of applications.

Recent events, whether natural disasters or human-initiated events, showed the susceptibility of prestressed concrete to high strain rate loading, particularly those resulting from collisions and blasts. These structures have come under the spotlight, requiring comprehensive assessments that consider their susceptibility as well as their ability to endure extreme dynamic loads such as hits and blasts (Ngo et al. 2007; Asprone, Cadoni, and Prota 2009a; 2009b).

In RC members subjected to severe dynamic loading, both the concrete and reinforcing bars experience high strain rates (10 s−1 to 1000 s−1) (Cadoni et al. 2015). Under such high strain rates, the apparent strength of these materials increases significantly, with reinforcing steel increasing by more than 50%, concrete in compression increasing by more than 100%, and concrete in tension increasing by more than 600%. These significant changes in material behavior highlight the vital need to take high strain-rate effects into account when evaluating the performance of reinforced concrete structures in dynamic loading scenarios.

A wide range of study work has been conducted on the static and dynamic characteristics of steel reinforcing bars (Mirone, Barbagallo, and Cadoni 2017). Under dynamic loading, rebar strength can rise by up to 60% for strain rates as low as 10 s−1 and up to 100% for strain rates as high as 225 s−1 (Marvar and Crawford 1998). However, while prestressed concrete applications are increasing, the behavior of the prestressing strands under a high strain rate has not been considered yet.

Low-relaxation Grade 270 steel is a high-strength steel that is widely used in construction applications where tensile strength is required. Grade 270 steel is well-suited for projects such as bridges, buildings, and infrastructure, as its tensile strength often exceeds 1280 MPa (Hill 2006; Myers and Bailey 2015). What distinguishes Grade 270 is its" low relaxation" feature, which indicates less prestress force loss over time. This property makes it ideal for prestressed concrete applications, in which the steel is preloaded before the concrete is poured to improve structural stability and reduce deflection and cracking. Grade 270 steel is well-known for its

durability and conformance to industry standards such as ASTM A416, making it a reliable choice for engineers and construction professionals looking for trustworthy high-strength reinforcement for long-lasting and resilient constructions (Myers and Bailey 2015; Shakya and Kodur 2016; Martin and Pellow 1983).

I.2 Experimental testing

The experimental tests were conducted to analyze the high strain rate behavior of low-relaxation grade 270 prestressing strands in tension, in accordance with ASTM E8. Specimens were prepared by machining the wires of a low-relaxation grade 270 prestressing strand to obtain a common geometry of 0.113 in. (2.5 mm) in diameter and 0.45 in. (10 mm) in gauge length. This geometry is commonly used for dynamic testing with the Split Hopkinson Tensile Bar (SHTB) systems. Figure I-59 shows the parent material before machining. Figure I-60 shows the standard specimen dimensions according to ASTM E8. A view of a sample in grips prior to testing is shown in Figure I-61.

Figure I-59. Parent material before machining

The tests were carried out using an REL Split Hopkinson Tensile Bar (SHTB) system, performed under room temperature conditions, and strain rates of 400, 800, and 1500 s−1. Each strain rate was applied using three samples, from which the average outcomes were computed. An illustration of the SHTB system is shown in Figure I-62. The stress, strain, and strain rate were evaluated over time based on the following equations (Cadoni et al. 2015; 2013).

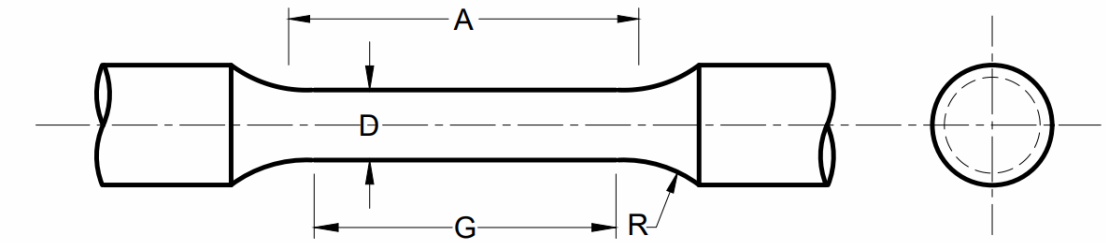

Dimensions, mm [in.]
For Test Specimens with Gauge Length Four times the Diameter [E8]
Small-Size Specimens

Gauge Length (G)	10.0 ± 0.1 [0.450 ± 0.005]
Diameter (D)	2.5 ± 0.1 [0.113 ± 0.002]
Radius of fillet (R)	2 [0.094]
Length of reduced section (A)	16 [0.625]

Figure I-60. Standard tensile sample dimensions according to ASTM E8

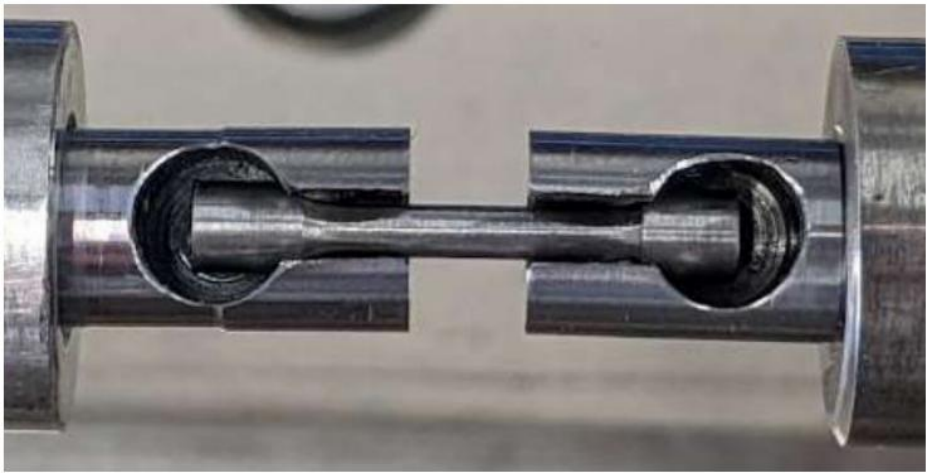

Figure I-61. Top view of sample in grips prior to testing

$$\sigma_E(t) = E_0 \frac{A_0}{A} \epsilon_T(t)$$ Equation I-22

$$\epsilon_E(t) = -\frac{2C}{L} \int_0^t \epsilon_R(t) dt$$ Equation I-23

$$\dot{\epsilon}(t) = -\frac{2C_0}{L} \epsilon_R(t)$$ Equation I-24

Where A_0 is the cross-sectional area, A is the initial cross-sectional area of the specimen's gauge length, L is the gauge length, t is the time, $C_0 = (E_0/\rho)^{1/2}$ is the elasticwave speed, E_0 is the elastic modulus of the bars and ρ is the bar density.

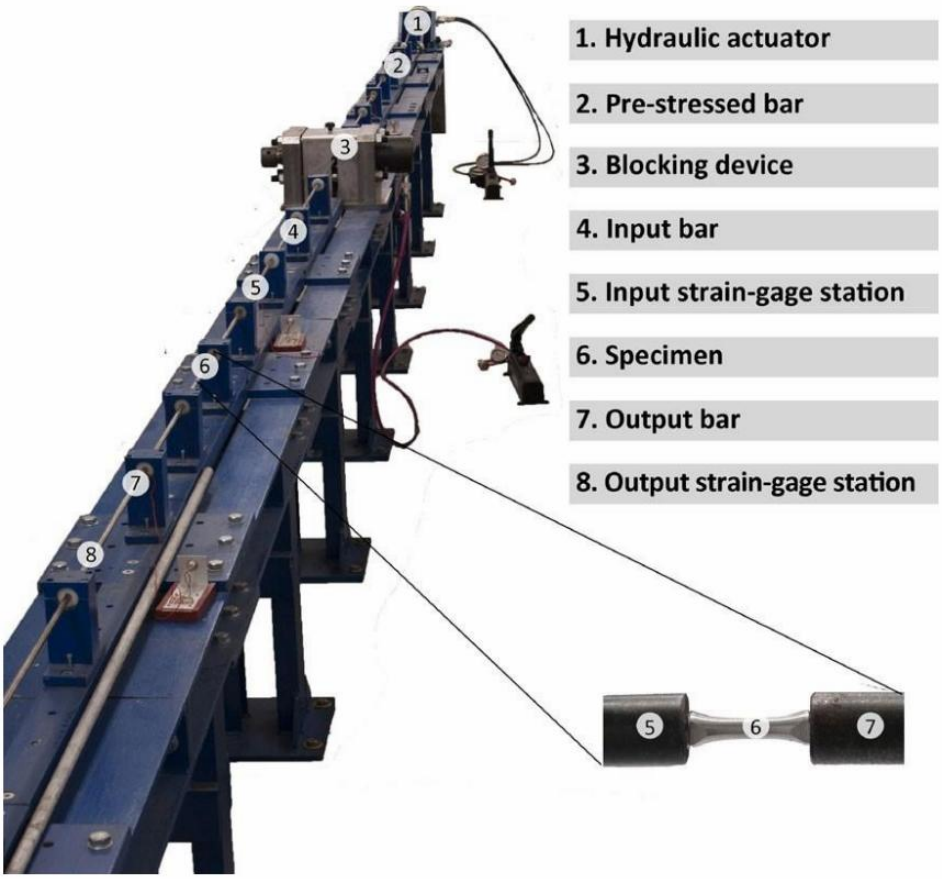

Figure I-62. Split Hopkinson Tensile Bar (SHTB) setup

The results of these tests contribute to a better understanding of the dynamic behavior of low relaxation grade 270, which is crucial for the structural assessment and design of prestressed concrete structures subjected to severe dynamic loading, such as impact and blast. The experimental data obtained from these tests were also used to calibrate material constitutive models, such as Johnson-Cook and Cowper-Symonds models, which are widely used in numerical simulations to predict the behavior of materials under high strain rate conditions.

I.3 Experimental results and discussion

Figure I-63a shows a comparison of the results obtained from the different strain rates. The results show a significant increase in the material's strength and strain as the strain rate increases. Strain rates of 400 s−1 and 800 s−1 have shown similar behavior under tension. The material initially experiences elastic deformation, with a modulus of elasticity equal to 29,000 ksi (200 GPa), when subjected to tensile loading. When the material exceeds a critical stress threshold, the yield stress, and plastic deformation begin. This plastic deformation continues until the material's ultimate tensile strength is attained. At this point, localized necking might appear, eventually leading to material failure via fracture. Remarkably, the strain rate of 1500 s−1 exhibits a distinct behavior. It shows a reduction in yield strength compared to lower strain rates but presents a substantial strain-hardening phase. This stage of strain hardening results in a significant increase in ultimate strength prior to failure.

Previous research has investigated the stress-strain behavior of the grade 270 low-relaxation prestressing strands (Devalapura and Tadros 1992). These studies have resulted in refined stress-strain relationships that line up with the PCI committee equations. To clarify the differences between the dynamic and static behavior of the low-relaxation grade 270 material, the averages of the results were compared to the PCI static equation, as shown in Figure I-63b. The rise in both the yield strength (fy) and the ultimate tensile strength (fu) is apparent as the strain rate increases. Consequently, the strain rate has a significant role in the failure strain and strength.

The 0.2% offset method was used to locate the material's yield strength. A horizontal line is drawn from the yield point, offsetting it by 0.2% strain. The stress value at the intersection of this offset line and the stress-strain curve is then taken as the yield strength (fy) of the material. Figure I-64 shows how the yield strength was determined for a specimen under 400 s−1 strain rate.

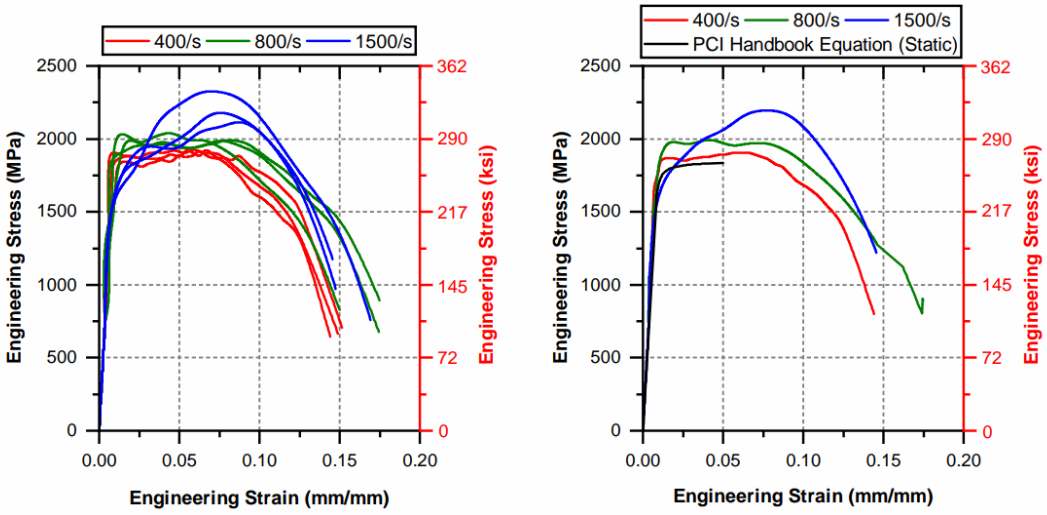

(a) Stress-Strain curves of the low relaxation grade 270 under different high strain rates

(b) Average results in comparison with the PCI equation

Figure I-63. Stress-strain relationship of the low relaxation grade 270

The Dynamic Increase Factors (DIF) for the yield strength of low-relaxation grade 270 were calculated in this study. These factors were calculated by dividing the dynamic strength (fdynamic) by the static strength (fstatic). As shown in Figure I-65, the computed DIF values were then compared to existing steel DIF data from the literature (Cadoni, Fenu, and Forni 2012; Cowell 1965; W. Keenan et al. 1983; W. A. Keenan and CA 1965). The results indicate an increase in DIF values for low-relaxation grade 270, ranging from approximately 5 to 15 percent, as the strain rate increases. In contrast to other steel materials, such as American Iron and Steel Institute (AISI) 304, which showed a significant DIF increase of 20 to 50% at high strain rates, low-relaxation grade 270 appears to be less sensitive to strain rate variations.

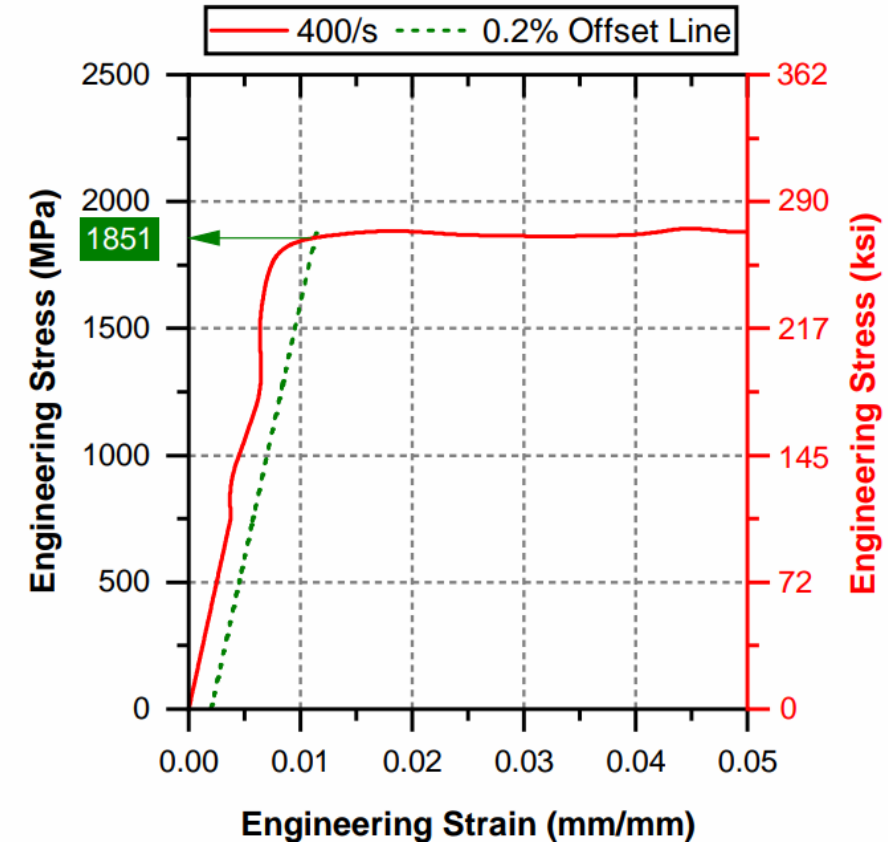

Figure I-64. Locating the yield strength of a 400 s^{-1} strain rate specimen using the 0.2% offset method

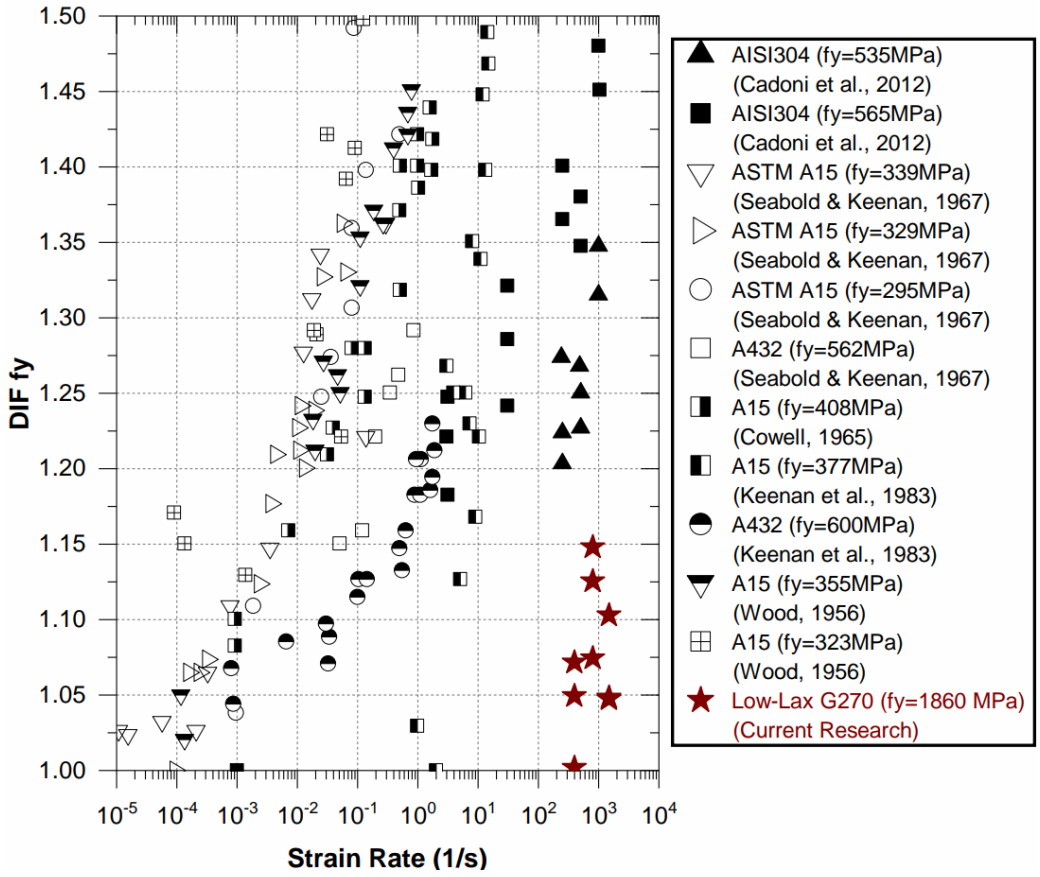

Figure I-65. DIF for yield stress at different strain rates (Cadoni, Fenu, and Forni 2012; Cowell 1965; W. Keenan et al. 1983; W. A. Keenan and CA 1965)

I.4 Calibration of material constitutive models

Numerous material constitutive models reported in the literature can be used to predict the strain rate sensitivity. These equations provide the ability to predict the dynamic behavior of materials as a function of strain rate, which is an essential stage in conducting finite element analysis for a variety of applications.

In this context, one extensively used constitutive model developed by Cowper and Symonds (Wood 1956), has acquired a lot of attention. This model establishes a connection between dynamic stress (fdynamic), static yield true stress (fstatic), and strain rate ($\dot{\varepsilon}$), all governed by two material constants, D and q, see Equation I-25. Using the obtained results, we were able to determine the Cowper-Symonds parameters, as shown in Figure I-66, enabling us to use them in the finite element modeling.

$$\frac{f_{dynamic}}{f_{static}} = 1 + \left(\frac{\dot{\varepsilon}}{D}\right)^{1/q}$$

Equation I-25

Furthermore, Johnson and Cook proposed an additional prominent constitutive materiel model (Cowper, Symonds, and others 1957), which is well known and is extensively used for

simulating dynamic events, particularly those involving material strength. The flow stress equation, Equation I-26, defines the relation between the equivalent stress σ, equivalent plastic strain ε, strain rate $\dot{\varepsilon}$, and the dimensionless temperature. T^{*m}.

$$\sigma = (A + B\varepsilon^{n})(1 + Cln\dot{\varepsilon}^{*})(1 - T^{*m})$$

Equation I-26

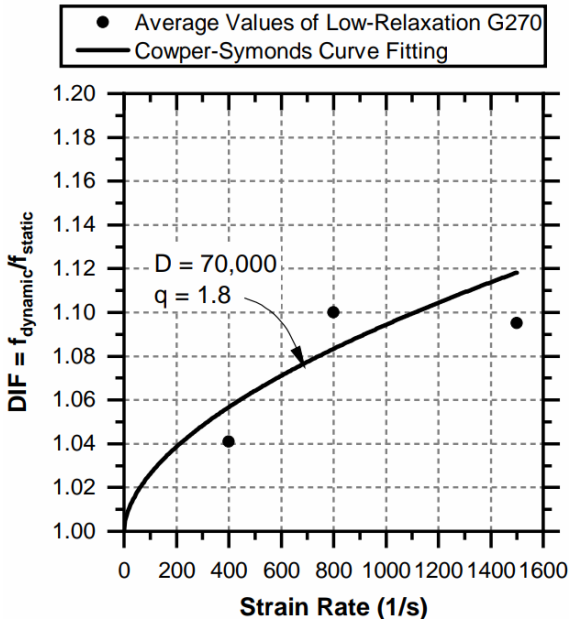

Figure I-66. Cowper-Symonds model calibration of the low-relaxation grade 270

The material is defined by a set of constants in the Johnson-Cook equation. These include A, which indicates the material's yield stress under standard conditions. The strain hardening variable is represented by parameter B, which provides information about the material's response to deformation. Another important factor is n, the strain hardening exponent, which is used to calculate the material's sensitivity to strain. Furthermore, C, the strain rate-related strengthening factor, determines how the material reacts to changes in deformation rate. Finally, m, the thermal softening coefficient, governs the material's sensitivity to thermal effects.

In order to determine the material constants required for the Johnson-Cook equation, the yield stress constant A was determined using the previously described 0.2% offset approach. Following that, the two constants B, which represents the strain hardening constant, and n, which represents the strain hardening exponent, were calculated after neglecting the thermal effect. The natural logarithm was applied on both sides of the equation to simplify our analysis, resulting in the modified form Equation I-27 (Johnson and Cook 1985). A linear relationship graph between ln(σ - A) and ln ε was developed. Then, linear regression was used to find the two constants B and n.

$$\ln(\sigma - A) = nln\varepsilon + lnB$$ Equation I-27

Following that, the material constant C was calculated using a linear regression fitting of the $\frac{\sigma}{A+B\varepsilon^n}$ and $ln\dot{\varepsilon}^*$ curve (Sirigiri et al. 2022). The effect of temperature was neglected in this study. The values of the used parameters are provided in Table I-12. To fully evaluate the material parameters, an FE model of the experimental test was performed using an ANSYS workbench. The specimens were modeled using solid elements and the Johnson-Cook material model. A maximum mesh size of 0.008 in. (0.2 mm) was maintained. The finite element model is shown in Figure I-67. In addition, the Johnson-Cook failure model was defined to include the material behavior under failure. The failure model successfully predicted the necking development and the failure pattern, closely matching the experimental observations, as shown in Figure I-68.

Table I-12: Johnson Cook material parameters

Property	Value
Initial Yield Stress (A)	255 ksi
Hardening Constant (B)	112 ksi
Hardening Exponent (n)	10
Strain Rate Constant (C)	0.1
Damage Constant (D1)	0.025
Damage Constant (D2)	16.93
Damage Constant (D3)	-14.8
Damage Constant (D4)	0.0214
Damage Constant (D5)	0

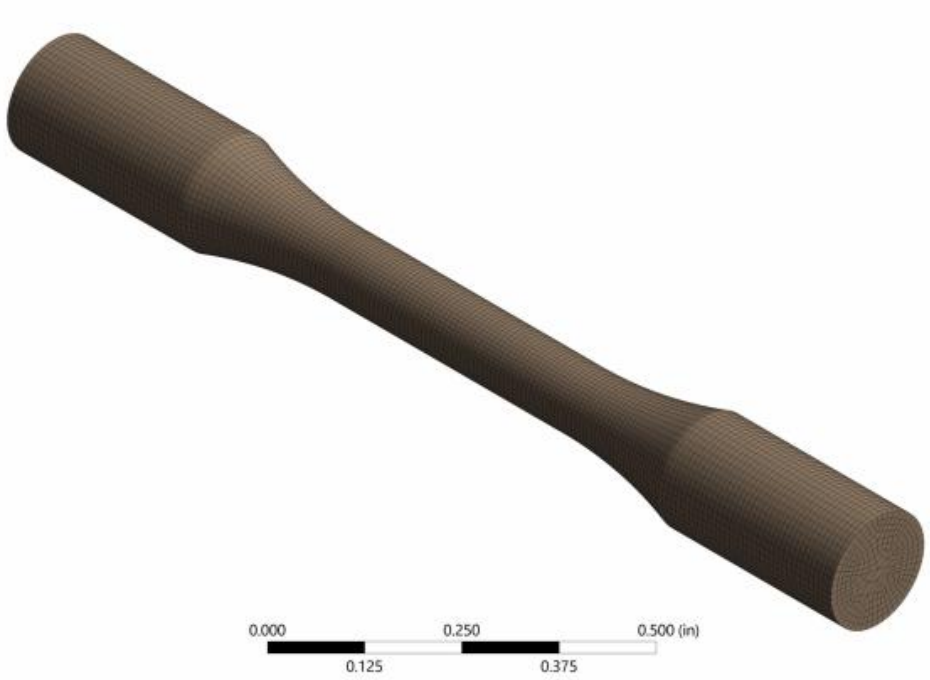

Figure I-67. The FE model of the low-relaxation grade 270 specimen (mesh size = 0.008 in.)

(a) Finite element model failure (b) Experimental specimen failure

Figure I-68. Failure shape of the low-relaxation grade 270 under high strain rates

A fixed boundary condition was applied at one end and a tension load was applied at the other end with strain rates of 400, 800, and 1500 s^{-1}. As can be seen in Figure I-69, the results were compared to the experimental results and showed a good agreement.

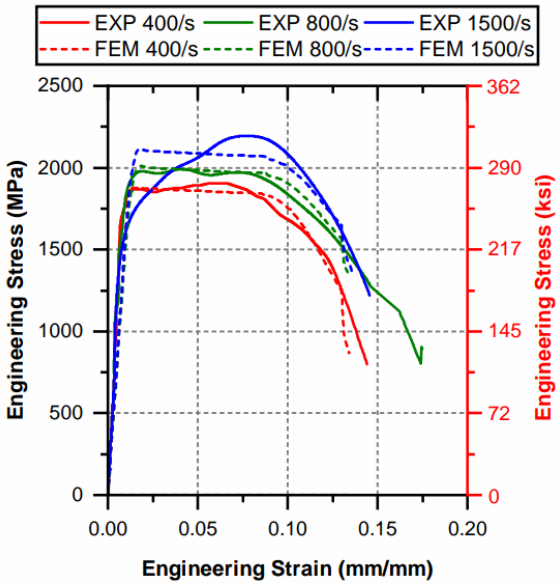

Figure I-69. Finite element model validation using Johnson-Cook material model

I.5 Summary

The high strain rate behavior in tension of low-relaxation grade 270 steel was investigated in this study. The results showed a significant increase in the material's strength and strain as the strain rate increased. Remarkably, the strain rate of 1500 s−1 exhibits a distinct behavior. It shows a reduction in yield strength compared to lower strain rates but presents a substantial strain-hardening phase. In addition, the dynamic increase factor (DIF) results showed an increase, ranging from 5 to 15 percent, as the strain rate increased. However, compared to other steel materials, low-relaxation grade 270 appears to be less sensitive to strain rate variations. The obtained results were used to calibrate two common material constitutive models, Cowper-Symonds and Johnson Cook. The calibrated models can be used to predict the dynamic behavior of materials as a function of strain rate, which is an essential stage in conducting finite element analysis for a variety of applications.